2019

# Manufacturing effects on water cavitation in long L/D sharp edge inlet orifices

Robert Dalton Hicks

# MANUFACTURING EFFECTS ON WATER CAVITATION IN LONG L/D SHARP EDGE INLET ORIFICES

by

ROBERT DALTON HICKS

A THESIS

Submitted in partial fulfillment of the requirements
for the degree of Master of Science in Mechanical Engineering
in
The Department of Mechanical and Aerospace Engineering
of
The School of Graduate Studies
of
The University of Alabama in Huntsville

HUNTSVILLE, ALABAMA
2019

In presenting this thesis in partial fulfillment of the requirements for a master's degree from The University of Alabama in Huntsville, I agree that the Library of this University shall make it freely available for inspection. I further agree that permission for extensive copying for scholarly purposes may be granted by my advisor or, in his/her absence, by the Chair of the Department or the Dean of the School of Graduate Studies. It is also understood that due recognition shall be given to me and to The University of Alabama in Huntsville in any scholarly use which may be made of any material in this thesis.

R Dalton Hicks 5/7/2019

(student signature) (date)

THESIS APPROVAL FORM

Submitted by Robert Hicks in partial fulfillment of the requirements for the degree of Master of Science in Mechanical Engineering and accepted on behalf of the Faculty of the School of Graduate Studies by the thesis committee.

We, the undersigned members of the Graduate Faculty of the University of Alabama in Huntsville, certify that we have advised and/or supervised the candidate on the work described in this thesis. We further certify that we have reviewed the thesis manuscript and approve it in partial fulfillment of the requirements of the degree of Master of Science in Aerospace Systems Engineering.

Robert A Frederick Jr Committee Chair

Dr. Robert A. Frederick (Date)

David Lineberry 5/7/2019

Dr. David M. Lineberry (Date)

J Schneider 4/30/19

Dr. Judith A. Schneider (Date)

D. Keith Hollingsworth 5/6/19 Department Chair

Dr. Keith Hollingsworth (Date)

Shankar Mahalingam for SM 5-8-19 College Dean

Dr. Shankar Mahalingam (Date)

5/29/19 Graduate Dean

Dr. David Berkowitz (Date)

ABSTRACT

The School of Graduate Studies

ABSTRACT

The School of Graduate Studies

The University of Alabama in Huntsville

Degree Master of Science College/Dept. Engineering/Mechanical and Aerospace Engineering

Name of Candidate Robert Dalton Hicks

Title Manufacturing Effects on Water Cavitation in Long L/ D Sharp Edge Inlet Orifices

Additive manufacturing is becoming prevalent in the field of fluids and flow control with the advent of Selective Laser Sintering (SLS) and Selective Laser Melting (SLM). Due to the roughness of additively manufactured components, parts routinely need post-machining to reduce surface roughness and match the characteristics of subtractively manufactured components. This research aims to quantify the effects of layer-induced surface roughness on effective cross-sectional area reduction and cavitation onset conditions.

Tests were performed on a 3/16" diameter, long length-to-diameter ratio ($L/D$ = 20), sharp edged inlet orifice geometry using water at ambient temperature conditions. Tests were performed over a range of Cavitation Numbers, $K$, from $K$=1.6 to $K$=1.0. This was achieved by measuring pressure upstream of the venturi and controlling the backpressure applied. Upstream pressure was 500 psig with a programmable backpressure globe valve set to follow a setpoint schedule of Cavitation Numbers. This was to determine the effective area ($C_c$*$A$) as used in the Nurick model and the cavitation onset cavitation number ($K_{crit}$) which will be compared between venturis with different manufacturing methods and therefore roughness. Arithmetic mean roughnesses ranging from 0.26 µm to 26.85 µm were tested using subtractive manufacturing techniques, Fused Deposition Modeling, and Selective Laser Melting.

Results found shown an appreciable reduction in effective flow area with increasing roughness. Decreases in $C_c$ of 12.3% from a smooth bore orifice to that of the roughest configuration tested were found. Additionally, delays in cavitation offset were observed with cavitation onset occurring at $K$=1.08 rather than the predicted $K$=1.45 for the roughest configuration tested.

Abstract Approval:

Committee Chair

Department Chair

Graduate Dean

ACKNOWLEDGEMENTS

I would like to thank my committee for their work in the late hours of the day to review my writings and the numerous emails back and forth to get this document to where it is. I would like to thank my advisor, Dr. Frederick for giving the amount of time that he has given. I want to thank my family; Lynda, Rob, and Collin, for dealing with the stress and confusing schedules that this has created along with all the nervous late-night phone calls and talks about my work, even though they didn't understand the subject matter. I want to thank the Center for Applied Optics and Mr. Ted Rogers for all the work they performed with the utmost quality, done out of the goodness of their hearts, the Alabama Space Grant Consortium for their financial support during the first year of this work, and Arctic Slope Regional Corporation Propulsion Engineering Center for the donation of time, materials, and expertise. I want to thank Evan Unruh, Evan Tingley, Erik Korzon, Amit Patel, and the rest of the research family at the UAH Propulsion Research Center for sharing in the work and good times in the office. I want to further give thanks to Evan Unruh for acting as my second pair of hands, shuttling parts to and from individuals while I've lived 700 miles away. Lastly, I'd like to thank Shelby Montgomery, who has spent this entire journey with me as my every day support team. She has dealt with the financial, time, and emotional results of this work and has helped to keep me moving in the forward direction from Day 1.

# TABLE OF CONTENTS

# LIST OF FIGURES

**Figure** **Page**

# LIST OF TABLES

# LIST OF SYMBOLS

| SYMBOL | DEFINITION |
|---|---|
| $A_{eff}$ | Effective Flow Area |
| $A_{geo}$ | Geometric Area |
| $C_c$ | Contraction Coefficient |
| $C_D$ | Discharge Coefficient |
| $C_v$ | Velocity Coefficient |
| $f$ | Frequency |
| $K$ | Cavitation Number |
| $St$ | Strouhal Number |
| $St_p$ | Peak Strouhal Number |
| $A$ | Area |
| $\varepsilon$ | Roughness |
| $\mu$ | Viscosity |
| $V$ | Velocity |
| $P$ | Pressure |
| $P_v$ | Vapor Pressure |
| $P_1$ | Upstream Pressure |
| $P_2$ | Downstream Pressure |
| $\dot{m}$ | Mass Flow |
| $\rho$ | Density |
| $r$ | Inlet Radius |
| $d$ | Orifice Diameter |
| $D$ | Orifice Diameter or Upstream Diameter |
| $L$ | Orifice Length |
| $t$ | Orifice Length/Thickness |
| $L_h$ | Hydrodynamic Entrance Length |
| $K_{crit}$ | Critical Cavitation Number |
| $C_{Dcrit}$ | Discharge Coefficient at Critical Cavitation Number |
| $Re$ | Reynolds Number |

| | |
|---|---|
| *Re\St* | Reynolds – Strouhal Number |
| *Rp* | Maximum profile peak height |
| *Rv* | Maximum profile valley depth |
| *Ry* | Maximum peak to valley height |
| *Rt* | Total height |
| *Ra* | Average deviation |
| *Rq* | Root Mean Square Deviation |
| *S* | Mean Spacing of local peaks in profile |
| *Sm* | Mean width of profile elements |
| *Rsk* | Skewness |
| *Rku* | Kurtosis |
| *Δq* | Root mean square slope |
| *v* | Kinematic Viscosity |

# CHAPTER 1

# INTRODUCTION

Cavitation is a phenomenon which occurs when the velocity of a fluid increases to the point where the minimum local static pressure drops below the fluid vapor pressure and the fluid effectively boils [1]. Cavitation has numerous beneficial uses across many industries as well as many consequences that present engineering design challenges. With uses in medical, manufacturing, and fluid control, the phenomenon's effects can be exploited for beneficial purposes. Notable work on the effects of cavitation are due to its consequences on propellers, turbomachinery, and other applications where high flow velocities substantially lower the fluid pressure. Osborne Reynolds published initial descriptions of the phenomena causing cavitation in 1873 [2]. He investigated why propellers on steamships would sometimes under high speed lose efficiency and grip on the water. Research work on cavitation has continued in applications such as pump design, inducer design, watercraft and propulsion design, in order to minimize the detrimental effects of the cavitation or increase its useful qualities. Recent work has been looking at the role of surface roughness on the cavitation phenomenon.

## 1.1 Objective

This work seeks to determine the relative effects of surface roughness on the cavitation phenomenon for long *L/D* sharp edge inlet orifices in quasi-steady-state operation. More specifically, the objective of the work is to investigate the effects of surface roughness on the effective flow area of these orifices and their resistance to flow along with any subsequent changes to the onset of cavitation. This will impact design considerations for long *L/D* sharp edge inlet orifice devices.

## 1.2 Scope

The scope of this experimental study includes the use of a long *L/D* (*L/D*=20) sharp edge inlet orifice geometry produced using Subtractive Manufacturing, Fused Deposition Modeling, and Selective Laser Melting manufacturing methods to create orifices with arithmetic mean roughnesses ranging from 0.26 μm to 26.85 μm  Tests were performed using manipulations of downstream pressure (0 - 200 psig) with constant upstream pressure of 500 psig to obtain a range of cavitation numbers ranging from $K$ = 1.6 to $K$ = 1.0 in a water flow system. Water flowrates during the tests are in the range of 1-2 lbm/sec. All test samples are designed to a 3/16" orifice diameter. This is all performed while attempts are made to offset effects of the inlet radius and deviations in orifice diameter due to manufacturing differences.

## 1.3 Approach

Tests were performed using the High Pressure Spray Facility (HPSF) at the Johnson Research Center Facility (JRC) of the Propulsion Research Center (PRC) of the University of Alabama in Huntsville (UAH). Using a controllable backpressure globe valve a simple flow circuit was created to control the set pressure downstream of the test samples in order to attain specific test conditions. Using both static pressure transducers and high frequency dynamic pressure transducers ahead of and behind the test section the conditions before and after the sample can be determined. To meet desired sample surface roughness, a variety of manufacturing methods were used. To simulate a prototype of a system, samples were manufactured using polylactic acid (PLA) with a Fused Deposition Modeling (FDM) process. This is used as a high roughness condition. Additional samples were made on a Selective Laser Melting (SLM) process which represents metal additive manufactured processing of parts suitable for high pressure fluid flows. Lastly,

subtractively manufactured samples were made to provide samples with the lowest surface roughness.

### 1.4 Anticipated Results

From this investigation, the anticipated outcome is that with controlled inlet edge radius and orifice diameter, the effective flow area of the orifice would decrease with increased roughness and the onset of cavitation would occur at a lower value of Cavitation Number than the onset in a smooth orifice [3].

### 1.5 Outline of Report

This report will first detail the background of the main research area and review the relevant literature. Additional discussion will be made on the area of cavitation and manufacturing processes. This includes the differentiating geometries and definitions of the phenomenon of cavitation. Discussion on the setup of the test section and the test procedures will precede the discussion of the results for all test specimens. Discussion of the results will then follow along with a recommendation of future work.

# CHAPTER 2

# BACKGROUND

## 2.1 Overview of Cavitation & Bubble Formation

Cavitation can be described as "as the process of nucleation in a liquid when the pressure falls below the vapor pressure" [4, Ch. 1]. Cavitation has effects both in internal flows such as venturi-style flowmeters, orifices, inducers in pumps, and in external flows such as submarines, propellers, etc. Cavitation can cause large degrees of damage to parts and systems [5]. This damage is due to the bubbles created during the process collapsing, leaving a high stress location in the fluid and a very high local temperature as the vapor is compressed by the liquid front. This temperature can be upwards of 6700 K [4, Ch. 3]. This process on the whole can be equivocated to boiling and shares many qualities with boiling but is complicated by the fluid dynamics of the system [4, Ch. 1].

This study focuses on internal pipe flow cavitation. Certain dimensionless parameters are used in the study of cavitation. The definitions of these parameters depend on the geometry under investigation and whether the flow is internal or external. The definitions that will be used in this work include the Cavitation Number, *K*.

$$\boldsymbol{K = \frac{P_1 - P_v}{P_1 - P_2}} \qquad \textbf{1}$$

and the Contraction Coefficient, $C_c$

$$\boldsymbol{C_c = \frac{A_{eff}}{A_{geo}} = \frac{\dot{m}}{A_{geo}\sqrt{2\rho(P_1 - P_v)}}} \qquad \textbf{2}$$

The Cavitation Number is used to describe the ratio of the pressure drop from the upstream injection pressure to the fluid vapor pressure to that of the pressure drop across the device [6]. Cavitation Number is generally a ratio showing the relative magnitudes of the stability of the fluid

state (pressure above saturation line) to the pressure drop across the device. The closer the cavitation number approaches to $K = 1.0$ the more likely it is to cavitate as the conditions that the fluid is being exposed to are approaching the stability limit of the fluid. A value of $K \leq 1$ indicates flashing flow in which the downstream fluid never re-collapses to a liquid state. A flow will cavitate when the Cavitation Number drops below a critical value ($K_{crit}$). The Critical Cavitation Number depends largely on the condition of solid boundaries, partial pressure of dissolved gases, turbulent and viscous effects, and dissolved solids in the water. All of these decrease the tensile strength of water or create local areas of lower static pressure such that the working fluid can more easily flash to a gaseous state [4, Ch. 1], [7].

For general fluid flows not undergoing cavitation, Discharge Coefficient is a parameter of use to describe the effective flow area during that regime of flow.

$$\boldsymbol{C_D = \frac{A_{eff}}{A_{geo}} = \frac{\dot{m}}{A_{geo}\sqrt{2\rho(P_1 - P_2)}}} \quad \textbf{3}$$

The two parameters are related through the Cavitation Number.

$$\boldsymbol{\frac{C_D}{C_c} = \sqrt{K}} \quad \textbf{4}$$

Figure 1 shows the relative locations of the upstream condition (1), the downstream condition (2), and the throat condition at the narrow point of the vena contracta (c). In quasi-steady-state operation the pressure at the location of the vena contracta can be assumed to equal across the liquid-vapor boundary. This assumption leads to the equation of mass flow through a cavitating orifice listed in Equation 5.

$$\boldsymbol{\dot{m} = C_c A_{geo}\sqrt{2\rho(P_1 - P_v)}} \quad 5$$

The Contraction Coefficient in Equation 5 is a ratio of the reduced effective orifice throat area and the actual orifice throat area. This reduction in area is due to the vena contracta in the

inlet of the orifice when cavitation occurs [6]. This is illustrated in Figure 1. The Contraction Coefficient can be affected by the surface finish, increasing boundary layer thickness, and viscous losses at the walls.

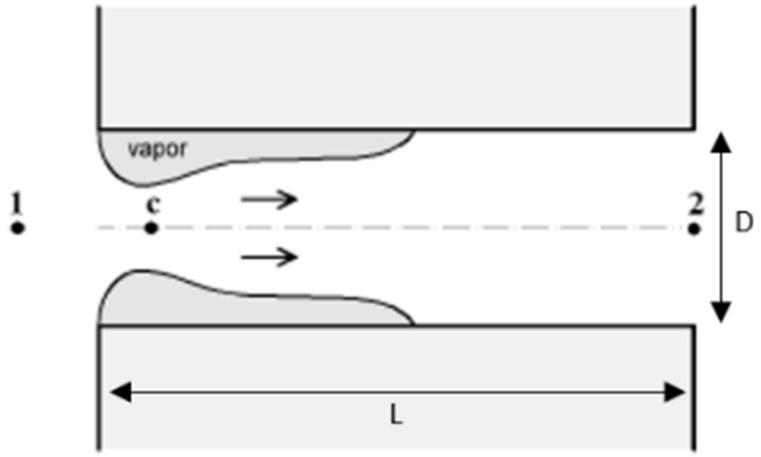


**Figure 1: Vena Contracta in the Nurick Model of Cavitation [8]**

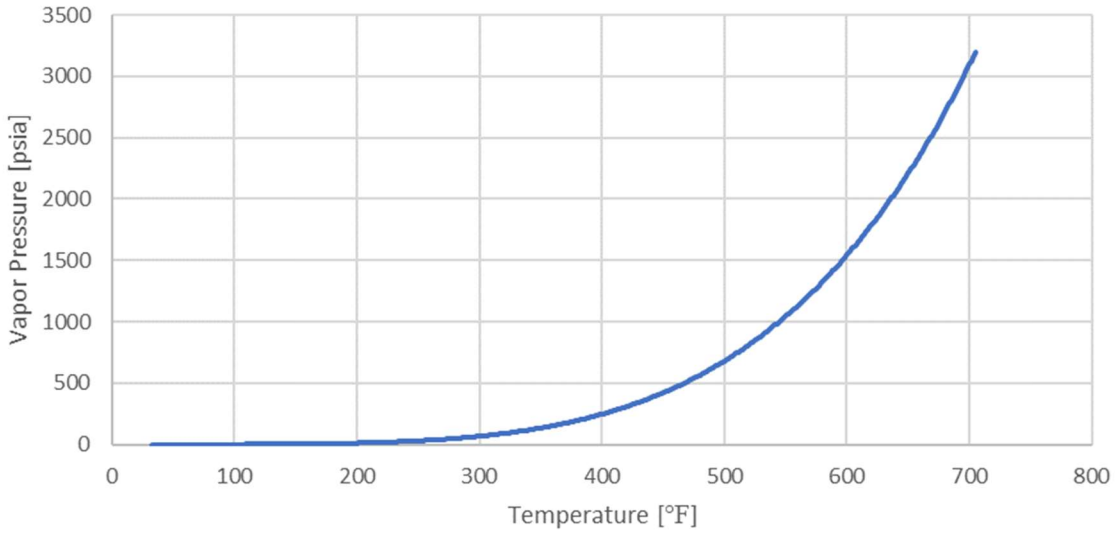


**Figure 2: Temperature vs Vapor Pressure Curve for Water [9]**

The Vapor Pressure curve [9] for water is shown in Figure 2. Water has a large range of available vapor pressures by increasing the fluid temperature. Figure 3 shows the Vapor Pressure curves [9] for Hydrogen, Oxygen, and Methane. Water is used as a simulant for those propellants

in flow characterization and can be heated to increase its vapor pressure to simulate the vapor pressure conditions for those propellants in cavitating flows.

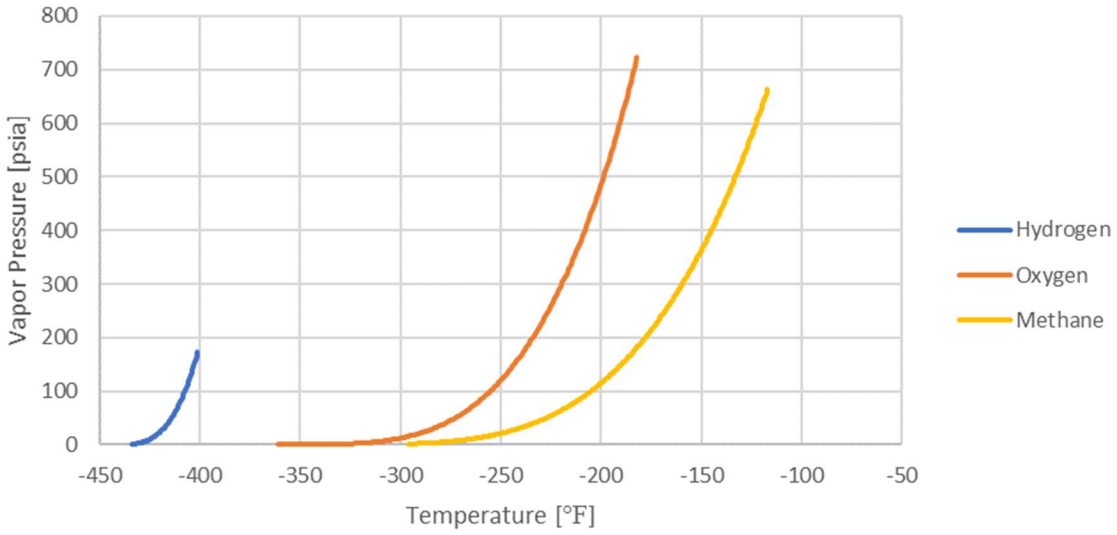


**Figure 3: $LH_2$, $LO_2$, and $LCH_4$ Vapor Pressure [9]**

### 2.1.1 Homogeneous Cavitation vs Heterogeneous Cavitation

Cavitation is affected by the properties of the liquid flowing. In the absence of solid-liquid boundaries and contamination of dissolved solids, the fluid undergoes cavitation as microscopic fluid voids grow to create bubbles in the flow. This is considered Homogeneous Cavitation. Heterogeneous Cavitation on the other hand requires nucleation sites to catalyze the creation of bubbles. In most engineering flows heterogeneous cavitation occurs given the inherent gasification of water, presence of dissolved solids (solid particle contaminants in the water such as dirt and dust), and solid boundaries (locations where the liquid water contacts non-liquid surfaces such as the surfaces of a propeller blade) [4, Ch. 1], [7]. Figure 4 shows the effects of water treatment on the reduction of sites for nucleation of cavitation. With filtered water free of sizable solid particles, the available number of nucleation sites decreases compared to that of

untreated water. Additionally, degassing the water reduces the number of air bubbles which can form voids in the water prematurely. These nucleation sites can lead to onset of cavitation at a higher Cavitation Number.

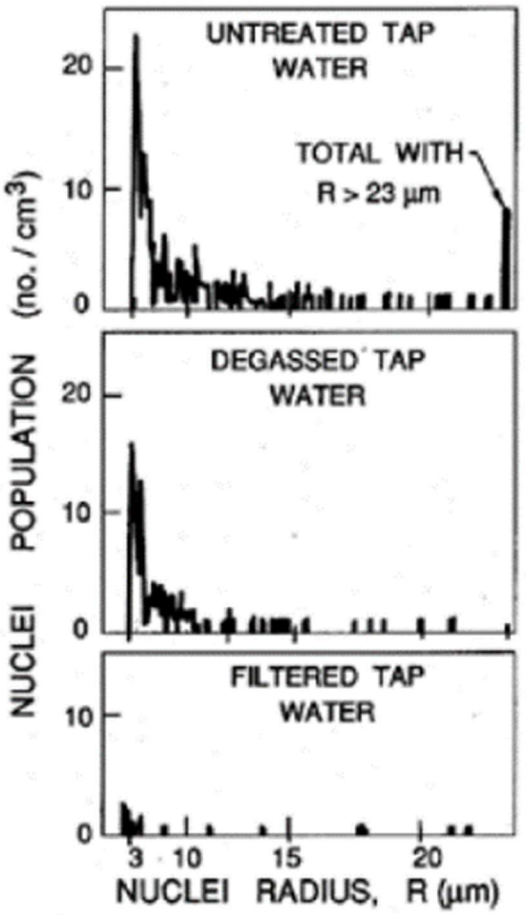


**Figure 4: Comparing Nucleation Site Quantity in Untreated, Degassed, Filtered Tap Water [4, Ch. 1]**

### 2.1.2 Bubble Collapse and Damage

With the creation of bubbles in the flow those bubbles will inevitably collapse. Bubble collapse can be used as a useful tool for mixing as well as a detrimental consequence causing damage to components. Damage is a less desired consequence of cavitation and one that a fluid system designer works to avoid. Investigations into the mechanics of bubble collapse damage and

conditions in which it is prevalent have been performed by a number of individuals [4], [5], [10]–[15].

The bubble collapse, given the high tensile capability of water [4, Ch. 1], [7] can carve into surfaces and create large amounts of damage to parts. This is caused by the large pressure differentials caused by the bubble, temperature increases at the collapse site, and high-amplitude acoustic effects upon collapse. Knapp [10] investigated the mechanics of fixed-type cavitation which refers to flows over static objects. His findings show a great deal of erosion due to the cyclical process of a re-entrant jet, shown in Figure 5, causing a shedding of a cavitation bubble and this bubble collapsing on the surface. Though, with fixed-type cavitation (cavitation over a fixed, non-moving geometry), Knapp found that this occurred very infrequently and therefore postulated that the effect of bubble collapse impingement on the fixed solid boundary operated at a high magnitude of force over larger time scales near 100 minutes for his samples. This is inherently different from that of cavitation with a moving boundary such as that of a propeller or pump.

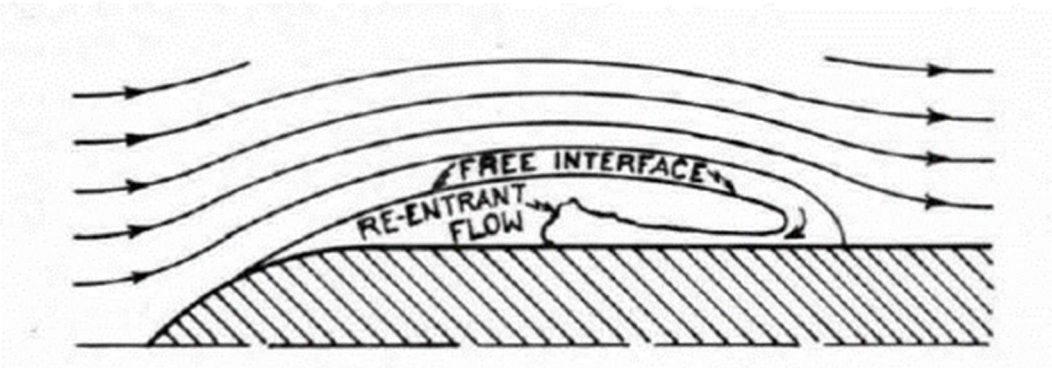


**Figure 5: Fixed-Type Cavitation w/ Re-Entrant Jet [10]**

Moving boundary cavitation deals with a moving solid-liquid boundary. When these surfaces move into the path of a shed, collapsing bubble, that bubble can then impinge and collapse on the surface. This explains a larger degree of damage in rotating systems such as pumps,

propellers, and other rotating machinery. Hammitt et al [11] detailed that pitting damage in flow geometry is locally random. Additionally, they determined previous damage due to bubble impact does not affect the location of future bubble impacts with the exception for extreme impact events which can create gouged areas with enough surface deformation to create local cavitation formation at that pit. Stinebring et al experimentally corroborated scaling laws for this damage and found that the rate of damage events (pits) scales with the sixth power of fluid velocity over the surface and the size of the damage in these events scales with the fifth power of fluid velocity [12]. This underscores the severity of cavitation in restrictive flow devices for long term use.

### 2.1.3 Analytical Modeling

Computational Flow Dynamics (CFD) and numerical modeling of cavitation under certain flow and geometrical conditions has been performed to predict the possibility of cavitation in specific flows and flow devices. Studies have been performed on the exit flow of cavitating devices used in spray generation [16], the application of previous literature and concepts to exceedingly high pressure fluid devices [1], and the effects of roughness [3] [17].

Schmidt and Corradini investigated the exit flow condition from cavitating devices and found that slug flow models for exit flow of a cavitating nozzle do not correctly account for the effects at the wall from the vapor pocket creating a local region of zero wall shear. With inclusion of the assumption of zero wall shear this one-dimensional model more closely matches that of accepted experimental data for cavitating flows as well as multi-dimensional CFD models [16].

Ebrahimi et al applied work on cavitation to high pressure flows (3000 – 7000 psia) and long $L/D$ orifices ($L/D$ >1.0) to create models for geometries and conditions more routinely seen in engineering practice. The findings again show that cavitation scales with cavitation number

rather than pressure and the critical cavitation number of 1.81 is not outside of the values found in literature. For a long *L/D* orifice, it was found that the flow undergoes a double expansion, with one expansion occurring in the orifice from the vena contracta to the wall after the vena contracta and the second occurring from the orifice to the downstream pipe. Downstream pipe flow additionally seems to have a small impact on the contraction coefficient upstream [1].

Echouchene et al investigated roughness in cavitating orifices. They utilized the modified law of the wall [18] to account for the internal roughness. They found that with low injection pressure, increasing roughness height reduces $C_D$. Additional observation of the analysis shows that the onset of cavitation is delayed in rough parts [3]. These observations can be seen in Figure 6. Other investigations with sheet cavitation show limited to no effect of roughness on the flow [19].

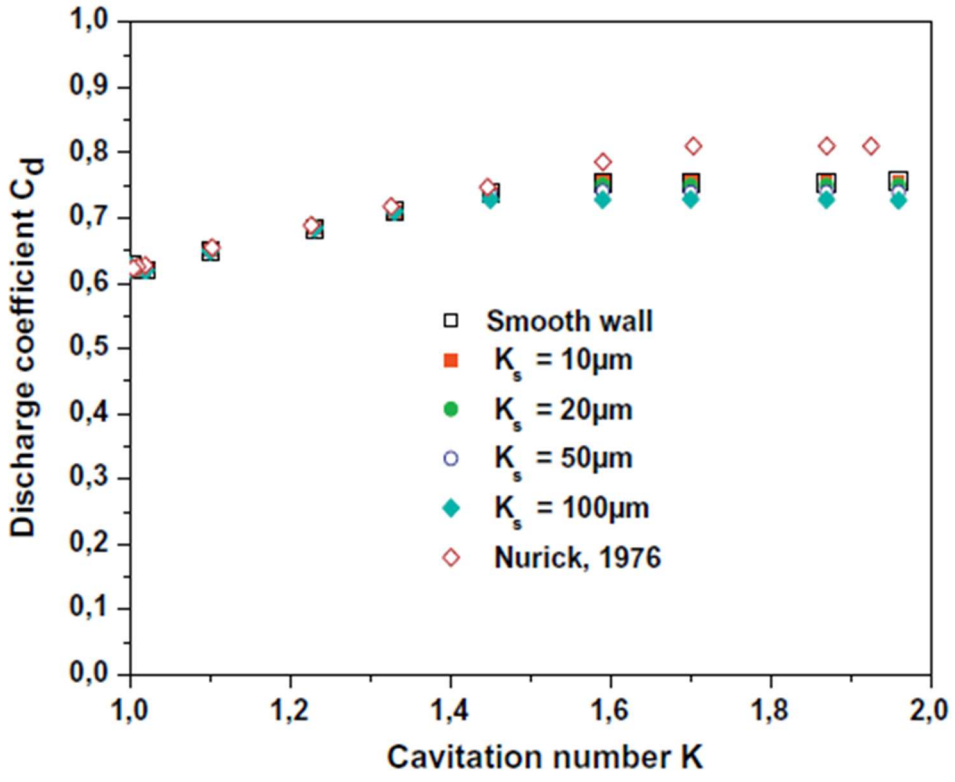


**Figure 6: $C_D$ vs $K$ Prediction with Roughness Model [3]**

### 2.1.4 Other Phenomena

Vortex whistling is another phenomena found with orifice devices [20]–[26]. Vortex whistling occurs with turbulence and vortex shedding in the orifice. The conditions for vortex shedding can be determined from the Strouhal Number,

$$St_X = \frac{f*X}{V}, \quad 6$$

Common values for the orifice thickness Strouhal number ($St_t$) where vortex shedding occurs in orifice devices ranges from 0.2 – 0.35 [20]–[23], [25], [26]. Additional definitions are based on the cavitation cavity length [27] and on the diameter of the orifice. [26].

The high-frequency environment derived from vortex shedding can be determined by calculating the peak Strouhal number [25] from equation 7

$$\boldsymbol{St_p = 0.2420\left(1 + \frac{31.69}{\sqrt{Re}} - 0.0657\frac{D}{D-d}\right), Re \gg 5\,x\,10^3} \quad 7$$

This value coincides with the expected frequency at which the maximum energy peak will occur, therefore when whistling occurs. Other dimensionless terms include the Reynolds-Strouhal number, which can more accurately account for mechanics at low flow rates.

$$\boldsymbol{Re/St = \frac{f*d^2}{\nu}} \quad 8$$

### 2.1.5 Sharp Edge inlet Orifices

One of the earlier works in cavitation was done by W.H. Nurick [8]. This work determined cavitation characteristics for sharp edge inlet orifices and the effect of cavitation on mixing of propellants [8]. Hydraulic flip is a phenomenon in which the cavitation bubble no longer reattaches to the wall of the orifice and instead attaches to the free stream atmospheric flow, this can lead to

a drastic change in flow characteristics and halt all the cavitation shedding processes as shown in Figure 8. Nurick, by using various length to diameter (*L/D*) factors for his orifices as shown in Figure 7 found that the *L/D* to limit hydraulic flip under their conditions was an *L/D* of 20. In Figure 7 the operation of the orifices over a range of cavitation numbers can be seen with the tell-tale sloping reduction in discharge coefficient in each plot once the flow starts to cavitate. The hydraulic flip can be seen when the discharge coefficient decreases promptly with a small decrease in cavitation number. Additionally, Nurick cited the theoretical value for the contraction coefficient at 0.62. This value was derived from Borda-Carnot losses which dictate fluid losses for flow geometries with a sudden change in cross sectional area. Howland and Richetta [28] derive this in full from the conservation of momentum and assumptions of the velocity field around the orifice and determined the theoretical contraction coefficient value to be 0.611[28]. Nurick found the cavitation onset to occur at $K = 1.45$ for an $L/D = 20$ with smooth bore, sharp edge inlet orifices.

Desantes et al [6] investigated similar geometry in a diesel injector and additionally found that while the mass flux of a cavitating venturi is dependent solely on the upstream pressure, the momentum flux is continually varying with backpressure which translates into continuously increasing downstream velocity with decreasing backpressure.

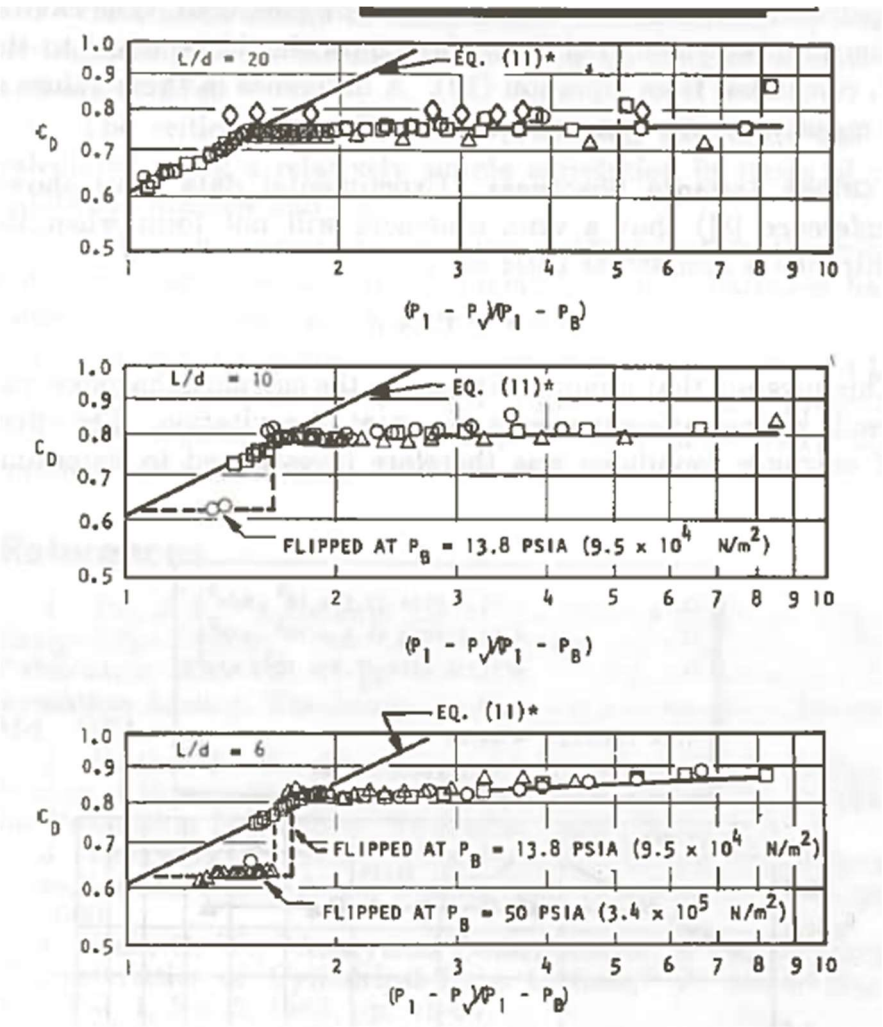


**Figure 7: $C_D$ vs $K$ at differing $L/D$ ratios [8]**

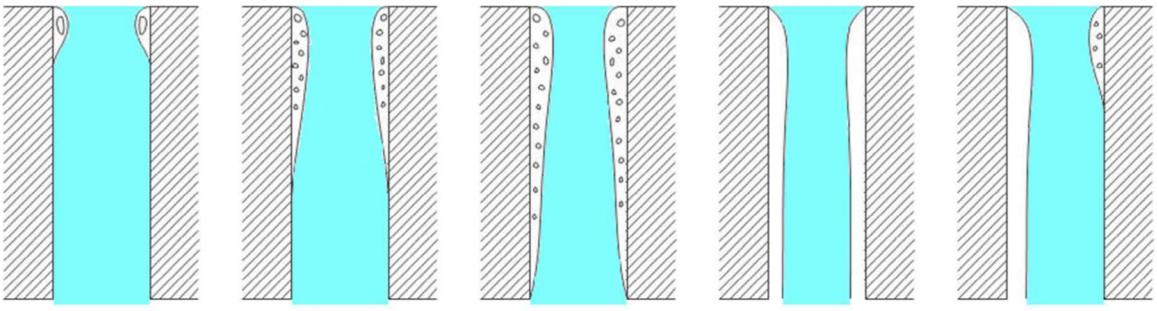


**Figure 8: Representations of vapor cavity characteristics in (a) Inception, (b) Growth, (c) Supercavitation, (d) Flip, (e) Asymmetry[29]**

Additional qualities of sharp edge inlet orifices are that the inlet radius into the orifice diameter influences the contraction coefficient as noted by Nurick [8] in Equation 9.

$$(C_c)_{\frac{r}{d}} = \left[\left(\frac{1}{(C_c)_{\frac{r}{d}=0}}\right)^2 - 11.4\left(\frac{r}{d}\right)\right]^{-\frac{1}{2}} \quad \textbf{9}$$

This was an additional influence on the investigated qualities of the venturis outside of the roughness and was accounted for in the final results. This effect is shown in Figure 9. The increases in inlet radius increases the contraction coefficient thereby increasing the effective flow area. This is due to lesser angle of separation from the bore of the orifice. This leads to the implication of why a venturi style geometry has a higher effective flow area than a similarly sized orifice.

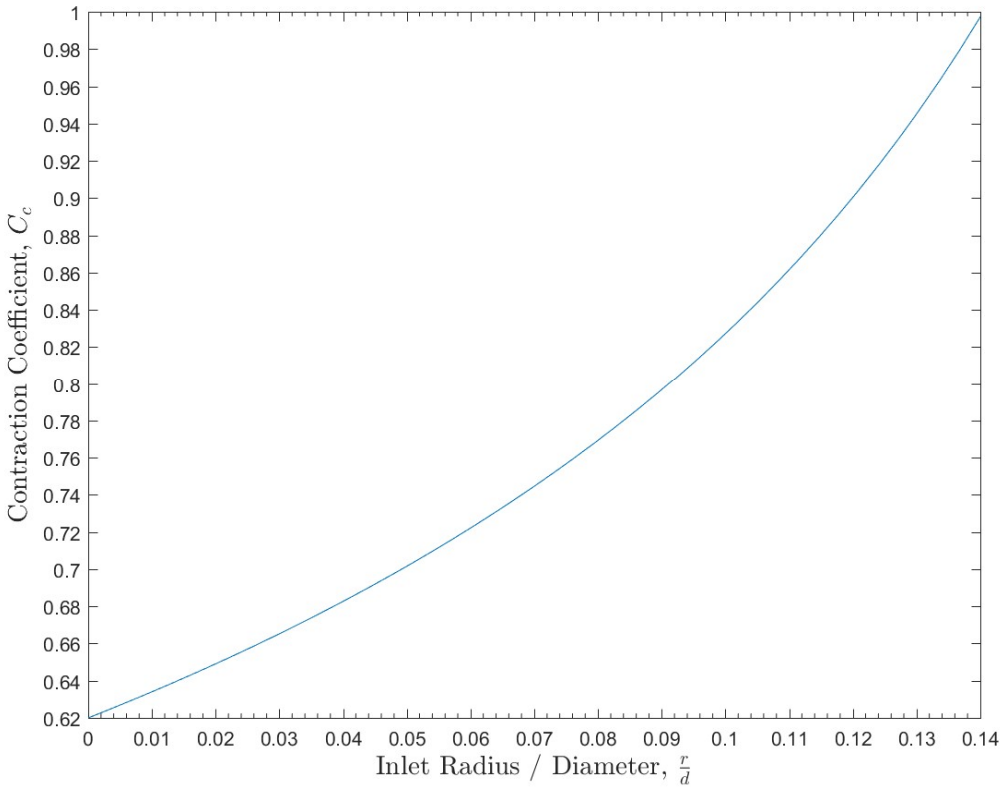


**Figure 9: Contraction Coefficient as a function of the ratio of inlet radius and bore diameter [8]**

Cui et al [29] investigated the effects of geometric irregularities such as conicality, inclinality, diameter errors, on the cavitation in an orifice. The experimental findings suggest that smaller diameter orifices cavitate and hydraulically flip at a lower upstream pressure at controlled downstream pressures compared to larger diameters. Divergent conicality achieves the same purpose by accelerating the flow and leading to a decrease in the required injection pressure to cavitate and the increase in critical cavitation number required.

### 2.1.6 Converging-Diverging Nozzles

Converging-Diverging Nozzles are used in a variety of applications. Notably they are used in mass flow measurement or control in the form of venturis. These devices use the Bernoulli principle to measure the flow of fluid by measuring the reduction in pressure between the inlet and the throat. This reduction in pressure can be correlated to a mass flow knowing the condition of the fluid. Undesired cavitation can limit the range of mass flow measurement and affect the accuracy of the measurement. Additionally, cavitation causes a large amount of pressure loss, which in the case of these devices is not always the desired outcome. Cavitating Venturis are designed to use this method of cavitation in the device to allow for a mass flow measurement using a single pressure measurement from the upstream location with a larger effective flow area than that of an orifice.[30]

### 2.1.7 Summary of Cavitation and Geometry Downselect

The choice of a long *L/D* sharp edge inlet orifice is made in order to exploit the differences caused by surface roughness. This includes hydraulic flip, reduced contraction coefficient, and a difference in the conditions needed for cavitation onset. Sharp edge inlet orifices have an already

existing database of knowledge and therefore the effects of roughness can be seen in comparison. Additionally, as the damage due to cavitation is not under investigation, using a fixed-type geometry reduces the likelihood of damage to the samples during testing allowing for a greater amount of repeatability between tests without accounting for damage due to bubble collapse

| Section | Topic | Comments | References |
|---|---|---|---|
| **Homogeneous and Heterogeneous Cavitation** | Homogeneous Cavitation | - Devoid of boundaries<br>- Assumes perfect fluid<br>- Uncommon in engineering flows | [4], [7] |
| | Heterogeneous Cavitation | - Most engineering flows<br>- Explains increases in cavitation at nucleation sites<br>- Found in flows with solid-liquid boundaries | [4], [7] |
| **Bubble Collapse &Damage** | Damage | - Damage occurs on long timescales w/ fixed type cavitation<br>- Damage scales w/ $5^{th}$ power of fliud velocity | [4], [5], [7], [10]–[15] |
| **Analytical Modeling** | Roughness | - leads to reduction in $C_D$ and $K_{crit}$ | [3], [7] |
| | Exit Flows | - cavitation does not lead to a perfect slug flow at exit | [16] |
| **Other Phenomena** | High-Frequency Environment | - Strouhal number determines the possibility for whistling<br>- Dependent on fluid velocity | [20]–[27] |
| **Sharp edge inlet Orifices** | General | - Theoretical $C_c$ = 0.611<br>- Simplistic geometry<br>- $L/D$ = 20 for no hydraulic flip | [6], [8], [28] |
| | Geometry Differences | - Inlet radius increases $C_c$<br>- Divergent Conicality and decreases in orifice diameter leads to slight increases in Kcrit | [29] |
| **C-D Nozzles** | General | - radius increases $C_c$<br>- angle of of entrance increases $C_c$ | [30] |

## 2.2 Overview of Manufacturing Technologies

Manufacturing of fluid systems has changed over the last 60 years. Manufacturing methods have expanded to include additive manufacturing specifically in the last couple decades. The first commercial use of additive manufacturing occurred in 1987 with Stereolithography and over the course of time, with the expiration of key patents, introductions of lower cost systems has permeated the market and led to greater adoption with a growing consumer base [31]. Additive manufacturing typically adds material in contrast to subtractive manufacturing which removes material [32] [33]. Manufacturing methods span materials, with many of these methods being applied to plastics and metals alike with adjustments made depending on the material. Additive manufacturing methods include Fused Filament Fabrication/ Fused Deposition Modeling (FFF/FDM), Selective Laser Sintering (SLS), and Selective Laser Melting (SLM). The selection of the process is determined by desired feature resolution, the physical size of the part to be manufactured, and desired surface condition and therefore is determined on a case-by-case basis for individual parts.

### 2.2.1 Fused Filament Fabrication/Fused Deposition Modeling Technology

Fused Filament Fabrication (FFF) or Fused Deposition Modeling (FDM) are both names for a system of additive manufacturing in which layers are produced through the heating up and extrusion of thermoforming or thermosetting plastics through a nozzle [32]. This method was first brought to market commercially by Stratasys in 1991 and through the timely release of patents has seen large adoption in the conventional consumer base [31].

Figure 10 shows the method by which parts are created by FDM printing. The diagram shows the extruder head which contains a heater and extrusion mechanism to heat the

thermoplastics up to the point of transition and squeeze the plastic through a nozzle of a certain diameter. This is then deposited onto a platform which moves in the X-Y plane while the extrusion head moves in the Y direction. Mechanical factors which affect the dimensional accuracy of this manufacturing method and therefore the roughness are the stepper motor precision, quality of mechanical assembly, drive system design (cartesian vs. delta), filament quality, nozzle diameter, and calibration method. Positional accuracy for a printer can be on the order of 0.1 mm (~0.005 in) for consumer printers [34]. With industrial grade printers these values do not appreciably increase but their repeatability increases greatly [35]. The build orientation and toolpath of the printer also has a large impact on the final roughness. Software Factors which affect dimensional accuracy and roughness include the sequence to print contours (inside out vs outside in), the number of contours, constant extrusion vs variable extrusion for thin wall treatment, infill/hatch overlap with contours, infill/hatch spacing, layer height, extrusion width, etc. This is all optimized by the manufacturing engineer in order to meet requirements. Examples of build orientation include whether to orient holes with the long axis perpendicular to the build table or parallel. The former orientation yields a much cleaner geometry with the latter suffering with bad surface condition on one side of the hole.

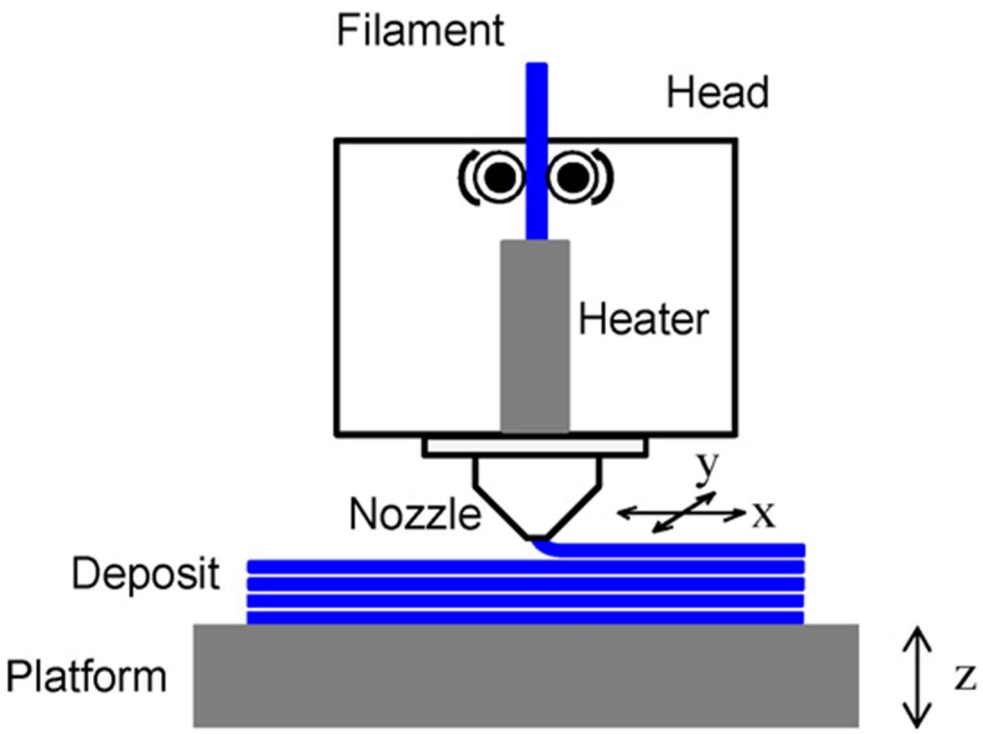


**Figure 10: FDM Printing Method [32]**

This method of depositing a part layer by layer creates a stair step effect in the finished part which creates a distinct waviness/roughness pattern to the part. This can be shown in Figure 11 from a test sample used in this work using 1.74mm filament size and a 300 µm z-height. Clear ridges can be seen in the part.

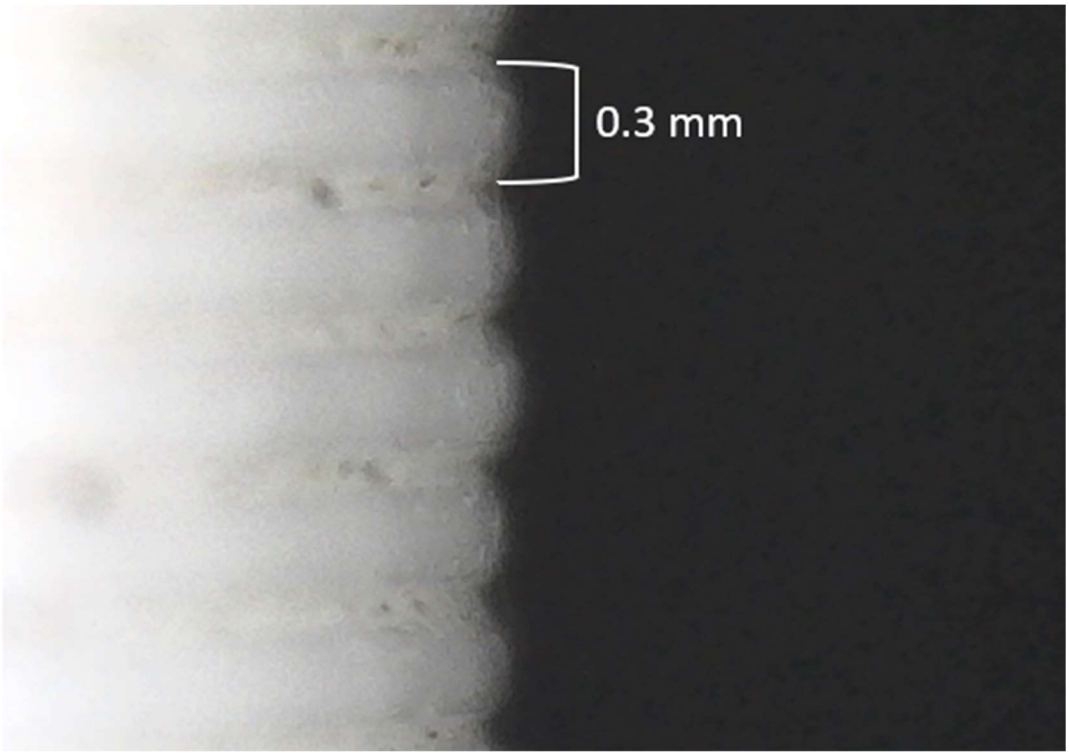


**Figure 11: FDM Sample Waviness Pattern**

### 2.2.2 SLS/SLM Technology

Selective Laser Sintering (SLS) and Selective Laser Melting (SLM) are both powder-based additive manufacturing technologies [33]. An illustration of how this system works is shown in Figure 12. In the figure a powder supply and build platform can be seen. During printing the roller moves a thin layer of powder to the platform and the mirrors move the laser through the toolpath to sinter or melt the powder to the build plate. After the layer is complete the platform lowers and another layer of powder is moved from the powder supply and process of sintering or melting is repeated. Both FDM and SLS/SLM systems use a layered process to create parts but unlike FDM the feedstock to create the parts is a powder.

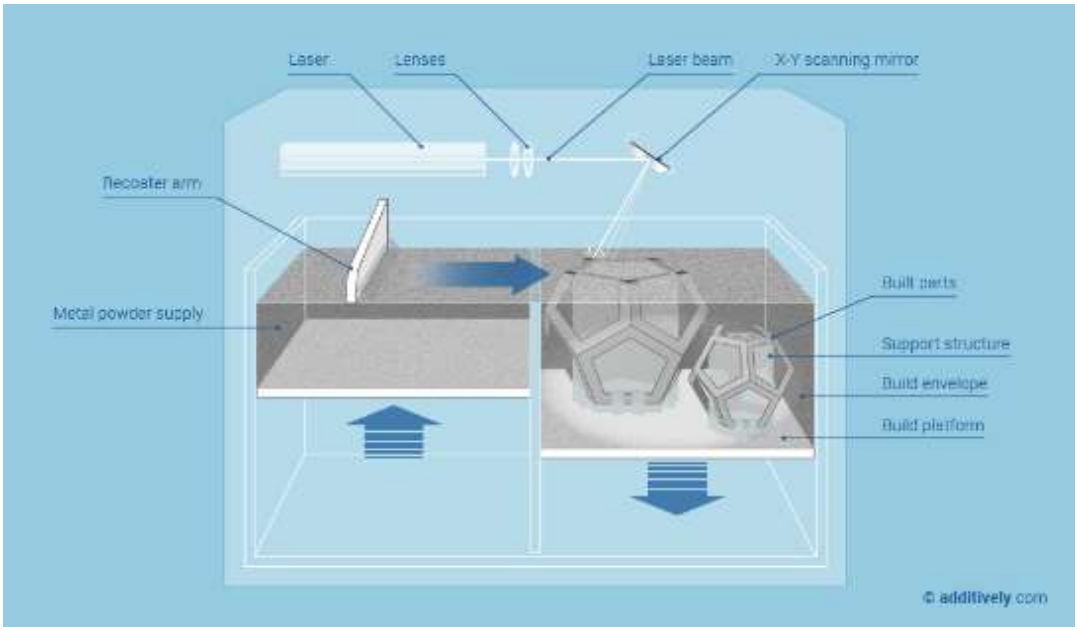


**Figure 12: Illustration of SLS/SLM Printing**[1]

Additionally, upon close examination, irregularities in the parts surface can be seen where powder was inadvertently sintered or melted on to the surface. This is shown in Figure 13. Positional accuracy and repeatability of these machines is on the same order of industrial grade FDM printers with less than 0.05 mm accuracy. The major driver of the roughness in these parts is build orientation and layer thickness much like that of FDM printers. Unlike FDM printers, SLM and SLS printers suffer from an issue of "balling" wherein unintended particles are sintered to the part surface leading to issues in lamination of the next layers and unintended porosity [33].

[1] Obtained from Additively.com, https://www.additively.com/en/learn-about/laser-melting

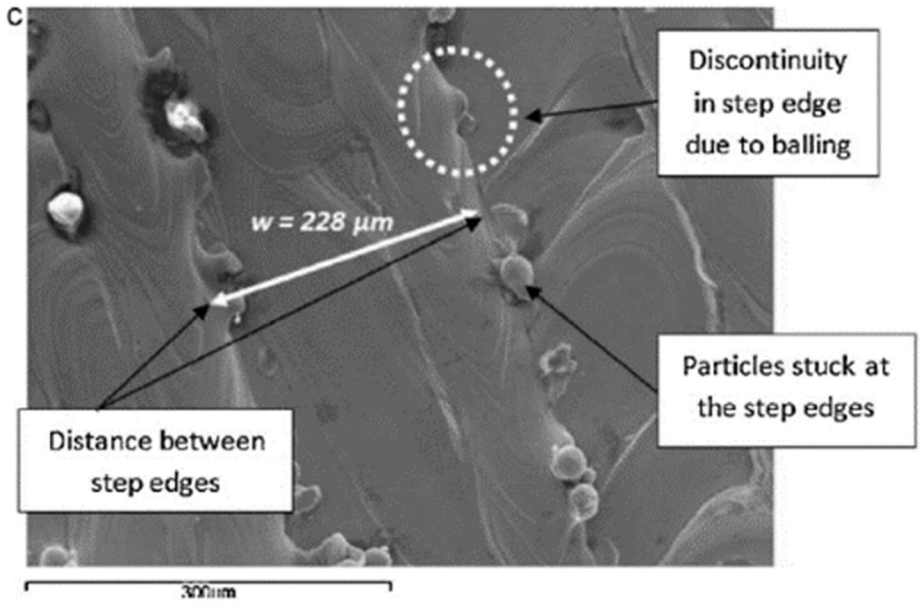


**Figure 13: Surface Irregularities in SLM Printing [1]**

### 2.2.3 Subtractive Manufacturing

Subtractive manufacturing is a common method through which parts are created by the process of removing material from a larger amount of raw material. Methods used include milling, drilling, turning, electrical discharge machining, abrasive flow machining, abrasive jet machining, electrochemical machining, etc. These methods and the subsequent post finishing processes affect the roughness patterns and degree of roughness. A chart of ranges for different post finishing processes is shown in Figure 14.

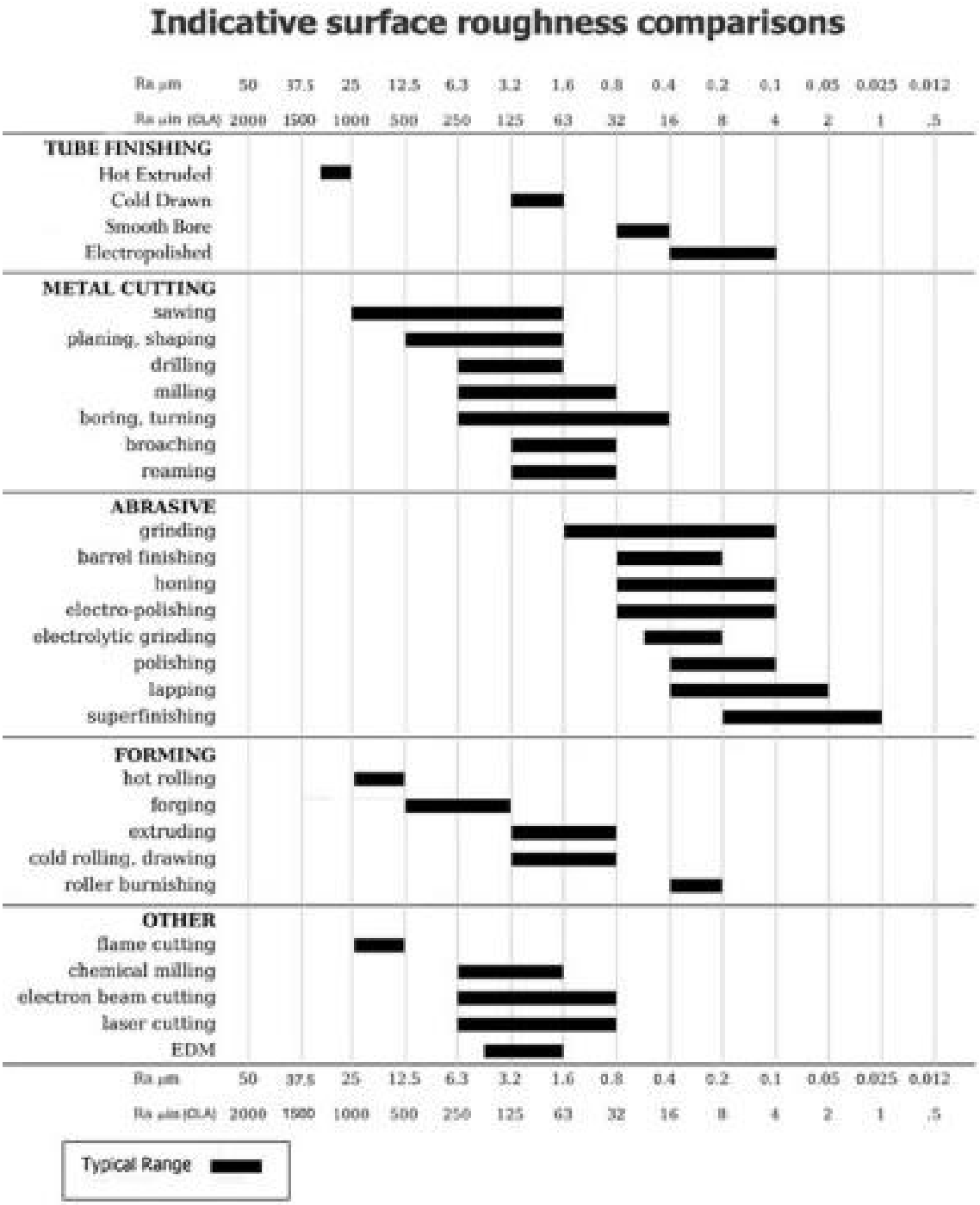


**Figure 14: Surface Roughness Comparisons[2]**

[2] Obtained from cnccookbook.com, https://www.cnccookbook.com/surface-finish-chart-symbols-measure-calculators/

Subtractive manufacturing is also traditionally used as a post-finishing processes for additive manufacturing processes and casting processes. This stems from the desire to remove the surface finish imperfections of SLS/SLM parts and create surface finishes similar to that of subtractively manufactured parts.

### 2.2.4 Summary of Manufacturing Technologies and Downselect of Manufacturing Methods

The chosen manufacturing technologies for this study span a range of expected roughnesses as shown in Figure 15. These also span a range of investment in a part's production with the FDM being the minimal investment in money and time and the subtractive manufacturing being the greatest in personnel time and cost. The manufacturing processes downselection to FDM, SLM, and subtractive processes was made in order to create a broad spectrum of processes found in engineering. The subtractive process is chosen in order to define a baseline. Both the FDM and SLM processes were chosen given their prevalence in additive manufacturing.

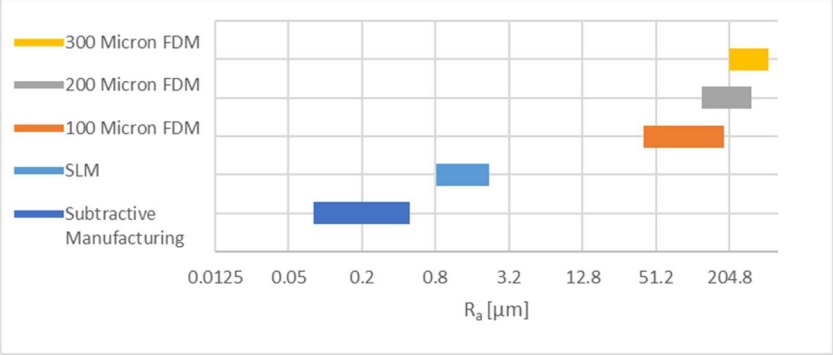


**Figure 15: Comparison of Expected Roughnesses for chosen technologies**

# CHAPTER 3

# TEST SYSTEM DESIGN & OPERATION

## 3.1 Choice of Geometry

The choice of system of interest dictates the choice of geometry. The interest of this study is long *L/D* sharp edge inlet orifices such as that commonly used in impinging injectors for liquid propellant rocket engines as well as flow control orifices in process control systems. Therefore, a long *L/D* sharp edge inlet orifice was chosen. An *L/D* of 20 was chosen in order to ensure hydraulic flip was not an issue. Inlet edge radius was maintained to as sharp as feasible with the process used and subsequently measured using a Form Talysurf surface profilometer.

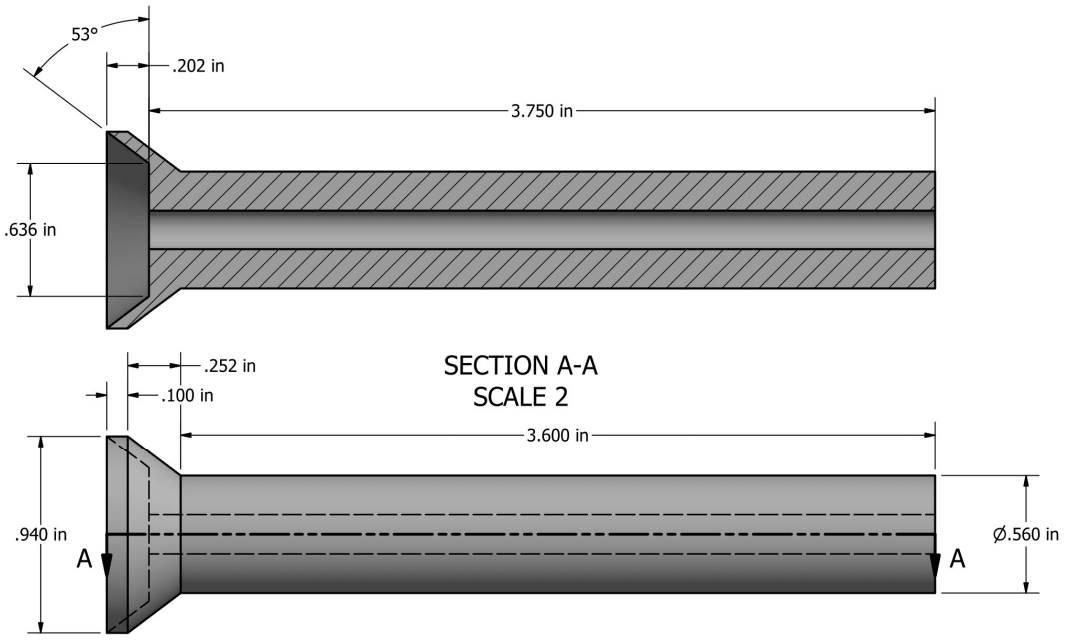


**Figure 16: Design Geometry for Samples**

### 3.2 Choice of Manufacturing Methods and Materials

In order to have a breadth of methods and subsequent surface finishes, five separate manufacturing conditions were chosen. This included three conditions of FDM, one SLM, and one Subtractively Manufactured. FDM used PLA 1.75 mm filament (1.74 mm measured) with settings optimized for the part geometry printed on a Rostock MAX V3 printer. The only allowable difference between the three different conditions is the programmed layer height, varying as 100 μm, 200 μm, and 300 μm. For the SLM condition a university partner, ASRC Federal Technical Services Propulsion Engineering Center, donated the time and material to print the test geometry on a Conceptlaser M2 using Monel K500. The M2 has a build volume of 250 x 250 x 350 mm and a layer thickness range of 20 - 80 μm with a focus diameter of 50 μm. The exact settings for the SLM printing are contained in Appendix L. For all of the printed conditions the part geometry was printed with the long axis perpendicular to the print bed with contour passes to increase model dimensional accuracy and surface condition.

The subtractively manufactured part was made on a Haas TL-1 CNC lathe using Aluminum 6061 bar stock. The subtractively manufactured condition samples (4) were twist drilled using a #15 drill bit, reamed with a 0.1875” reamer, and then honed successively at 320, 600, and 800 grit using silicon carbide flex-hones with final treatment of an abrasive aluminum polish. These parts were, in post, sharpened by using the lathe to take 0.002” off the inlet face returning the orifice to its condition prior to bore polishing. These defining manufacturing features are summarized in Table 1.

**Table 1: Configuration Summary**

| Sample | Defining Features |
|---|---|
| 100 µm FDM | 100 µm layer height, FDM, PLA Material, 1.74 mm dia feedstock |
| 200 µm FDM | 200 µm layer height, FDM, PLA Material, 1.74 mm dia feedstock |
| 300 µm FDM | 300 µm layer height, FDM, PLA Material, 1.74 mm dia feedstock |
| SLM | Laser Melting, Monel K500 Material, 45 µm Average Powder Size |
| Subtractively Manufactured | Turned, Reamed, Honed, and Polished 800 grit. Aluminum 6061 Material |

### 3.3 Physical Dimensions, Surface Roughness, and Inlet Radius Data

The inlet radius of the parts was measured using a Form Talysurf Profilometer with a 60 mm long diamond tipped stylus allowing for a resolution of 10 nm. All data was analyzed in Matlab[36]. After finding the linear fit of the profile line of both the inlet bore and the outside face (as shown in Figure 17), an intersection point is found and the translation position value is used as a "zero" point and a half-width is defined.

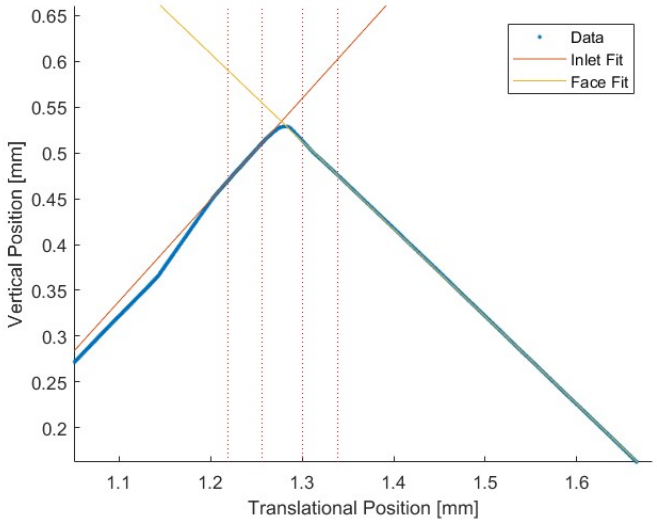


**Figure 17: Example of Inlet Radius Fit Methodology**

A circular curve fit is used to fit an appropriate radius in this area of interest. This is completed for a predetermined set of half-widths and the results are filtered with a floor of 0.0001 in radius and a ceiling of 0.010 in radius. After filtering, the mode of the radius values is determined for each dataset and the average across all datasets for the same part is made. This value is then accepted as the inlet radius for that part. The inlet radii for each part is listed in Table 2.

**Table 2: Test Sample Inlet Radii**

| Sample | | Inlet Radius | Sample | | Inlet Radius | Sample | | Inlet Radius |
|---|---|---|---|---|---|---|---|---|
| Subtractive | #1 | 0.00129 in | 300 µm | #1 | 0.006285 in | 200 µm | #1 | 0.005003 in |
| | #2 | 0.00079 in | | #2 | 0.006692 in | | #2 | 0.004117 in |
| | #3 | 0.00155 in | | #3 | 0.006331 in | | #3 | 0.004746 in |
| | #4 | 0.00114 in | | #4 | 0.005926 in | 100 µm | #1 | 0.002362 in |
| SLM | #1 | 0.00322 in | | #5 | 0.006562 in | | #2 | 0.003102 in |
| | #2 | 0.00416 in | | | | | #3 | 0.002866 in |
| | #3 | 0.00321 in | | | | | | |
| | #4 | 0.00493 in | | | | | | |

The roughness of the parts interior bores was additionally measured using a Form Talysurf Profilometer with a 60 mm long diamond tipped stylus. The Talysurf used five sample lengths in each evaluation length of 12.5 to 13mm. This evaluation length was then used to find an arithmetic mean roughness (*Ra*), root mean squared roughness (*Rq*), highest peak (*Rp*), lowest valley (*Rv*), mean roughness spacing (*Sm*), peak-to-peak spacing, as well as many other variables. These values are shown in Table 3 and the procedure, background, and full dataset related to the roughness of the parts is included in Appendix J.

**Table 3: Test Article Roughness**

| | 100 µm FDM #4 | 200 µm FDM #3 | 300 µm FDM #1 | SLM #1 | Subtractive #1 | Subtractive #2 |
|---|---|---|---|---|---|---|
| Ra [µm] | 14.266 | 19.108 | 26.851 | 5.959 | 0.372 | 0.262 |
| Rq [µm] | 18.100 | 24.191 | 33.486 | 7.915 | 0.468 | 0.391 |
| Rsk [µm] | -0.200 | -0.378 | -0.156 | 1.122 | -0.089 | -0.867 |
| Rku [µm] | 3.367 | 3.389 | 3.144 | 4.933 | 4.167 | 6.644 |
| Delq [°] | 29.881 | 32.411 | 32.982 | 16.294 | 0.326 | 0.431 |
| Lamq [µm] | 199.124 | 239.672 | 322.422 | 169.244 | 494.344 | 335.229 |
| S [µm] | 105.324 | 185.294 | 291.024 | 99.034 | 79.742 | 60.621 |
| Sm [µm] | 176.759 | 244.900 | 338.544 | 223.771 | 296.371 | 340.601 |
| R3z [µm] | 60.104 | 78.383 | 97.932 | 29.733 | 1.247 | 0.914 |
| R3y [µm] | 77.196 | 101.226 | 116.745 | 35.756 | 1.765 | 1.635 |
| Rp [µm] | 47.743 | 63.999 | 87.880 | 33.266 | 1.185 | 0.841 |
| Rv [µm] | 60.472 | 81.974 | 97.473 | 18.444 | 1.662 | 1.900 |
| Rt [µm] | 108.215 | 145.973 | 185.353 | 51.710 | 2.847 | 2.741 |
| Rtm [µm] | 84.067 | 106.785 | 135.771 | 41.856 | 1.614 | 1.348 |
| Rpm [µm] | 37.537 | 47.300 | 57.552 | 27.452 | 0.731 | 0.506 |
| Ry [µm] | 103.494 | 137.209 | 181.499 | 49.273 | 2.596 | 2.417 |

The physical dimensions of the orifice in the part is documented in Table 4. This table includes information on the inlet and outlet diameters (measured using pin gages) and allows for us to see what degree of conicality the test articles have.

**Table 4: Test Article Dimensions**

| Sample | | Inlet Diameter | Outlet Diameter |
|---|---|---|---|
| Subtractive | #1 | 0.1920 in | 0.1920 in |
| | #2 | 0.1900 in | 0.1920 in |
| | #3 | 0.1920 in | 0.1920 in |
| | #4 | 0.1900 in | 0.1920 in |
| SLM | #1 | 0.1870 in | 0.1850 in |
| | #2 | 0.1870 in | 0.1850 in |
| | #3 | 0.1870 in | 0.1860 in |
| | #4 | 0.1870 in | 0.1850 in |
| 300 µm | #1 | 0.1810 in | 0.1820 in |
| | #2 | 0.1800 in | 0.1810 in |
| | #3 | 0.1800 in | 0.1810 in |
| | #4 | 0.1800 in | 0.1810 in |
| | #5 | 0.1800 in | 0.1810 in |
| 200 µm | #1 | 0.1800 in | 0.1810 in |
| | #2 | 0.1800 in | 0.1820 in |
| | #3 | 0.1800 in | 0.1810 in |
| 100 µm | #1 | 0.1800 in | 0.1850 in |
| | #2 | 0.1800 in | 0.1850 in |
| | #3 | 0.1810 in | 0.1860 in |

### 3.4 Planned Test Conditions

Forty-Five Tests in this work were planned with a profile from $K$=1.6 to $K$=1.0 and a constant upstream pressure of 500 psig. This choice of upstream pressure was to allow for ample flexibility in attaining very low cavitation numbers close to 1.0. The choice of an upper bound of $K$ = 1.6 came from reviews of other experiments and with the understanding that most likely the onset of cavitation would occur near or lower than 1.45 [2] [3]. Three test articles were to be made of each configuration and each sample was planned to be tested three times. The actual number of tests completed was sixty-six with the extra tests coming from an additional block of testing with the subtractively manufactured parts sharpened to a sharper edge as well as additionally tests performed to replace tests with less than optimal data due to underperforming back pressure

control or broken test articles. All of the test articles and the number of tests performed along with defining parameters are described in Table 5.

**Table 5: Test Matrix**

| Block | Sample | Sample Type | K Lower | K Upper | # of Tests | Upstream Press |
|---|---|---|---|---|---|---|
| 1 | 300 #0 | 300 µm FDM | 1.0 | 1.6 | 2 | 500 psig |
| | 300 #0 | 300 µm FDM | 1.0 | 1.6 | 2 | 500 psig |
| | 100 #0 | 100 µm FDM | 1.0 | 1.6 | 2 | 500 psig |
| | 100 #0 | 100 µm FDM | 1.0 | 1.6 | 2 | 500 psig |
| 2 | 300 #1 | 300 µm FDM | 1.0 | 1.6 | 1 | 500 psig |
| | 300 #2 | 300 µm FDM | 1.0 | 1.6 | 3 | 500 psig |
| | 300 #3 | 300 µm FDM | 1.0 | 1.6 | 3 | 500 psig |
| | 300 #4 | 300 µm FDM | 1.0 | 1.6 | 3 | 500 psig |
| | 300 #5 | 300 µm FDM | 1.0 | 1.6 | 3 | 500 psig |
| | 200 #1 | 200 µm FDM | 1.0 | 1.6 | 3 | 500 psig |
| | 200 #2 | 200 µm FDM | 1.0 | 1.6 | 3 | 500 psig |
| | 200 #3 | 200 µm FDM | 1.0 | 1.6 | 3 | 500 psig |
| | 100 #1 | 100 µm FDM | 1.0 | 1.6 | 3 | 500 psig |
| | 100 #2 | 100 µm FDM | 1.0 | 1.6 | 3 | 500 psig |
| | 100 #3 | 100 µm FDM | 1.0 | 1.6 | 3 | 500 psig |
| 3 | SLM #2 | SLM | 1.0 | 1.6 | 3 | 500 psig |
| | SLM #3 | SLM | 1.0 | 1.6 | 3 | 500 psig |
| | SLM #4 | SLM | 1.0 | 1.6 | 3 | 500 psig |
| 4 | SRM #2 | SRM | 1.0 | 1.6 | 3 | 500 psig |
| | SRM #3 | SRM | 1.0 | 1.6 | 3 | 500 psig |
| | SRM #4 | SRM | 1.0 | 1.6 | 3 | 500 psig |
| 5 | SRM #2 | SRM Sharpened | 1.0 | 1.6 | 3 | 500 psig |
| | SRM #3 | SRM Sharpened | 1.0 | 1.6 | 3 | 500 psig |
| | SRM #4 | SRM Sharpened | 1.0 | 1.6 | 3 | 500 psig |

| # Tests | 66 |
|---|---|

### 3.5 Inlet and Exit Conditions

The test article inlet conditions were set via the run tank pressure and set each test day to approximately 500 psig. The exact setting of the pressure does not entirely matter once the backpressure is accounted for as the experiment system operates on pressure drop over the test sample. Differences in upstream pressure only affect the minimum attainable cavitation number. Exit pressure was varied from approximately 200 psig to atmospheric pressure. The tests were

instead controlled via Cavitation Number which varied from 1.6 to 1.0 moving from no cavitation to heavy cavitation ($K \sim 1.0$) in the part. Reynolds Numbers at the inlet were of the order of 200,000 and sufficient hydrodynamic entrance length was accounted for to ensure that at the inlet plane of the orifice the flow is fully developed and turbulent. Figure 18 shows the approximate ranges of testing on a moody chart for single phase liquid flow.

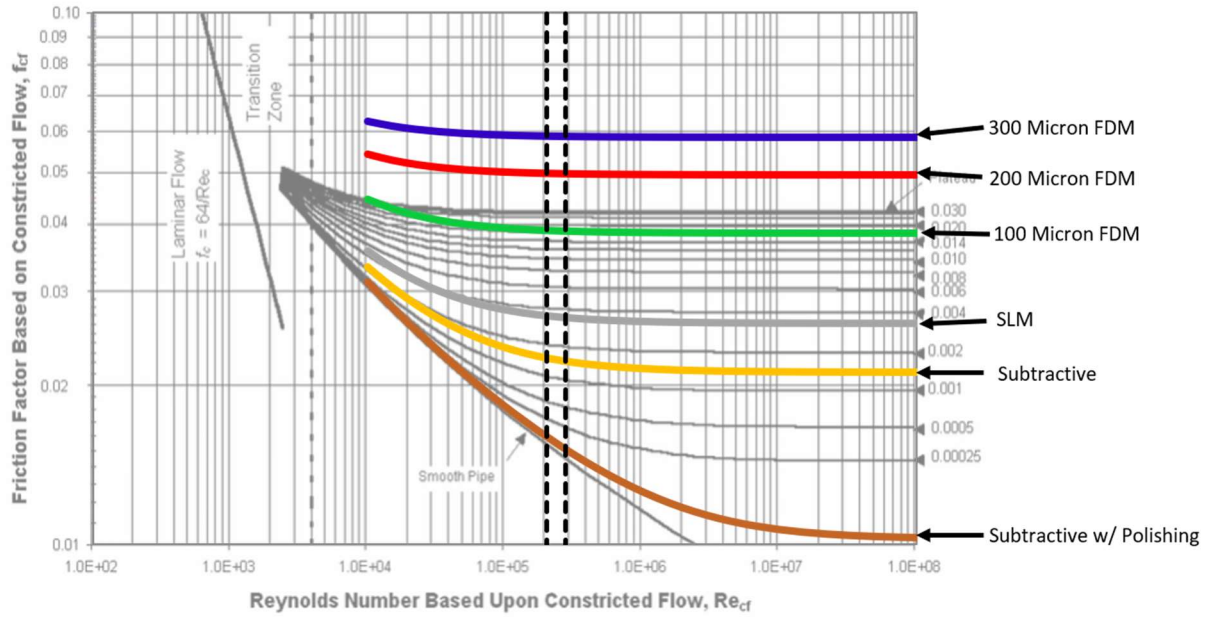


**Figure 18: Range of Testing Reynolds Numbers and Expected Roughnesses**

### 3.6 Fluid System Design, Sizing, and Selection

The Plumbing and Instrumentation Diagram (P&ID) for the HPSF is attached in Appendix A and the P&ID for the cavitation test setup is attached in Appendix H. This section will be focusing on the fluid system specific to this experiment. Components in the system are a venturi flowmeter, a liquid rated relief valve, a type K thermocouple, two high frequency dynamic pressure transducers, three static pressure transducers, a domotor actuated globe valve, a Bellofram

electrical control regulator, a high pressure gas service regulator, a needle valve, and the test sample being tested. Major components will be discussed individually.

### 3.6.1 Venturi Flowmeter ASF-FQ-W003

Preliminary sizing was performed once a venturi flowmeter was selected and before full flow characterization of the venturi was performed. A Flowmaxx Venturi Flowmeter currently in possession of the PRC was chosen and verified to have the correct mass flow range capability. The method by which the venturi flowmeter measures mass flow is expressed in Equation 10. By which the difference in pressures is measured from the inlet to the throat of the meter.

$$\dot{m} = C_D A \sqrt{2\rho(P_1 - P_2)} \qquad 10$$

Manufacturer suggested use is to only measure within a 10% - 90% range of the maximum mass flow capability of the flowmeter of 8.13 lbm/s at 500 psig with a flowmeter $C_c$ of 0.9 (assuming highly polished converging-diverging nozzle geometry). At the low-flow worst case condition, assuming a 50% effective area of the orifice being tested in both cavitation and non-cavitation use ($C_c$ and $C_D$ of 0.5) with delta-pressure operation across the sample of 500 psig to 200 psig, the mass flow is 14.13% of maximum. A 50% effective geometry is lower than what would be expected with this geometry but was chosen for increased margin. The high-flow worst case condition, assuming 95% effective area of the orifice being tested ($C_c$ and $C_D$ of 0.95) with cavitation operation across the sample at 500 psig upstream pressure, the mass flow is 36.63% of maximum. This flow exists in the lower half of the flowmeter's range ensuring good pressure recovery across the device to alleviate pressure loss prior to the inlet of the test sample. Further detail of sizing assumptions are detailed in Appendix B.

The actual flow capability of the venturi is characterized as an effective flow area, combining $C_D$ and area. This was measured to be 0.07889 $in^2$ +/- 0.181%. The venturi's maximum limit can not be tested without the possibility of damaging the instrumentation and the internal surface finish. The cases used in the preliminary sizing are conservative enough to allow for the cavitation properties to be assumed. Additionally, there is significant distance to allow for any vortex shedding or bubble formation from the flowmeter to not impact the test section.

### 3.6.2 System Backpressure Control Valve ASF-CV-W011

In order to allow for the 10 setpoints to occur in the same contiguous test, a variable position globe valve was used to regulate the backpressure on the sample. This valve is an Annin 2600 Series Split Body Globe Valve positioned using a Domotor Actuator (ASF-CV-W011) and is controlled using a Bellofram controller (ASF-PC-N003). Details about the fluid control properties of the valve and actuator is contained in Appendix E. The valve and controller both require a pneumatic supply which is supplied using the gas simulant line to the atmospheric spray bench. This supply needs to be stepped down from a high pressure (500-3000 psig) down to the supply of 60 psig for both the controller and valve. This is performed by a Tescom hand actuated pressure reducing regulator (ASF-PR-N002). A photo of the valve and its setup is included in Figure 19.

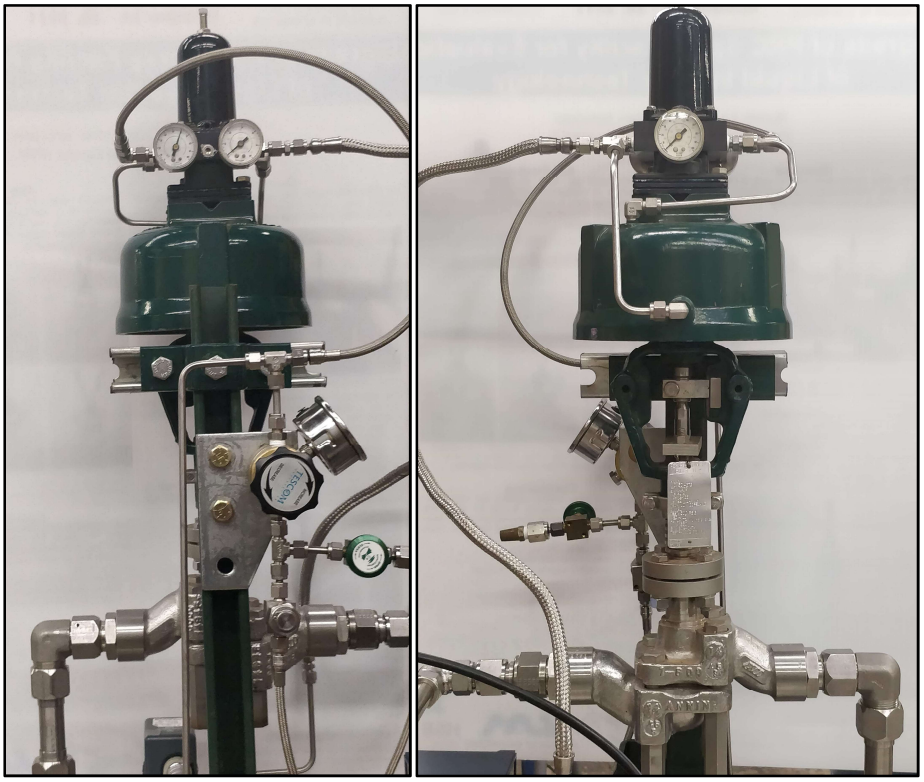

**Figure 19: Backpressure Control Valve**

In order to determine the response of the valve and pneumatic controls to a current applied to the controller a test was performed sweeping the controller through a range of 4-20 mA and determining associated value of the pressure of interest (ASF-PY-W010). This was used in a multi-gain proportional-integral-derivative controller to control the valve in test. A plot of the valves control response is shown in Figure 20.

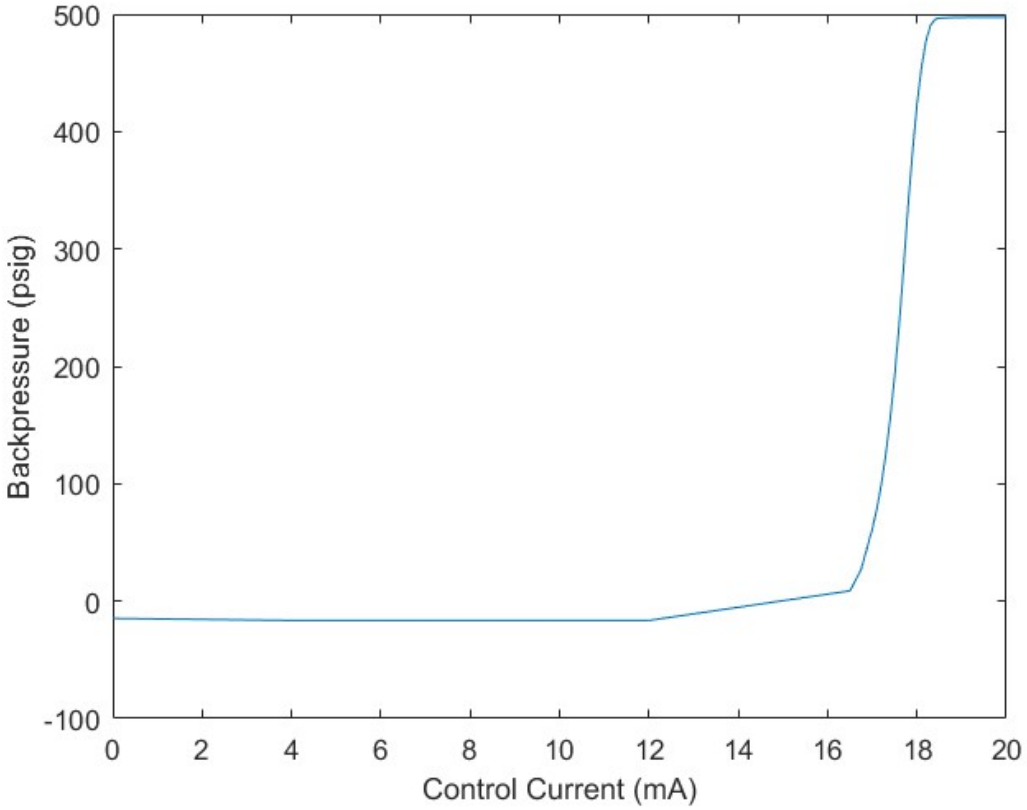


**Figure 20: Backpressure Valve Static Pressure Response**

### 3.6.3 Test Sample ASF-OR-W008

After choice of a test sample size and flow conditions, a determination of hydrodynamic entrance length was made to specify the inlet tube length. This calculation was made using Equation 11.

$$L_{h,turbulent} = 4.4 * D * Re^{1/6} \text{ [37]} \quad (11)$$

The resulting value, assuming worst case conditions, came to be 22.01". The actual produced entrance length was 22.375" so to be fully developed turbulent flow at the entrance of the test sample. The sample is sandwiched between an AN-12 37° flare fitting and a flared tube section.

### 3.6.4 Instrumentation and Plumbing

Table 6 includes a list of all the instrumentation used in the system along with model and serial number for the device. A list of all necessary calibration sheets are included in Appendix C. Appendix H shows a schematic for the system used in this testing and Table 6 lists any pertinent component information. Figure 21 shows a view of the test section with information on placement of instrumentation with respect to the orifice.

**Table 6: Instrumentation Used in Testing**

| Name | DAQ Channel | Patch Panel Channel | Manufacturer | Serial Number | Model | Range | Accuracy | Resolution | |
|---|---|---|---|---|---|---|---|---|---|
| Venturi DP | 16 | B1-Ch2 | Sensotec | 750329 | Z/741-03ZD | 0-50 psid | +/- 0.25% FS | 0.000762939 | psi |
| Upstream Pres | 0 | B1-Ch1 | Omegadyne | 103110D878 | PX-309-500G5V | 0-500 psig | +/- 0.25% FS | 0.007629395 | psi |
| Source Pres | 18 | B1-Ch4 | Honeywell | 1249468 | FPG | 0-1500 psig | +/- 0.25% FS | 0.022888184 | psi |
| Downstream Pres | 17 | B1-Ch3 | Omegadyne | 083131D112 | PX-309-500G5V | 0-500 psig | +/- 0.25% FS | 0.007629395 | psi |
| Source Temp | TC-6 | B1-TC Ch1 | Omega | N/A | KMQSS-125G-6 | -454°F-2501°F | 1.46 °F | 0.558 | °F |
| Run Tank Pres | 10 | B3-Ch19 | Honeywell | 1196154 | FPG | 0-3000 psig | +/- 0.25% FS | 0.045776367 | psi |
| System Pres | 6 | B3-Ch14 | Dwyer | 3000A | N/A | 0-3000 psig | +/- 0.25% FS | 0.045776367 | psi |
| Run Tank Dome | 8 | B1-Ch9 | Honeywell | 1196158 | FPG | 0-3000 psig | +/- 0.25% FS | 0.045776367 | psi |
| Liquid Sim | 15 | B2-Ch10 | Honeywell | 1195664 | FPG | 0-3000 psig | +/- 0.25% FS | 0.045776367 | psi |
| Current Control | cDAQ Ch0 | N/A | Bellofram | 967-020-000 | T1001 | N/A | N/A | N/A | |
| Downstream HF | USB Ch0 | B1-Ch14 | PCB | 32256 | 112A05 | -10% to 25% Steady State | +/- 1.00% FS | 0.004 | psi |
| Upstream HF | USB Ch1 | B1-Ch15 | PCB | 32324 | 112A05 | -10% to 25% Steady State | +/- 1.00% FS | 0.004 | psi |

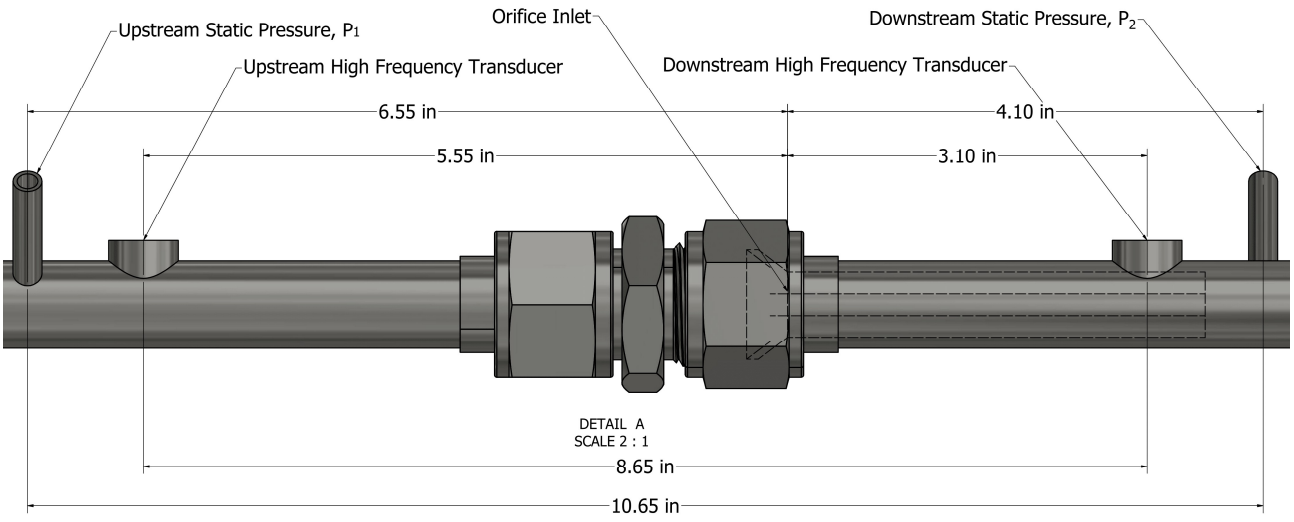


**Figure 21: Test Section Instrumentation Locations**

### 3.7 Test Setup, Operation, and Procedure

Operations for the setup are controlled using a Standard Operating Procedure (SOP) approved by the system owners of the HPSF (PRC-SOP-JRC-032-A2) and an experiment procedure which is included in Appendix K. Operations start with the standard procedures to bring the facility to a state of readiness and fill the run tank with deionized water. This works by first ensuring the system is in a known state and that all valves actuate correctly. After this, the run tank is filled with deionized water from the holding tank. A floorplan of the facility is shown in for reference.

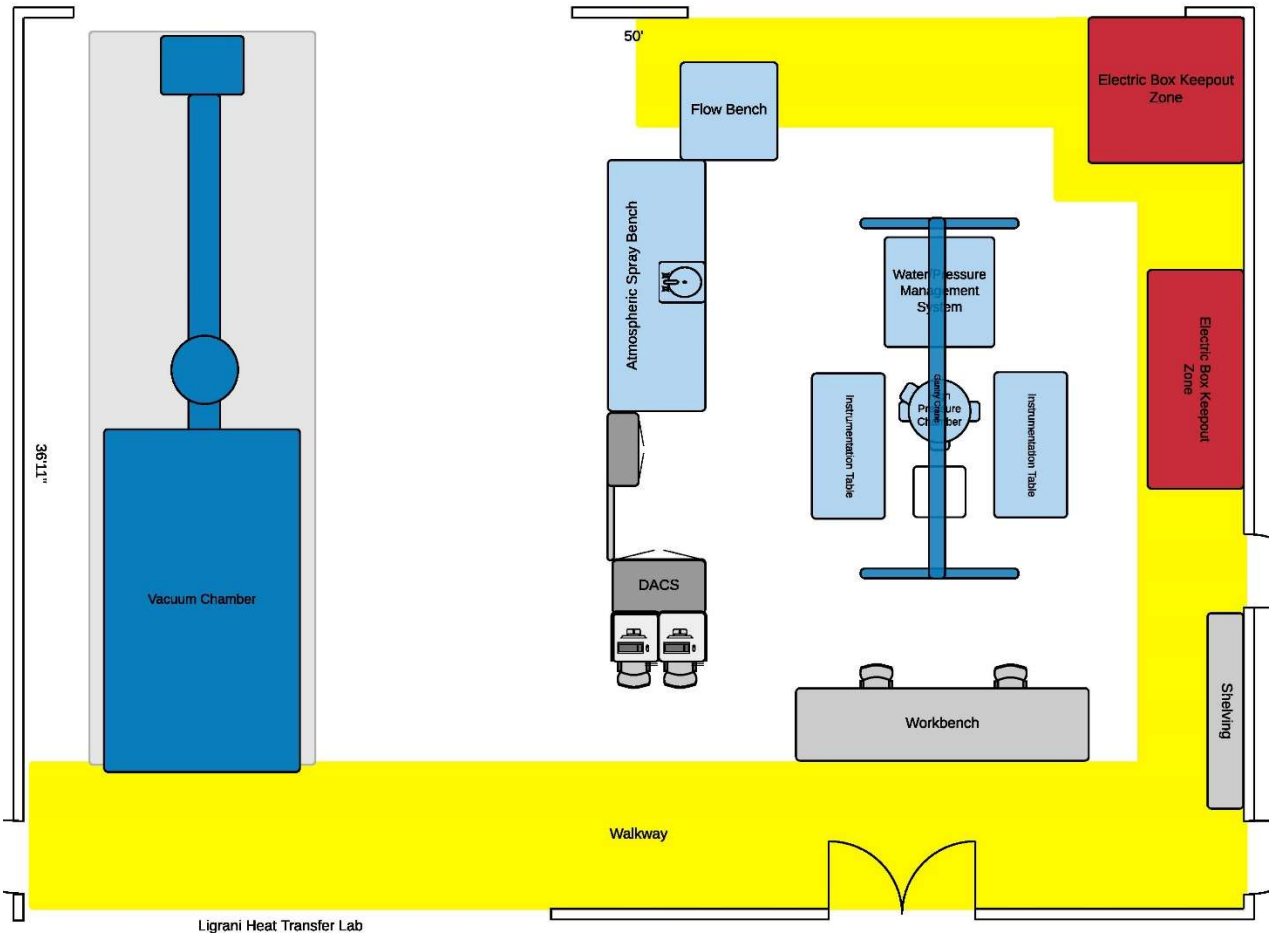


**Figure 22: High Pressure Spray Facility Floorplan**

Once the system is determined to be in a safe state and ready for pressure to be applied then the gas bottles can be opened and the pressure can be brought up to ~2600 psig at the Main Isolation Valve 10.01. Once this is opened then pressures for the different systems can be set by the dome-loaded regulators 14.03, 14.04, 14.05, and 14.06. After pressure has been brought up to 100 psig for valve actuation then additional valve checkouts can be performed. Once the facility is deemed ready then the Run Tank Dome Pressure can be set to ~515 psig such that the Run Tank reads ~500 psig. At this point the Experiment Procedure can be used and the Gas Simulant Pressure can be set to ~ 500 psig on the panel and the diverter valve can be set to pressurize. At this point the Gas Sim Fire Valve (10.06) can be opened. At this point the control valve regulator is set to ~60-65 psig, any excess pressure will be audibly vented out the valve weep hole. Now that pressure has been brought up on both systems instrumentation checks in Labview can be performed by verifying that all transducers are reading near zero and thermocouple readings are nominal. Once that check has been performed the names for the files for both the low speed (1 kHz) and high speed (100 kHz) data files. Then a check of the backpressure control valve is performed by forcing the valve full open and full closed to verify proper actuation. After this has been performed then the valve is overridden full open and the Liquid Sim Fire Valve is opened and the Atmospheric Spray Facility isolation valve is slowly opened. Once this valve has been fully opened the valve can be turned to closed loop control and the test schedule can be started. After this the test is now in hands off condition until the schedule is completed and the valve partially closes. At this point the Atmospheric Spray Facility isolation valve can be closed and the schedule stopped, therefore stopping the recording.

### 3.8 Test Cases

Tests are scheduled using a setpoint scheduler in Labview. The setpoints are set to a *K* of 1.6 - 1.0. A graph of the timings of these setpoints is shown in Figure 23. Each test would perform a sweep as shown in the figure. For the tests there are 5 unique test configurations in the Test Matrix (100, 200, 300 µm FDM, SLM, and Subtractive Manufacturing) each with 3-4 test samples.

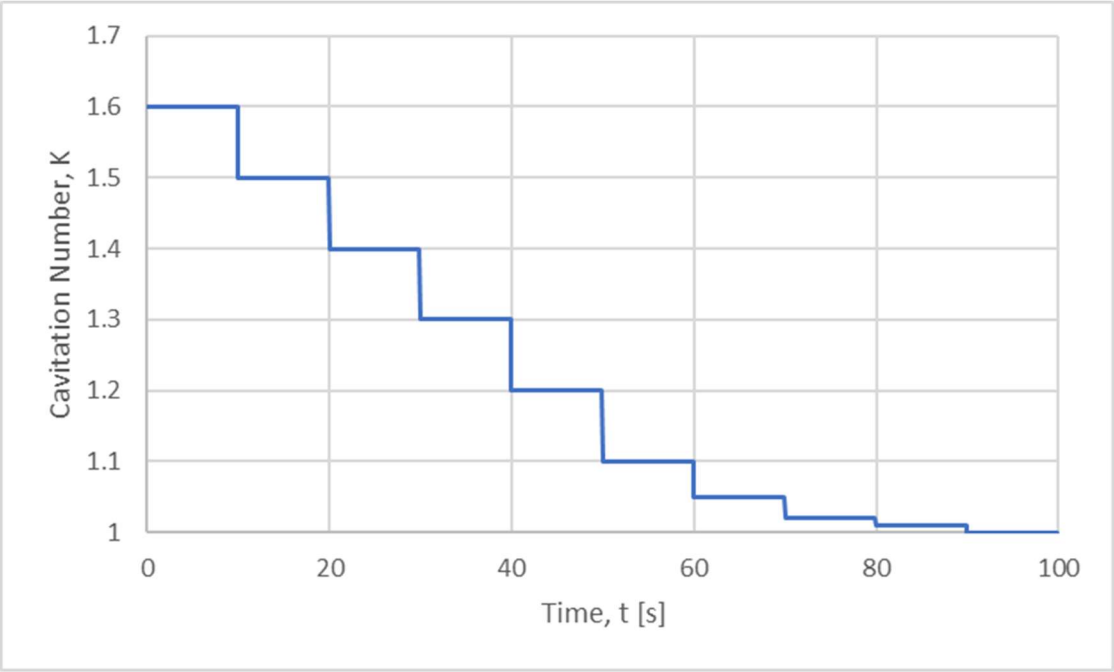


**Figure 23: Setpoint Schedule**

# CHAPTER 4

# RESULTS

## 4.1 FDM PLA Orifice Data

Tests in Block 1 and 2 of testing were performed on FDM PLA samples. Block 1 was a preliminary set of tests and are omitted from this report. Figure 24 shows the response of the Block 2 tests to the set conditions controlled by the globe valve. The x-axis is the time during the test and the y-axis is the cavitation number at that point in the test. Cavitation Number is seen decreasing in steps as the test progresses. The results in Figure 24 closely follow the expected setpoint schedule shown in Figure 23 terminating at a full open globe valve condition for $K \approx 1.0$. Fluctuations seen in the cavitation number can be attributed to the closed loop control by the globe valve and when nondimensionalized and averaged over an entire setpoint the values are valid for use in further analyses. For configurations that had large deviations from the planned setpoints, additional tests were performed. The legend for all these figures uses the following naming convention for the tests, [Block Number] – [Sample Type] – [Sample Number] – [Test Number].

Figure 25 shows the mass flow during the tests. The x-axis for this figure is the time during the test and the y-axis is the mass flow in kg/s calculated using the venturi flowmeter and Equation 10. During Block 2 testing the mass flow can be seen changing through a majority of the test. The individual steps in mass flow is due to the step-wise nature of the testing and the transient movement to each setpoint is due to the closed loop control of the globe valve in the test. The mass flow rate differences from configuration-to-configuration can be seen, as well as the test-to-test and part-to-part deviation possibly due to slight differences in inlet radius, roughness, cavitation number, etc.

Figure 26 shows the mass flow with reference to a nondimensional cavitation number which removes the influence of test-to-test differences in upstream pressures, downstream pressures, and time. The increasing mass flow section of the figure from $K = 1.6$ until $K \approx 1.1$ indicates non-cavitating operation whereby the decreasing downstream pressure increases mass flow up until the cavitation point. The constant mass flow section of the figure from $K \approx 1.1$ to $K = 1.0$ indicates cavitation in the test sample and constant mass flow control whereby the mass flow is only due to the upstream pressure. The figure shows that these samples do not restrict mass flow until $K \approx 1.1$-$1.15$ as until that point in the plot the mass flow is still changing. This is much lower than the predicted value of $K = 1.45$ for the cavitation mechanism to start based on work by Nurick [8]. This could be attributed to roughness effects as it is a deviation from expected. This is backed up by fact that the lower roughness 100 µm samples trip to cavitation at a lower value of $K \approx 1.15$.

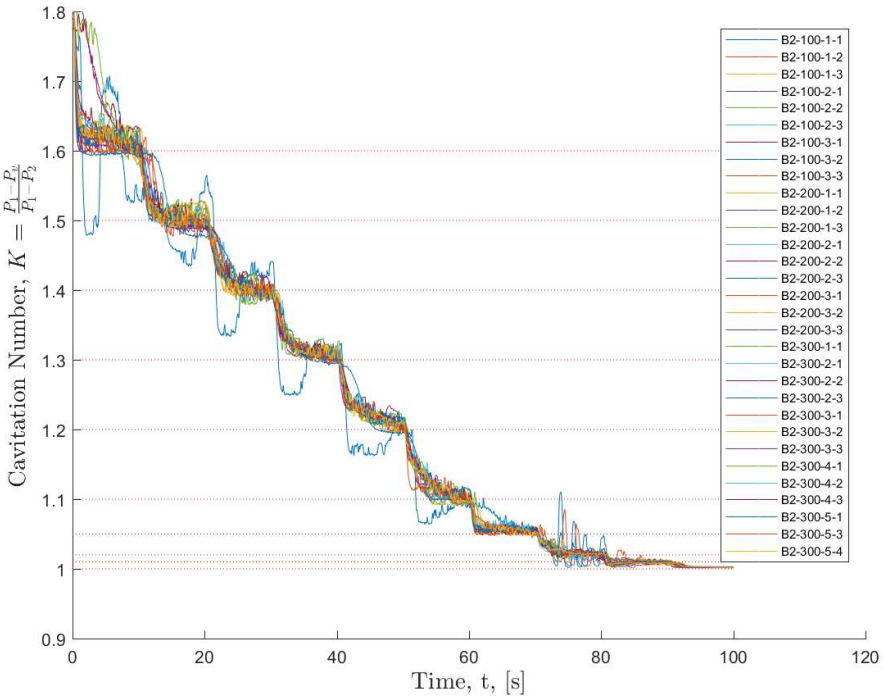


**Figure 24: Block 2 Sample Cavitation Number trend with Time**

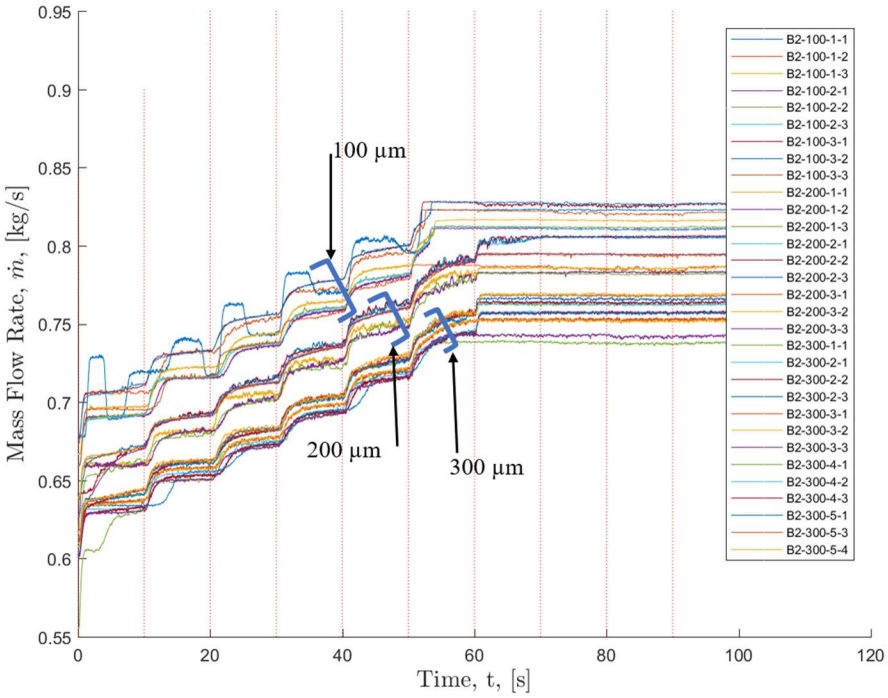


**Figure 25: Block 2 Sample Mass Flow trend with Time**

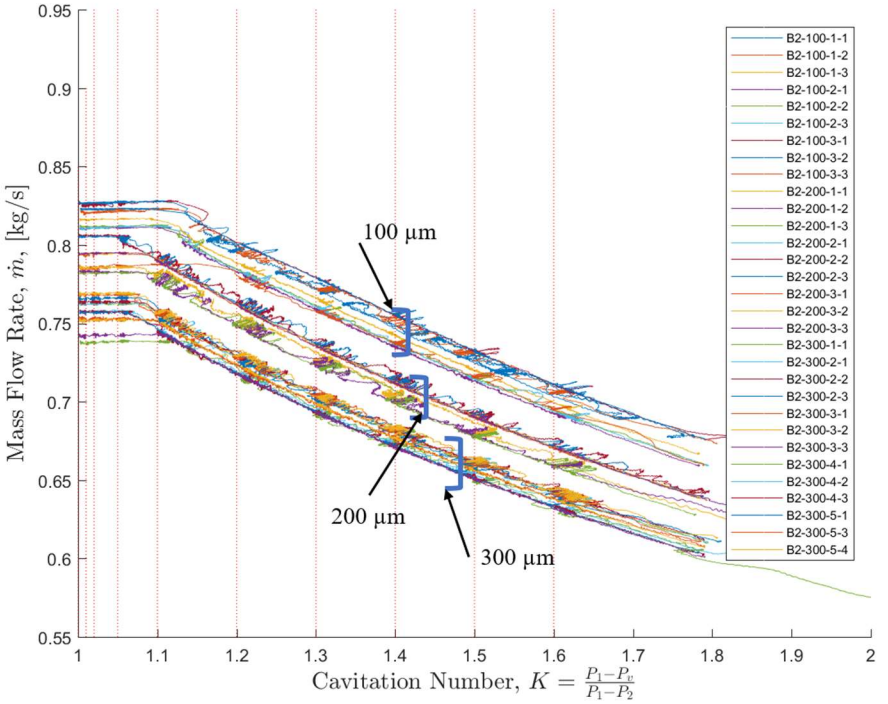


**Figure 26: Block 2 Sample Mass Flow Relation to Cavitation Number**

For comparisons sake, Figure 27 shows the discharge coefficient with respect to nondimensional cavitation number for all of the Block 2 tests compared to the predicted value for a sharp edge inlet orifice transitioning to cavitation at $K$ = 1.45 derived from Equation 3 and Equation 5. By plotting the data with respect to the discharge coefficient and the cavitation number the variance due to testing variables such as upstream and downstream pressure are factored out of the data. The differences between the curves is now solely due to the inlet radius, roughness, other geometrical effects, as well as uncontrollable deviances such as differences in water purity and gasification. At this point two tests were removed from the analysis set using Chauvenet's Criterion. These tests (B2-100-3-3 & B2-300-1-1) are annotated in Figure 27. Additionally, as Equation 4 shows, the values of $C_D$ and $K$ are related through $C_c$ which therefore means that Figure 27 can be used to graphically analyze the differences in cavitation operation for the different configurations and tests. Three groupings can be seen in Figure 27 and are annotated. The tests group by configuration with the 100 µm parts having an overall larger value of $C_D$ than the other configurations and 300 µm parts having a lower value of $C_D$ than the other configurations. In Figure 27, the knee in the curves is the cavitation number at which the tests transition from non-cavitating orifice flow to cavitation.

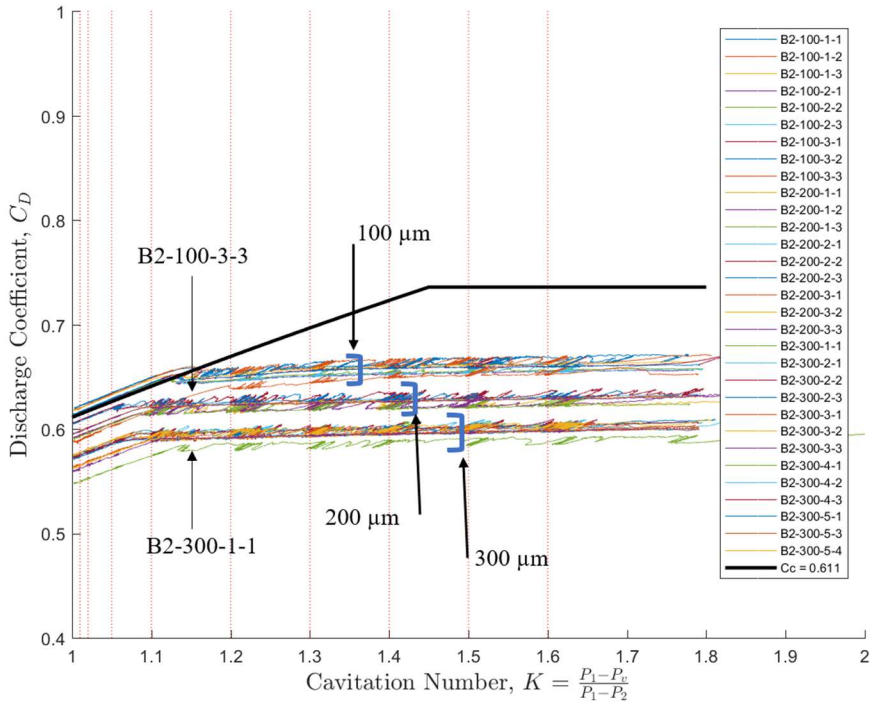


**Figure 27: Block 2 Sample Discharge Coefficient and Cavitation Number Relationship (Prediction and Measured)**

### 4.1.1 Contraction Coefficient

Contraction Coefficient for each test was determined using,

$$\boldsymbol{C_c = \left(\frac{C_E}{A_{geo}}\right)\sqrt{\frac{DP_{meter}}{P_1 - P_v}}} \qquad 12$$

This equation uses the flowmeter flow coefficient ($C_E$), which combines $C_D$ and Area, and flowmeter drop in pressure ($DP_{meter}$) to measure the mass flow during the test. This is then used in Equation 2 to determine the $C_c$. The last 5000 points of each test are used to determine the $C_c$ for the test. These $C_c$ values are then averaged across all tests for a certain configuration to find the configuration $C_c$. Uncertainty analysis described in Appendix I shows a maximum ± 0.584% uncertainty in $C_c$ when all factors are accounted for. Standard deviation of the calculated variable from measurement is at ± 0.0227% and therefore the uncertainty analysis is assumed to yield the

uncertainty of the mean value for each test. Bias in the measurement values is tared out at the beginning of the testing day, thereby negating bias errors between tests. This analysis does not include correlated bias factors.

To compare the contraction coefficient value for each sample configuration an average and 95% confidence limits of the mean was determined. Figure 28 shows a probability distribution function for each Block 2 configuration and is shown with the dotted lines demarcating the 95% confidence limits. This shows that the mean configurations are statistically different with respect to their mean contraction coefficient values. Values determined were 0.6146 for 100 µm, 0.5969for 200 µm, and 0.5699 for 300 µm. These values can be adjusted for their inlet edge radius using a relation derived by Nurick [2]. This empirical relation, outlined in Equation 9, adjusts these $C_c$ values to account for their varying inlet radii. Using the measured inlet radii of each part as well as the inlet diameter one can find an inlet *r/d*. This is then used in the empirical relation, rewritten to convert to sharp edge inlet equivalent value, in Equation 13.

$$(\boldsymbol{C_c})_{\frac{r}{d}=0} = \left[\left(\frac{1}{(C_c)_{\frac{r}{d}}}\right)^{2} + \mathbf{11.4}\left(\frac{r}{d}\right)\right]^{-\frac{1}{2}} \qquad 13$$

Each part's measured $C_c$ is then converted to the equivalent sharp edge inlet value and then the average for the configuration is found. The original values for each configuration and the values after sharp-edge adjustment are listed in Table 7 with the average inlet *r/d* measured for each configuration and the limits for 95% confidence in the mean. An uncertainty analysis for this calculation is included in Appendix I. These values can be compared to that of the reference derived from work by Nurick[8] and Howland and Richetta[28].

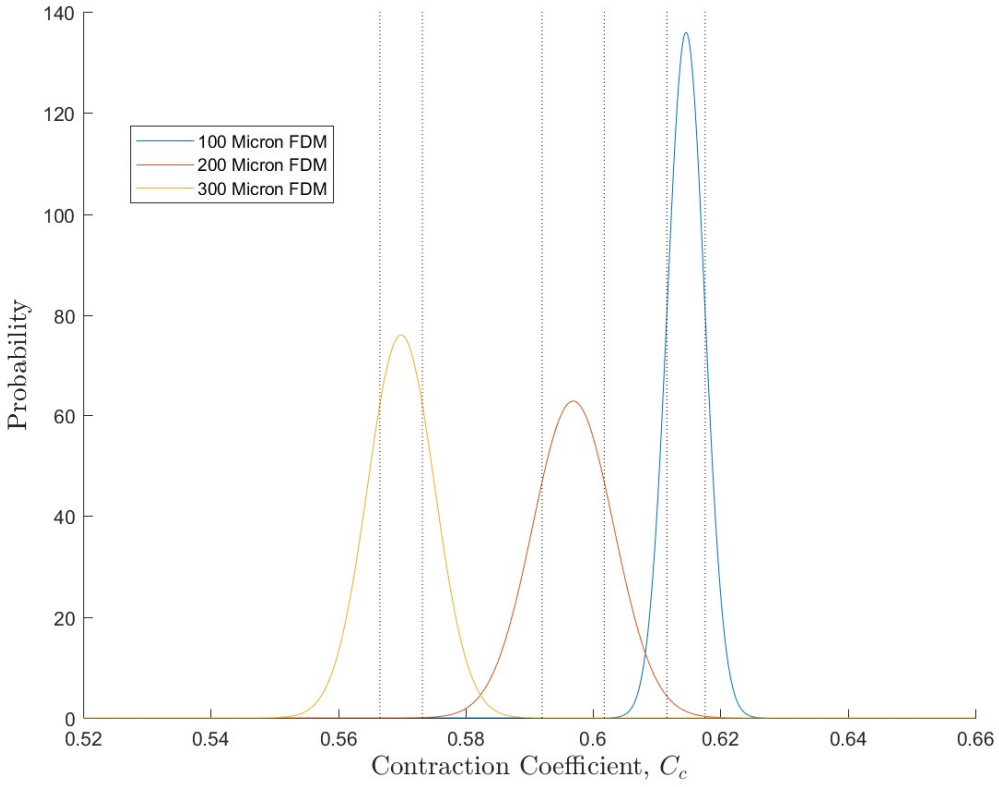


**Figure 28: Block 2 Contraction Coefficient Probability Density Functions**

**Table 7: Original and Adjusted Values for Block 2 Average Contraction Coefficient**

| | Cc | | | | |
|---|---|---|---|---|---|
| Sample Type | Original | 95% Limits | Radius Adjustment | 95% Limits | Average r/d |
| 100 µm FDM | 0.6146 | ± 0.0030 | 0.5953 | ± 0.0059 | 1.54E-02 |
| 200 µm FDM | 0.5969 | ± 0.0049 | 0.5681 | ± 0.0060 | 2.57E-02 |
| 300 µm FDM | 0.5699 | ± 0.0033 | 0.5358 | ± 0.0039 | 3.53E-02 |
| Reference | 0.611 | ± N/A | 0.611 | ± N/A | 0.00E+00 |

### 4.1.2 Critical Cavitation Number

The critical cavitation number for each test was determined by averaging the $C_D$ and $K$ at each setpoint in the individual test. The data for each test was then fit to a set of linear functions of $C_D$ as a function of the square root of $K$ for the cavitating and non-cavitating regimes of flow as

we know that these values are related to each other linearly through Equation 9. Through inspection of the data the ranges for each curve fit were determined. The intersection point of the two linear curve fits is taken to be the critical cavitation number. Figure 29 shows a representative plot of the two curve fits and their resulting intersection points for each of the FDM configurations. Table 8 lists the average $K_{crit}$ for each sample configuration.

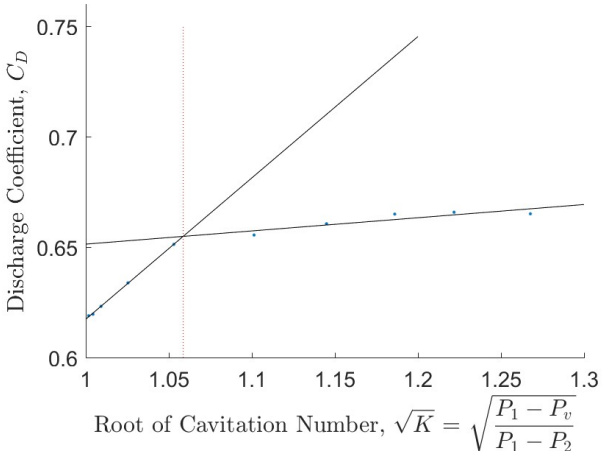


(a)

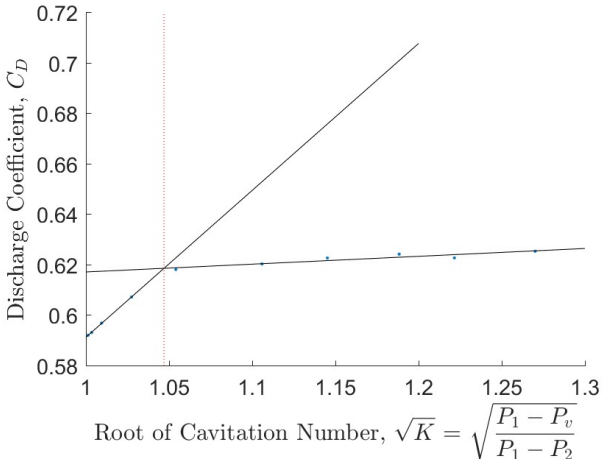


(b)

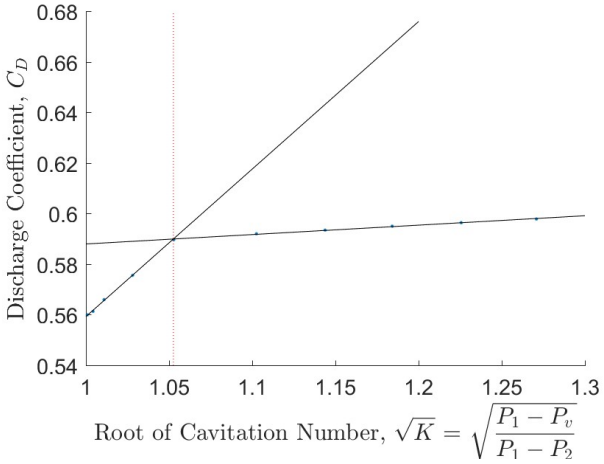


**Figure 29: Block 2 Results to Determine $K_{crit}$: (a) B2-100-1-2, (b) B2-200-1-2, (c) B2-300-3-3**

**Table 8: Block 2 and Reference $K_{crit}$ & Associated CDcrit Values**

| Sample Configuration | $K_{crit}$ | $C_{Dcrit}$ |
|---|---|---|
| 300 µm | 1.078 | 0.6151 |
| 200 µm | 1.083 | 0.6462 |
| 100 µm | 1.116 | 0.6877 |
| Reference | 1.45 | 0.7360 |

### 4.1.3: High Frequency Results

The results of the high-frequency pressure measurements for a single representative test for this block of testing is shown in Figure 30. The individual plots are fast fourier transforms taken over differing timeframes during the test. This is presented as such given the test's step-wise nature. Notable frequency peaks are identified with markers. Note that the y-axis is not constant across all plots. This is done in order to view some of the lower intensity peaks. The sampling frequency was 100 kHz with both the charge amplifier used as well as the data acquisition unit having a frequency limit of 100 kHz. The charge amplifier acts as a low pass filter with a cutoff at 100 kHz. No additional anti-aliasing filter was used due to restrictions on the data acquisition unit used. The main frequencies are still considered to be valid due to the explanation via Strouhal number analysis later in the section.

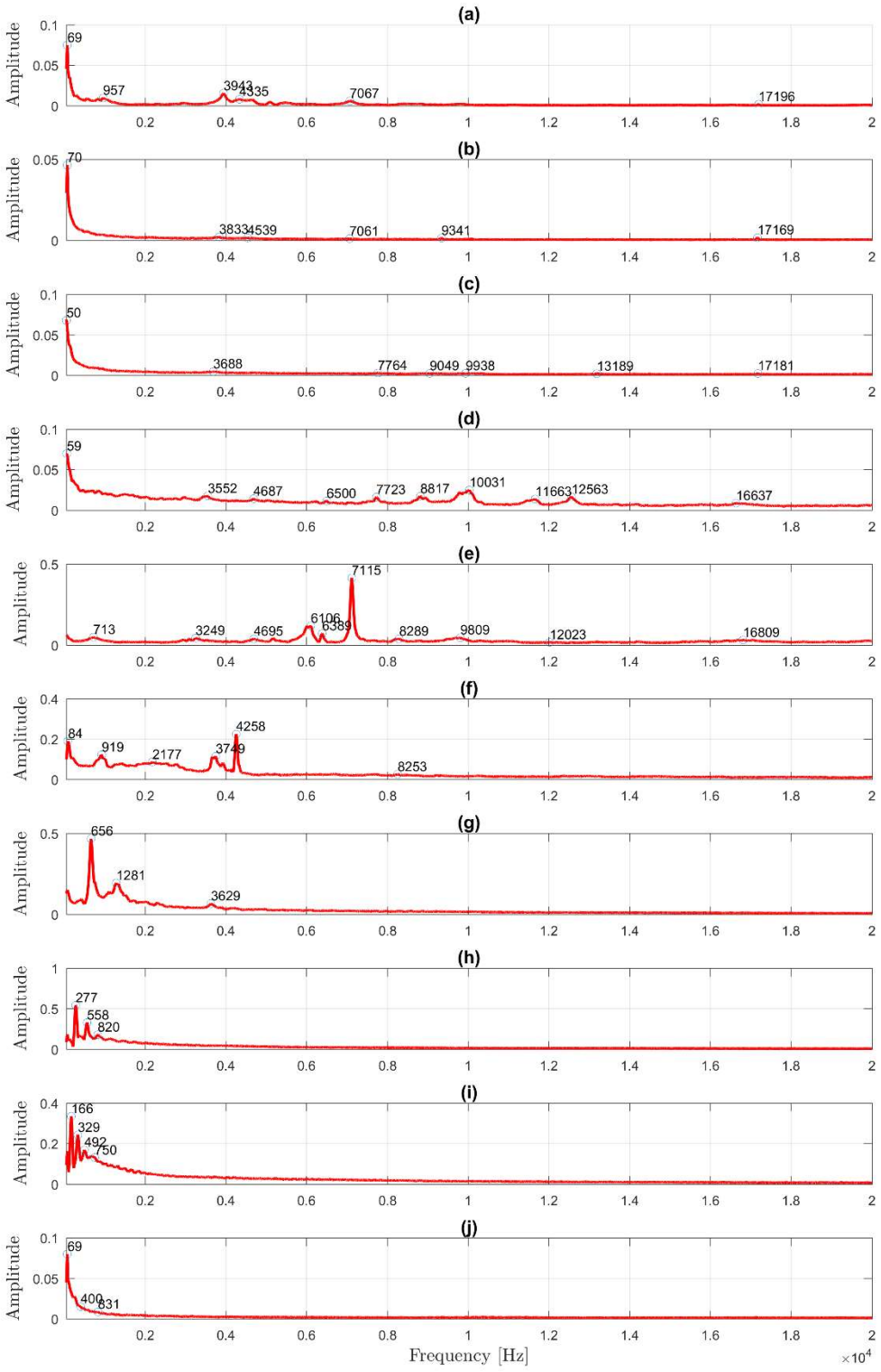


**Figure 30: B2-100-3-1 HF Plots: (a) t = 6-9s *K* = 1.6, (b) t = 16-19s *K* = 1.5, (c) t = 26-29s *K* = 1.4, (d) t = 36-39s *K* = 1.3, (e) t = 46-49s *K* = 1.2, (f) t = 56-59s *K* = 1.1, (g) t = 66-69s *K* = 1.05, (h) t = 76-79s *K* = 1.02, (i) t = 86-89s *K* = 1.01, (j) t = 96-99s *K* = 1.0**

At the $K$ = 1.2 setpoint in Figure 30 (e) a frequency peak of 7115 Hz is identified. This peak frequency decreases with cavitation number decrease as seen in Figure 30 (f)-(j). Due to its shifting nature with $K$, the peak frequency is likely not tied to the mass flow of the device. The peak amplitude at $K$ = 1.2 setpoint occurs at a Strouhal number of 0.668 based on no restriction in flow area or increase in fluid velocity at the vena contracta. This is outside the range of expected values as determined by a variety of sources previously reviewed[20]–[27]. Once cavitation is assumed by decreasing the effective area using the contraction coefficient and increasing the fluid velocity through the same decrease in area, the Strouhal number becomes 0. 248 which is well within the expected range and only 5.7% different from the peak Strouhal number of 0.234 calculated for the orifice at that point during the test. The further peak amplitudes of 4258 Hz in Figure 30 (f) at $K$ = 1.1 and 656 Hz in Figure 30 (g) at $K$ = 1.05 don't appropriately line up with any expected Strouhal numbers. This could be attributed to the increase in flow velocity downstream with decreasing Cavitation Number which would need to be measured in order to determine the Strouhal numbers downstream of the inlet cavitation bubble. Although not the primary focus of this thesis, other similar frequency analyses of unsteady pressure phenomenon for these tests are included in Appendix E for future analysis. They generally show the same Strouhal number agreement as the test presented.

### 4.2 SLM Orifice Data

Block 3 Testing contained tests spanning the SLM configuration. Figure 31 shows the response of these tests to the set conditions as controlled by the globe valve. The x-axis of the chart shows the time during the test with the cavitation number plotted in the y-axis. Cavitation number is seen decreasing in planned steps as the test progresses. This results in Figure 31 closely follows the expected setpoint schedule in Figure 23 as well as the FDM data in Figure 24. The legend for these figures used the same naming convention as previously used. As previously mentioned, any fluctuations in the setpoint and transient movement is due to the closed loop control of the globe valve during the test.

Mass flow rates during the test are shown in Figure 32. The x-axis for this figure is the time in test and the y-axis is the mass flow of the test in kg/s calculated using the venturi flowmeter and Equation 10. Of note, the mass flows for the SLM configurations have a much tighter grouping than that of the FDM configurations as previously described in Figure 25. Much like in the Block 2 testing, shown in Figure 25, the mass flow can be seen changing through a majority of the test. The individual steps in mass flow is due to the step-wise nature of the testing and the transient movement to each setpoint is due to the closed loop control of the globe valve in the test. A lack of flow control occurs at the $K = 1.02$ setpoints for a few tests. This is due to the difference in fluid resistance from part-to-part which leads to a loss of closed loop control stability at certain conditions. This lack of setpoint control does lead to an increase in variance for cavitation number and discharge coefficient for that setpoint. However, due to the nature of the cavitation number at values close to $K = 1.0$, the fact that the setpoint occurs below the critical cavitation number, and the fact that this variance is due to a modulation of downstream pressure rather than upstream pressure, this variance does not affect the contraction coefficient calculation. The mass flow rate

differences from test-to-test can be seen, as well as the part-to-part deviation possibly due to slight differences in inlet radius, roughness, etc. The test-to-test deviation is especially apparent with the differences between tests B3-SLM-4-1, B3-SLM-4-2, and B3-SLM-4-3. These differences are factored out of the results when the results are compared by way of cavitation number – discharge coefficient relationship later in the analysis.

Figure 33 details the mass flow relationship with the nondimensional cavitation number for the Block 3 samples. Calculating the cavitation number and using it for comparative purposes should remove influences from the test-to-test deviations in upstream and downstream pressures. The undulations seen in the data about each of the cavitation number setpoints is due to the closed loop control of the globe valve and the process of the system steering to the setpoint. This does not adversely affect the results when accounted for using the relationship between the cavitation number and discharge coefficient. The increasing mass flow section of the figure from $K = 1.6$ until $K \approx 1.2$ indicates non-cavitating operation whereby the decreasing downstream pressure increases mass flow up until the cavitation point. The constant mass flow section of the figure from $K \approx 1.2$ to $K = 1.0$ indicates cavitation in the test sample and constant mass flow control whereby the mass flow is only due to the upstream pressure. Figure 33 shows indications of choking as indicated by the leveling of the discharge coefficient happening at $K \approx 1.2$ rather than $K \approx 1.1$-$1.15$ for the FDM samples. This transition value is lower than the reference value of $K = 1.45$ from work by Nurick [8]. This could be attributed to a difference in waviness and/or roughness profiles from that of the FDM parts as detailed in Table 3.

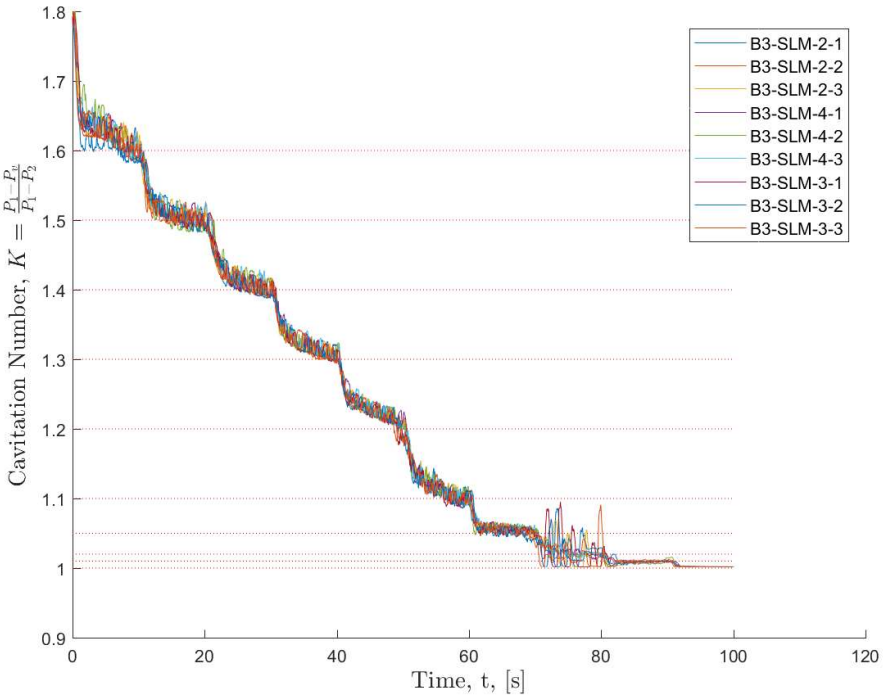


**Figure 31: Block 3 Sample Cavitation Number Trend with Time**

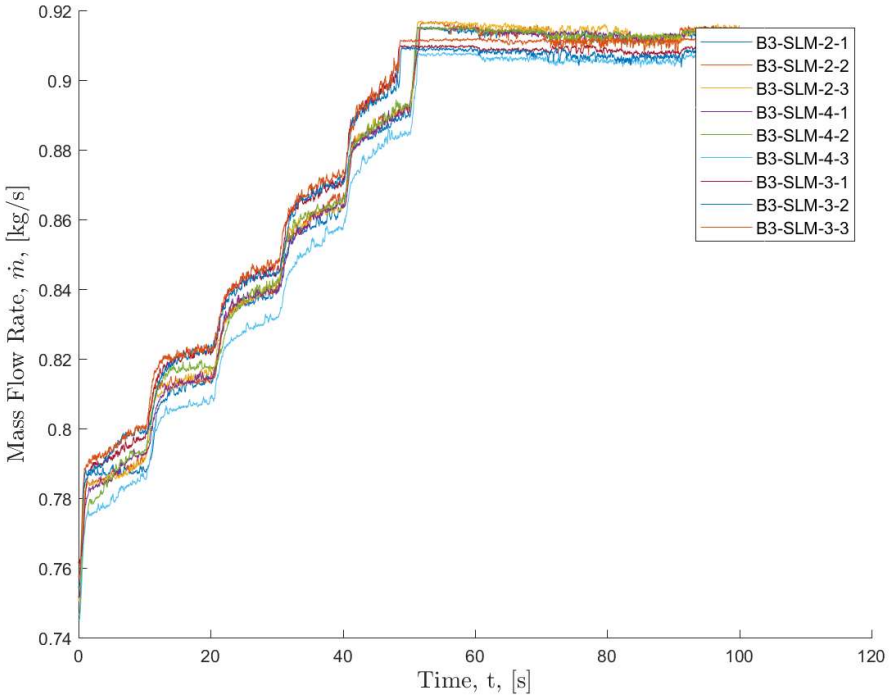


**Figure 32: Block 3 Sample Mass Flow trend with Time**

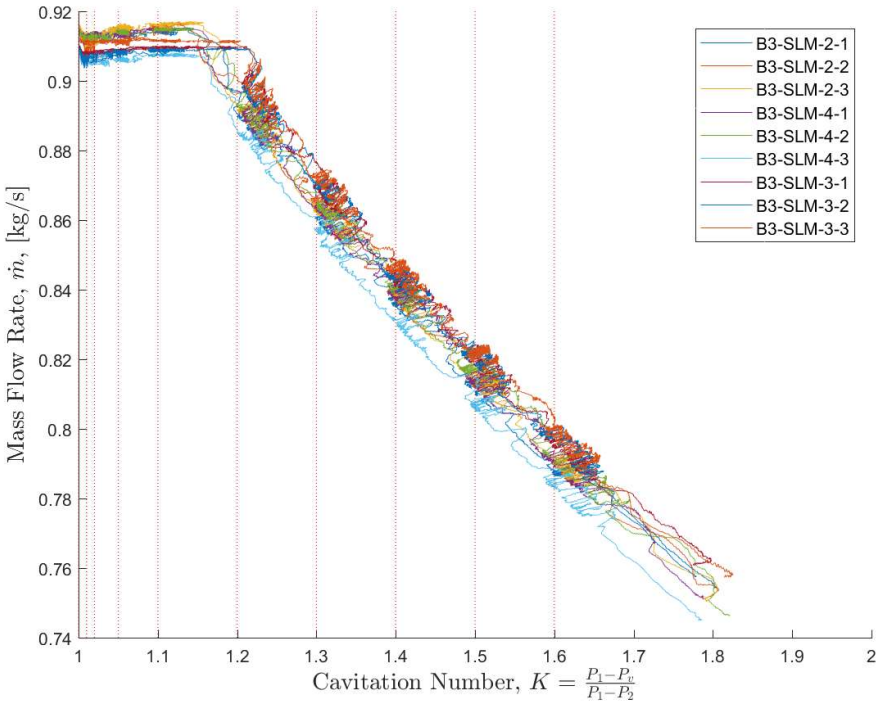


**Figure 33: Block 3 Sample Mass Flow Relation to Cavitation Number**

A trace of the discharge coefficient and nondimensional cavitation number for the Block 3 samples is shown in Figure 34. Plotting the data by way of nondimensional cavitation number and discharge coefficient will factor out the test-to-test differences in upstream pressure and downstream pressure as well as diameter differences between parts. The differences between the curves should be due to part-to-part differences in roughness, inlet radius, and other geometrical effects as well as test-to-test deviations that are uncontrolled such as differences in gasification and water purity. Additionally, as Equation 4 shows, the values of $C_D$ and $K$ are related through $C_c$ which therefore means that Figure 34 can be used to graphically analyze the differences in cavitation operation. Compared to the accepted baseline of a $C_c$ of 0.611 and transition cavitation number of $K = 1.45$ the SLM samples transition at a lower value of $K$ at $K \approx 1.2$ and have a higher $C_c$ of 0.6462. This value has not been adjusted for the inlet radius which may account for the increase over 0.611. In Figure 34, the knee in the curves is the cavitation number at which the tests

transition from non-cavitating orifice flow to cavitation. The difference in transitional cavitation number and contraction coefficient could be due to the roughness and waviness information detailed in Table 3 and its differences from that of the traditionally smooth orifices used in Nurick [8] and others. Further discussion on this is in Section 4.2.1, 4.2.2, and 4.4.

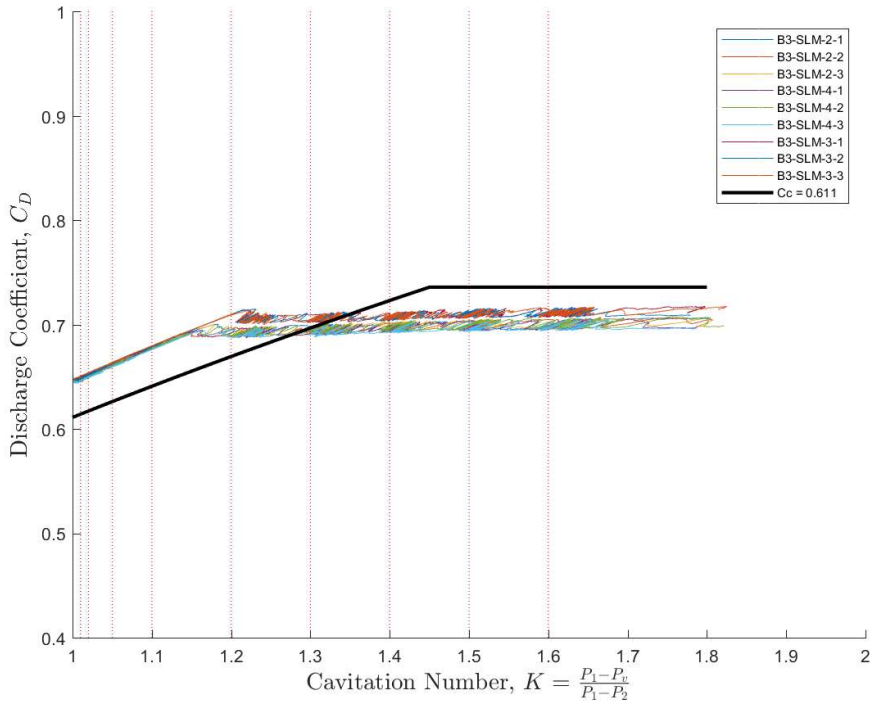


**Figure 34: Block 3 Sample Discharge Coefficient and Cavitation Number Relationship (Prediction and Measured)**

### 4.2.1 Contraction Coefficient

The Contraction Coefficient and related uncertainty for each test was determined using the same approach as used in 4.1.2. To compare the contraction coefficient value for each sample configuration an average and 95% confidence limits of the mean was determined. Figure 35 shows a probability distribution function for each configuration. Dotted lines demarcate the 95% confidence limits. This shows that the configurations are statistically different with respect to their

mean contraction coefficient values. The value determined was 0.6462 for the SLM configuration. This value can be adjusted for the inlet edge radius using a relation derived by Nurick [2]. This empirical relation outlined in Equation 13 adjusts this $C_c$ value as previously documented in Section 4.1.2. The original value and the adjusted value is listed in Table 9 with the Block 2 FDM values and the reference derived from work by Nurick[8] and Howland and Richetta[28]

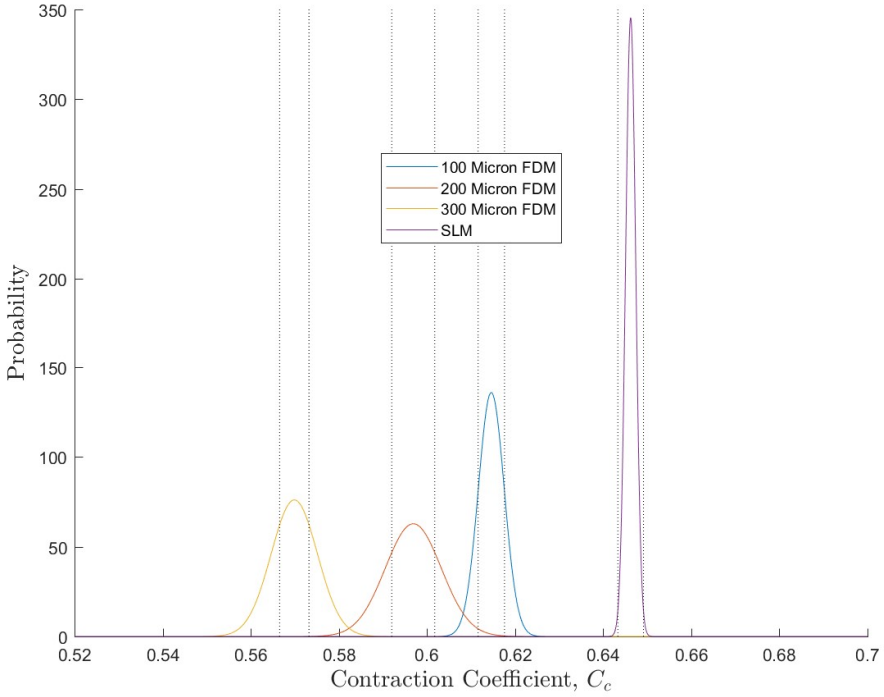


**Figure 35: Block 2 and 3 Contraction Coefficient Probability Density Functions**

**Table 9: Original and Adjusted Values for Contraction Coefficient**

| | Cc | | | | |
|---|---|---|---|---|---|
| Sample Type | Original | 95% Limits | Radius Adjustment | 95% Limits | Average r/d |
| 100 µm FDM | 0.6146 | ± 0.0030 | 0.5953 | ± 0.0059 | 1.54E-02 |
| 200 µm FDM | 0.5969 | ± 0.0049 | 0.5681 | ± 0.0060 | 2.57E-02 |
| 300 µm FDM | 0.5699 | ± 0.0033 | 0.5358 | ± 0.0039 | 3.53E-02 |
| SLM | 0.6462 | ± 0.0029 | 0.6150 | ± 0.0084 | 2.07E-02 |
| Reference | 0.611 | ± N/A | 0.611 | ± N/A | 0.00E+00 |

### 4.2.2 Critical Cavitation Number

The critical cavitation number for each test was determined by averaging the $C_D$ and $K$ at each setpoint in the individual test. The data for each test was then fit to a set of linear functions of $C_D$ as a function of the square root of $K$ for the cavitating and non-cavitating regimes of flow as we know that these values are related to each other linearly through Equation 4. Through inspection of the data the ranges for each curve fit were determined. The intersection point of the two linear curve fits is taken to be the critical cavitation number. Figure 36 shows a representative plot of the two curve fits and their resulting intersection point for the SLM configuration. lists the average $K_{crit}$ for each sample configuration including the previously mentioned FDM configurations.

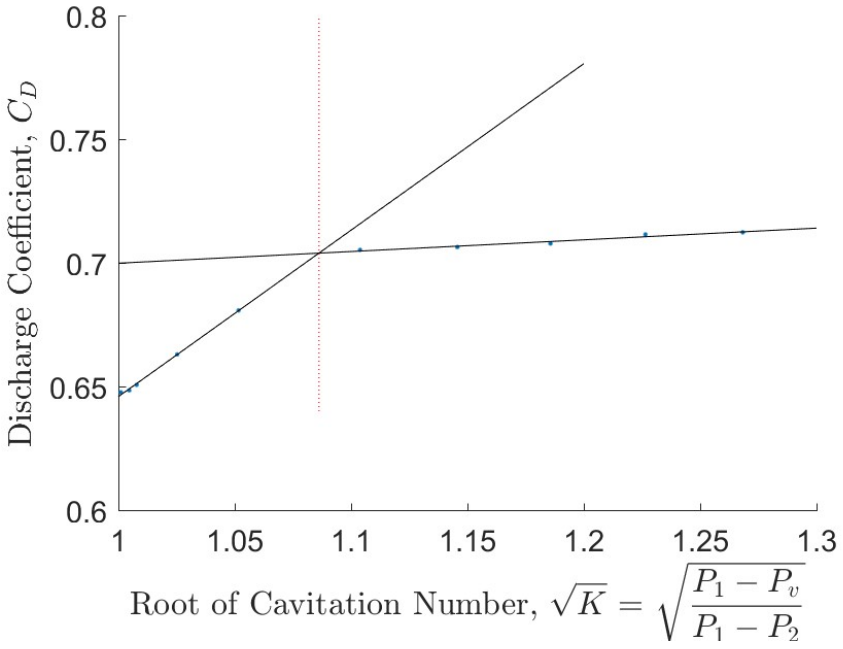


**Figure 36: SLM $K_{crit}$ Identification**

**Table 10: Block 2, Block 3, and Reference $K_{crit}$ Values**

| Sample Configuration | $K_{crit}$ | $C_{Dcrit}$ |
|---|---|---|
| 300 µm | 1.078 | 0.6151 |
| 200 µm | 1.083 | 0.6462 |
| 100 µm | 1.116 | 0.6877 |
| SLM | 1.154 | 0.7487 |
| Reference | 1.45 | 0.7360 |

### 4.2.3 High Frequency Results

A set of High Frequency plots at progressing times in the test are shown in Figure 37 for a representative test, SLM Test 4-2. Notable frequency peaks are identified with markers. Each subplot in the figure is at a separate setpoint in the test.

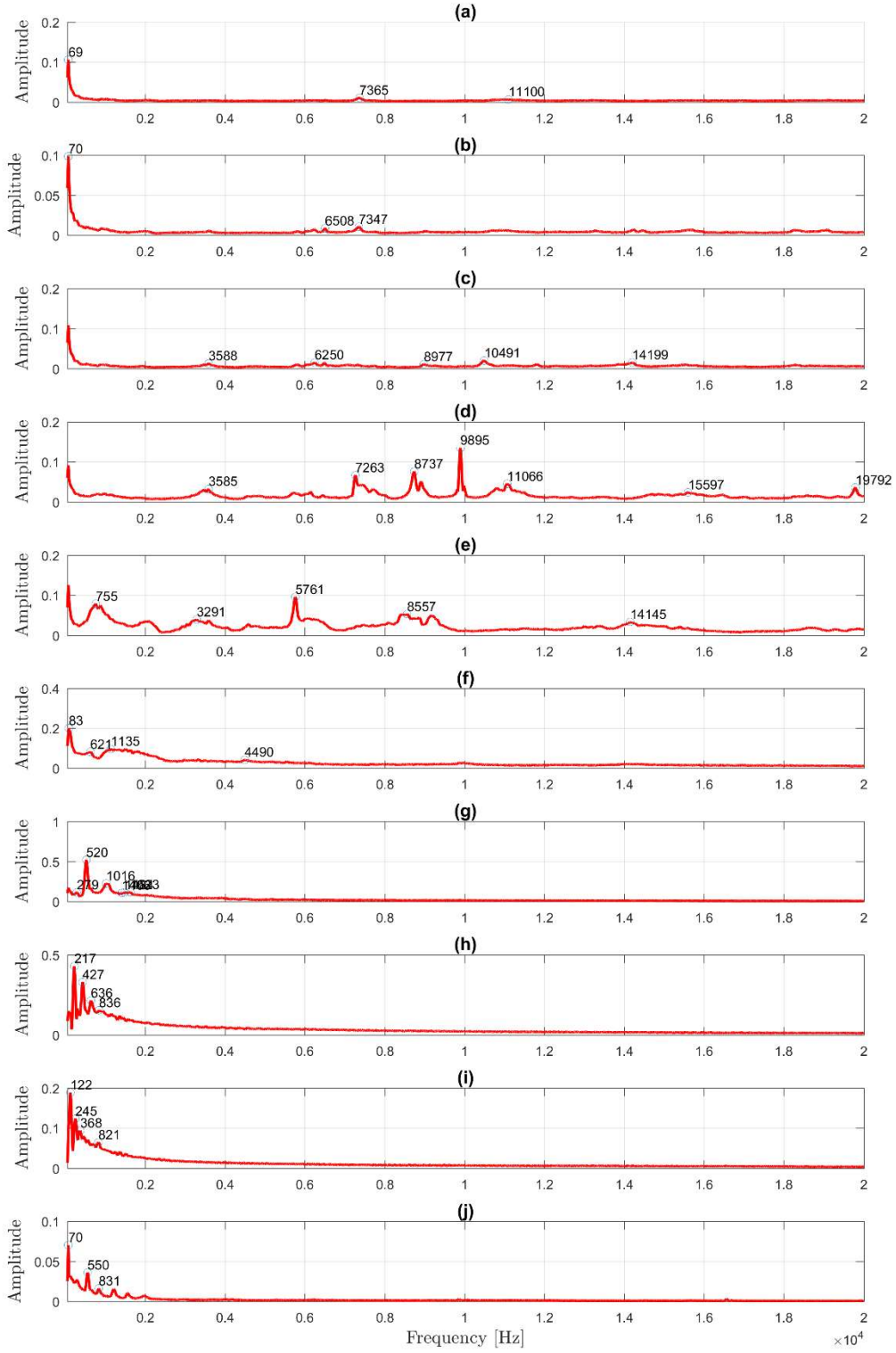


**Figure 37: B3-SLM-4-2 HF Plots: (a) t = 6-9s *K* = 1.6, (b) t = 16-19s *K* = 1.5, (c) t = 26-29s *K* = 1.4, (d) t = 36-39s *K* = 1.3, (e) t = 46-49s *K* = 1.2, (f) t = 56-59s *K* = 1.1, (g) t = 66-69s *K* = 1.05, (h) t = 76-79s *K* = 1.02, (i) t = 86-89s *K* = 1.01, (j) t = 96-99s *K* = 1.0**

At the $K$ = 1.3 setpoint in Figure 37 (d) three frequencies are prevalent at 7263 Hz, 8737 Hz, and 9895 Hz. All three of these frequencies fall within Strouhal numbers that are likely for vortex shedding [20]–[27] based on the reductions in area by way of the contraction coefficient as done previously. The 7263 Hz frequency falls at a $St$ = 0.259 with the peak Strouhal number being calculated to be 0.234 at that point in the test. At the $K$ = 1.2 in Figure 37 (e) setpoint in the test the frequency peak shifts to 5761 Hz which is at a $St$ value of 0.214 versus the peak value calculated to be 0.234. Further reductions in the peak frequency in Figure 37 (f)-(j) can't be explained from the data available and may be due to increase in flow velocity downstream with decreasing Cavitation Number which would need to be measured in order to determine the Strouhal numbers downstream of the inlet cavitation bubble.

Although not the primary focus of this thesis, other similar frequency analyses of unsteady pressure phenomenon for these tests are included in Appendix F for future analysis. They generally show the same Strouhal number agreement as the test presented.

### 4.3 Subtractively Manufactured Orifice Data

Block 4 and Block 5 tests were performed on subtractively manufactured samples. Block 4 tests were used to determine if additional sharpening of the inlet was needed and after testing it was determined that sharpening was necessary and therefore Block 4 testing data will not be included in this thesis.

Figure 38 shows the response of the Block 5 tests to the set conditions controlled by the globe valve. The x-axis is the time of the test and the y-axis is the cavitation number during the test. Cavitation Number is seen decreasing in steps as the test progresses. The results in Figure 38 closely follow the expected setpoint schedule shown in Figure 23The fluctuations seen in the cavitation number can be attributed to the closed loop control by the globe valve as previously described in 4.2. The instability at $K = 1.02$ is due to the flow resistance as previously described in 4.3.

Figure 39 shows the mass flow trends for this block of testing. The x-axis is the time during the test and the y-axis is the mass flow in kg/s. Notably, over nearly the entire test, mass flow is generally constant and invariant to the changes in cavitation number as defined in the test. This is much different than the previous configurations. The mass flow rate differences from part-to-part can be seen, as well as the test-to-test deviation possibly due to differences in upstream pressure, cavitation number, etc. These test-to-test deviations can be partially accounted for when analyzed in the context of nondimensional cavitation number.

Figure 40 shows the relation of mass flow on the y-axis to a nondimensional cavitation number, thereby removing test-to-test differences in upstream and downstream pressure, on the x-axis which shows as cavitation number decreases from $K = 1.6$ the mass is invariant rather than increasing with increasing steps in cavitation number indicating that the mass flow is choked. The

critical cavitation number is therefore greater than $K = 1.6$ which is greater than the predicted value by Nurick [8]. This could be attributed to a roughness difference from that of the articles Nurick tested and the articles used in this work.

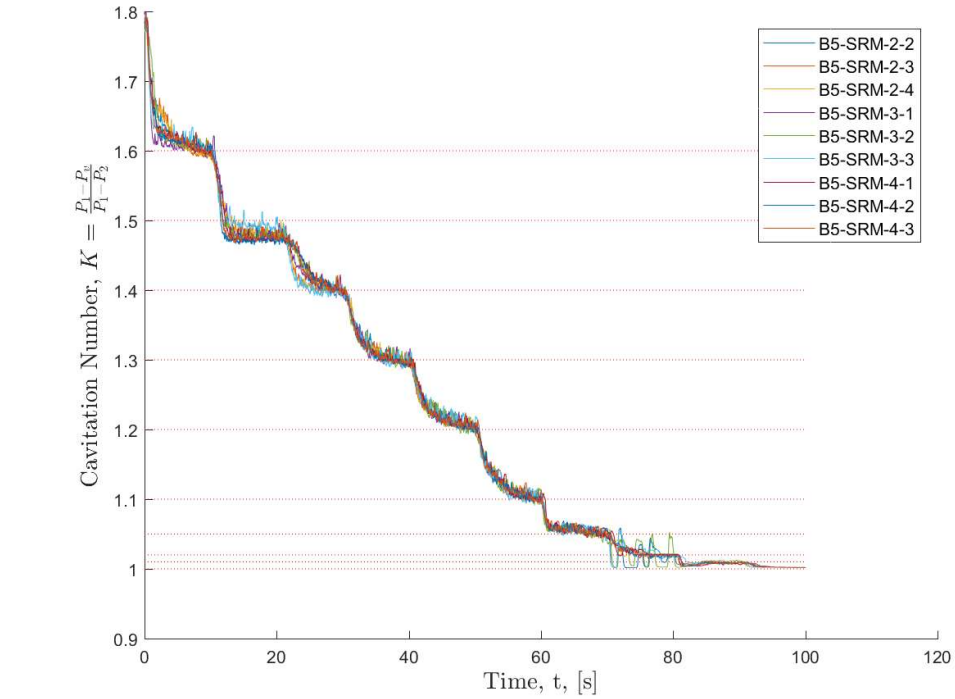


**Figure 38: Block 5 Sample Cavitation Number trend with Time**

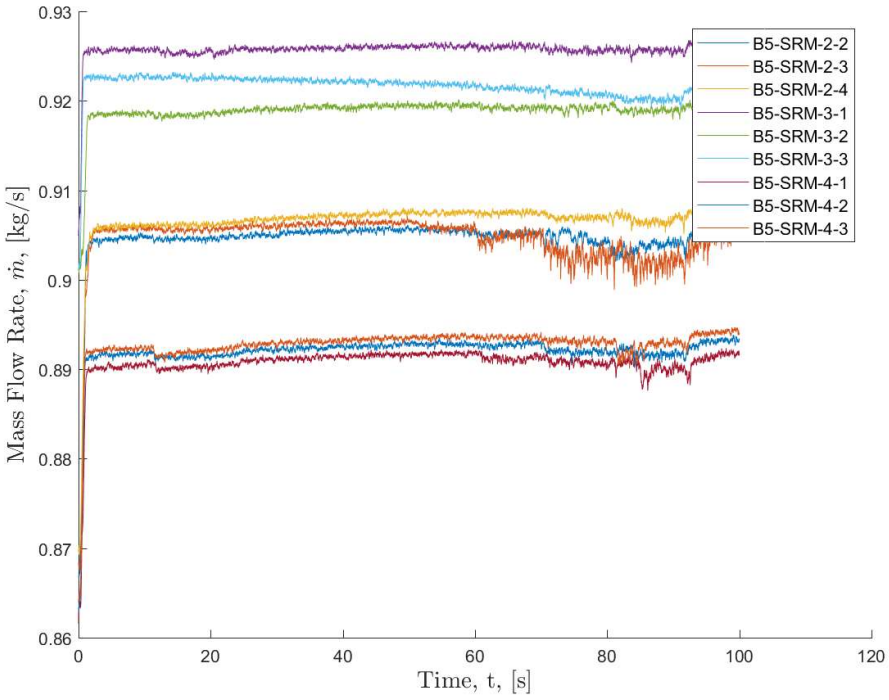


**Figure 39: Block 5 Sample Mass Flow trend with Time**

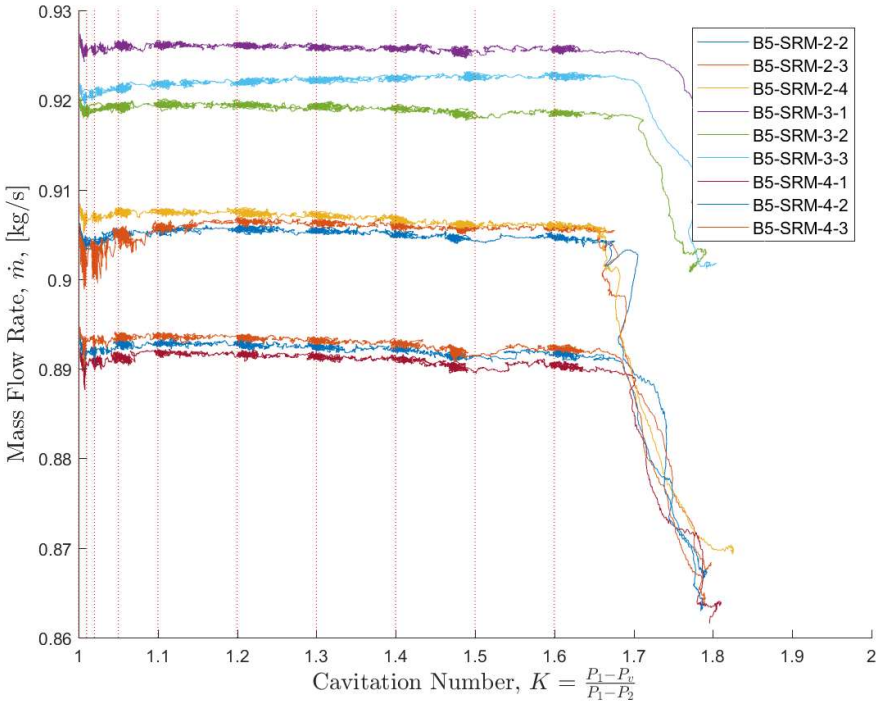


**Figure 40: Block 5 Sample Mass Flow Relation to Cavitation Number**

Figure 41 shows the nondimensional discharge coefficient on the y-axis with respect to the nondimensional cavitation number on the x-axis for all Block 5 tests and a predicted value for a sharp edge inlet orifice transitioning to cavitation at $K$ = 1.45 derived from Equation 3 and Equation 5. This relationship shown Figure 41 shows close agreement between the subtractively manufactured configuration and the accepted reference except for the transition cavitation number. By plotting the data with respect to the discharge coefficient and the cavitation number the variance due to testing variables such as upstream and downstream pressure are factored out of the data. The differences between the curves is now solely due to the inlet radius, roughness, other geometrical effects, as well as uncontrollable deviances such as differences in water purity and gasification. Additionally, as Equation 4 shows, the values of $C_D$ and $K$ are related through $C_c$ which therefore means that Figure 41 can be used to graphically analyze the differences in cavitation operation for the different articles and tests. This is likely due to difference in roughness from the subtractively manufactured configuration to that of the reference. In Figure 41, the knee in the curves is the cavitation number at which the tests transition from non-cavitating orifice flow to cavitation. The transition cavitation number from the data looks to be $K \approx 1.7$ rather than the accepted $K = 1.45$. The average cavitation number across the samples is 0.6161 compared to 0.611 of the accepted reference which is effectively in the noise.

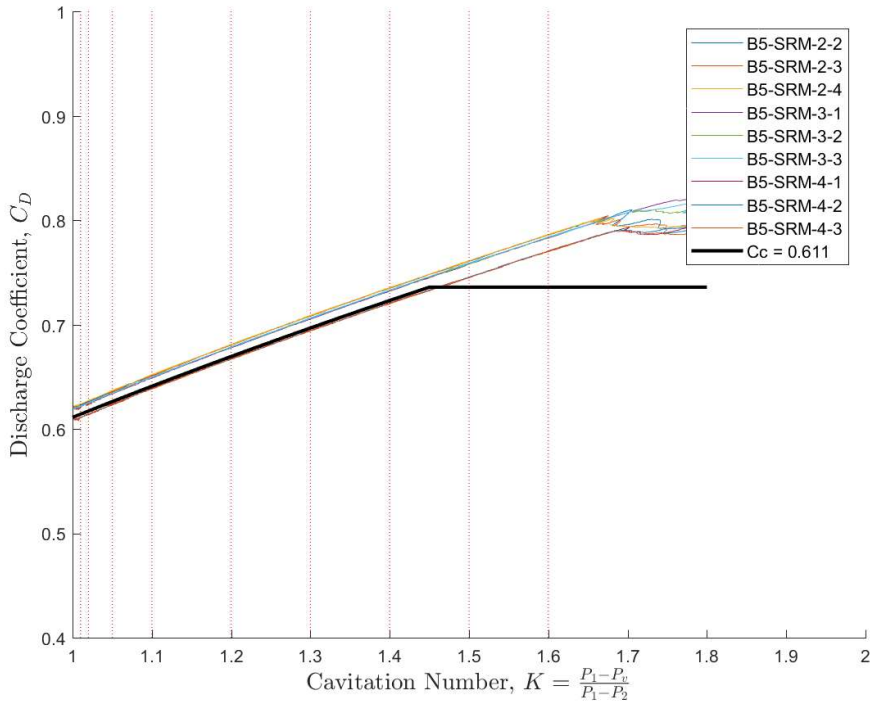


**Figure 41: Block 5 Sample Discharge Coefficient and Cavitation Number Relationship (Predicted and Measured)**

### 4.3.1 Contraction Coefficient

The Contraction Coefficient and related uncertainty for each test was determined using the same approach as used in 4.1.2. To compare the contraction coefficient value for each sample configuration an average and 95% confidence limits of the mean was determined. Figure 42 shows a probability distribution function for each configuration. Dotted lines demarcate the 95% confidence limits. This shows that the configurations are statistically different with respect to their mean contraction coefficient values. The value determined was 0.6161. This value can be adjusted for the inlet edge radius using a relation derived by Nurick [2]. This empirical relation outlined in Equation 9 adjusts this $C_c$ value as previously documented in Section 4.1.2. The original value and the adjusted value is listed in Table 11 with the Block 2 FDM, Block 3 SLM values, and the reference derived from work by Nurick[8] and Howland and Richetta[28].

.

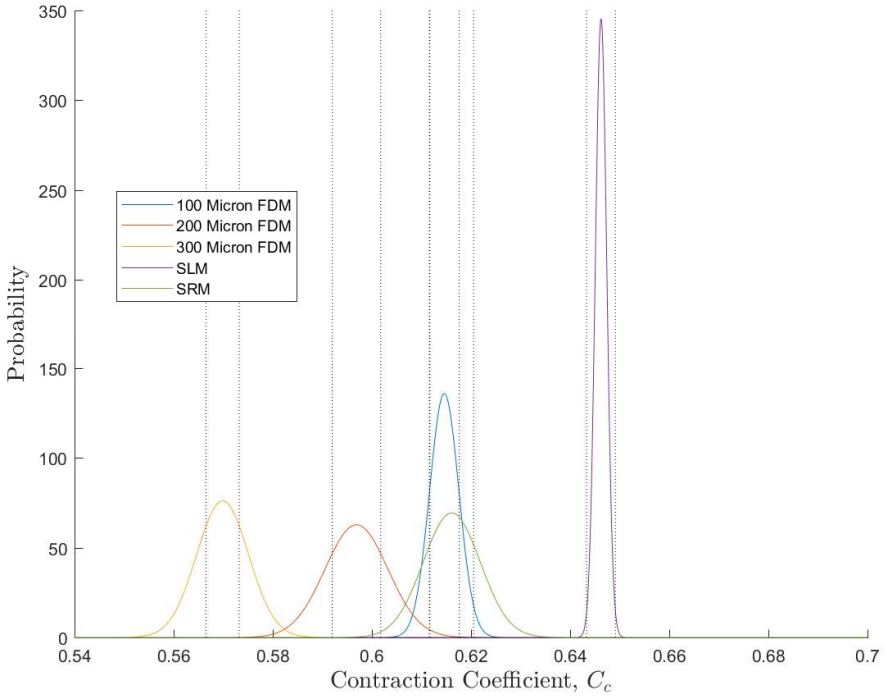


**Figure 42: Block 2, 3, and 5 Contraction Coefficient Probability Density Function**

**Table 11: Original and Adjusted Values for Contraction Coefficient**

| | Cc | | | | |
|---|---|---|---|---|---|
| Sample Type | Original | 95% Limits | Radius Adjustment | 95% Limits | Average r/d |
| 100 µm FDM | 0.6146 | ± 0.0030 | 0.5953 | ± 0.0059 | 1.54E-02 |
| 200 µm FDM | 0.5969 | ± 0.0049 | 0.5681 | ± 0.0060 | 2.57E-02 |
| 300 µm FDM | 0.5699 | ± 0.0033 | 0.5358 | ± 0.0039 | 3.53E-02 |
| SLM | 0.6462 | ± 0.0029 | 0.6150 | ± 0.0084 | 2.07E-02 |
| SRM | 0.6161 | ± 0.0044 | 0.6082 | ± 0.0056 | 6.23E-03 |
| Reference | 0.611 | ± N/A | 0.611 | ± N/A | 0.00E+00 |

### 4.3.2 Critical Cavitation Number

The critical cavitation number for the subtractively manufactured configuration was unable to be determined from the data as all the data points are in the cavitating regime of flow. Figure 43 shows a representative plot of this.

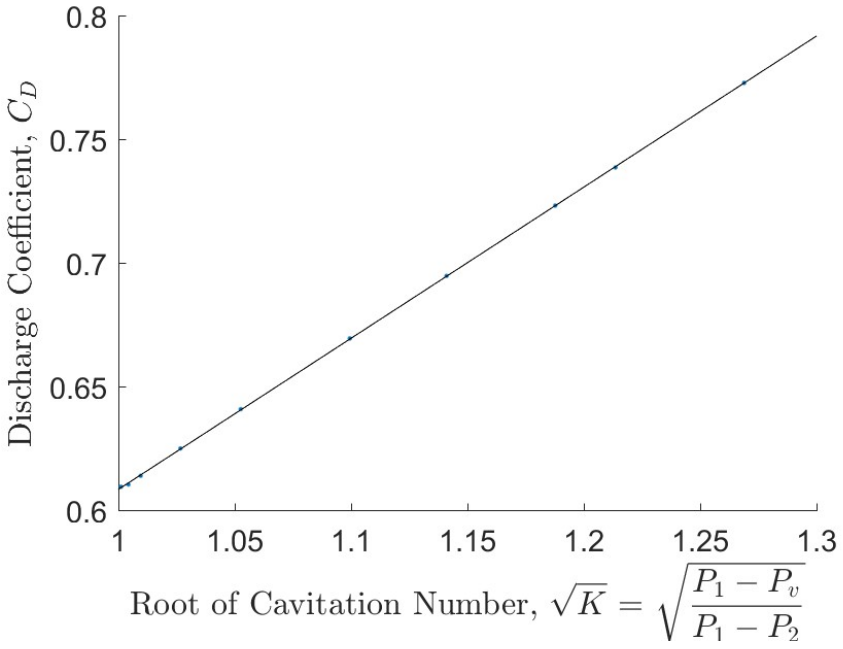


**Figure 43: Block 5 $K_{crit}$ Identification**

### 4.3.3 High Frequency Results

A set of High Frequency plots at progressing times in the test are shown in Figure 43 for a representative test, Subtractively Manufactured Test 2-3. Notable frequency peaks are identified with markers. Each subplot in the figure is at a separate setpoint in the test.

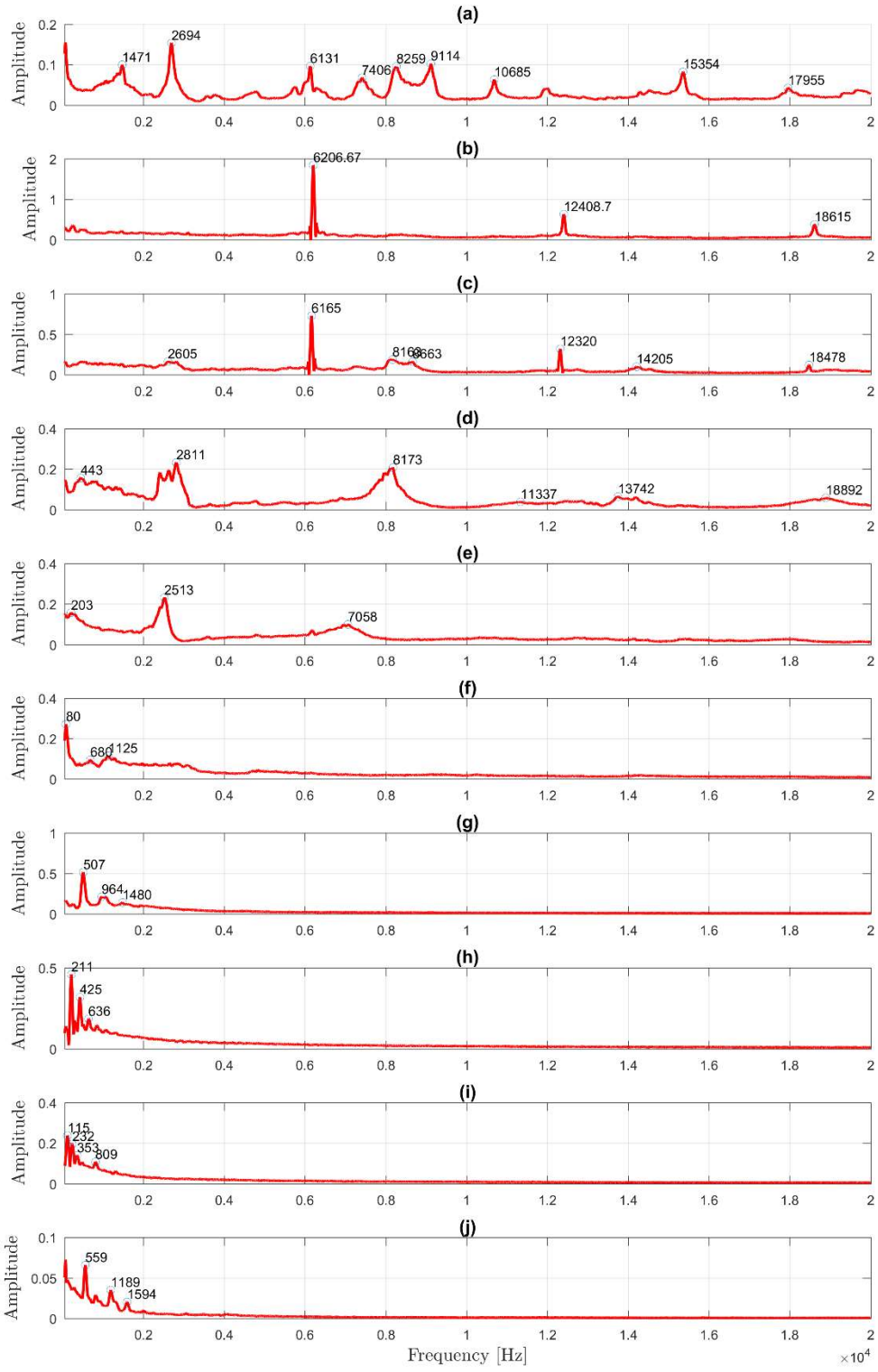


**Figure 44: B5-SRM-2-3 HF Plots: (a) t = 6-9s *K* = 1.6, (b) t = 16-19s *K* = 1.5, (c) t = 26-29s *K* = 1.4, (d) t = 36-39s *K* = 1.3, (e) t = 46-49s *K* = 1.2, (f) t = 56-59s *K* = 1.1, (g) t = 66-69s *K* = 1.05, (h) t = 76-79s *K* = 1.02, (i) t = 86-89s *K* = 1.01, (j) t = 96-99s *K* = 1.0**

At the $K$ = 1.5 setpoint in Figure 44 (b) a frequency peak of 6207 Hz is identified. This peak corresponds with a Strouhal number of 0.233 whereas the peak Strouhal number for this point during the test is identified to be 0.234. This close agreement between the peak Strouhal number and the number attained during the test along with the high intensity of the frequency peak suggests that this peak is due to a vortex shedding frequency of the fluid device. Additionally, at the $K$ = 1.4 setpoint a similar peak at 6165 Hz is identified which corresponds with $St$ = 0.231 whereas the peak is at $St$ = 0.234. This is additionally explained by way of the vortex shedding frequency**.** Further reductions in the peak frequency in Figure 44 (d)-(j) can't be explained from the data available and may be due to increase in flow velocity downstream with decreasing Cavitation Number which would need to be measured in order to determine the Strouhal numbers downstream of the inlet cavitation bubble.

Although not the primary focus of this thesis, other similar frequency analyses of unsteady pressure phenomenon for these tests are included in Appendix F for future analysis. They generally show the same Strouhal number agreement as the test presented.

## 4.4 Roughness Relationships to the Contraction Coefficient and Critical Cavitation Number

By comparing the contraction coefficient and critical cavitation number across multiple configurations by way of certain roughness variables, some relationships and trends can be seen in the data. Roughness variables analyzed in this section include the FDM layer height, $h$, the arithmetic mean roughness, $Ra$, the mean roughness spacing, $S$, and the highest peak value, $Rp$ all documented in Table 1 or Table 3.

### 4.4.1 FDM Layer Height

FDM layer height was used to analyze tests in Block 2. Figure 45 shows the data along with a linear fit of the data. The equation for the linear fit of the data is shown in Equation 14. This equation predicts a value of 0.6259 for a part with "zero layer height" which is close to the value of the sharp edge inlet reference. This indicates not only a generally good agreement with the Block 2 data but also with the accepted reference value for $C_c$.

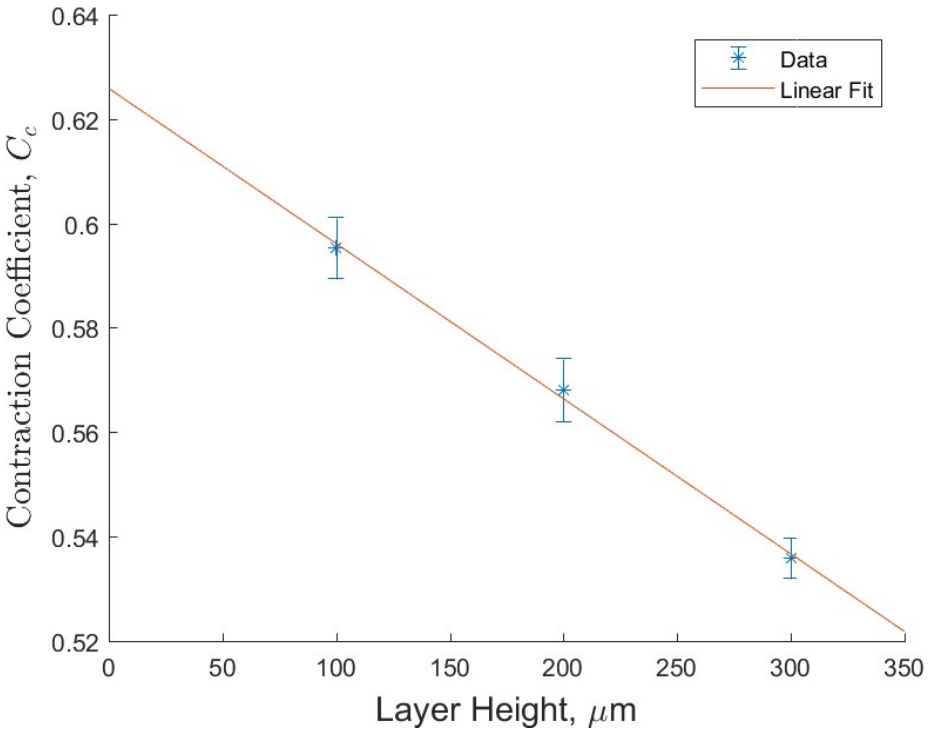


**Figure 45: Layer Height - Contraction Coefficient Relationship**

$$\boldsymbol{C_c = (-2.9735 * 10^{-4}) * h + \ 0.6259} \qquad 14$$

When comparing $K_{crit}$ using this variable, Figure 46 shows a few fits to the data. The limited datapoints for this variable limit the degree of information we can glean but an exponential fit does well to predict the zero layer height critical cavitation number of $K$ = 1.45 – 1.6.

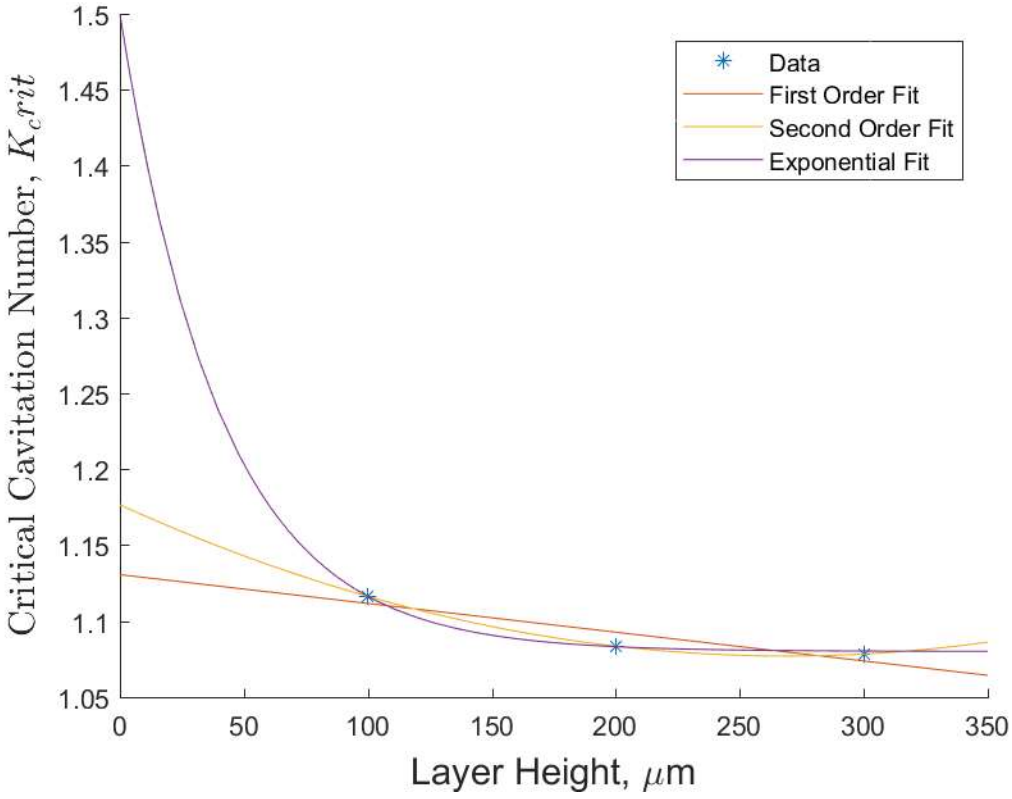


**Figure 46: Layer Height - Critical Cavitation Number Relationship**

### 4.4.2 Arithmetic Mean Roughness (*Ra*)

Figure 47 compares contraction coefficient using arithmetic mean roughness (*Ra*) of the part configurations. Both a linear fit and second order fit do well to predict values close the ideal value of 0.611 predicted by Howland and Richetta [28]. The linear fit predicts a zero roughness $C_c$ of 0.6230 whereas the second order fit predicts a value of 0.6111 for the y-intercept value. Therefore, both of these functions fit the data well and fit predictions for zero roughness ideal configurations More information would allow for the finer details of this relationship to be understood.

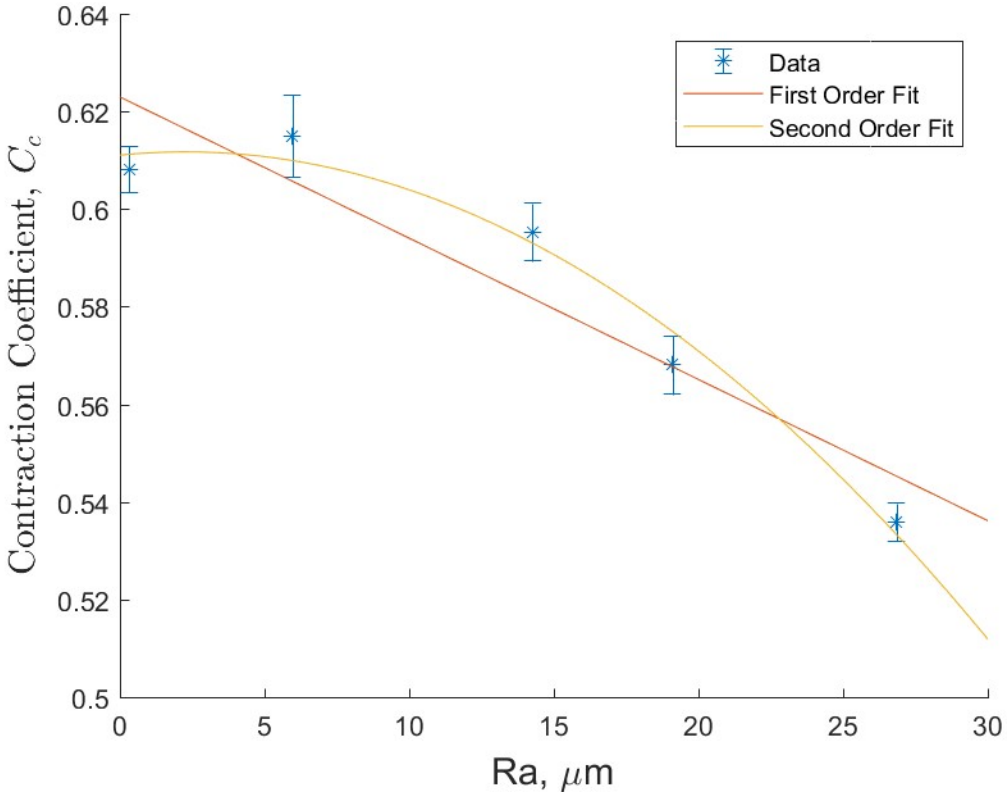


**Figure 47: Mean Roughness - Contraction Coefficient Relationship**

Figure 48 compares critical cavitation number using arithmetic mean roughness. None of the chosen fits shows good agreement to the data. This may mean that arithmetic mean roughness is not tied to the onset of cavitation.

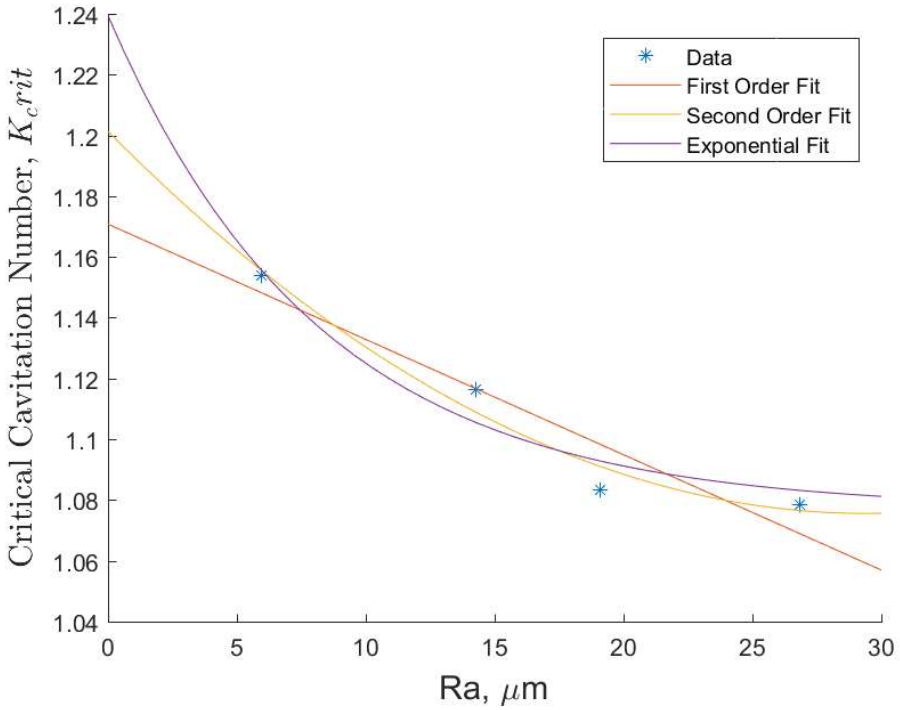


**Figure 48: Mean Roughness - Critical Cavitation Number Relationship**

### 4.4.3 Roughness Profile Spacing (*S*)

Using the roughness profile spacing. One can draw a possible linear fit to the data for contraction coefficient as shown in Figure 49. This fit is very similar to that of the layer height due to the intrinsic link between the layer height and peak-to-peak spacing of the roughness profile of the parts. The fit slightly over predicts a "zero" value closer to 0.64. Comparing the critical cavitation number with the peak-to-peak spacing does not find any significant curve fits to the data as shown in Figure 50.

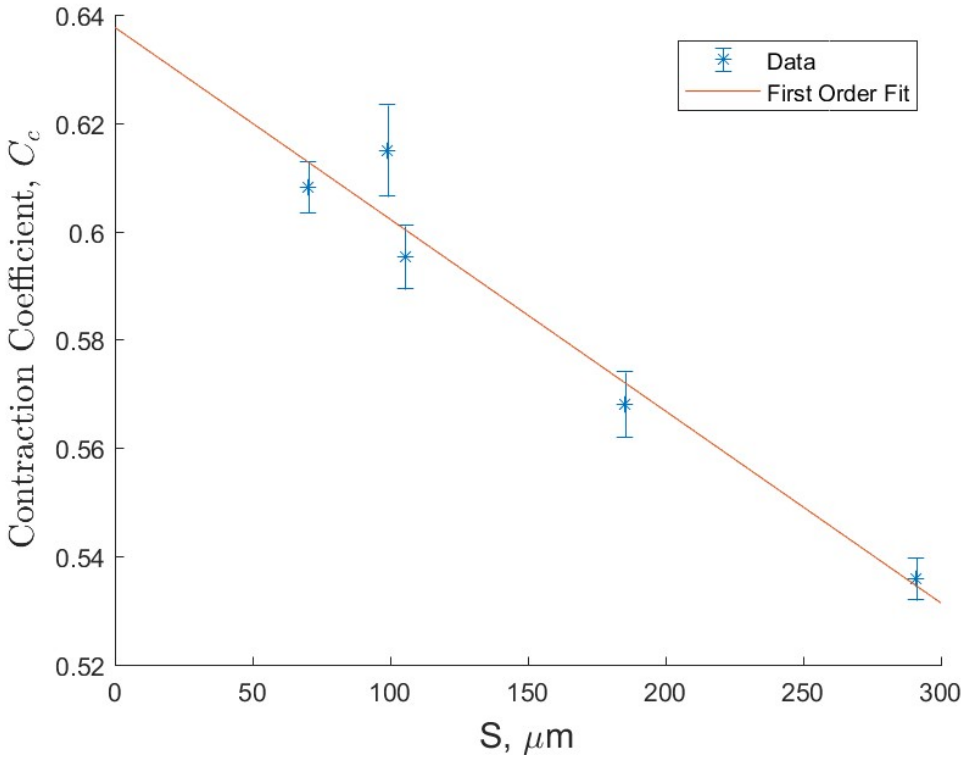


**Figure 49: Peak-to-Peak Spacing - Contraction Coefficient Relationship**

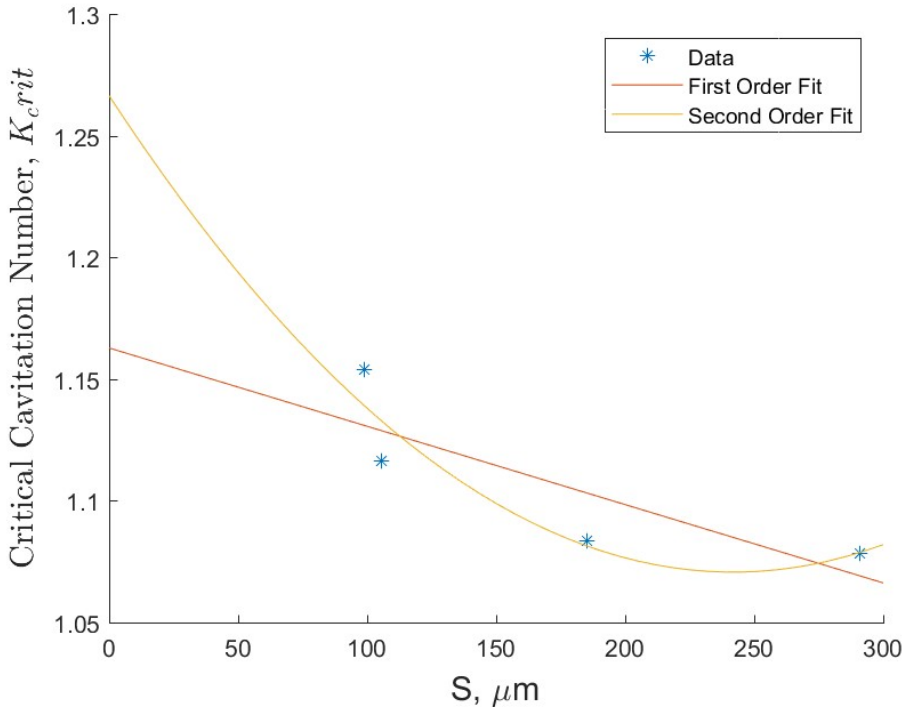


**Figure 50: Peak-to-Peak Spacing - Critical Cavitation Number Relationship**

### 4.4.4 Peak Height (*Rp*)

The peak height in the internal bore of the parts does well to characterize the level of obstruction in the diameter of the orifice. Figure 51 shows the peak height in micrometers on the x-axis and the contraction coefficient value in the y-axis. None of the fits chosen for the data show good agreement to the data. Figure 52 shows the peak height in micrometers on the x-axis in relation to the critical cavitation number on the y-axis. The exponential fit closely aligns with the data available and predicts a y-intercept of 1.6296. The second order fit aligns well but predicts a y-intercept of 1.3058. More information is necessary to find detailed trends of the data and how the variables effect the fluid phenomena in a more detailed way.

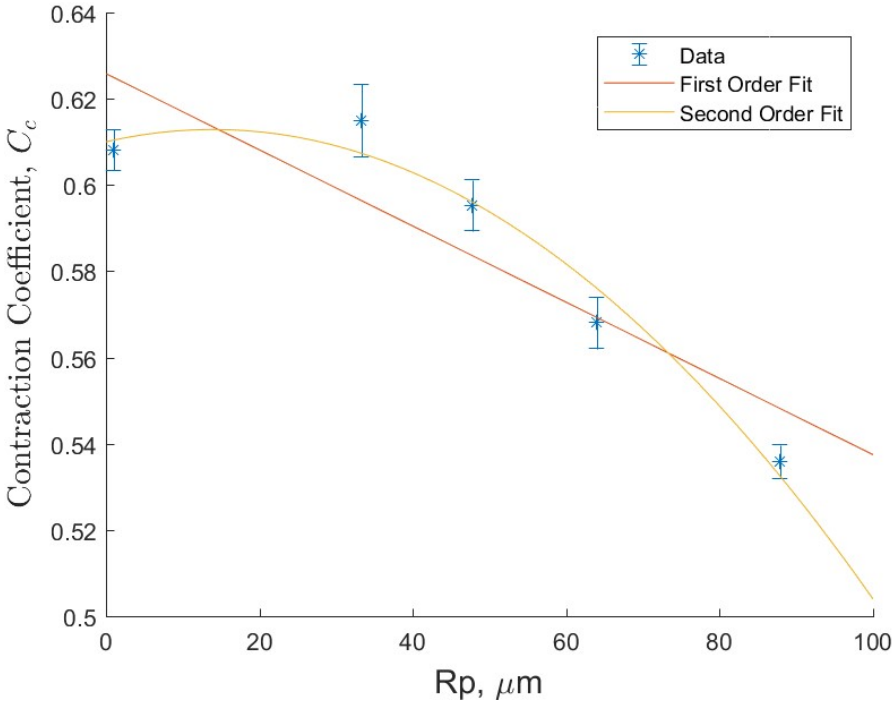


**Figure 51: Peak Height - Contraction Coefficient Relationship**

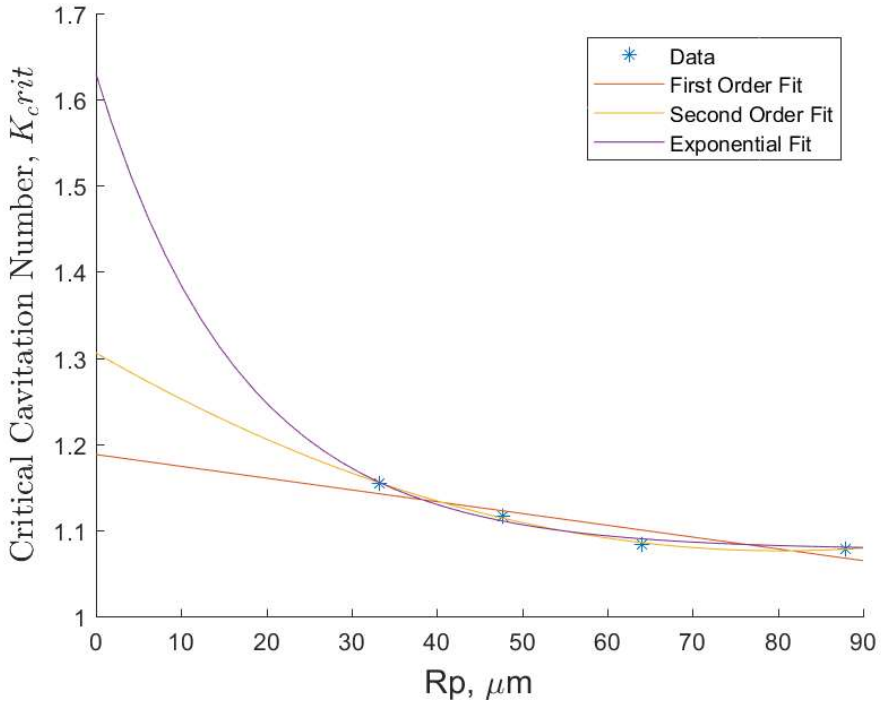


**Figure 52: Peak Height - Critical Cavitation Number Relationship**

# CHAPTER 5

# CONCLUSIONS

From these results a few conclusions can be inferred. These are both qualitative observations as well as quantitative differences between the five different configurations.

1. Effective area decreases with increasing roughness spacing/manufacturing characteristic length. The FDM parts have a known characteristic length of their layer height. By fitting the adjusted Contraction Coefficient data to the layer height, a possible linear trend, detailed in Equation 14, appears as shown in Figure 45. With accounting for the inlet radius of the parts the 200 μm parts yield a 4.6% reduction in effective area when compared to the 100 μm parts and the 300 μm parts have a 10.0% reduction. When compared to the baseline value of 0.611 the 100 μm parts have a 2.6% reduction, the 200 μm parts have a 7.0% reduction and the 300 μm parts have a 12.3% reduction. This can additionally be shown in a plot of the peak-to-peak spacing of the roughness peaks to the contraction coefficient shown in Figure 49.
2. Onset of the cavitation occurs at a lower value of $K$ in rougher/larger characteristic manufacturing length parts. In the higher roughness configurations, the onset of the cavitation occurs later than expected and the discharge coefficient on the whole is reduced when compared to the subtractively manufactured parts. This could be due in part to the large viscous boundary layer inhibiting the production of cavitation cavities along the wall at the inlet and reducing the free movement of the re-entrant jet. An exponential relationship looks to be apparent with $K_{crit}$ and Peak Roughness Height ($Rp$) with a critical cavitation number floor of around 1.077. Figure 52 shows this exponential relationship. This relationship explains the plateau effect we see with increasing layer

heights/roughnesses not drastically changing the critical cavitation number for the configuration. Additionally, it predicts a "zero roughness" critical cavitation number value close to the values found in literature and close to the estimate for the subtractive parts in this study.

3. The acoustic environment in rougher configurations, characterized by higher *Rp*, *Ra*, and other roughness variables, is more broadband in nature. Compared to the narrow frequency bands in the subtractively manufactured parts the FDM and SLM parts have lower amplitude frequency peaks when vortex shedding is predicted. With the subtractive parts the peak frequencies are at a high amplitude and situated in close proximity to the peak Strouhal Number associated with vortex shedding for the part during that point in the test. Whereas, the FDM and SLM parts have lower amplitude frequency peaks with a greater offset from the peak Strouhal number. Qualitatively, this is also backed up by a loud high-pitched whistling noise that could be heard during testing of the subtractively manufactured parts. Likely this frequency, as previously described, is not tied to cavitation directly but instead tied to the turbulent vortex shedding flow condition inside of the orifice. Nonetheless, the rough parts such as the SLM and the FDM parts do not allow for such frequencies to persist in the device.

Future Work on this topic should be focused in the area of expanding the dataset with samples of greater layer height and more intermediate layer heights to determine the scaling function with layer height on FDM type samples. This can also be duplicated on the SLM type samples looking at profile spacing or layer height. Additional work expanding the dataset with

more inlet diameters and *L/D* ratios would allow for determination of the scaling relationship with those values.

# Appendices

## Appendix A: HPSF Plumbing & Instrumentation Diagram

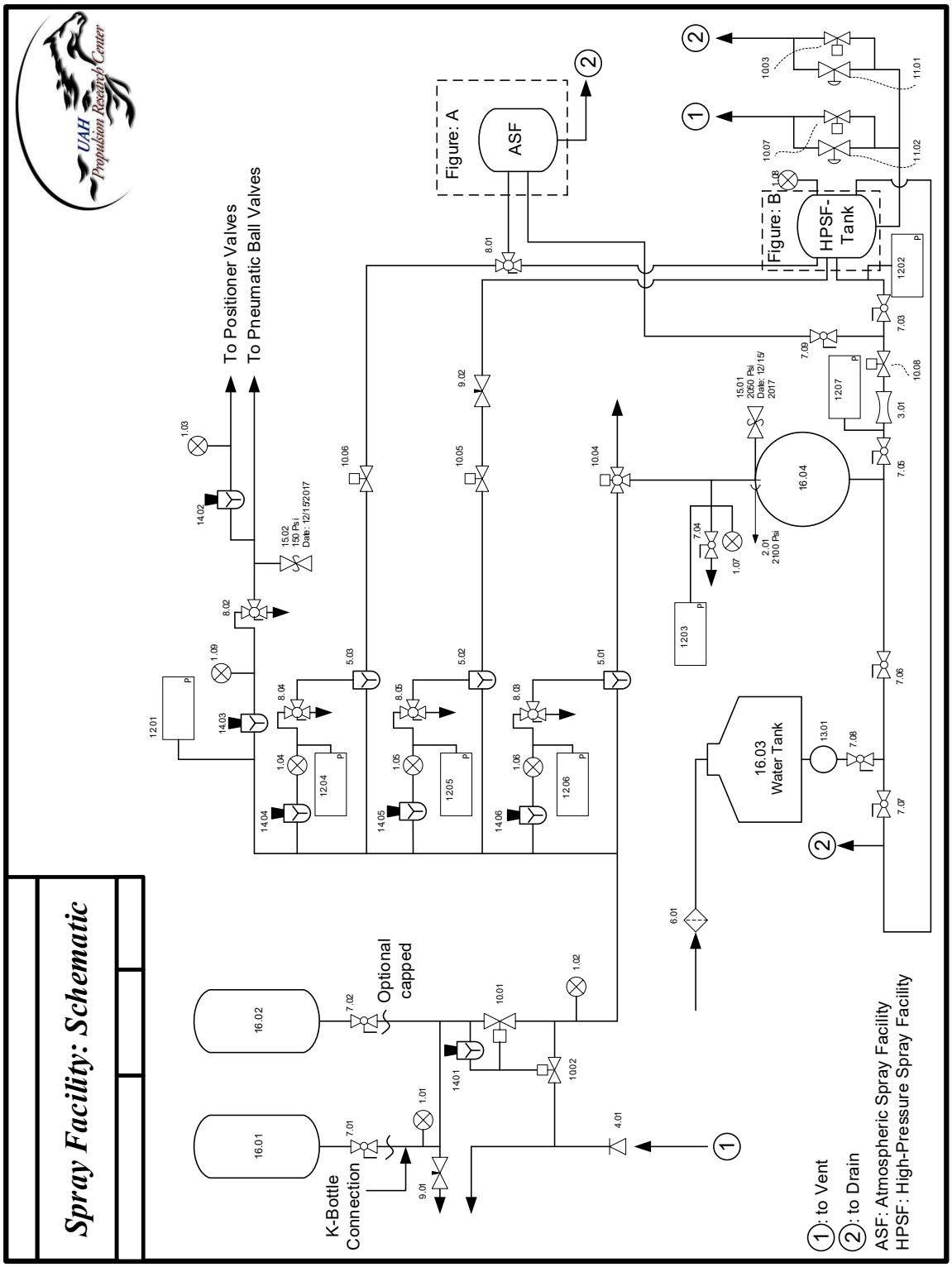

# Appendix B: Detailed Sizing Assumptions related to Venturi Flowmeter

| Worst Case Low | | | | | | | |
|---|---|---|---|---|---|---|---|
| Backpressure: Ambient | | | | Backpressure: 200 psig | | | |
| DP Operation | | Cav Operation | | DP Operation | | Cav Operation | |
| rho | 998 kg/m3 | rho | 998 kg/m3 | rho | 998 kg/m3 | rho | 998 kg/m3 |
| P1 | 3193858.8 Pa | P1 | 3193859 Pa | P1 | 3193859 Pa | P1 | 3193859 Pa |
| PB | 101325 Pa | PB | 101325 Pa | PB | 1480304 Pa | PB | 1480304 Pa |
| Pv | 3170 Pa | Pv | 3170 Pa | Pv | 3170 Pa | Pv | 3170 Pa |
| Cc | 0.5 | Cc | 0.5 | Cc | 0.5 | Cc | 0.5 |
| D | 0.1875 in | D | 0.1875 in | D | 0.1875 in | D | 0.1875 in |
| | 0.0047625 m | | 0.004763 m | | 0.004763 m | | 0.004763 m |
| A | 1.78139E-05 m2 | A | 1.78E-05 m2 | A | 1.78E-05 m2 | A | 1.78E-05 m2 |
| K | 1.031739346 | K | 1.031739 | K | 1.862029 | K | 1.862029 |
| mdot | 0.699789399 kg/s | mdot | 0.710808 kg/s | mdot | 0.520906 kg/s | mdot | 0.710808 kg/s |
| | | | | | | | |
| D2 | 0.62 in | D2 | 0.62 in | D2 | 0.62 in | D2 | 0.62 in |
| | 0.015748 m | | 0.015748 m | | 0.015748 m | | 0.015748 m |
| A2 | 0.003116454 m2 | A2 | 0.003116 m2 | A2 | 0.003116 m2 | A2 | 0.003116 m2 |
| Vline | 39.36198205 m/s | Vline | 39.98176 m/s | Vline | 29.30007 m/s | Vline | 39.98176 m/s |
| Vinlet | 0.224996696 m/s | Vinlet | 0.228539 m/s | Vinlet | 0.167482 m/s | Vinlet | 0.228539 m/s |
| P1 | 463.230055 psi | P1 | 463.2301 psi | P1 | 463.2301 psi | P1 | 463.2301 psi |
| | | | | | | | |
| rho | 998 kg/m3 | rho | 998 kg/m3 | rho | 998 kg/m3 | rho | 998 kg/m3 |
| P1 | 3548732 Pa | P1 | 3548732 Pa | P1 | 3548732 Pa | P1 | 3548732 Pa |
| PB | 101325 Pa | PB | 101325 Pa | PB | 1480304 Pa | PB | 1480304 Pa |
| Pv | 3170 Pa | Pv | 3170 Pa | Pv | 3170 Pa | Pv | 3170 Pa |
| Cc | 0.9 | Cc | 0.9 | Cc | 0.9 | Cc | 0.9 |
| D | 0.31 in | D | 0.31 in | D | 0.31 in | D | 0.31 in |
| | 0.007874 m | | 0.007874 m | | 0.007874 m | | 0.007874 m |
| A | 4.86946E-05 m2 | A | 4.87E-05 m2 | A | 4.87E-05 m2 | A | 4.87E-05 m2 |
| K | 1.028472124 | K | 1.028472 | K | 1.714134 | K | 1.714134 |
| mdot | 3.686769808 kg/s | mdot | 3.68677 kg/s | mdot | 3.68677 kg/s | mdot | 3.68677 kg/s |
| | | | | | | | |
| D2 | 0.62 in | D2 | 0.62 in | D2 | 0.62 in | D2 | 0.62 in |
| | 0.015748 m | | 0.015748 m | | 0.015748 m | | 0.015748 m |
| A2 | 0.003116454 m2 | A2 | 0.003116 m2 | A2 | 0.003116 m2 | A2 | 0.003116 m2 |
| Vline | 75.8638325 m/s | Vline | 75.86383 m/s | Vline | 75.86383 m/s | Vline | 75.86383 m/s |
| Vinlet | 1.185372383 m/s | Vinlet | 1.185372 m/s | Vinlet | 1.185372 m/s | Vinlet | 1.185372 m/s |
| P1 | 514.7000611 psi | P1 | 514.7001 psi | P1 | 514.7001 psi | P1 | 514.7001 psi |
| | | | | | | | |
| % limit | 0.189810982 | % limit | 0.1928 | % limit | 0.141291 | % limit | 0.1928 |
| viscosity | 0.000853477 | viscosity | 0.000853 | viscosity | 0.000853 | viscosity | 0.000853 |
| Re | 219205.1762 | Re | 222656.7 | Re | 163170.8 | Re | 222656.7 |

| Worst Case High | | | | | | | |
|---|---|---|---|---|---|---|---|
| Backpressure: Ambient | | | | Backpressure: 200 psig | | | |
| DP Operation | | Cav Operation | | DP Operation | | Cav Operation | |
| rho | 998 kg/m3 | rho | 998 kg/m3 | rho | 998 kg/m3 | rho | 998 kg/m3 |
| P1 | 3193858.8 Pa | P1 | 3193859 Pa | P1 | 3193859 Pa | P1 | 3193859 Pa |
| PB | 101325 Pa | PB | 101325 Pa | PB | 1480304 Pa | PB | 1480304 Pa |
| Pv | 3170 Pa | Pv | 3170 Pa | Pv | 3170 Pa | Pv | 3170 Pa |
| Cc | 0.95 | Cc | 0.95 | Cc | 0.95 | Cc | 0.95 |
| D | 0.1875 in | D | 0.1875 in | D | 0.1875 in | D | 0.1875 in |
| | 0.0047625 m | | 0.004763 m | | 0.004763 m | | 0.004763 m |
| A | 1.78139E-05 m2 | A | 1.78E-05 m2 | A | 1.78E-05 m2 | A | 1.78E-05 m2 |
| K | 1.031739346 | K | 1.031739 | K | 1.862029 | K | 1.862029 |
| mdot | 1.329599858 kg/s | mdot | 1.350535 kg/s | mdot | 0.989721 kg/s | mdot | 1.350535 kg/s |
| | | | | | | | |
| D2 | 0.62 in | D2 | 0.62 in | D2 | 0.62 in | D2 | 0.62 in |
| | 0.015748 m | | 0.015748 m | | 0.015748 m | | 0.015748 m |
| A2 | 0.003116454 m2 | A2 | 0.003116 m2 | A2 | 0.003116 m2 | A2 | 0.003116 m2 |
| Vline | 74.7877659 m/s | Vline | 75.96535 m/s | Vline | 55.67014 m/s | Vline | 75.96535 m/s |
| Vinlet | 0.427493723 m/s | Vinlet | 0.434225 m/s | Vinlet | 0.318216 m/s | Vinlet | 0.434225 m/s |
| P1 | 463.230055 psi | P1 | 463.2301 psi | P1 | 463.2301 psi | P1 | 463.2301 psi |
| | | | | | | | |
| rho | 998 kg/m3 | rho | 998 kg/m3 | rho | 998 kg/m3 | rho | 998 kg/m3 |
| P1 | 3548732 Pa | P1 | 3548732 Pa | P1 | 3548732 Pa | P1 | 3548732 Pa |
| PB | 101325 Pa | PB | 101325 Pa | PB | 1480304 Pa | PB | 1480304 Pa |
| Pv | 3170 Pa | Pv | 3170 Pa | Pv | 3170 Pa | Pv | 3170 Pa |
| Cc | 0.9 | Cc | 0.9 | Cc | 0.9 | Cc | 0.9 |
| D | 0.31 in | D | 0.31 in | D | 0.31 in | D | 0.31 in |
| | 0.007874 m | | 0.007874 m | | 0.007874 m | | 0.007874 m |
| A | 4.86946E-05 m2 | A | 4.87E-05 m2 | A | 4.87E-05 m2 | A | 4.87E-05 m2 |
| K | 1.028472124 | K | 1.028472 | K | 1.714134 | K | 1.714134 |
| mdot | 3.686769808 kg/s | mdot | 3.68677 kg/s | mdot | 3.68677 kg/s | mdot | 3.68677 kg/s |
| | | | | | | | |
| D2 | 0.62 in | D2 | 0.62 in | D2 | 0.62 in | D2 | 0.62 in |
| | 0.015748 m | | 0.015748 m | | 0.015748 m | | 0.015748 m |
| A2 | 0.003116454 m2 | A2 | 0.003116 m2 | A2 | 0.003116 m2 | A2 | 0.003116 m2 |
| Vline | 75.8638325 m/s | Vline | 75.86383 m/s | Vline | 75.86383 m/s | Vline | 75.86383 m/s |
| Vinlet | 1.185372383 m/s | Vinlet | 1.185372 m/s | Vinlet | 1.185372 m/s | Vinlet | 1.185372 m/s |
| P1 | 514.7000611 psi | P1 | 514.7001 psi | P1 | 514.7001 psi | P1 | 514.7001 psi |
| | | | | | | | |
| % limit | 0.360640866 | % limit | 0.366319 | % limit | 0.268452 | % limit | 0.366319 |
| viscosity | 0.000853477 | viscosity | 0.000853 | viscosity | 0.000853 | viscosity | 0.000853 |
| Re | 416489.8347 | Re | 423047.8 | Re | 310024.6 | Re | 423047.8 |

## Appendix C: Detailed Calibration Reports

# PRC Calibration Report

Date: 7/26/2018

Operator : Dalton Hicks

Instrument Pressure Transducer

Range 0-500 (psig)

Manufacturer Omegadyne

Model PX309-500G5V

Serial Number 083131D112

Calibration Source: Instrument Type: Dead Weight Pressure Tester
Model #: R 50
Serial #: 17745

Slope 101.05 psi/V

Offset -1.64 psi

| Known Pressure [psig] | Measured Voltage [V] |
|---|---|
| 0 | 0.004221 |
| 5 | 0.065222 |
| 10 | 0.114711 |
| 15 | 0.1643 |
| 20 | 0.213592 |
| 25 | 0.263261 |
| 25 | 0.263322 |
| 30 | 0.312684 |
| 35 | 0.361935 |
| 40 | 0.41142 |
| 45 | 0.460641 |
| 45 | 0.460488 |
| 50 | 0.51006 |
| 60 | 0.608957 |
| 70 | 0.708069 |
| 80 | 0.806813 |
| 90 | 0.905461 |
| 100 | 1.005638 |
| 100 | 1.003914 |
| 120 | 1.201726 |
| 140 | 1.39958 |
| 160 | 1.601325 |
| 180 | 1.799197 |
| 200 | 1.996977 |
| 220 | 2.194906 |
| 240 | 2.392552 |
| 260 | 2.590554 |
| 280 | 2.788461 |
| 300 | 2.98622 |
| 325 | 3.233351 |
| 350 | 3.480575 |
| 375 | 3.728031 |

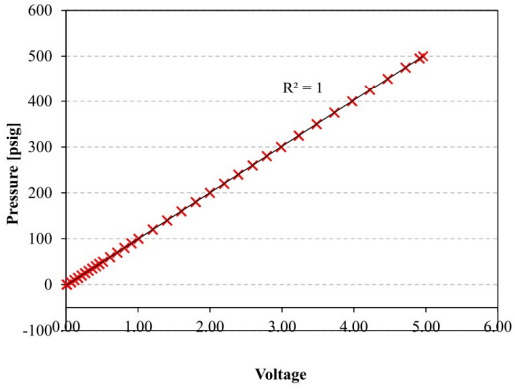

| | |
|---|---|
| 400 | 3.974383 |
| 425 | 4.221788 |
| 450 | 4.468337 |
| 475 | 4.715461 |
| 495 | 4.912183 |
| 500 | 4.961287 |
| 495 | 4.911791 |
| 475 | 4.715631 |
| 450 | 4.468841 |
| 425 | 4.221949 |
| 400 | 3.97461 |
| 375 | 3.728152 |
| 350 | 3.481134 |
| 325 | 3.233464 |
| 300 | 2.986172 |
| 280 | 2.788386 |
| 260 | 2.590768 |
| 240 | 2.393 |
| 220 | 2.195204 |
| 200 | 1.997444 |
| 180 | 1.79954 |
| 160 | 1.601454 |
| 140 | 1.403778 |
| 120 | 1.205881 |
| 90 | 0.908732 |
| 80 | 0.809563 |
| 70 | 0.710317 |
| 60 | 0.610878 |
| 50 | 0.511876 |
| 45 | 0.462449 |
| 40 | 0.412931 |
| 35 | 0.363368 |
| 30 | 0.313908 |
| 25 | 0.264441 |
| 20 | 0.214878 |
| 15 | 0.165333 |
| 10 | 0.115819 |
| 5 | 0.066348 |
| 0 | 0.015199 |

# PRC Calibration Report

Date: 5/30/2018

Operator : Erik Korzon

Instrument Pressure Transducer

Range 0-500 (psig)

Manufacturer Omegadyne

Model PX309-500G5V

Serial Number 103110D878

Calibration Source: Instrument Type: Dead Weight Pressure Tester
Model #: R 50
Serial #: 17745

Slope 100.33 psi/V

Offset -0.36 psi

| Known Pressure [psig] | Measured Voltage [V] |
|---|---|
| 0 | -0.000406 |
| 50 | 0.499474 |
| 100 | 0.999998 |
| 150 | 1.498578 |
| 200 | 1.99669 |
| 250 | 2.493887 |
| 300 | 2.991094 |
| 350 | 3.48799 |
| 400 | 3.99023 |
| 450 | 4.48852 |
| 500 | 4.983268 |
| 450 | 4.488874 |
| 400 | 3.99176 |
| 350 | 3.495569 |
| 300 | 2.997966 |
| 250 | 2.498952 |
| 200 | 2.000952 |
| 150 | 1.502293 |
| 100 | 1.002848 |
| 50 | 0.501631 |
| 0 | 0.002651 |

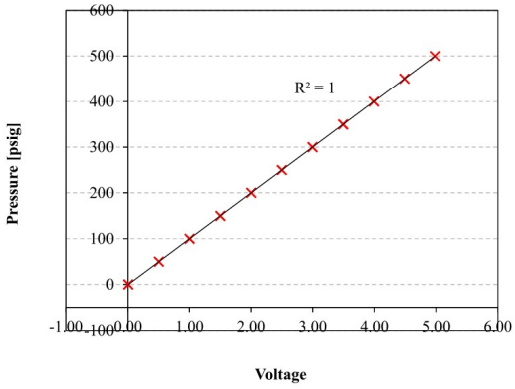

# PRC Calibration Report

Date: 7/12/2018

Operator : Jacey Allen

Instrument Pressure Transducer

Range 0-3000 (psig)

Manufacturer Honeywell

Model FPG

Serial Number 1144528

Calibration Source: Instrument Type: Dead Weight Pressure Tester
Model #: R-50
Serial #: 17745

Slope 607.27 psi/V

Offset -12.59 psi

| Known Pressure [psig] | Measured Voltage [V] |
|---|---|
| 0 | 0.085592 |
| 50 | 0.086885 |
| 250 | 0.41743 |
| 500 | 0.831121 |
| 700 | 1.161442 |
| 900 | 1.490363 |
| 1100 | 1.820972 |
| 1300 | 2.15255 |
| 1500 | 2.477123 |
| 1750 | 2.973038 |
| 2000 | 3.388498 |
| 2250 | 3.718924 |
| 2500 | 4.128329 |
| 2750 | 4.542052 |
| 3000 | 4.953651 |
| 2750 | 4.54238 |
| 2500 | 4.130769 |
| 2250 | 3.719144 |
| 2000 | 3.307009 |
| 1750 | 2.896078 |
| 1500 | 2.485174 |
| 1300 | 2.155942 |
| 1100 | 1.824403 |
| 900 | 1.493685 |
| 700 | 1.162999 |
| 500 | 0.831025 |
| 250 | 0.401857 |
| 50 | 0.08637 |
| 0 | 0.076036 |

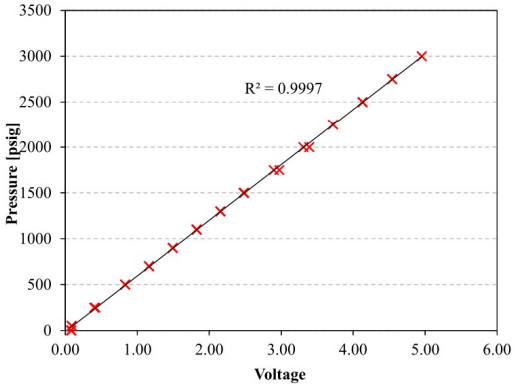

# PRC Calibration Report

Date: 5/30/2018

Operator : Dalton Hicks

Instrument Pressure Transducer

Range 0-50 (psig)

Manufacturer Sensotec

Model 2/741-OJZD

Serial Number 750329

Calibration Source: Instrument Type: Dead Weight Pressure Tester
Model #: TQ-130
Serial #: 1230

Slope 9.98 psi/V

Offset -6.71 psi

| Known Pressure [psig] | Measured Voltage [V] |
|---|---|
| 0 | 0.668344 |
| 5 | 1.180787 |
| 10 | 1.672311 |
| 15 | 2.169637 |
| 20 | 2.670883 |
| 25 | 3.172368 |
| 30 | 3.675807 |
| 35 | 4.179203 |
| 40 | 4.68225 |
| 40 | 4.68291 |
| 35 | 4.181713 |
| 30 | 3.679285 |
| 25 | 3.177233 |
| 20 | 2.675866 |
| 15 | 2.175701 |
| 10 | 1.679082 |
| 5 | 1.183619 |
| 0 | 0.668241 |

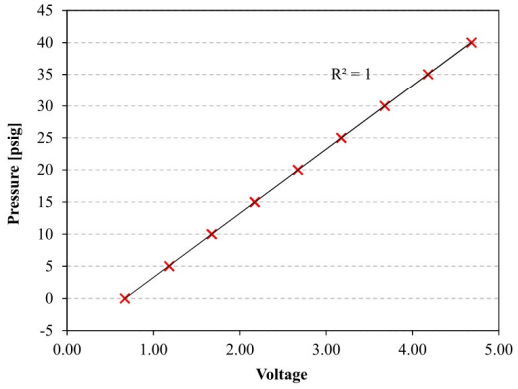

## Appendix D: Backpressure Control Valve Cutsheet

Specification Data CK5000
5/92

# 2600 Series
# Split Body Control Valve
# Building Blocks

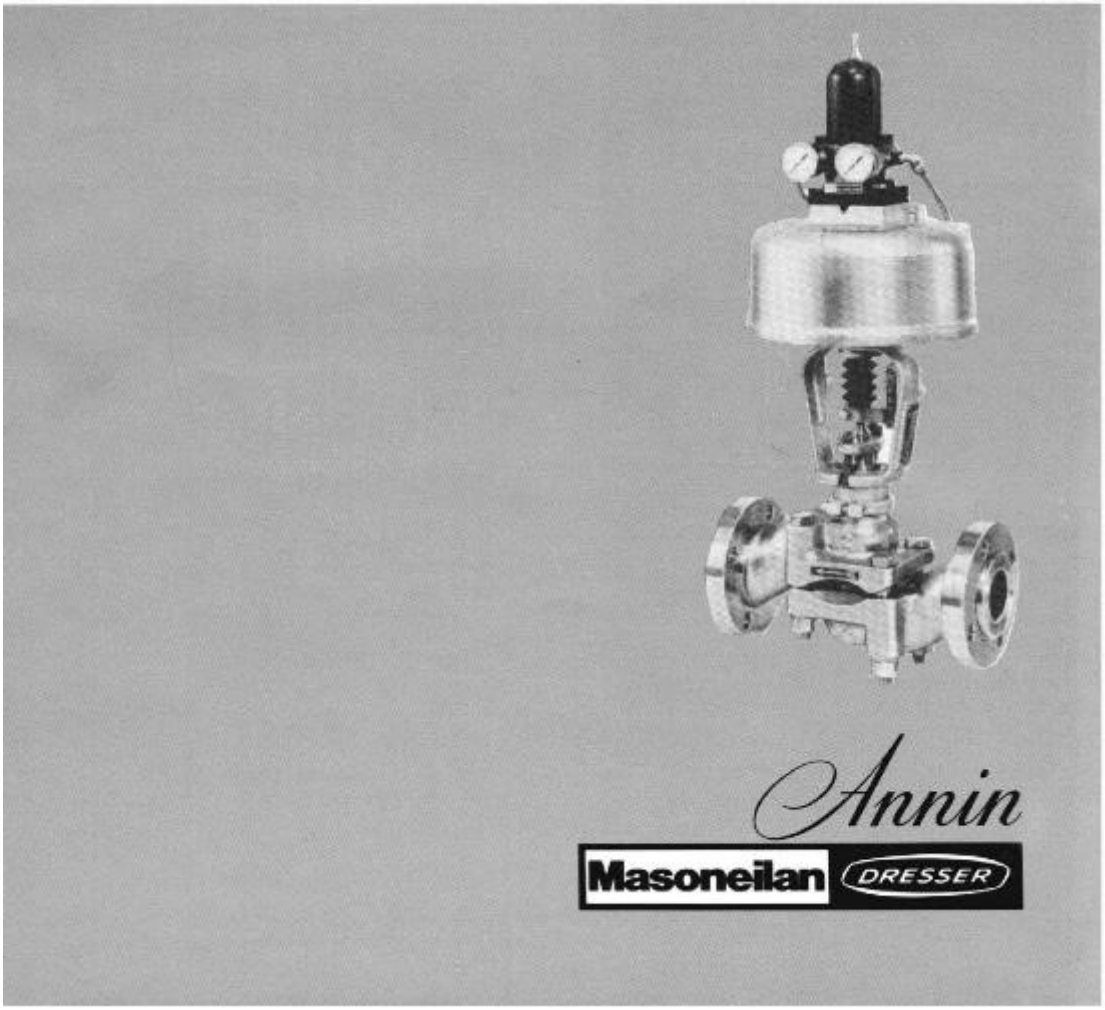

## Table of Contents



## Foreword

The Group 26 split body control valve is the product of over 35 years of experience (longest in the industry) in the design and manufacture of split body valves. Designed as a standardized valve, it covers most normal applications and fulfills control requirements demanded of highly specialized valves.

The 2600 Series control valves are designed for applications requiring versatility as well as economy and where exotic material selections are a necessity. With its varied range of materials, configurations, trim options and the selection of actuators, it is a most versatile control valve. Features include:

**Modular Construction**
Allows one valve line to equip an entire plant for standard and severe services.

**Quick Trim Changeout**
Clamped-in seat ring allows "in line" trim replacement on corrosive services.

**Smooth Internal Flow Passages**
No-pocket design prevents material buildup.

**Stem Guiding**
Stem guiding avoids buildup of sticky substances and plastic particles which collect behind conventional valve plugs guided by plug post and bushing.

Low weight and separable flanges permit low cost alloy bodies; one valve body adapts to ANSI Class 150 through 600 line flanges.

Domotor® actuator has maximum thrust to free valve plug in sticky service; integral positioner has no external feedback linkages, ideal in corrosive atmospheres. The positioner is mounted on top of the actuator, away from the packing box.

## Numbering System

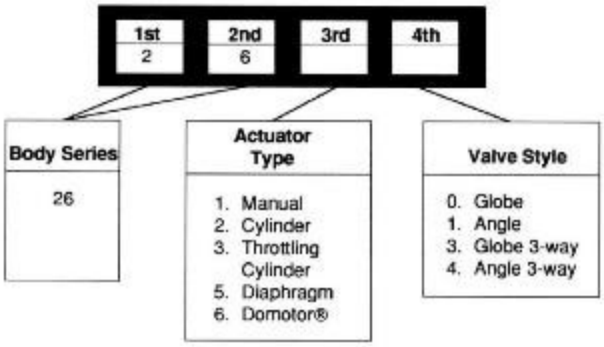


## General Data

- **Body**

| | |
|---|---|
| types: | cast split body<br>globe<br>angle<br>3-way globe<br>3-way angle |
| flow direction: | flow to open<br>flow to close |
| $C_v$ ratio: | 50:1 |
| materials: | carbon and chrome-molybdenum steel; 316 and other 300 Series stainless steels; Alloy 20; Hastelloy "B" and "C", Monel and others |

- **Flow Characteristics**

linear, equal percentage, semi-throttle

- **Actuator**

| | |
|---|---|
| type: | manual, cylinder, diaphragm Domotor® |
| auxiliary handwheel: | optional with Domotor® |

- **Trim**

| | |
|---|---|
| types: | contoured plug<br>LO-DB® multi-hole cage<br>Pee-Wee trim (½" - 1") |
| materials: | plug/stem<br>316 St. St.;<br>hardfaced 316 St. St.; Alloy 20; other materials according to body material<br>seat ring<br>316 St. St.; Alloy 20;<br>hardfaced 316 St. St.;<br>solid Stellite; soft seat ①<br>TFE or FEP Teflon and Kel-F; other materials according to body material<br>guide<br>Stellite (Standard);<br>Chrome plated 316 St. St.;<br>Aluminum bronze;<br>glass loaded Teflon;<br>Alloy 20; Monel |

① Not available on LO-DB® trim or 3-way construction

## Temperature Range/Seat Leakage

| Valve Size (inches) | ANSI Class | Seat Type | Temperature Range | | Globe & Angle | LO-DB® ① |
|---|---|---|---|---|---|---|
| | | | Min. | Max. | Maximum Seat Leakage ANSI/FCI 70.2 Class | |
| ½ - 8 | 150 - 600 | Metal | -320°F | +1200°F | Class IV | Class IV |
| | 150 - 600 | Soft Seat | -320°F | +400°F | Class VI | - |
| 10 | 150 - 300 | Metal | -320°F | +1200°F | Class IV | - |
| | 150 - 300 | Soft Seat | -320°F | +400°F | Class VI | - |

③ LO-DB® through 6" only

## Ratings/Connections

- • Threaded (NPT)
- ▲ Separable Flange③
- ■ Integral Flange
- □ Grayloc and Weld Ends

| Valve Size (inches) | ANSI Class | | |
|---|---|---|---|
| | 150 | 300 | 600 |
| ½ - 2 | •▲■□ | •▲■□ | •▲■□ |
| 3 & 4 | ▲■□ | ▲■□ | ▲■□ |
| 6 & 8 | ■□ | ■□ | ■□ |
| 10 | ■□ | ■□ | - |

① Carbon steel is standard
304 stainless steel is optional
other alloys available

## Actuator Data

**Manual**

type: non-rising handwheel
material: ductile iron

**Cylinder**

type: pneumatic spring cylinder for on-off or throttling applications. (See SD CR5030 for additional information.)
material: glass fiber reinforced epoxy cylinder, steel piston, caps and connecting rods
action: spring to retract stem or spring to extend stem (also available without springs). Operated by a double acting positioner or a 3 or 4 way solenoid valve
supply: 40 - 150 psi
connections: ¼" NPT upper and lower

**Diaphragm**

type: field reversible spring diaphragm
positioner: Moore 750P
handwheel: not available

**Domotor®**

type: positioning pneumatic cylinder with integral positioner and loading regulator. (See SD CR4000 for additional information.)
material: cast aluminum
action: increasing instrument signal retracts stem (direct positioner) increasing instrument signal extends stem (reverse positioner)
instrument signal: common full and split range signals
supply: 40 - 100 psi
loading pressure: depends on available supply pressure, process conditions, fluid flow direction and fail safe action
static air consumption: 0.5 SCFM @ 60 psi supply pressure
air connections: ¼" NPT instrument and supply

| Nominal Effective Area (sq. in.) | Maximum Stroke (in.) | Available Spring Ranges (psig) All Sizes |
|---|---|---|
| 38 | 1.5 | 10-20 |
| 78 | 2.5 | 15-30 |
| 154 | 6.0 | or |
| 314 | 6.0 | 25-50 |

| Domotor® Size | Maximum Stroke (in.) | Nominal Effective Area (sq. in.) |
|---|---|---|
| A | ¾ | 25 |
| B | 1½ | 50 |
| C | 2½ | 100 |
| D | 6 | 200 |

**Standard actuator sizes**

| Valve Size (inches) | Actuator Size | | | |
|---|---|---|---|---|
| | Manual (in.) | Cylinder | Disphragm | Domotor® |
| ½ | 7 | 38 sq. in. | 6 | A |
| ¾ | 7 | 38 sq. in. | 6 | A |
| 1 | 7 | 38 sq. in. | 6 | A |
| 1½ | 12 | 38 sq. in. | 10 | B |
| 2 | 12 | 38 sq. in. | 10 | B |
| 3 | 18 | 78 sq. in. | 16 | C |
| 4 ANSI Class 300 or 600 ① | 18 | 78 sq. in. | 16 | C |
| 4 ANSI Class 600 | 18 ② | 154 sq. in. | --- | D |
| 6 ANSI Class 150 or 300 ① | 18 | 78 sq. in. | --- | C |
| 6 ANSI Class 300 | 18 ② | 154 sq. in. | --- | D |
| 6 ANSI Class 600 | 18 ② | 154 sq. in. | --- | D |
| 8 | 18 ③ | C/F | --- | D |
| 10 | 18 ③ | C/F | --- | D |

① Body for Series "C" actuators only
② 12" Yoke
③ 16" Yoke

## Flow Coefficients - Rated $C_v$ ②

| Valve Size (inches) | Travel (inches) | Globe, Angle | | | | | | | LO-DB® | 3-way |
|---|---|---|---|---|---|---|---|---|---|---|
| | | Pee-Wee Trim ① | | | Reduced Trim | | | Full Trim | | |
| ½ | .75 | .04 | .10 | .25 | 0.6 | 1.5 | | 4 | 4 | 4 |
| ¾ | .75 | .04 | .10 | .25 | 0.6 | 1.5 | 4 | 6 | 4 | 6 |
| 1 | .75 | .04 | .10 | .25 | 0.6 | 1.5 | 4 | 6 | 12 | 6 | 10 |
| 1½ | 1.5 | | | | | 12 | 16 | 25 | 16 | 25 |
| 2 | 1.5 | | | | | 16 | 25 | 46 | 25 | 40 |
| 3 | 2.5 | | | | | 46 | 75 | 110 | 75 | 95 |
| 4 | 2.5 | | | | | 75 | 110 | 195 | 110 | 175 |
| 6 | 2.5 | | | | | 195 | 275 | ----- | ----- | ----- |
| 6 | 3 | | | | | ----- | ----- | 400 | 275 | 360 |
| 8 | 5 | | | | | 275 | 400 | 640 | ----- | 480 |
| 10 | 5 | | | | | 400 | 640 | 1000 | ----- | 820 |

① $C_v$ ratio 10:1
② Consult factory for other available Cv's

## Critical Flow Factor $F_L$

Critical Flow Factor $F_L$
Valve Fully Open

| Valve Configuration | Flow to Close | Flow to Open |
|---|---|---|
| Globe, Full Trim | .80 | .75 |
| Angle, Full Trim | .80 | .75 |
| Globe, Reduced Trim | .80 | .75 |
| Angle, Reduced Trim | .80 | .75 |
| LO-DB® Trim | .95 | .95 |
| 3-way Trim | .80 | .80 |

## $C_v$ and $F_L$ versus Travel

**Standard Trim**
Flow Direction: Flow to Open
ANSI Class: 150 through 600
Sizes: ½" through 10"

Flow Characteristic: **SEMI-THROTTLE**

| Percent (%) of Travel | | | 10 | 20 | 30 | 40 | 50 | 60 | 70 | 80 | 90 | 100 |
|---|---|---|---|---|---|---|---|---|---|---|---|---|
| $F_L$ | | | 0.90 | 0.88 | 0.87 | 0.84 | 0.82 | 0.79 | 0.78 | 0.77 | 0.76 | 0.75 |
| Valve Size (inches) | Orifice Diameter (inches) | Travel (inches) | Rated $C_v$ | | | | | | | | | |
| ½ | .500 | .50 | .40 | 1.00 | 2.52 | 3.28 | 3.64 | 3.84 | 3.88 | 3.92 | 3.96 | 4 |
| ¾ | .625 | .50 | .60 | 1.50 | 3.78 | 4.92 | 5.46 | 5.76 | 5.82 | 5.88 | 5.94 | 6 |
| 1 | .812 | .50 | 1.20 | 3.00 | 7.50 | 9.80 | 10.90 | 11.52 | 11.60 | 11.70 | 11.80 | 12 |
| 1½ | 1.250 | .75 | 2.50 | 6.25 | 15.70 | 20.50 | 22.70 | 24.00 | 24.20 | 24.50 | 24.70 | 25 |
| 2 | 1.625 | .75 | 4.60 | 11.50 | 28.90 | 37.70 | 41.80 | 44.16 | 44.60 | 45.00 | 45.50 | 46 |
| 3 | 2.625 | 1.50 | 11.00 | 27.50 | 69.30 | 90.20 | 100.00 | 105.80 | 106.00 | 107.00 | 108.00 | 110 |
| 4 | 3.500 | 1.50 | 19.50 | 48.75 | 122.00 | 159.00 | 177.00 | 187.20 | 189.00 | 191.10 | 193.00 | 195 |
| 6 300 ANSI | 4.625 | 2.50 | 40.00 | 100.00 | 252.00 | 328.00 | 364.00 | 384.00 | 388.00 | 392.00 | 396.00 | 400 |
| 6 300 ANSI | 4.250 | 2.50 | 27.50 | 68.75 | 173.00 | 225.00 | 250.00 | 264.00 | 266.00 | 269.00 | 272.00 | 275 |
| 6 600 ANSI | 4.500 | 2.50 | 40.00 | 100.00 | 252.00 | 328.00 | 364.00 | 384.00 | 388.00 | 392.00 | 396.00 | 400 |
| 8 | 6.250 | 5.00 | 64.00 | 160.00 | 403.00 | 524.00 | 582.00 | 614.40 | 620.00 | 627.00 | 633.00 | 640 |
| 10 | 8.000 | 5.00 | 100.00 | 250.00 | 630.00 | 820.00 | 910.00 | 960.00 | 970.00 | 980.00 | 990.00 | 1000 |

## $C_v$ and $F_L$ versus Travel

**Standard Trim**
Flow Direction: Flow to Open
ANSI Class: 150 through 600
Sizes: ½" through 10"

Flow Characteristic: **EQUAL PERCENTAGE**

| Percent (%) of Travel | | | 10 | 20 | 30 | 40 | 50 | 60 | 70 | 80 | 90 | 100 |
|---|---|---|---|---|---|---|---|---|---|---|---|---|
| $F_L$ | | | 0.90 | 0.90 | 0.89 | 0.89 | 0.89 | 0.87 | 0.86 | 0.83 | 0.78 | 0.75 |
| Valve Size (inches) | Orifice Diameter (inches) | Travel (inches) | Rated $C_v$ | | | | | | | | | |
| ½ | .500 | .75 | .10 | .18 | .30 | .48 | .64 | .92 | 1.24 | 1.80 | 2.70 | 4 |
| ¾ | .625 | .75 | .15 | .24 | .45 | .72 | .96 | 1.38 | 1.86 | 2.70 | 4.02 | 6 |
| 1 | .812 | .75 | .30 | .48 | .90 | 1.44 | 1.92 | 2.76 | 3.72 | 5.40 | 8.04 | 12 |
| 1½ | 1.250 | 1.50 | .62 | 1.00 | 1.87 | 3.00 | 4.00 | 5.75 | 7.75 | 11.20 | 16.70 | 25 |
| 2 | 1.625 | 1.50 | 1.15 | 1.84 | 3.45 | 5.52 | 7.36 | 10.50 | 14.20 | 20.70 | 30.80 | 46 |
| 3 | 2.625 | 2.50 | 2.75 | 4.40 | 8.25 | 13.20 | 17.60 | 25.30 | 34.10 | 49.50 | 73.70 | 110 |
| 4 | 3.500 | 2.50 | 4.87 | 7.80 | 14.60 | 23.40 | 31.20 | 44.80 | 60.40 | 87.70 | 130.00 | 195 |
| 6 300 ANSI | 4.625 | 2.50 | 10.00 | 16.00 | 30.00 | 48.00 | 64.00 | 92.00 | 124.00 | 180.00 | 268.00 | 400 |
| 6 300 ANSI | 4.250 | 2.50 | 6.87 | 11.00 | 20.60 | 33.00 | 44.00 | 63.20 | 85.20 | 123.00 | 184.00 | 275 |
| 6 600 ANSI | 4.500 | 3.00 | 10.00 | 16.00 | 30.00 | 48.00 | 64.00 | 92.00 | 124.00 | 180.00 | 268.00 | 400 |
| 8 | 6.250 | 5.00 | 16.00 | 25.60 | 48.00 | 76.80 | 102.00 | 147.00 | 198.00 | 288.00 | 428.00 | 640 |
| 10 | 8.000 | 5.00 | 25.00 | 40.00 | 75.00 | 120.00 | 160.00 | 230.00 | 310.00 | 450.00 | 670.00 | 1000 |

**Standard Trim**
Flow Direction: Flow to Open
ANSI Class: 150 through 600
Sizes: ½" through 10"

Flow Characteristic: **LINEAR**

| Percent (%) of Travel | | | 10 | 20 | 30 | 40 | 50 | 60 | 70 | 80 | 90 | 100 |
|---|---|---|---|---|---|---|---|---|---|---|---|---|
| $F_L$ | | | 0.90 | 0.88 | 0.87 | 0.84 | 0.82 | 0.79 | 0.78 | 0.77 | 0.76 | 0.75 |
| Valve Size (inches) | Orifice Diameter (inches) | Travel (inches) | Rated $C_v$ | | | | | | | | | |
| ½ | .500 | .75 | .36 | .72 | 1.04 | 1.40 | 1.80 | 2.24 | 2.64 | 3.08 | 3.52 | 4 |
| ¾ | .625 | .75 | .54 | 1.08 | 1.56 | 2.10 | 2.70 | 3.36 | 3.96 | 4.62 | 5.28 | 6 |
| 1 | .812 | .75 | 1.08 | 2.16 | 3.12 | 4.20 | 5.40 | 6.72 | 7.92 | 9.24 | 10.56 | 12 |
| 1½ | 1.250 | 1.50 | 2.25 | 4.50 | 6.50 | 8.75 | 11.20 | 14.00 | 16.50 | 19.20 | 22.00 | 25 |
| 2 | 1.625 | 1.50 | 4.14 | 8.28 | 11.90 | 16.10 | 20.70 | 25.70 | 30.30 | 35.40 | 40.40 | 46 |
| 3 | 2.625 | 2.50 | 9.90 | 19.80 | 28.60 | 38.50 | 49.50 | 61.60 | 72.60 | 84.70 | 96.80 | 110 |
| 4 | 3.500 | 2.50 | 17.50 | 35.10 | 50.70 | 68.20 | 87.70 | 109.00 | 128.00 | 150.10 | 171.00 | 195 |
| 6 300 ANSI | 4.625 | 2.50 | 36.00 | 72.00 | 104.00 | 140.00 | 180.00 | 224.00 | 264.00 | 308.00 | 352.00 | 400 |
| 6 300 ANSI | 4.250 | 2.50 | 24.70 | 49.50 | 71.50 | 96.20 | 123.00 | 154.00 | 181.00 | 211.00 | 242.00 | 275 |
| 6 600 ANSI | 4.500 | 3.00 | 36.00 | 72.00 | 104.00 | 140.00 | 180.00 | 224.00 | 264.00 | 308.00 | 352.00 | 400 |
| 8 | 6.250 | 5.00 | 57.60 | 115.00 | 166.00 | 224.00 | 288.00 | 358.00 | 422.00 | 492.00 | 563.00 | 640 |
| 10 | 8.000 | 5.00 | 90.00 | 180.00 | 260.00 | 350.00 | 450.00 | 560.00 | 660.00 | 770.00 | 880.00 | 1000 |

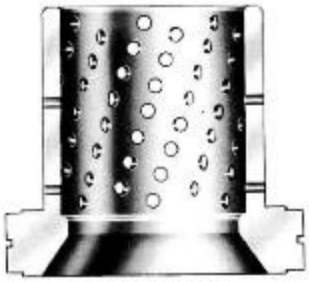

LO-DB Seat Ring

LO-DB Plug and Stem

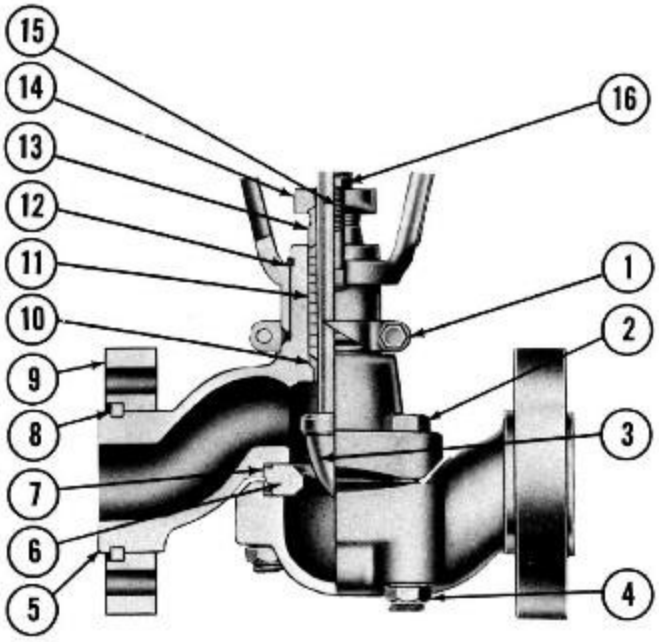

## Materials

| Part No. | Temperatures / Description | -320°F to -20°F | +400°F to +450°F | +750°F to +1000°F | +1200°F |
|---|---|---|---|---|---|
| | | Standard Materials | | | |
| 1 | Yoke Clamp | 304 St. St. | | | |
| 2 | Valve Body Bolting | Alloy Steel ASTM A193 Gr B7 | | | |
| | | Stainless Steel ASTM A193 Gr B8 | | | A453 |
| 3 | Plug/Stem | 316 St. St. ASTM A479 TY | | | |
| | | Hardfaced 316 St. St. ASTM A479 TY (Std. on LO-DB®, opt. on others) ① | | | |
| 4 | Valve Body Nuts | Stainless Steel ASTM A194 Gr 8 | | | |
| | | Alloy Steel ASTM A194 Gr 2H | | | |
| 5 | Body | 316 St. St. ASTM A351 Gr CF8M | | | |
| | | Carbon Steel ASTM A216 Gr WC B | | | |
| 6 | Seat Ring | 316 St. St. ASTM A479 TY | | | |
| | | 316 St. St./TFE | | | |
| | | Hardfaced 316 St. St. ASTM A479 TY (optional) | | | |
| 7 | Seat Ring Gasket | Teflon | | | |
| | | Non-asbestos Sheet | | | |
| | | Inconel X-750 Metal O-ring | | | |
| 8 | Flange Half Rings | Carbon Steel | | | |
| | | 304 St. St. (optional) | | | |
| 9 | Separable End Flange | 304 St. St. (optional) | | | |
| | | Carbon Steel ASTM A515 Gr 70 | | | |
| 10 | Stem Guide | Stellite | | | |
| | | AL/BZ | | | |
| | | 25% GLT | | | |
| 11 | Packing | Teflon V-ring ② | | | |
| | | Grafoil | | | |
| 12 | Yoke Half Rings | 304 St. St. | | | |
| 13 | Packing Follower | 316 St. St. ASTM A479 TY 316 | | | |
| | | Alloy 20 ASTM B473 (for Alloy 20 valves) | | | |
| 14 | Gland Flange | 316 St. St. ASTM A351 Gr CF8M | | | |
| 15 | Packing Box Studs | 304 St. St. ASTM A193 Gr B8 | | | |
| 16 | Packing Box Stud Nuts | 304 St. St. ASTM A194 Gr 8F | | | |

① Hardfacing of stem is mandatory on LO-DB trim and services over 750°F

② No bonnet insulation allowed for teflon packings

Note: Extension bonnet is required for service temperature below -20°F and above +600°F
Grafoil packing necessary for services between 450°F to 600°F without extension

## Bonnet Extension and Packing Arrangements

Plain extension

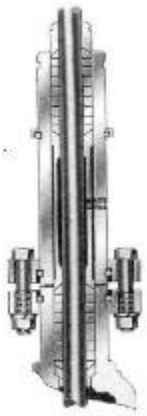

Doolseal extension

Bellows seal extension

Typical extension
for D actuators

## 3-Way Globe Valve Orientation

Orientation of the end connections of a 3-way valve is described with clock positions, when viewing the valve from above with the side of the yoke bearing the stroke indicator plate at 6 o'clock. for example, the 3-way globe, pictured here, has the body at 9 o'clock, the intermediate body at 6 o'clock and the adapter at 3 o'clock. This also applies to corner valves.

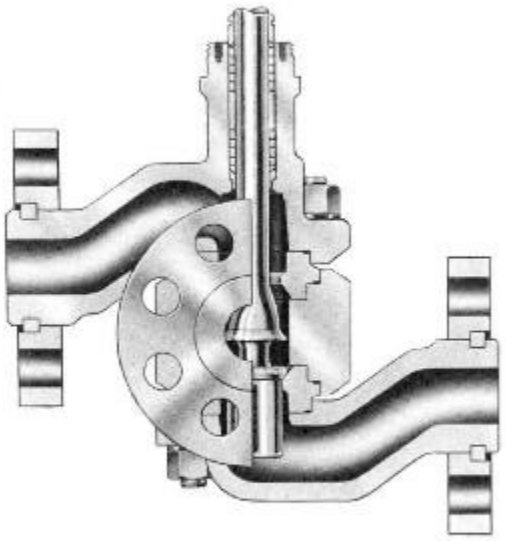

## Allowable Pressure Drops (psi) - Manual Actuator — Flow to Close

**Manually Actuated Valves**
**Metal Seat (Class VI) ①**
**Temperature: -320°F to +1200°F**
**Body Ratings: ANSI Class 150 through 600**
**Seat Leakage: per ANSI/FCI 70.2, Class IV**

| Valve Size (in.) | Travel (in.) | Rated $C_v$ | Actuator Size (in.) | Metal Seat | Soft Seat |
|---|---|---|---|---|---|
| ½ | 0.75 | 4 | 7 | 1500 | 1000 |
| ¾ | 0.75 | 6 | 7 | 1500 | 1000 |
| 1 | 0.75 | 12 | 7 | 1500 | 1000 |
| 1½ | 1.50 | 16 | 12 | 1500 | 1000 |
| | | 25 | 12 | 1500 | 1000 |
| 2 | 1.50 | 46 | 12 | 1085 | 1000 |
| 3 | 2.50 | 75 | 18 | 1500 | 1000 |
| | | 110 | 18 | 765 | 765 |
| 4 | 2.50 | 195 ② | 18 | 415 | 415 |
| | | | 18 ④ | 650 | 650 |
| 6 | 2.50 | 275 | 18 | 280 | 280 |
| | | | 18 ③ | 555 | 555 |
| | | 400 | 18 | 235 | 235 |
| | | | 18 ③ | 490 | 490 |
| | 3.00 | 400 | 18 ③ | 400 | 400 |
| 8 | 5.00 | 640 | 18 ④ | 260 | 260 |
| 10 | 5.00 | 1000 | 18 ④ | 155 | 155 |

① Soft seats are limited to 1000 psi pressure drop. The preferred flow direction is flow to close.
② Body designed for 150 lb and 300 lb ratings, "C" Series yoke
③ 12" Yoke
④ 16" Yoke

**Notes:** LO-DB trim allowable pressure drop is equivalent to the allowable pressure drop for full area standard trim in each size
The pressure drops shown are independent of ANSI pressure ratings
When allowable pressure drops exceed ANSI ratings the ANSI ratings must govern

## Allowable Pressure Drops (psi) - Diaphragm Actuator — Air to Open/Air to Close

**Diaphragm Actuated Globe and Angle Valves (87/88 Actuators)**
**Metal and Soft Seat**
**Temperature: -320°F to +1200°F**
**Body Ratings: ANSI Class 150 through 600**
**Seat Leakage: per ANSI/FCI 70.2, Class IV, Class VI**

| Valve Size (inches) | Travel (inches) | $C_v$ | Act. Size (In.) | Flow to Open - Air to Close 3-15 Spring Air Supply Pressure | | F to O - A to O | | F to C - A to O | |
|---|---|---|---|---|---|---|---|---|---|
| | | | | 20 | 35 | 6-30 | 11-22 | 3-15 | 6-30 |
| | | | | | | 35 | 35 | 20 | 35 |
| ½ | 0.75 | 4 | 6 | 660 | 1440 | 920 | 1440 | 915 | 1440 |
| ¾ | 0.75 | 6 | 6 | 330 | 1440 | 510 | 1395 | 585 | 1170 |
| 1 | 0.75 | 12 | 6 | 100 | 1440 | 210 | 755 | 345 | 675 |
| 1½ | 1.50 | 16 | 10 | 230 | 1440 | 350 | 930 | 380 | 750 |
| | | 25 | 10 | 95 | 1250 | 170 | 560 | 240 | 470 |
| 2 | 1.50 | 46 | 10 | 5 | 700 | 50 | 285 | 145 | 260 |
| 3 | 2.50 | 75 | 16 | 60 | 770 | 105 | 340 | 150 | 300 |
| | | 110 | 16 | --- | 425 | 30 | 170 | 85 | 165 |
| 4 ① | 2.50 | 195 | 16 | --- | 215 | --- | 70 | 50 | 100 |

① 150 and 300 ANSI only

**Notes:** LO-DB® trim allowable pressure drop is equivalent to the allowable pressure drop for full area standard trim in each valve size
The pressure drops shown are independent of ANSI pressure ratings
When allowable pressure drops exceed ANSI ratings the ANSI ratings must govern

## Allowable Pressure Drops (psi) - Cylinder Actuator — Air to Open/Air to Close

**Cylinder Actuated Globe and Angle Valves**
**Metal and Soft Seat**
**Temperature: -320°F to +1200°F**
**Body Ratings: ANSI Class 150 through 600**
**Seat Leakage: per ANSI/FCI 70.2, Class IV, Class VI ③**

| Valve Size (inches) | Travel (inches) | $C_v$ | Act. Size (in.) | Flow to Open - Air to Close 10 - 20 Spring Air Supply Pressure | | | | F to C - A to O | | | F to O - A to O | | |
|---|---|---|---|---|---|---|---|---|---|---|---|---|---|
| | | | | 40 | 50 | 60 | 100 | 10-20 | 15-30 | 25-50 | 10-20 | 15-30 | 25-50 |
| | | | | | | | | 40 | 60 | 100 | 40 | 40 | 60 |
| 1/2 | 0.75 | 4 | 38 | 1440 | 1440 | 1440 | 1440 | 1440 | 1440 | 1440 | 1000 | 1440 | 1440 |
| 3/4 | 0.75 | 5 | 38 | 1440 | 1440 | 1440 | 1440 | 1440 | 1440 | 1440 | 600 | 1100 | 1440 |
| 1 | 0.75 | 12 | 38 | 950 | 1440 | 1440 | 1440 | 450 | 1100 | 1440 | 250 | 600 | 950 |
| 1 1/2 | 1.50 | 16 | 38 | 550 | 1000 | 1440 | 1440 | 250 | 900 | 1440 | 100 | 300 | 550 |
| | 1.50 | 25 | 38 | 300 | 600 | 900 | 1440 | 100 | 650 | 1440 | 50 | 150 | 300 |
| 2 | 1.50 | 46 | 38 | 150 | 300 | 500 | 1200 | ------ | 300 | 1000 | ------ | 50 | 150 |
| | 1.50 | 46 | 78 | 500 | 850 | 1200 | 1200 | 250 | 750 | 1440 | 150 | 300 | 500 |
| 3 | 2.50 | 75 | 78 | 250 | 550 | 750 | 1440 | 200 | 950 | 1440 | 50 | 150 | 250 |
| | 2.50 | 110 | 78 | 150 | 250 | 400 | 900 | 100 | 400 | 800 | ------ | 50 | 150 |
| 4① (150 & 300) | 2.50 | 195 | 78 | ------ | 100 | 200 | 500 | ------ | 150 | 400 | ------ | ------ | ------ |
| 4② (600) | 2.50 | 195 | 154 | 200 | 350 | 600 | 1200 | 250 | 600 | 1100 | 100 | 150 | 200 |
| 6① (150) | 2.50 | 275 | 78 | ------ | 75 | 125 | 325 | ------ | 50 | 300 | ------ | ------ | ------ |
| | 2.50 | 400 | 78 | ------ | 25 | 75 | 225 | ------ | ------ | 250 | ------ | ------ | ------ |
| 6② (300) | 3.00 | 275 | 154 | 175 | 300 | 375 | 800 | 200 | 450 | 750 | 75 | 125 | 175 |
| | 3.00 | 400 | 154 | 125 | 200 | 275 | 575 | 150 | 350 | 550 | 50 | 75 | 125 |

① Body designed for Series "C" yoke
② Body designed for Series "D" bolted yoke
③ Soft seats limited to 1000 psi drop. Preferred flow direction is flow to close

**Notes:** LO-DB® trim allowable pressure drop is equivalent to the allowable pressure drop for full area standard trim in each valve size
The pressure drops shown are independent of ANSI pressure ratings
When allowable pressure drops exceed ANSI ratings the ANSI ratings must govern

## Allowable Pressure Drops (psi) - Domotor® Actuator — Air to Open/Air to Close ②

**Domotor Actuated Globe and Angle Valves**
**Metal and Soft Seats**
**Temperature: -320°F to +1200°F**
**Body Ratings: ANSI Class 150 through 600**
**Seat Leakage: per ANSI/FCI 70.2, Class IV, Class VI ①**

| Valve Size (inches) | Travel (inches) | Rated $C_v$ | Acutator Size | Flow to Open - Fail Open ② | | | Flow to Close - Fail Closed ② | | |
|---|---|---|---|---|---|---|---|---|---|
| | | | | Supply 40 psi Preload 30 psi | Supply 60 psi Preload 50 psi | Supply 80 psi Preload 60 psi | Supply 40 psi Preload 30 psi | Supply 60 psi Preload 30 psi | Supply 90 psi Preload 50 psi |
| 1/2 | 0.75 | 4 | A | 1500 | 1500 | 1500 | 1025 | 1500 | 1500 |
| | | | B | 1500 | 1500 | 1500 | 1500 | 1500 | 1500 |
| 3/4 | 0.75 | 6 | A | 1150 | 1500 | 1500 | 550 | 1500 | 1500 |
| | | | B | 1500 | 1500 | 1500 | 1500 | 1500 | 1500 |
| 1 | 0.75 | 12 | A | 800 | 1500 | 1500 | 275 | 1500 | 1500 |
| | | | B | 1500 | 1500 | 1500 | 850 | 1500 | 1500 |
| 1 1/2 | 1.50 | 16 | B | 1150 | 1500 | 1500 | 600 | 1500 | 1500 |
| | | | C | 1500 | 1500 | 1500 | 1425 | 1500 | 1500 |
| | | 25 | B | 700 | 1475 | 1500 | 350 | 1300 | 1500 |
| | | | C | 1500 | 1500 | 1500 | 825 | 1500 | 1500 |
| 2 | 1.50 | 46 | B | 375 | 850 | 1075 | 200 | 725 | 975 |
| | | | C | 1025 | 1175 | 1175 | 475 | 1500 | 1500 |
| 3 | 2.50 | 75 | C | 625 | 1200 | 1500 | 350 | 1100 | 1500 |
| | | | D | 1500 | 1500 | 1500 | 725 | 1500 | 1500 |
| | | 110 | C | 325 | 700 | 875 | 175 | 600 | 800 |
| | | | D | 850 | 925 | 925 | 375 | 1150 | 1225 |
| 4 ③ | 2.50 | 195 | C | 150 | 375 | 475 | 100 | 325 | 425 |
| | | | D | 450 | 500 | 500 | 200 | 625 | 650 |
| 4 ④ | 2.50 | 195 | D | 450 | 850 | 1025 | 200 | 625 | 825 |
| 6 ③ | 2.50 | 275 | C | 100 | 225 | 300 | 50 | 200 | 275 |
| | | | D | 300 | 325 | 325 | 125 | 400 | 450 |
| | | 400 | C | 50 | 150 | 200 | 50 | 150 | 200 |
| | | | D | 200 | 225 | 225 | 100 | 300 | 300 |
| 6 ⑤ | 3.00 | 275 | D | 300 | 550 | 675 | 150 | 425 | 575 |
| | | 400 | D | 250 | 475 | 600 | 125 | 375 | 500 |
| 8 | 5.00 | 640 | D | 100 | 225 | 300 | 50 | 200 | 250 |
| 10 | 5.00 | 1000 | D | 50 | 125 | 175 | 50 | 100 | 150 |

① Soft seats are limited to 1000 psi pressure drop. The preferred flow direction is flow to close
② For flow to open/fail closed or flow to close/fail open actions, fail-safe volume tanks are required
③ Body designed for 150 lb and 300 lb ratings, "C" Series yoke
④ Body designed for 600 lb rating, "D" Series yoke
⑤ Body designed for 300 lb and 600 lb ratings, "D" Series yoke

**Notes:** LO-DB® trim allowable pressure drop is equivalent to the allowable pressure drop for full area standard trim in each valve size
The pressure drops shown are independent of ANSI pressure ratings
When allowable pressure drops exceed ANSI ratings the ANSI ratings must govern

## Allowable Pressure Drops (psi)

**Combining and Diverting Service**

**Globe and Angle 3-way Valves**
**Metal Seat**
**Temperature: -320°F to +1200°F**
**Body Ratings: ANSI Class 150 through 600**
**Seat Leakage: per ANSI/FCI 70.2, Class IV**

### Domotor® Actuator

| Valve Size (inches) | Rated $C_v$ | Travel (inches) | Acutator Size | Actuator Pressures | | |
|---|---|---|---|---|---|---|
| | | | | Supply 40 psi Preload 30 psi | Supply 80 psi Preload 40 psi | Supply 100 psi Preload 50 psi |
| ½ | 4 | 0.75 | A | 640 | 1500 | 1500 |
| | | | B | 1430 | 1500 | 1500 |
| ¾ | 6 | 0.75 | A | 500 | 1480 | 1500 |
| | | | B | 1150 | 1500 | 1500 |
| 1 | 10 | 0.75 | A | 355 | 1080 | 1440 |
| | | | B | 830 | 1500 | 1500 |
| 1½ | 25 | 1.50 | B | 340 | 888 | 1160 |
| | | | C | 775 | 1500 | 1500 |
| 2 | 40 | 1.50 | B | 220 | 590 | 780 |
| | | | C | 520 | 1230 | 150 |
| 3 | 95 | 2.50 | C | 230 | 500 | 750 |
| | | | D | 540 | 900① | ------ |
| 4 | 175 | 2.50 | C | 120 | 320 | 410 |
| | | | D | 300 | 535① | ------ |
| 6 | 275 | 2.50 | C | 75 | 212 | 280 |
| | 320 | 2.50 | C | 45 | 140 | 190 |
| | 275 | 2.50 | D | 200 | 375① | ------ |
| | 320 | 3.00 | D | 130 | 310 | 400 |
| 8 | 480 | 5.00 | D | 80 | 175 | 260 |
| 10 | 820 | 5.00 | D | 45 | 100 | 155 |

① 60 psi supply, 30 psi preload max. to prevent damage to valve

**Notes:** LO-DB® trim allowable pressure drop is equivalent to the allowable pressure drop for full area standard trim in each valve size
The pressure drops shown are independent of ANSI pressure ratings
When allowable pressure drops exceed ANSI ratings the ANSI ratings must govern
Volume tanks required for fail-safe action

### Cylinder Actuator

| Valve Size (inches) | Travel (inches) | Rated $C_v$ | Acutator Size | Supply 40 psi Spring Range 10-20 | Supply 60 psi Spring Range 15-30 | Supply 80 psi Spring Range 25-50 |
|---|---|---|---|---|---|---|
| ½ | 0.75 | 4 | 3B | 325 | 750 | 1500 |
| ¾ | 0.75 | 6 | 3B | 225 | 550 | 1200 |
| 1 | 0.75 | 12 | 3B | 100 | 350 | 825 |
| 1½ | 1.50 | 25 | 3B | 0 | 70 | 275 |
| | | | 7B | 175 | 400 | 825 |
| 2 | 1.50 | 46 | 3B | 0 | 10 | 150 |
| | | | 7B | 90 | 225 | 525 |
| 3 | 2.50 | 75 | 7B | 0 | 70 | 200 |
| 4① | 2.50 | 195 | 7B | 0 | 15 | 90 |

① Body designed for 150 lb and 300 lb ratings, "C" Series yoke

**Notes:** The pressure drops shown are independent of ANSI pressure ratings
When allowable pressure drops exceed ANSI ratings the ANSI ratings must govern

## Dimensions (inches)

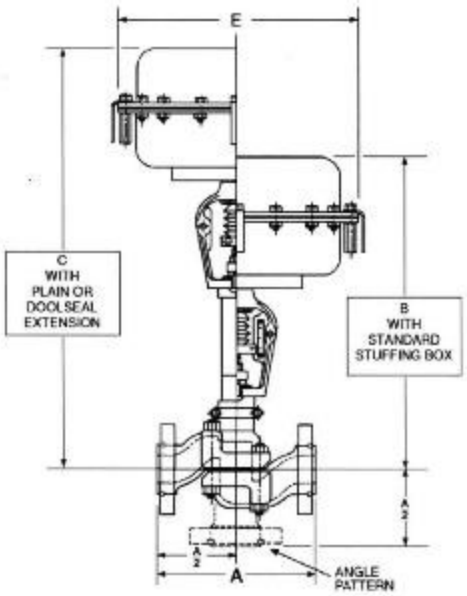


**Diaphragm Actuator (87/88)**

| Valve Size (inches) | ANSI Class 150, 300 & 600 | | | |
|---|---|---|---|---|
| | A | B ① | C ① | E |
| ½ | 6.75 | 13.7 | 17.7 | 11.9 |
| ¾ | 6.75 | 13.7 | 17.7 | 11.9 |
| 1 ② | 8.50 | 13.7 | 17.7 | 11.9 |
| 1½ ② | 9.50 | 19.5 | 25.5 | 14.7 |
| 2 ② | 11.50 | 20.0 | 26.0 | 14.7 |
| 3 ② | 14.00 | 28.0 | 37.0 | 18.8 |
| 4 ②③ | 17.00 | 28.0 | 37.0 | 18.8 |

① Add 4½" to B, C or D dimension for actuator removal clearance
② Dimension A is for separable flanges or weld ends only. See table on page 19 for integral flange dimension A (to ISA standards as noted)
③ 150 and 300 ANSI only

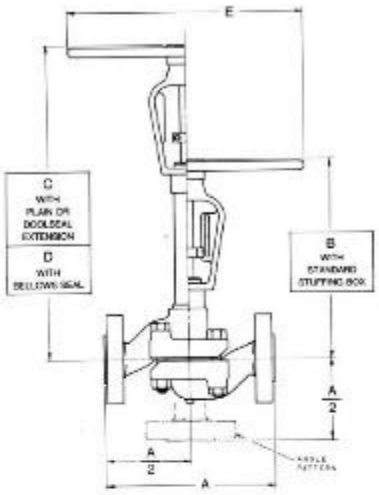


Manual Actuator

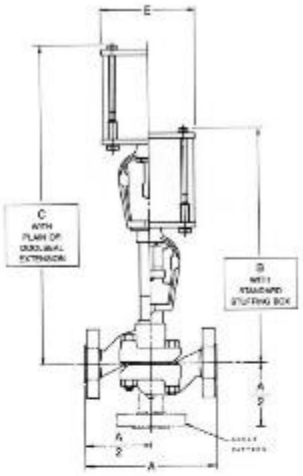


Cylinder Actuator

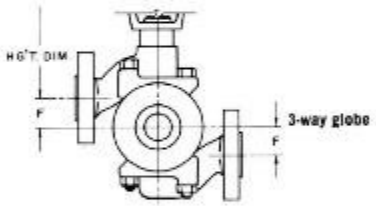


3-way globe

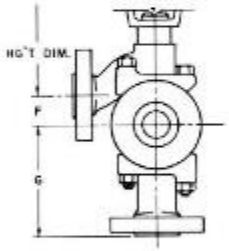


3-way angle

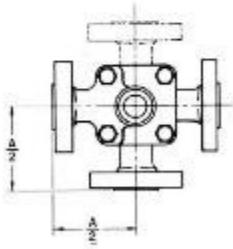


3-way globe
(flange rotation)

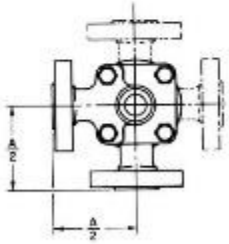


3-way angle
(flange rotation)

Add the following to B, C or D dimension when a side-mounted auxiliary handwheel is used with a Domotor® or cylinder
Series A Domotor® (7⅜" O.D.) or A cylinder (4¾" O.D.) - 4½"
Series B Domotor® (9¼" O.D.) or B cylinder (7" O.D.) - 5"
Series C Domotor® (13½" O.D.) or C cylinder (9¼" O.D.) - 6"

## Dimensions (inches)

### Manual Actuator

| Valve Size (in.) | ANSI Class 150 | | | | | | | | ANSI Class 300 | | | | | | | | ANSI Class 600 | | | | | | | |
|---|---|---|---|---|---|---|---|---|---|---|---|---|---|---|---|---|---|---|---|---|---|---|---|---|
| | A | B① | C① | D① | E | F | G | H② | A | B① | C① | D① | E | F | G | H② | A | B① | C① | D① | E | F | G | H② |
| ½ | 6.75 | 9.2 | 13.2 | 16.9 | 7.0 | 1.03 | 4.41 | ----- | 6.75 | 9.2 | 13.2 | 16.9 | 7.0 | 1.03 | 4.41 | ----- | 6.75 | 9.2 | 13.2 | 16.9 | 7.0 | 1.03 | 4.41 | ----- |
| ¾ | 6.75 | 9.2 | 13.2 | 16.9 | 7.0 | 1.03 | 4.41 | ----- | 6.75 | 9.2 | 13.2 | 16.9 | 7.0 | 1.03 | 4.41 | ----- | 6.75 | 9.2 | 13.2 | 16.9 | 7.0 | 1.03 | 4.41 | ----- |
| 1 ② | 8.50 | 9.2 | 13.2 | 16.9 | 7.0 | 1.16 | 5.41 | ----- | 8.50 | 9.2 | 13.2 | 16.9 | 7.0 | 1.16 | 5.41 | ----- | 8.50 | 9.2 | 13.2 | 16.9 | 7.0 | 1.16 | 5.41 | ----- |
| 1½ ② | 9.50 | 11.9 | 17.9 | 24.6 | 12.0 | 1.66 | 6.41 | ----- | 9.50 | 11.9 | 17.9 | 24.6 | 12.0 | 1.66 | 6.41 | ----- | 9.50 | 11.9 | 17.9 | 24.6 | 12.0 | 1.66 | 6.41 | ----- |
| 2 ② | 11.50 | 12.2 | 18.2 | 25.0 | 12.0 | 2.00 | 7.75 | ----- | 11.50 | 12.2 | 18.2 | 25.0 | 12.0 | 2.00 | 7.75 | ----- | 11.50 | 12.2 | 18.2 | 25.0 | 12.0 | 2.00 | 7.75 | ----- |
| 3 ② | 14.00 | 17.8 | 27.4 | 40.7 | 18.0 | 3.00 | 10.00 | ----- | 14.00 | 17.8 | 27.4 | 40.7 | 18.0 | 3.00 | 10.00 | ----- | 14.00 | 17.8 | 27.4 | 40.7 | 18.0 | 3.00 | 10.00 | ----- |
| 4 ② | 17.00 | 17.8 | 27.4 | 40.7 | 18.0 | 3.62 | 12.12 | ----- | 17.00 | 17.8 | 27.4 | 40.7 | 18.0 | 3.62 | 12.12 | ----- | 15.50 ③ | 17.8 | 27.4 | 40.7 | 18.0 | 3.62 | 11.38 | ----- |
| 4 ③ | ----- | ----- | ----- | ----- | ----- | ----- | ----- | ----- | ----- | ----- | ----- | ----- | ----- | ----- | ----- | ----- | 15.50 ③ | 23.7 | 35.6 | ----- | 18.0 | ----- | ----- | ----- |
| 6 ④ | 24.00 | 20.0 | 29.5 | 42.9 | 18.0 | 4.25 | 16.25 | 7.7 | 22.00 | 21.5 | 31.0 | ----- | 18.0 | ----- | ----- | 7.7 | ----- | ----- | ----- | ----- | ----- | ----- | ----- | ----- |
| 6 ⑤ | ----- | ----- | ----- | ----- | ----- | ----- | ----- | ----- | 22.00 | 25.7 | 36.7 | ----- | 18.0 | 5.25 | 16.38 | 7.7 | 28.00 | 33.1 | 43.8 | ----- | 18.0 | 5.38 | 18.38 | 8.5 |
| 8 | 32.00 | 34.1 | 44.8 | ----- | 18.0 | 5.69 | 21.69 | 9.5 | 32.00 | 34.1 | 44.8 | ----- | 18.0 | 5.69 | 21.69 | 9.5 | 36.50 | 34.8 | 45.3 | ----- | 18.0 | ----- | ----- | 10.0 |
| 10 | 37.00 | 35.3 | 46.1 | ----- | 18.0 | 7.00 | 25.50 | 10.8 | 37.00 | 35.3 | 46.1 | ----- | 18.0 | 7.00 | 25.50 | 10.8 | ----- | ----- | ----- | ----- | ----- | ----- | ----- | ----- |

① Add 4½" to B, C or D dimension for actuator removal clearance
② Dimension A is for separable flanges or weld ends only. See table on page 19 for integral flange dimension A (to ISA standards as noted)
③ Bottom of valve extends below end flanges
④ Valve body with Series C actuators
⑤ Valve body with Series D actuators

### Cylinder Actuator

| Valve Size (in.) | ANSI Class 150 | | | | | | | ANSI Class 300 | | | | | | | ANSI Class 600 | | | | | | |
|---|---|---|---|---|---|---|---|---|---|---|---|---|---|---|---|---|---|---|---|---|---|
| | A | B① | C① | E | F | G | H② | A | B① | C① | E | F | G | H② | A | B① | C① | E | F | G | H② |
| ½ | 6.75 | 16.5 | 20.5 | 7.60 | 1.03 | 4.41 | ----- | 6.75 | 16.5 | 20.5 | 7.60 | 1.03 | 4.41 | ----- | 6.75 | 16.5 | 20.5 | 7.60 | 1.03 | 4.41 | ----- |
| ¾ | 6.75 | 16.5 | 20.5 | 7.60 | 1.03 | 4.41 | ----- | 6.75 | 16.5 | 20.5 | 7.60 | 1.03 | 4.41 | ----- | 6.75 | 16.5 | 20.5 | 7.60 | 1.03 | 4.41 | ----- |
| 1 ② | 8.50 | 16.5 | 20.5 | 7.60 | 1.16 | 5.41 | ----- | 8.50 | 16.5 | 20.5 | 7.60 | 1.16 | 5.41 | ----- | 8.50 | 16.5 | 20.5 | 7.60 | 1.16 | 5.41 | ----- |
| 1½ ② | 9.50 | 19.1 | 25.1 | 7.60 | 1.66 | 6.41 | ----- | 9.50 | 19.1 | 25.1 | 7.60 | 1.66 | 6.41 | ----- | 9.50 | 19.1 | 25.1 | 7.60 | 1.66 | 6.41 | ----- |
| 2 ② | 11.50 | 19.6 | 25.6 | 7.60 | 2.00 | 7.75 | ----- | 11.50 | 19.6 | 25.6 | 7.60 | 2.00 | 7.75 | ----- | 11.50 | 19.6 | 25.6 | 7.60 | 2.00 | 7.75 | ----- |
| 3 ② | 14.00 | 28.8 | 37.8 | 10.50 | 3.00 | 10.00 | ----- | 14.00 | 28.8 | 37.8 | 10.50 | 3.00 | 10.00 | ----- | 14.00 | 28.8 | 37.8 | 10.50 | 3.00 | 10.00 | ----- |
| 4 ② | 17.00 | 28.8 | 37.8 | 10.50 | 3.62 | 12.12 | ----- | 17.00 | 28.8 | 37.8 | 10.50 | 3.62 | 12.12 | ----- | 15.50 | 28.8 | 37.8 | 10.50 | 3.62 | 11.38 | ----- |
| 4 ③ | ----- | ----- | ----- | ----- | ----- | ----- | ----- | ----- | ----- | ----- | ----- | ----- | ----- | ----- | 15.50 | 37.6 | 48.3 | 14.75 | ----- | ----- | ----- |
| 6 ④ | 24.00 | 40.6 | 50.1 | 10.50 | 4.25 | 16.25 | 7.7 | ----- | ----- | ----- | ----- | ----- | ----- | ----- | ----- | ----- | ----- | ----- | ----- | ----- | ----- |
| 6 ⑤ | 24.00 | 49.4 | 60.1 | 14.75 | 4.25 | 16.25 | 7.7 | ----- | ----- | ----- | ----- | ----- | ----- | ----- | ----- | ----- | ----- | ----- | ----- | ----- | ----- |

① Add 4½" to B or C dimension for actuator removal clearance
② Dimension A is for separable flanges or weld ends only. See table on page 19 for integral flange dimension A (to ISA standards as noted)
③ Bottom of valve extends below end flanges
④ Valve body with 154 sq. in. actuator

## Dimensions (inches)

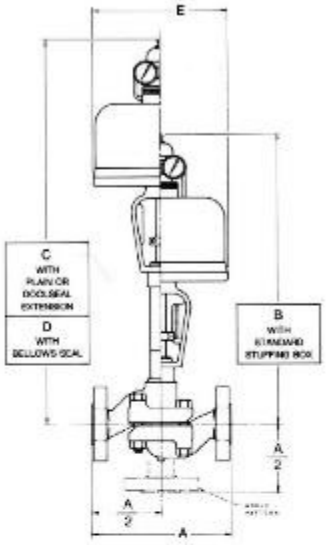


**Domotor® actuator**

**Domotor® Actuator**

| Valve Size (in.) | ANSI Class 150 | | | | | | | | ANSI Class 300 | | | | | | | | ANSI Class 600 | | | | | | | |
|---|---|---|---|---|---|---|---|---|---|---|---|---|---|---|---|---|---|---|---|---|---|---|---|---|
| | A | B① | C① | D① | E | F | G | H② | A | B① | C① | D① | E | F | G | H③ | A | B① | C① | D① | E | F | G | H③ |
| ½ | 6.75 | 20.3 | 24.3 | 28.0 | 7.62 | 1.03 | 4.41 | ----- | 6.75 | 20.3 | 24.3 | 28.0 | 7.62 | 1.03 | 4.41 | ----- | 6.75 | 20.3 | 24.3 | 28.0 | 7.62 | 1.03 | 4.41 | ----- |
| ¾ | 6.75 | 20.3 | 24.3 | 28.0 | 7.62 | 1.03 | 4.41 | ----- | 6.75 | 20.3 | 24.3 | 28.0 | 7.62 | 1.03 | 4.41 | ----- | 6.75 | 20.3 | 24.3 | 28.0 | 7.62 | 1.03 | 4.41 | ----- |
| 1④ | 8.50 | 20.3 | 24.3 | 28.0 | 7.62 | 1.16 | 5.41 | ----- | 8.50 | 20.3 | 24.3 | 28.0 | 7.62 | 1.16 | 5.41 | ----- | 8.50 | 20.3 | 24.3 | 28.0 | 7.62 | 1.16 | 5.41 | ----- |
| 1½② | 9.50 | 23.6 | 29.6 | 36.4 | 9.25 | 1.66 | 6.41 | ----- | 9.50 | 23.6 | 29.6 | 36.4 | 9.25 | 1.66 | 6.41 | ----- | 9.50 | 23.6 | 29.6 | 36.4 | 9.25 | 1.66 | 6.41 | ----- |
| 2③ | 11.50 | 24.0 | 30.0 | 36.7 | 9.25 | 2.00 | 7.75 | ----- | 11.50 | 24.0 | 30.0 | 36.7 | 9.25 | 2.00 | 7.75 | ----- | 11.50 | 24.0 | 30.0 | 36.7 | 9.25 | 2.00 | 7.75 | ----- |
| 3③ | 14.00 | 31.3 | 40.9 | 54.3 | 13.25 | 3.00 | 10.00 | ----- | 14.00 | 31.3 | 40.9 | 54.3 | 13.25 | 3.00 | 10.00 | ----- | 14.00 | 31.3 | 40.9 | 54.3 | 13.25 | 3.00 | 10.00 | ----- |
| 4③ | 17.00 | 31.3 | 40.9 | 54.3 | 13.25 | 3.62 | 12.12 | ----- | 17.00 | 31.3 | 40.9 | 54.3 | 13.25 | 3.62 | 12.12 | ----- | 15.50⑤ | 31.3 | 40.9 | 54.3 | 13.25 | 3.62 | 11.38 | ----- |
| 4③ | ----- | ----- | ----- | ----- | ----- | ----- | ----- | ----- | ----- | ----- | ----- | ----- | ----- | ----- | ----- | ----- | 15.50⑤ | 44.0 | 54.9 | ----- | 18.00 | ----- | ----- | ----- |
| 6③ | 24.00 | 33.6 | 43.1 | 56.5 | 13.25 | 4.25 | 16.25 | 7.7 | 22.00 | 35.0 | 44.5 | ----- | 13.25 | 5.25 | 16.38 | 7.7 | ----- | ----- | ----- | ----- | ----- | ----- | ----- | ----- |
| 6① | ----- | ----- | ----- | ----- | ----- | ----- | ----- | ----- | 22.00 | 46.0 | 57.0 | ----- | 18.00 | 5.25 | 16.38 | 7.7 | 28.00 | 51.1 | 61.8 | ----- | 18.00 | 5.38 | 18.38 | 8.5 |
| 8 | 32.00 | 52.1 | 62.8 | ----- | 18.00 | 5.69 | 21.69 | 9.5 | 32.00 | 52.1 | 62.8 | ----- | 18.00 | 5.69 | 21.69 | 9.5 | 36.50 | 52.6 | 63.3 | ----- | 18.00 | ----- | ----- | 10.0 |
| 10 | 37.00 | 53.3 | 64.1 | ----- | 18.00 | 7.00 | 25.50 | 10.8 | 37.00 | 53.3 | 64.1 | ----- | 18.00 | 7.00 | 25.50 | 10.8 | ----- | ----- | ----- | ----- | ----- | ----- | ----- | ----- |

① Add 4½" to B, C or D dimension for actuator removal clearance
② Dimension A is for separable flanges or weld ends only. See table on page 19 for integral flange dimension A (to ISA standards as noted)
Valve size 6" & larger are integral flange ends
③ Bottom of valve extends below end flanges
④ Valve body with Series C actuators
⑤ Valve body with Series D actuators

See page 16 for definition of dimensions F and G

## Dimensions - Integral Flanged (inches)

**Dimension A (face to face) for valves with integral flanges not covered above (Conforms to ISA standard for 1" to 4" valves)**

| Valve Size (inches) | End Connection Type | ANSI Class 150 | ANSI Class 300 | ANSI Class 600 |
|---|---|---|---|---|
| 1 | L & S Tongue | 7.75 | 8.25 | 8.25 |
| | L & S Groove | 7.63 | 8.13 | 8.13 |
| | Ring Joint | 7.75 | 8.25 | 8.25 |
| | Raised & Flat Face | 7.25 | 7.75 | 8.25 |
| 1½ | L & S Tongue | 9.25 | 9.75 | 9.88 |
| | L & S Groove | 9.13 | 9.63 | 9.75 |
| | Ring Joint | 9.25 | 9.75 | 9.88 |
| | Raised & Flat Face | 8.75 | 9.25 | 9.88 |
| 2 | L & S Tongue | 10.50 | 11.00 | 11.25 |
| | L & S Groove | 10.38 | 10.88 | 11.13 |
| | Ring Joint | 10.50 | 11.13 | 11.38 |
| | Raised & Flat Face | 10.00 | 10.50 | 11.25 |
| 3 | L & S Tongue | 12.25 | 13.00 | 13.25 |
| | L & S Groove | 12.13 | 12.88 | 13.13 |
| | Ring Joint | 12.25 | 13.13 | 13.38 |
| | Raised & Flat Face | 11.75 | 12.50 | 13.25 |
| 4 | L & S Tongue | 14.38 | 15.00 | 15.50 |
| | L & S Groove | 14.25 | 14.88 | 15.38 |
| | Ring Joint | 14.38 | 15.13 | 15.63 |
| | Raised & Flat Face | 13.88 | 14.50 | 15.50 |

## Approximate Shipping Weights (lbs)

| Valve Size (inches) | ANSI Class | With Diaphragm Actuator | With Manual Actuator | With Cylinder Actuator | With Domotor Actuator | Extra for Bonnet Extension |
|---|---|---|---|---|---|---|
| ½ | 600 | 35 | 18 | 24 | 30 | 3 |
| ¾ | 600 | 36 | 19 | 25 | 31 | 3 |
| 1 | 600 | 41 | 24 | 30 | 36 | 3 |
| 1½ | 600 | 75 | 45 | 48 | 56 | 5 |
| 2 | 600 | 100 | 57 | 60 | 68 | 5 |
| 3 | 600 | 225 | 122 | 126 | 136 | 12 |
| 4 | 300 | 285 | 176 | 180 | 190 | 12 |
| 4 | 600 | ---- | 415 | 573 | 522 | 65 |
| 6 | 150 | ---- | 303 | 307 | 317 | 12 |
| 6 | 300 | ---- | 403 | 561 | 510 | 85 |
| 6 | 600 | ---- | 767 | 925 | 874 | 130 |
| 8 | 300 | ---- | 662 | 820 | 769 | 130 |
| 8 | 600 | ---- | 1081 | 1239 | 1188 | 130 |
| 10 | 300 | ---- | 1144 | 1302 | 1251 | 130 |

## Accessories and Options

Auxiliary Handwheels

Handwheel Sizes A, B, C

Oversize Actuators

| Standard | to | Oversize |
|---|---|---|
| A | | B |
| B | | C |
| C | | D |

Model 6000 Electropneumatic Transducer
(See Specification Data CS6600)
Input Range 4-20 mA
Output Range 3-15 psi

Internal Regulator
Intergral Universal Mounting Bracket

8005A/8006A Electropneumatic Transducer
(See Specification Data CS6000)
Input Signals 10-50 mA, 104 ohms
4-20 mA, 173 ohms
Output Signals (Direct or Reverse)
Model 8005A: 3-15 psi
Model 8006A: 3-15, 6-30, 0-20, or 0-35 psi

I/PEX 9000 Electropneumatic Transducer
(See Specification Data CS9000)
Input Range 4-20 mA
Split range up to 3 times
Output (Direct or Reverse)
3-15 psi, adjustable to 0-20 psi

Moore 750P Positioner
3-15 psi Instrument Signal

Refer to specific actuator and accessory specification literature for complete information.

Microswitches
EXAR, EXHAR, EXDAR, OPAR, OPHAR

496 Rotary Switches
496-2 (2 switches) Limit Switch
496-3 Position Transmitter
(See Specification Data CS7000)

80-4 or 80-40 Airset
(See Specification Data CY7800)

77-6 or 77-60 Lockup Valve
(See Specification Data CY7700)

2" Gauge 0-30 psi

For Solenoid Valves Consult Price List

2700 Controllers
(See Specification Data CW6000)

Fail-safe Volume Tanks
w/ 77-8/77-80 Trip Valve
Super Response
Moore 61H Volume Booster

Additional Options Available

Other Body Materials
Other Flange Facings
U.O.P. Trim
N.A.C.E. Compliance
Non-Destructive Examination
Doolseal Double Packing
Bellows Seal Bonnets

Facilities: Brazil, Canada, France, Germany, Italy, Japan, Mexico, Netherlands, Singapore, Spain, United Kingdom, United States

Masoneilan North American Operations
Dresser Valve and Controls Division
Marketing Services
15112 Morales Road
P.O. Box 60078 (77205-0078)
Houston, Texas 77032
Tel: (281) 871-6500 Fax: (281) 871-6569

Masoneilan DRESSER

Signature Press 10/97/4M

## Appendix E: Block 2 High Frequency Charts

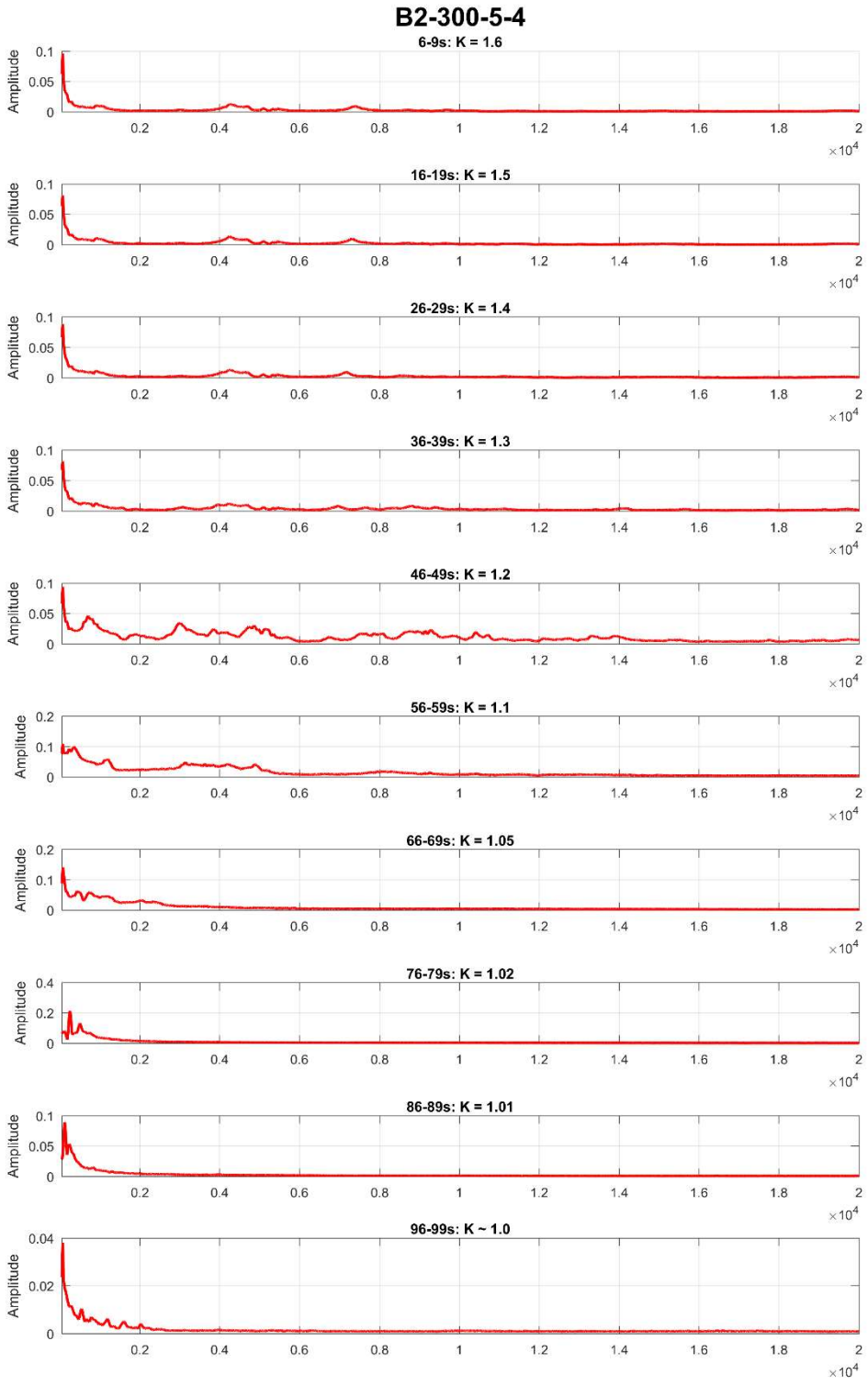
B2-300-5-4
6-9s: K = 1.6
16-19s: K = 1.5
26-29s: K = 1.4
36-39s: K = 1.3
46-49s: K = 1.2
56-59s: K = 1.1
66-69s: K = 1.05
76-79s: K = 1.02
86-89s: K = 1.01
96-99s: K ~ 1.0
Amplitude
×10^4

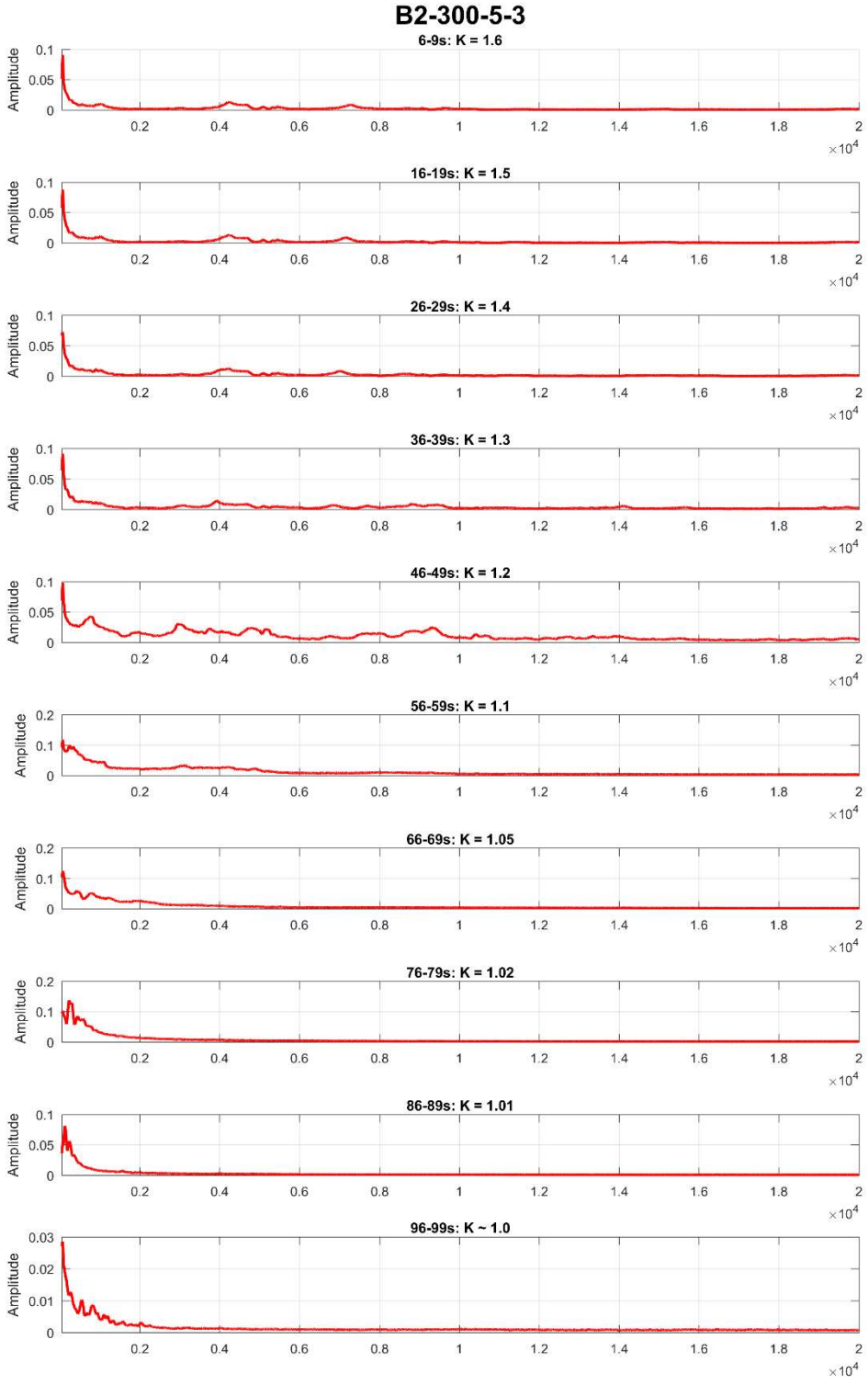
B2-300-5-3
6-9s: K = 1.6
16-19s: K = 1.5
26-29s: K = 1.4
36-39s: K = 1.3
46-49s: K = 1.2
56-59s: K = 1.1
66-69s: K = 1.05
76-79s: K = 1.02
86-89s: K = 1.01
96-99s: K ~ 1.0
Amplitude
×10^4

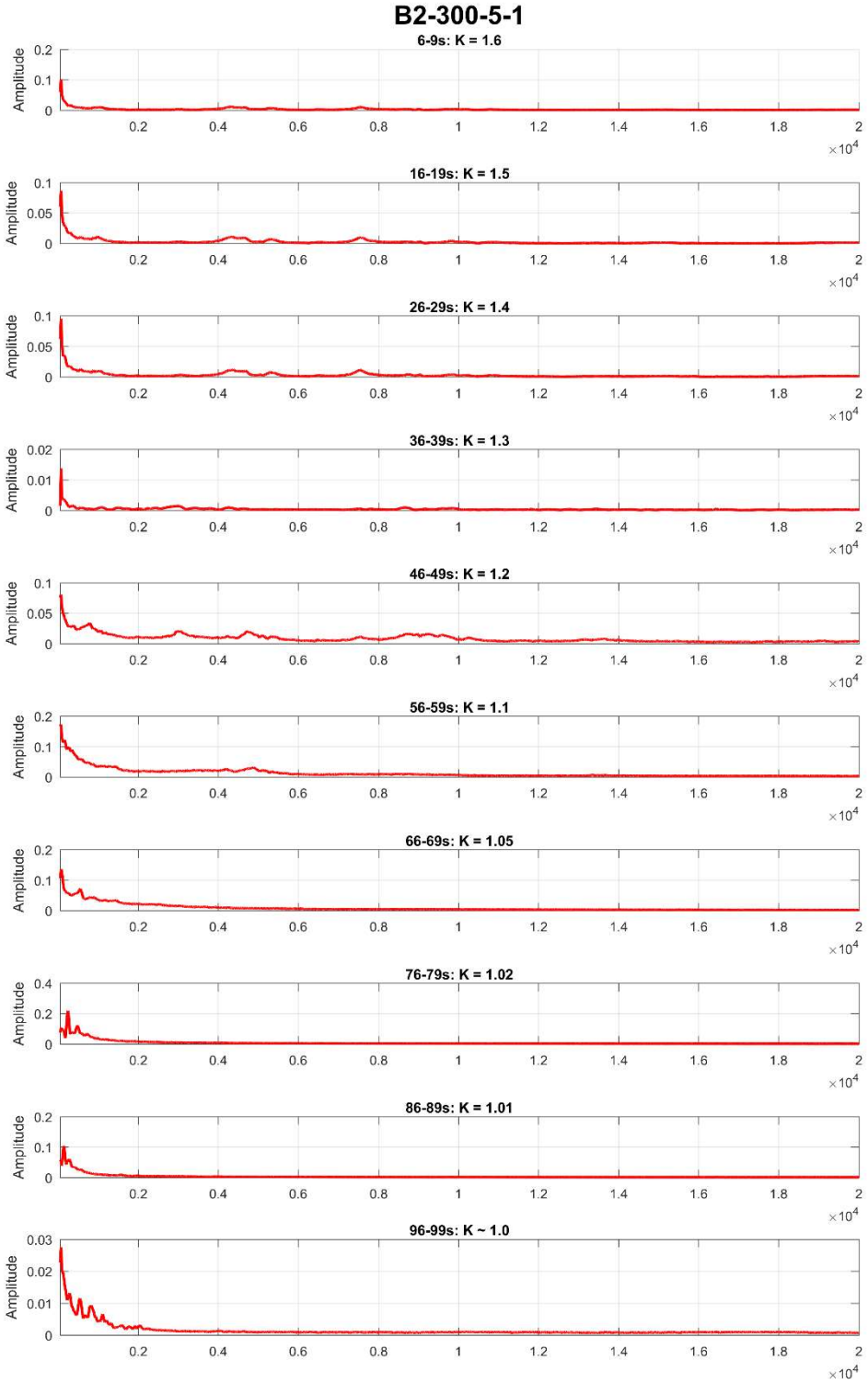
B2-300-5-1
6-9s: K = 1.6
16-19s: K = 1.5
26-29s: K = 1.4
36-39s: K = 1.3
46-49s: K = 1.2
56-59s: K = 1.1
66-69s: K = 1.05
76-79s: K = 1.02
86-89s: K = 1.01
96-99s: K ~ 1.0
Amplitude
×10^4

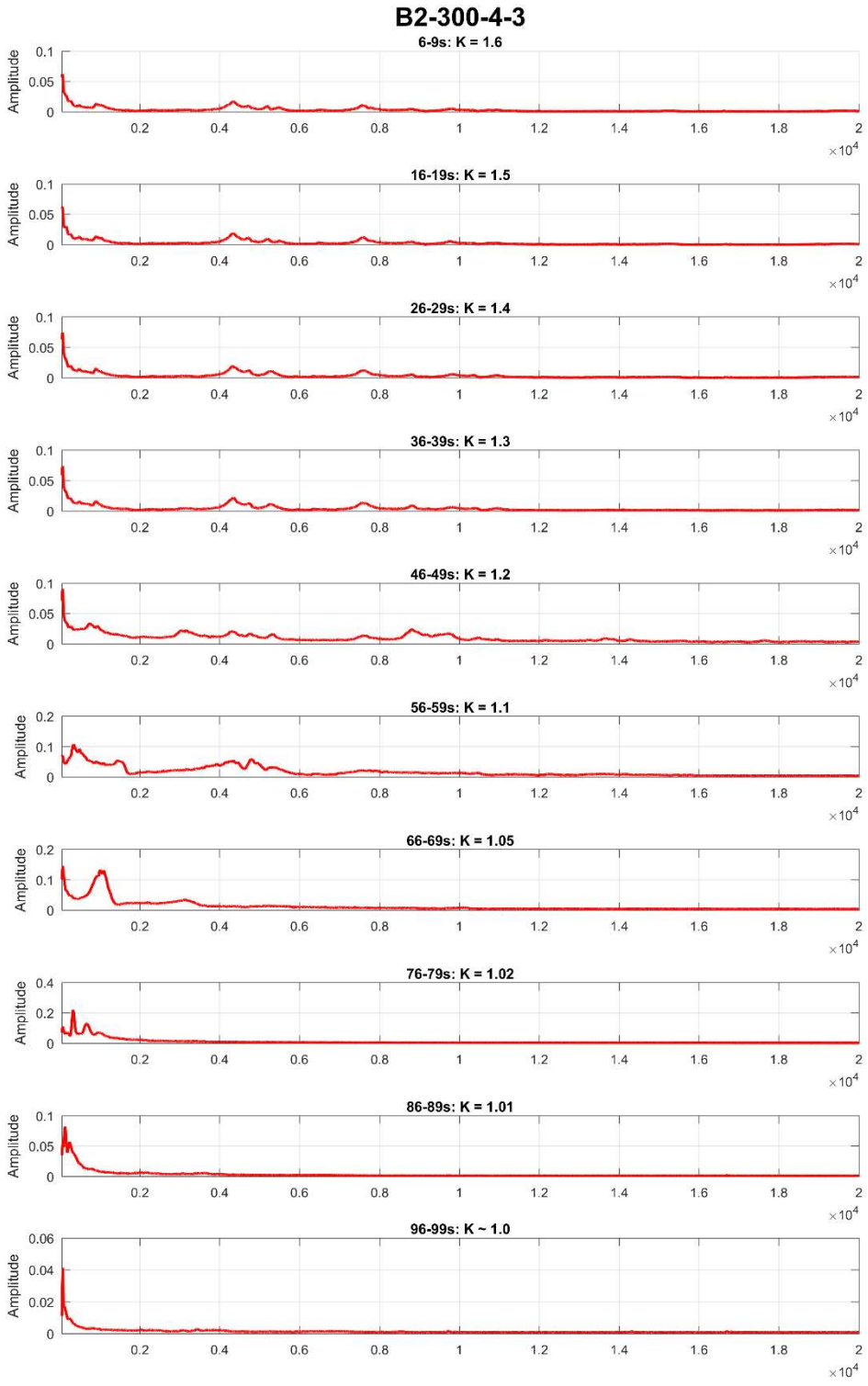
B2-300-4-3
6-9s: K = 1.6
16-19s: K = 1.5
26-29s: K = 1.4
36-39s: K = 1.3
46-49s: K = 1.2
56-59s: K = 1.1
66-69s: K = 1.05
76-79s: K = 1.02
86-89s: K = 1.01
96-99s: K ~ 1.0
Amplitude
×10^4

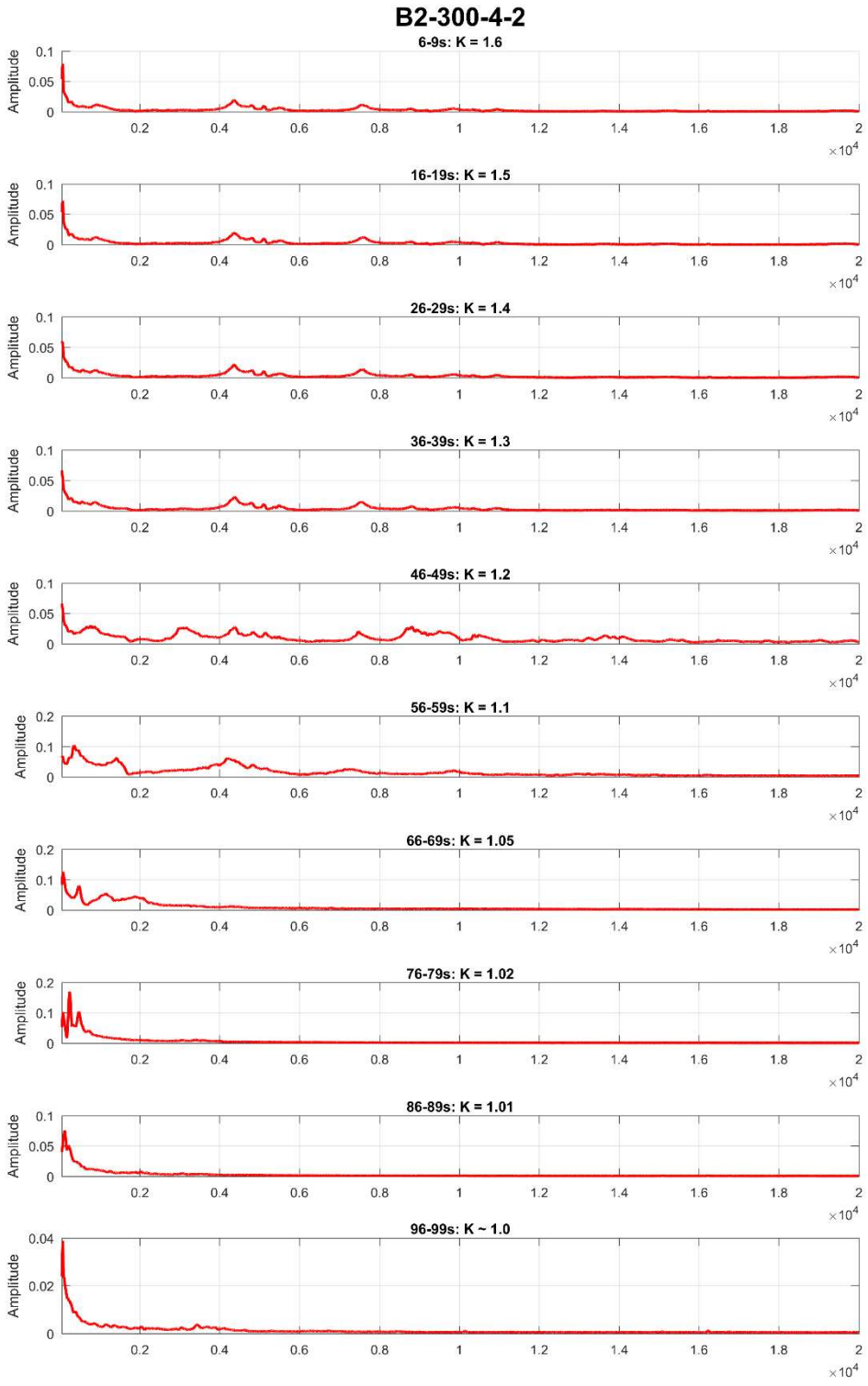
B2-300-4-2
6-9s: K = 1.6
16-19s: K = 1.5
26-29s: K = 1.4
36-39s: K = 1.3
46-49s: K = 1.2
56-59s: K = 1.1
66-69s: K = 1.05
76-79s: K = 1.02
86-89s: K = 1.01
96-99s: K ~ 1.0
Amplitude
×10^4

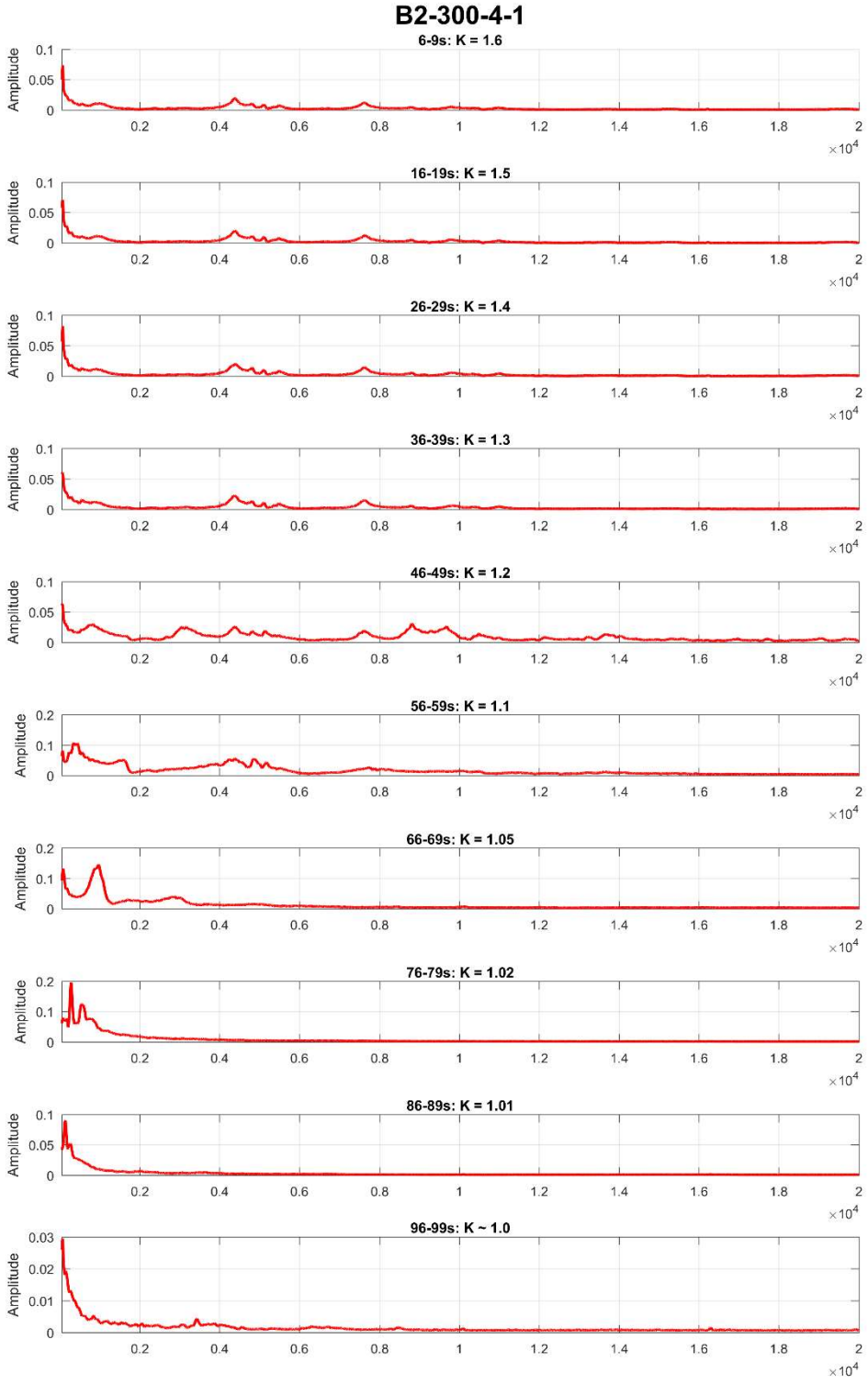
B2-300-4-1
6-9s: K = 1.6
16-19s: K = 1.5
26-29s: K = 1.4
36-39s: K = 1.3
46-49s: K = 1.2
56-59s: K = 1.1
66-69s: K = 1.05
76-79s: K = 1.02
86-89s: K = 1.01
96-99s: K ~ 1.0
Amplitude
×10^4

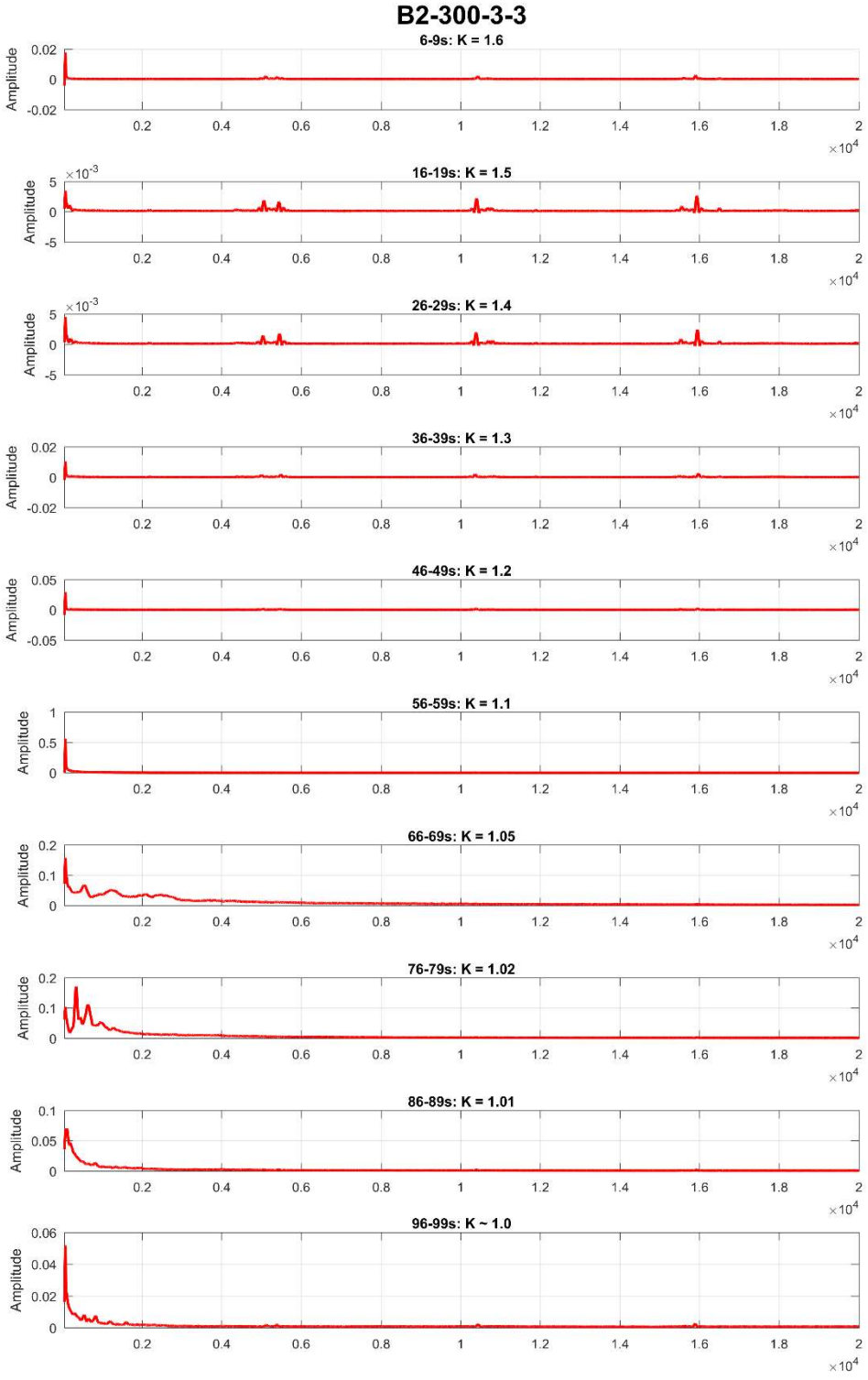
B2-300-3-3
6-9s: K = 1.6
16-19s: K = 1.5
26-29s: K = 1.4
36-39s: K = 1.3
46-49s: K = 1.2
56-59s: K = 1.1
66-69s: K = 1.05
76-79s: K = 1.02
86-89s: K = 1.01
96-99s: K ~ 1.0
Amplitude
×10^4
×10^-3

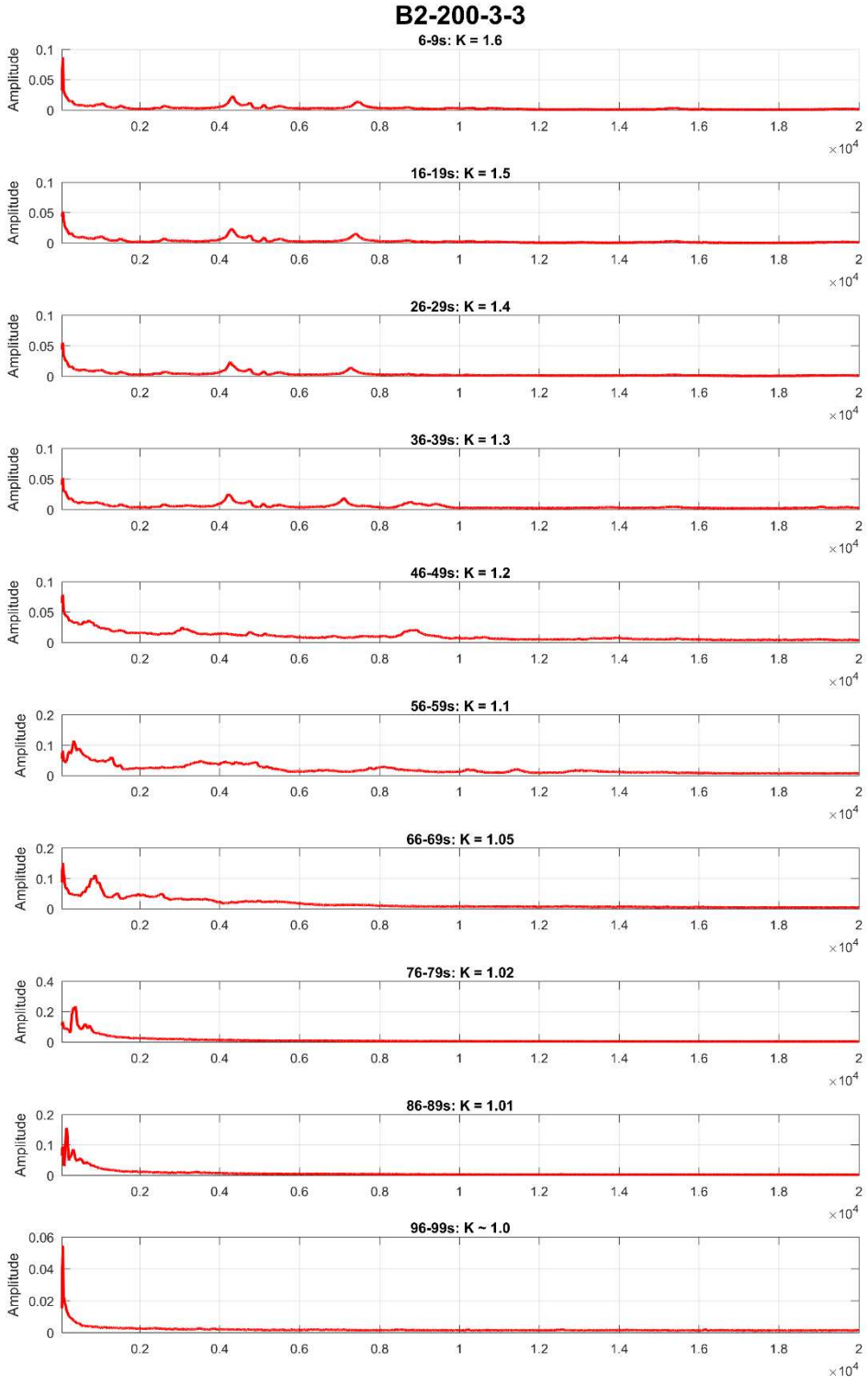
B2-200-3-3
6-9s: K = 1.6
16-19s: K = 1.5
26-29s: K = 1.4
36-39s: K = 1.3
46-49s: K = 1.2
56-59s: K = 1.1
66-69s: K = 1.05
76-79s: K = 1.02
86-89s: K = 1.01
96-99s: K ~ 1.0
Amplitude
×10^4

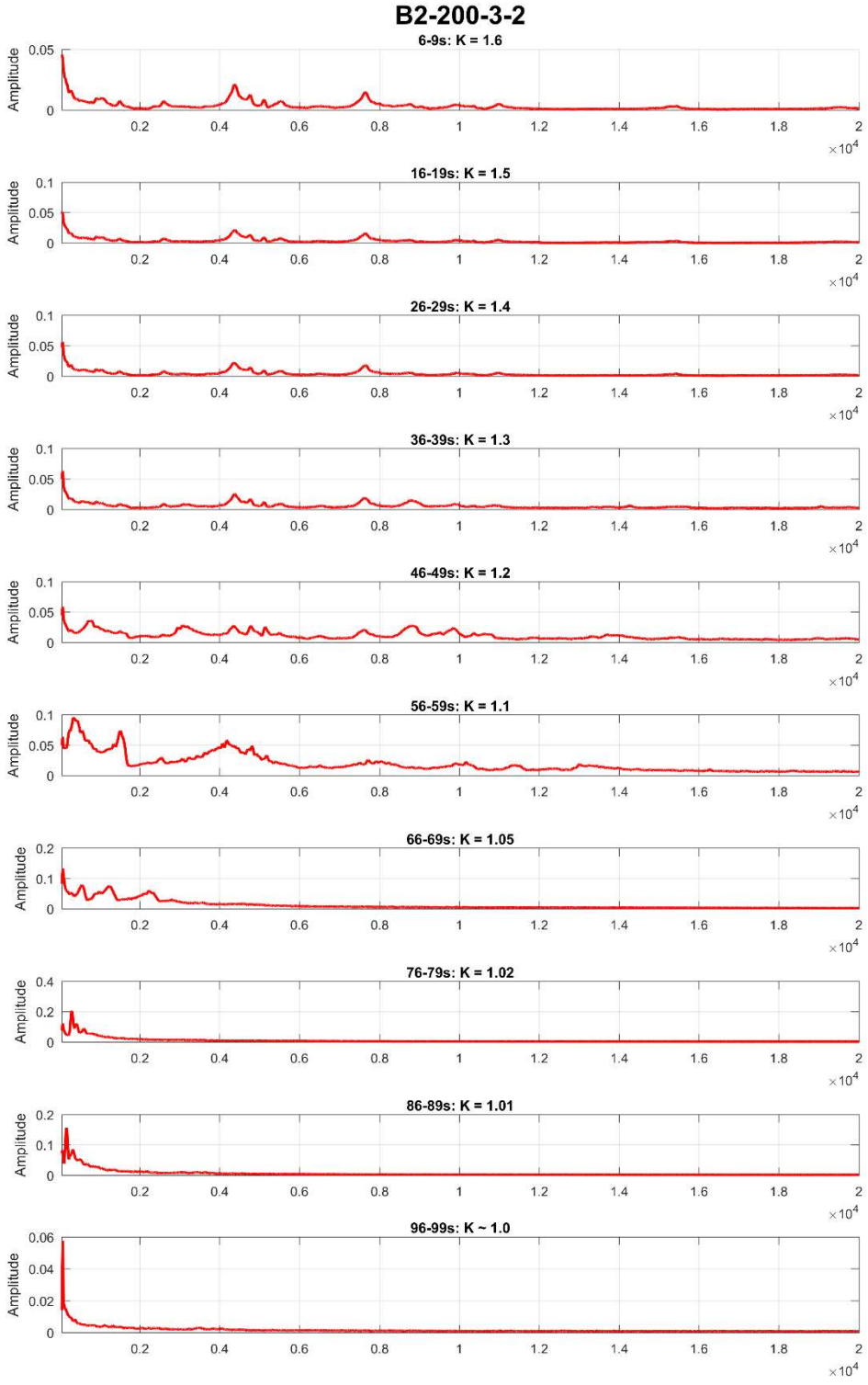
B2-200-3-2
6-9s: K = 1.6
16-19s: K = 1.5
26-29s: K = 1.4
36-39s: K = 1.3
46-49s: K = 1.2
56-59s: K = 1.1
66-69s: K = 1.05
76-79s: K = 1.02
86-89s: K = 1.01
96-99s: K ~ 1.0
Amplitude
×10^4

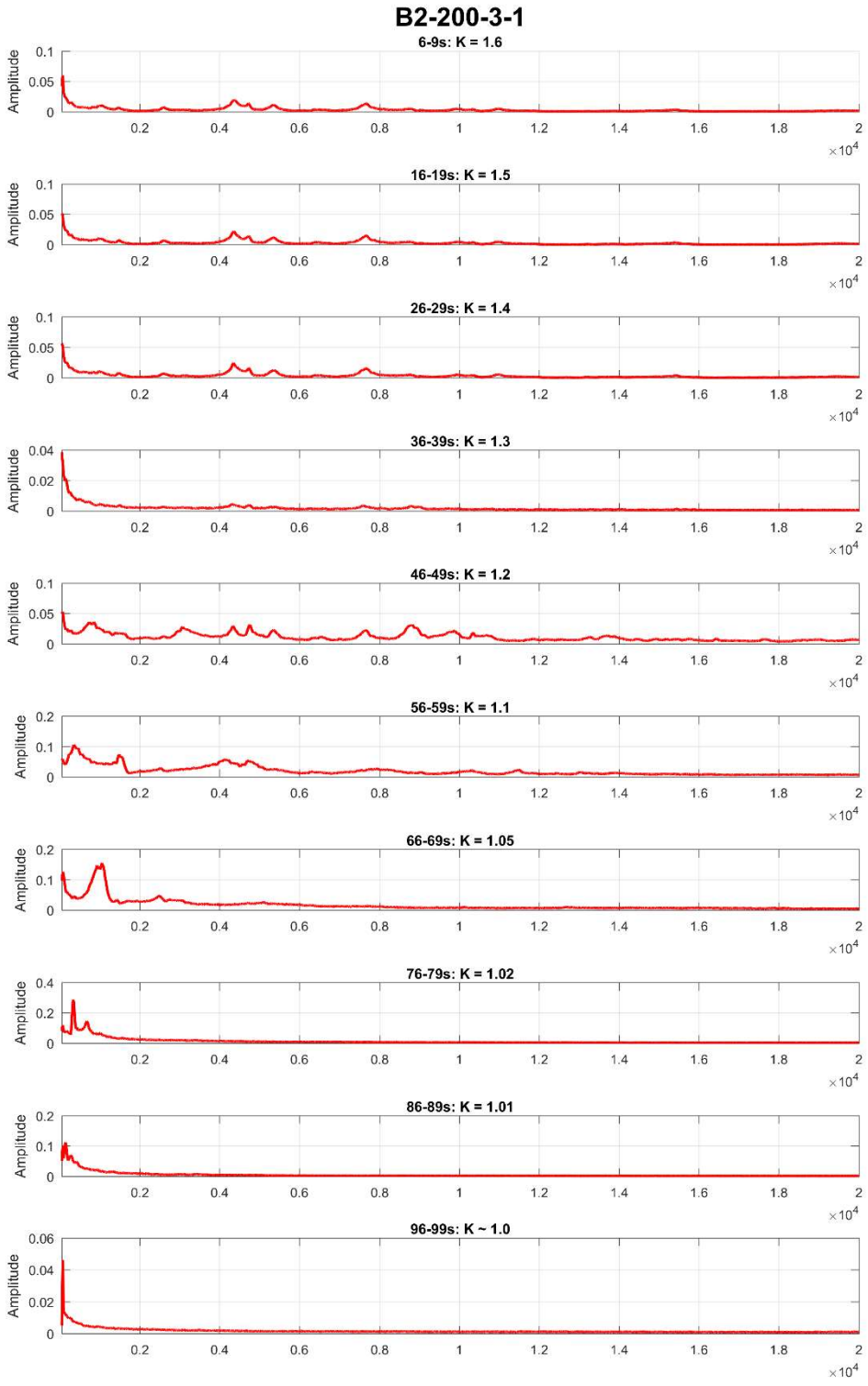
B2-200-3-1
6-9s: K = 1.6
16-19s: K = 1.5
26-29s: K = 1.4
36-39s: K = 1.3
46-49s: K = 1.2
56-59s: K = 1.1
66-69s: K = 1.05
76-79s: K = 1.02
86-89s: K = 1.01
96-99s: K ~ 1.0
Amplitude
×10^4

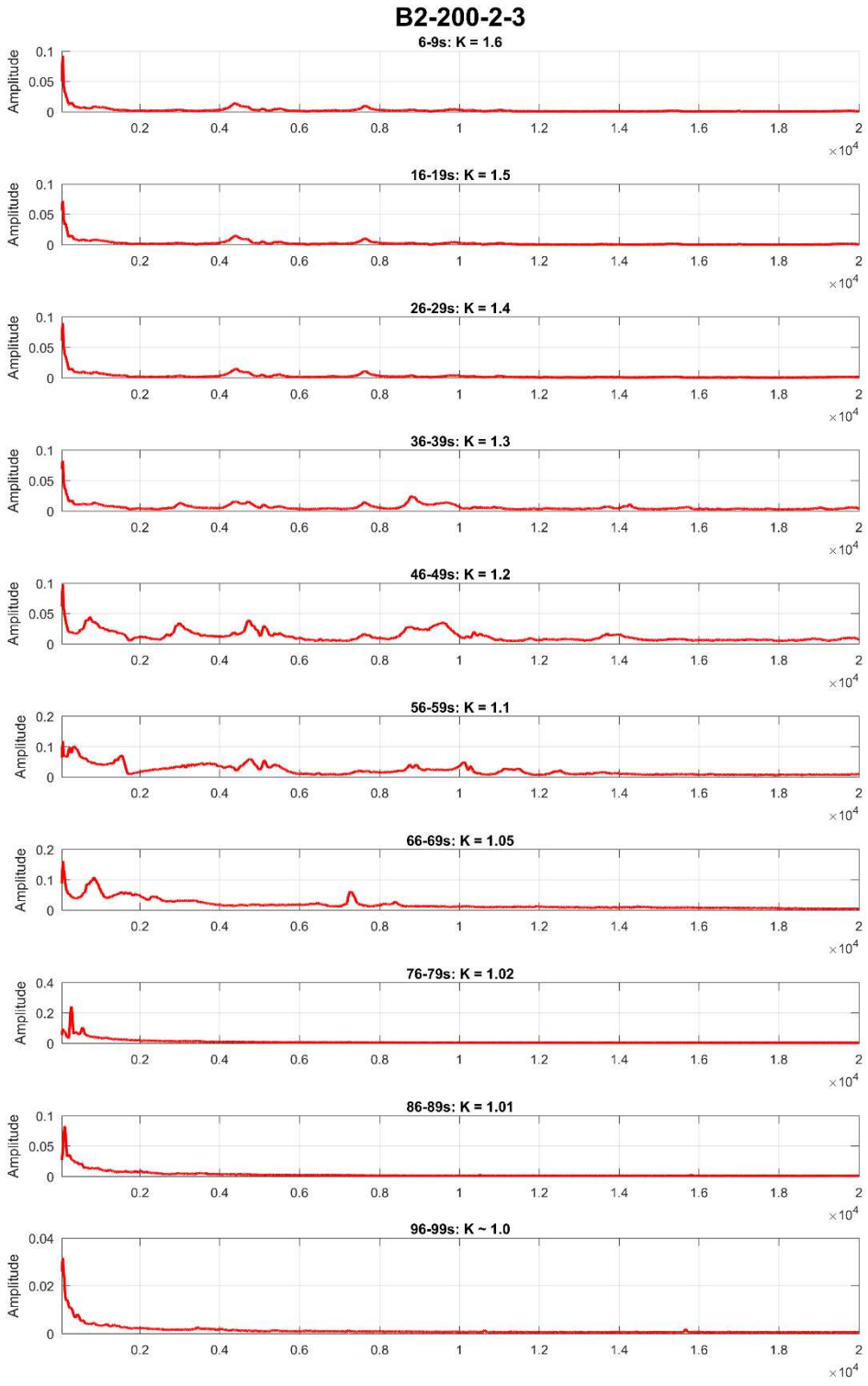
B2-200-2-3
6-9s: K = 1.6
16-19s: K = 1.5
26-29s: K = 1.4
36-39s: K = 1.3
46-49s: K = 1.2
56-59s: K = 1.1
66-69s: K = 1.05
76-79s: K = 1.02
86-89s: K = 1.01
96-99s: K ~ 1.0
Amplitude
×10^4

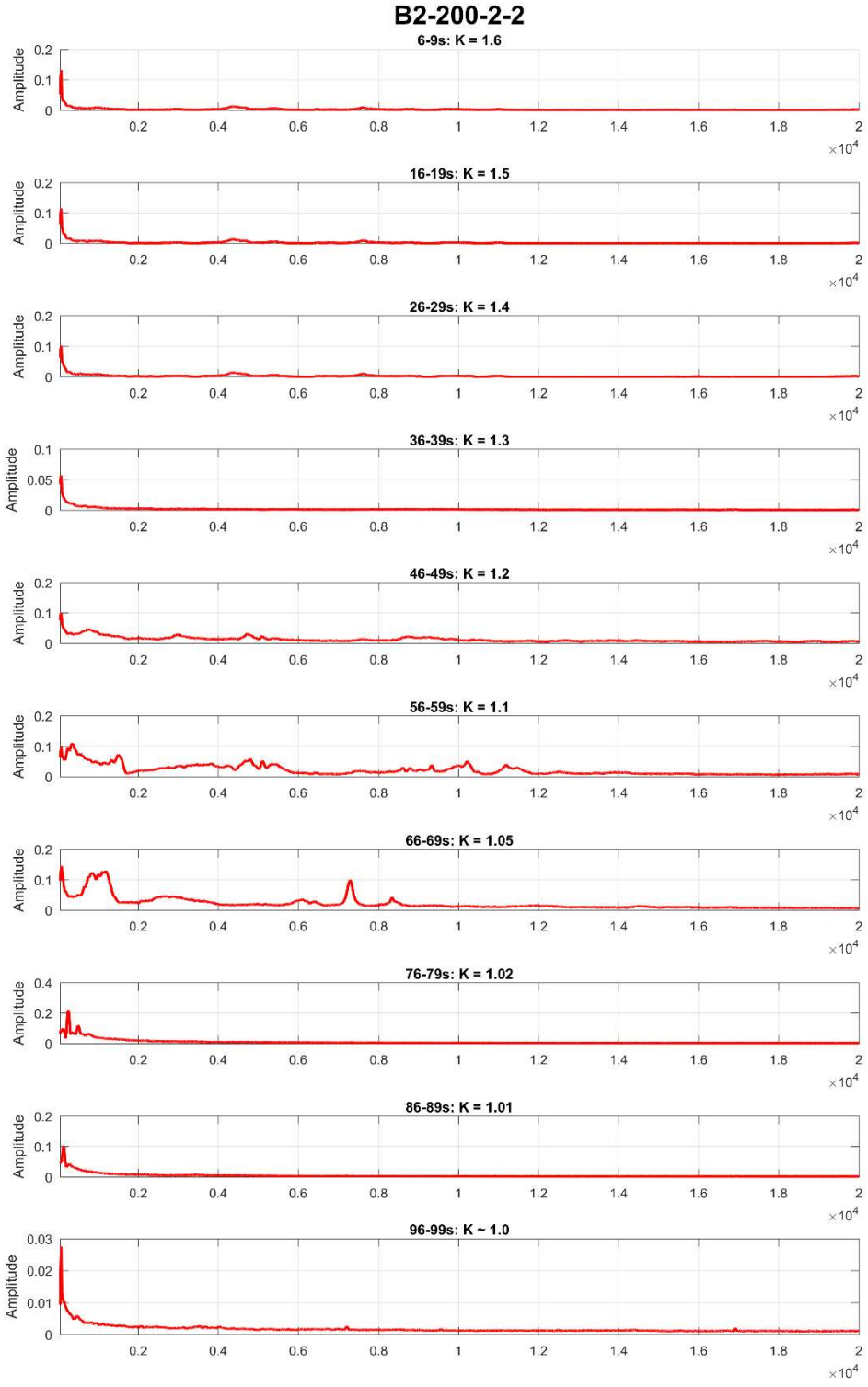
B2-200-2-2
6-9s: K = 1.6
16-19s: K = 1.5
26-29s: K = 1.4
36-39s: K = 1.3
46-49s: K = 1.2
56-59s: K = 1.1
66-69s: K = 1.05
76-79s: K = 1.02
86-89s: K = 1.01
96-99s: K ~ 1.0
Amplitude
×10^4

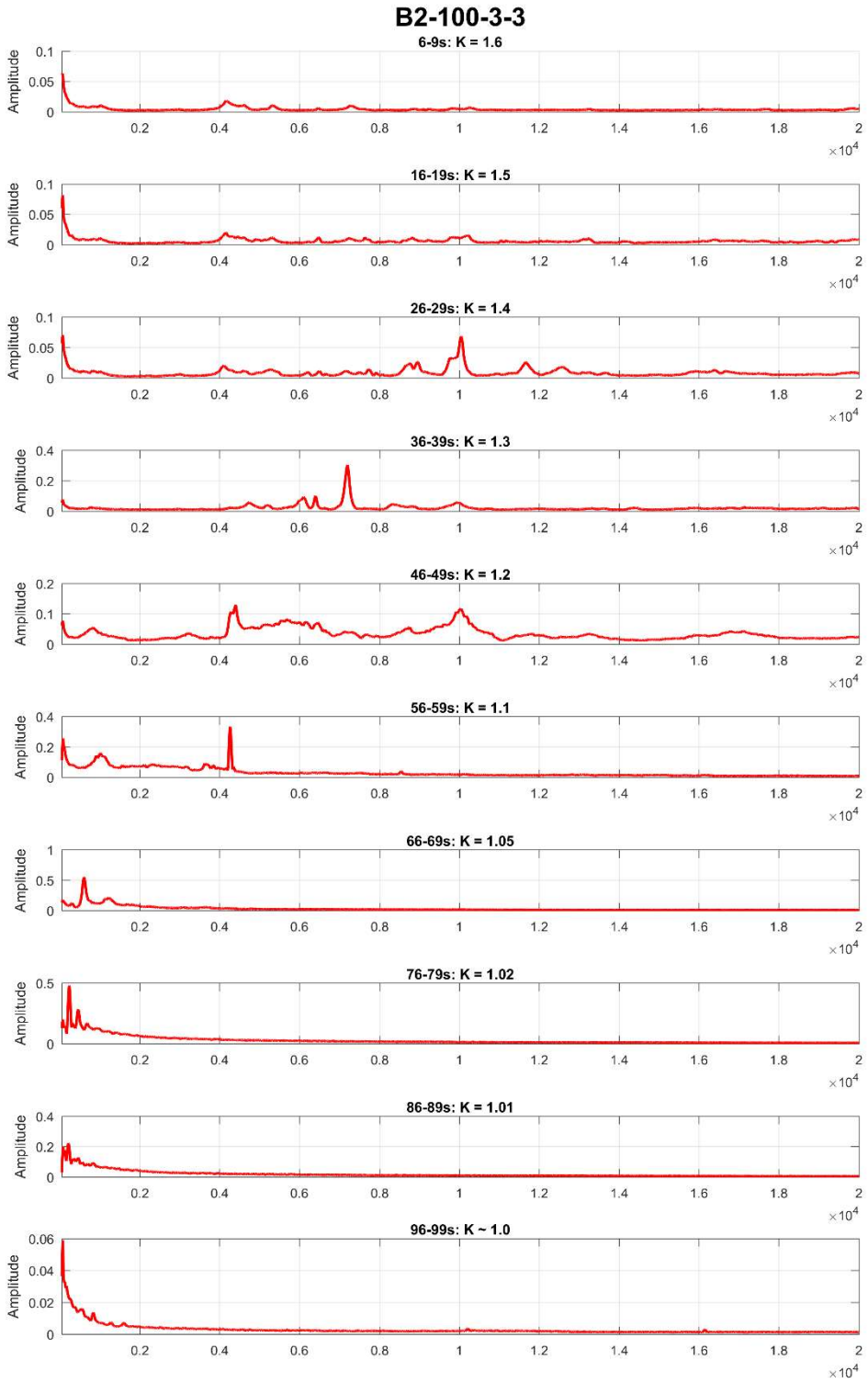
B2-100-3-3
6-9s: K = 1.6
16-19s: K = 1.5
26-29s: K = 1.4
36-39s: K = 1.3
46-49s: K = 1.2
56-59s: K = 1.1
66-69s: K = 1.05
76-79s: K = 1.02
86-89s: K = 1.01
96-99s: K ~ 1.0
Amplitude
×10^4

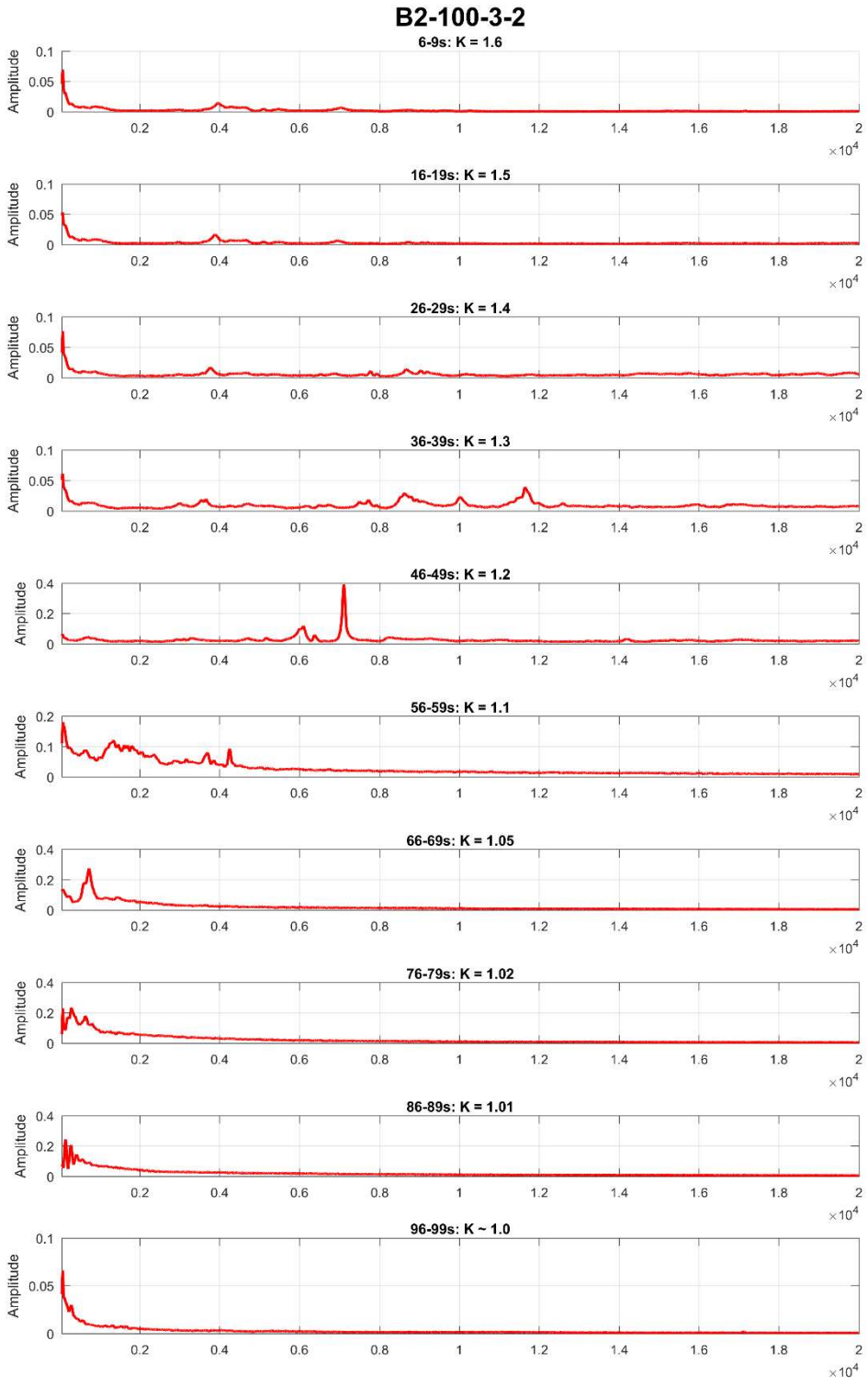
B2-100-3-2
6-9s: K = 1.6
16-19s: K = 1.5
26-29s: K = 1.4
36-39s: K = 1.3
46-49s: K = 1.2
56-59s: K = 1.1
66-69s: K = 1.05
76-79s: K = 1.02
86-89s: K = 1.01
96-99s: K ~ 1.0
Amplitude
×10^4

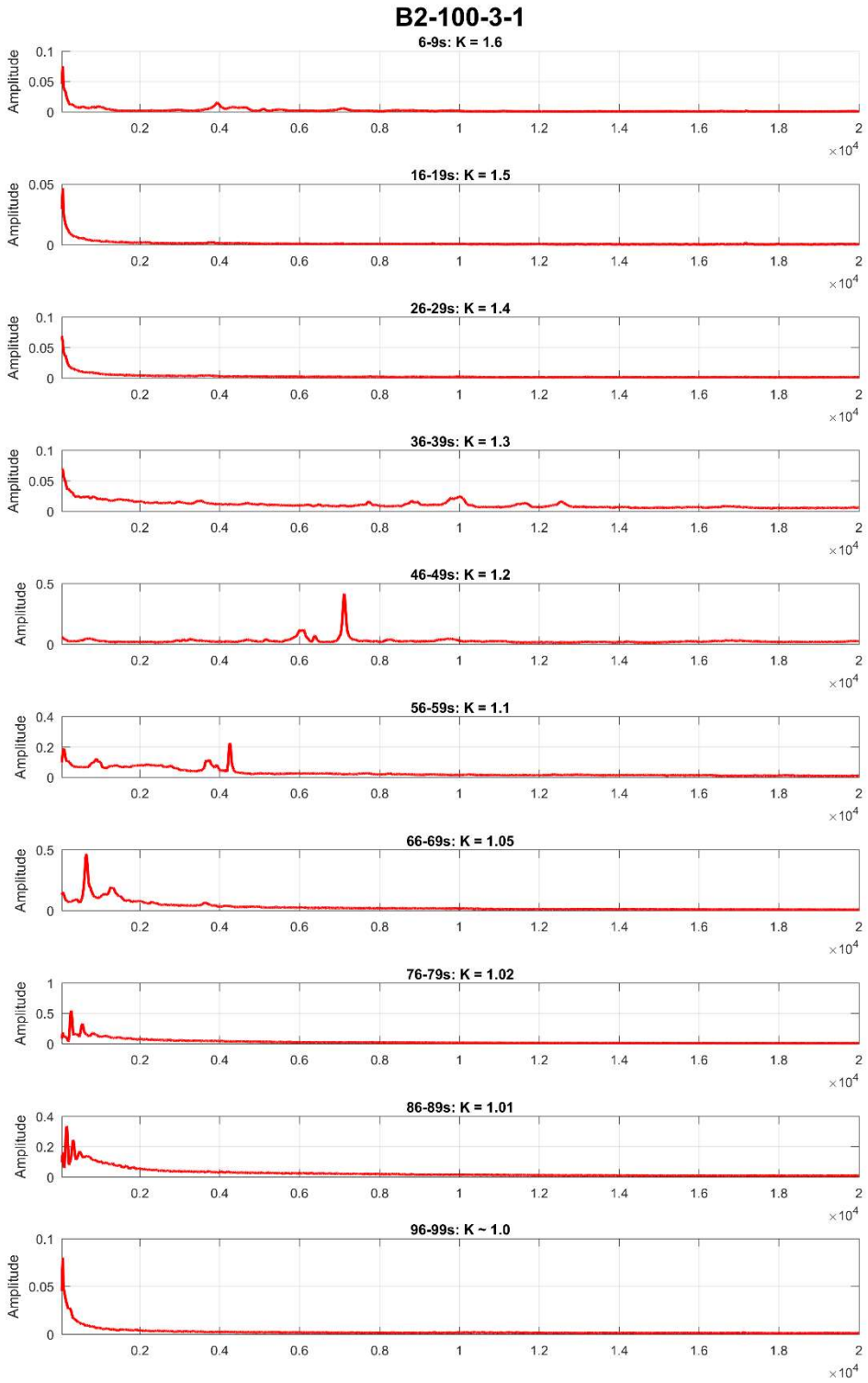
B2-100-3-1
6-9s: K = 1.6
16-19s: K = 1.5
26-29s: K = 1.4
36-39s: K = 1.3
46-49s: K = 1.2
56-59s: K = 1.1
66-69s: K = 1.05
76-79s: K = 1.02
86-89s: K = 1.01
96-99s: K ~ 1.0
Amplitude
×10^4

## Appendix F: Block 3 High Frequency Charts

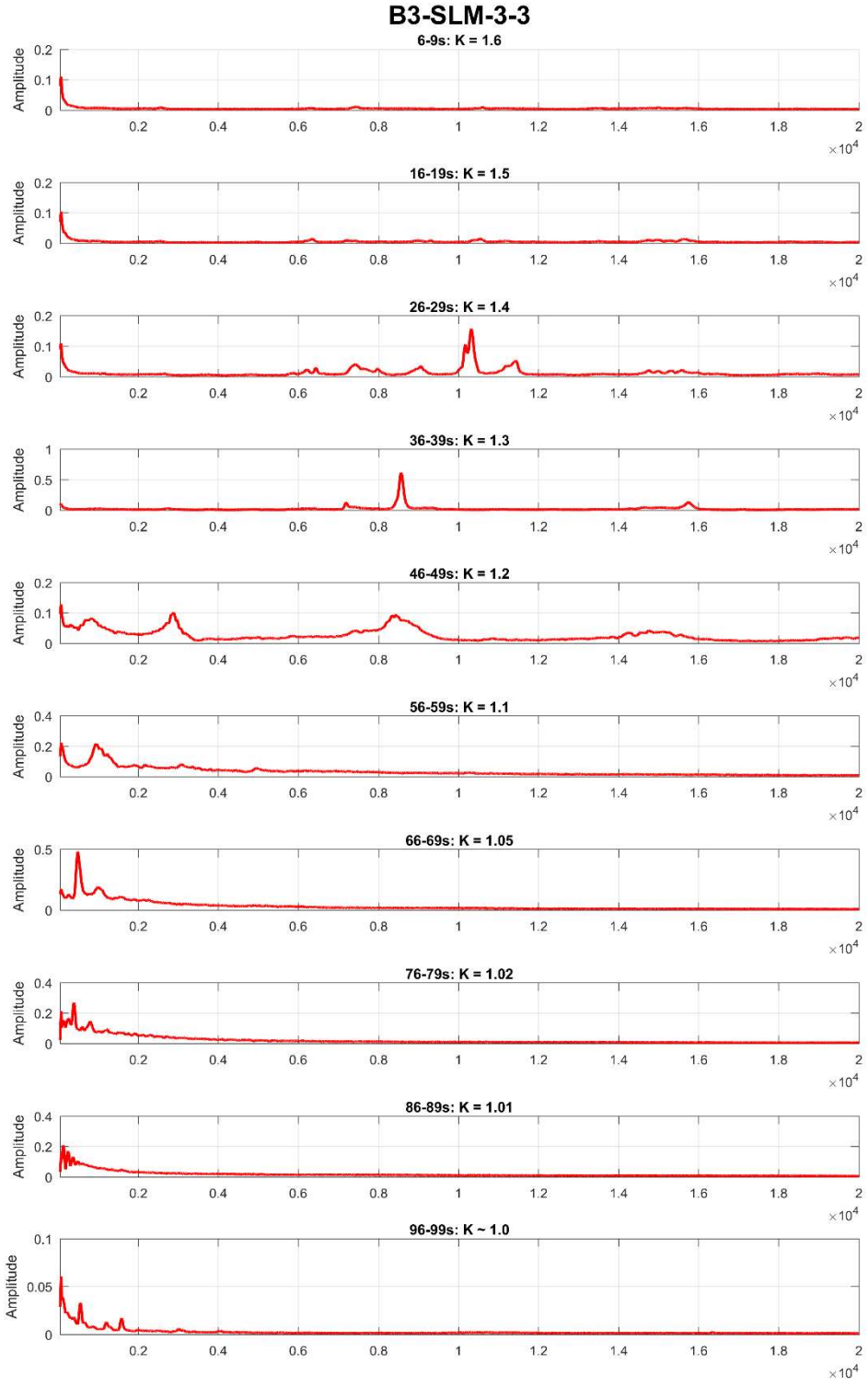
B3-SLM-3-3
6-9s: K = 1.6
16-19s: K = 1.5
26-29s: K = 1.4
36-39s: K = 1.3
46-49s: K = 1.2
56-59s: K = 1.1
66-69s: K = 1.05
76-79s: K = 1.02
86-89s: K = 1.01
96-99s: K ~ 1.0
Amplitude
×10^4

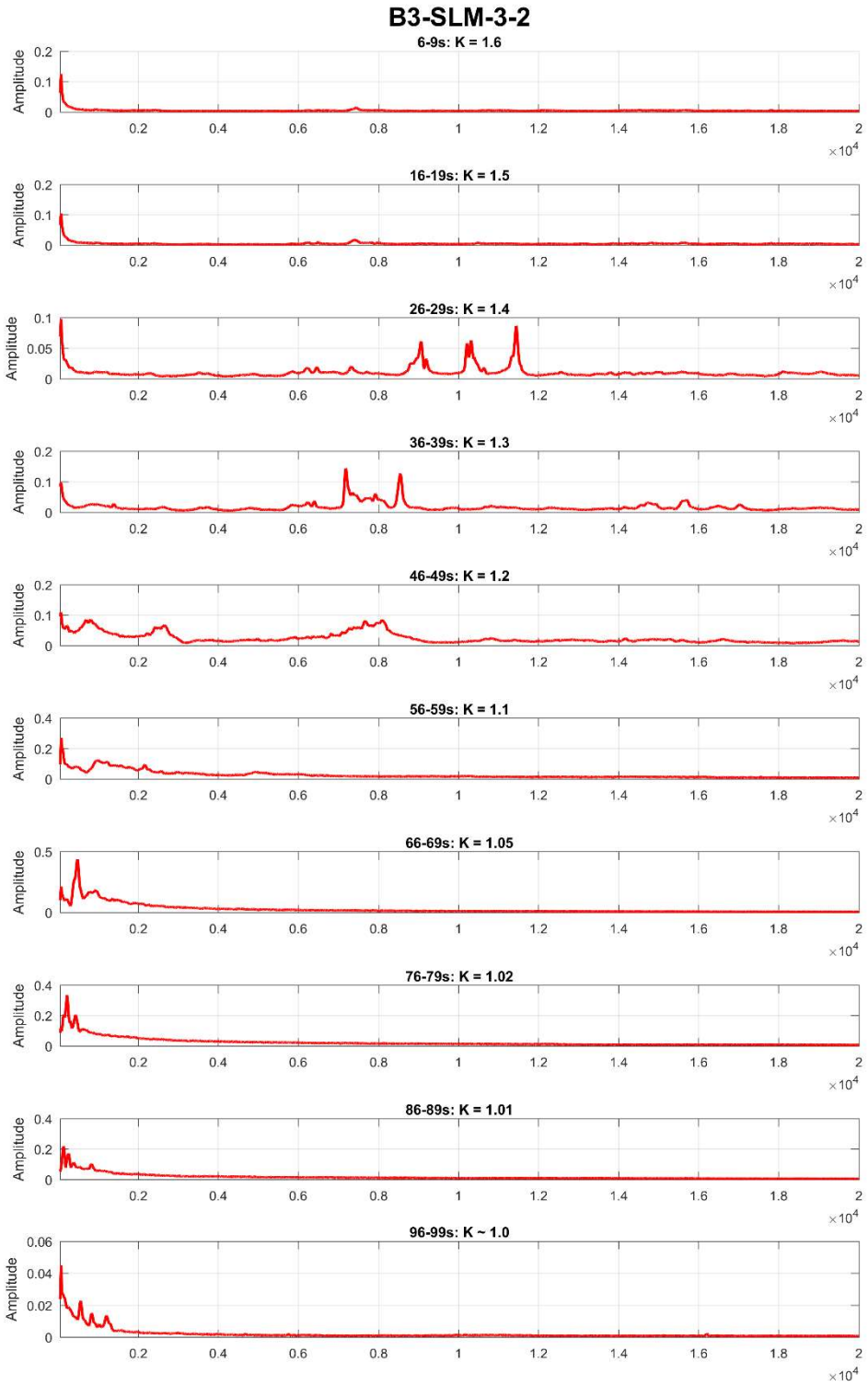
B3-SLM-3-2
6-9s: K = 1.6
16-19s: K = 1.5
26-29s: K = 1.4
36-39s: K = 1.3
46-49s: K = 1.2
56-59s: K = 1.1
66-69s: K = 1.05
76-79s: K = 1.02
86-89s: K = 1.01
96-99s: K ~ 1.0
Amplitude
×10^4

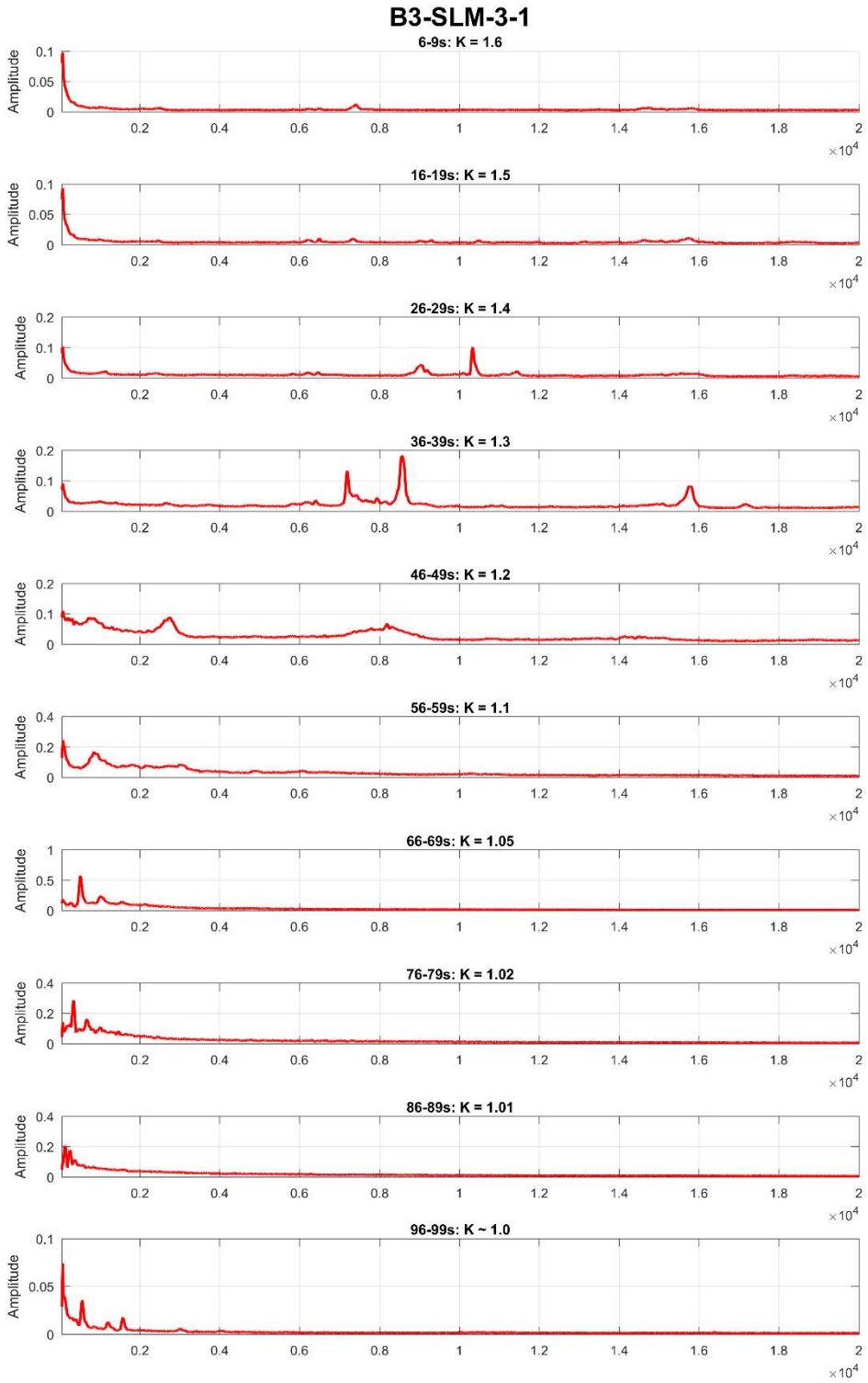
B3-SLM-3-1
6-9s: K = 1.6
16-19s: K = 1.5
26-29s: K = 1.4
36-39s: K = 1.3
46-49s: K = 1.2
56-59s: K = 1.1
66-69s: K = 1.05
76-79s: K = 1.02
86-89s: K = 1.01
96-99s: K ~ 1.0
Amplitude
×10^4

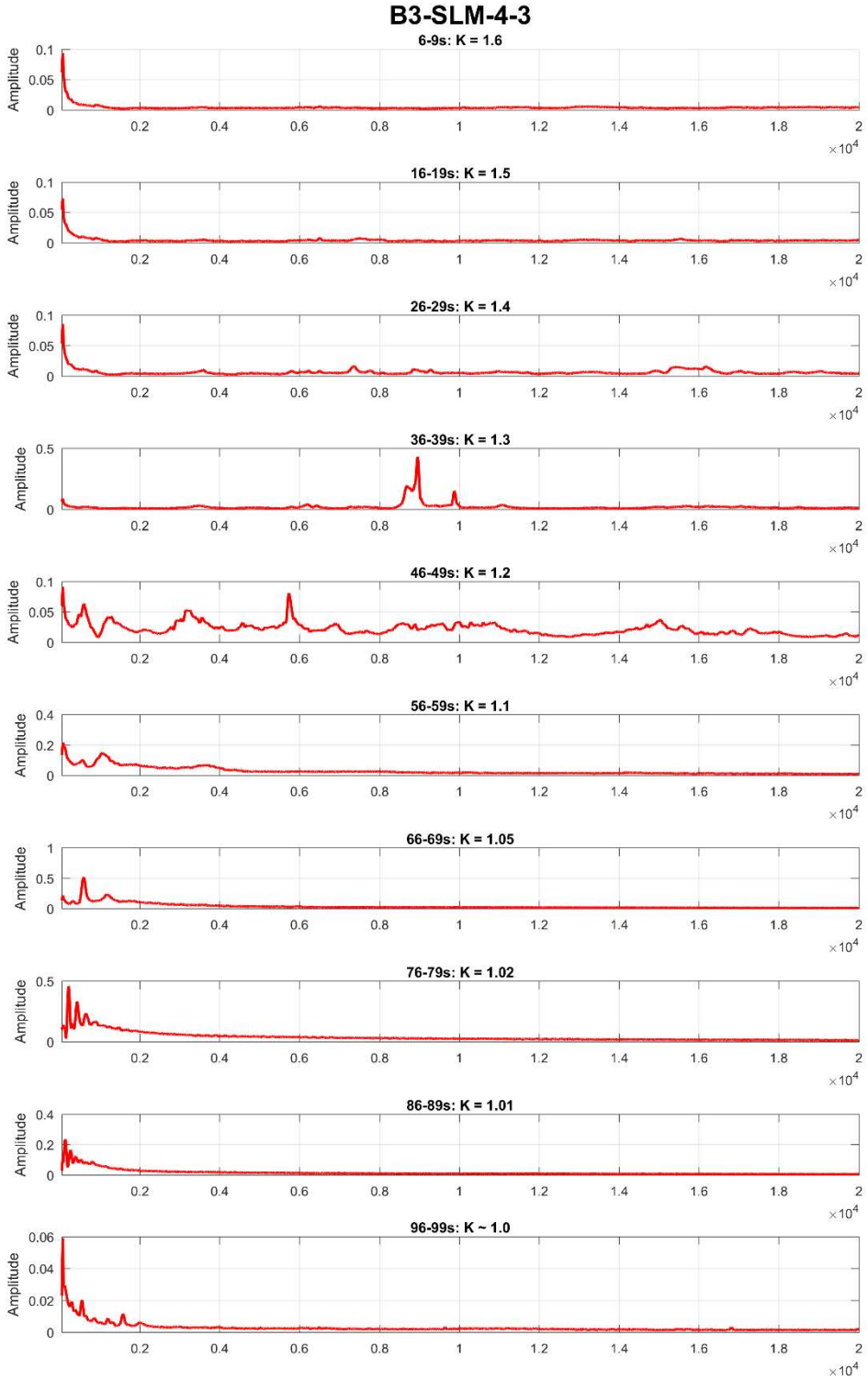
B3-SLM-4-3
6-9s: K = 1.6
16-19s: K = 1.5
26-29s: K = 1.4
36-39s: K = 1.3
46-49s: K = 1.2
56-59s: K = 1.1
66-69s: K = 1.05
76-79s: K = 1.02
86-89s: K = 1.01
96-99s: K ~ 1.0
Amplitude
×10^4

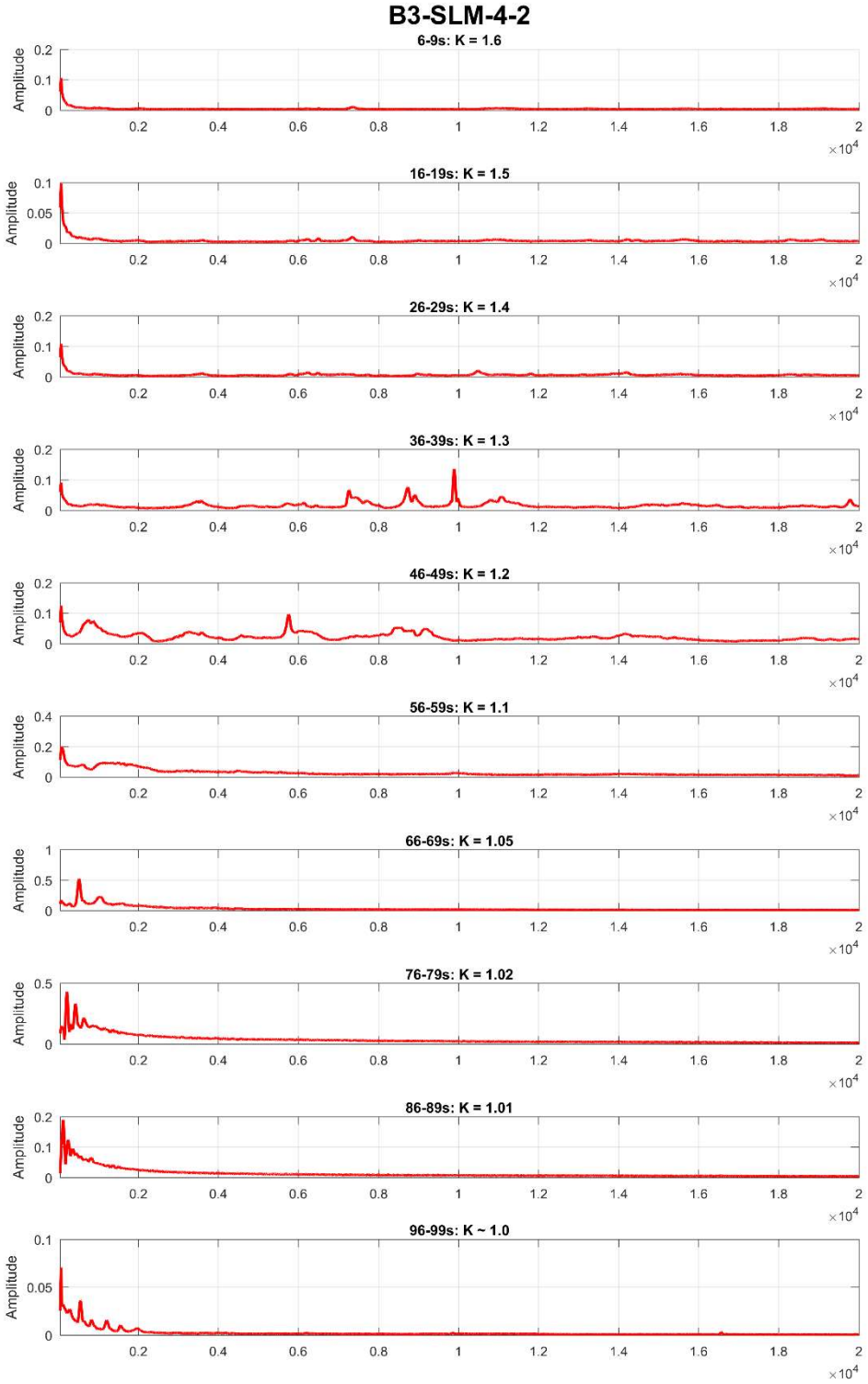
B3-SLM-4-2
6-9s: K = 1.6
16-19s: K = 1.5
26-29s: K = 1.4
36-39s: K = 1.3
46-49s: K = 1.2
56-59s: K = 1.1
66-69s: K = 1.05
76-79s: K = 1.02
86-89s: K = 1.01
96-99s: K ~ 1.0
Amplitude
×10^4

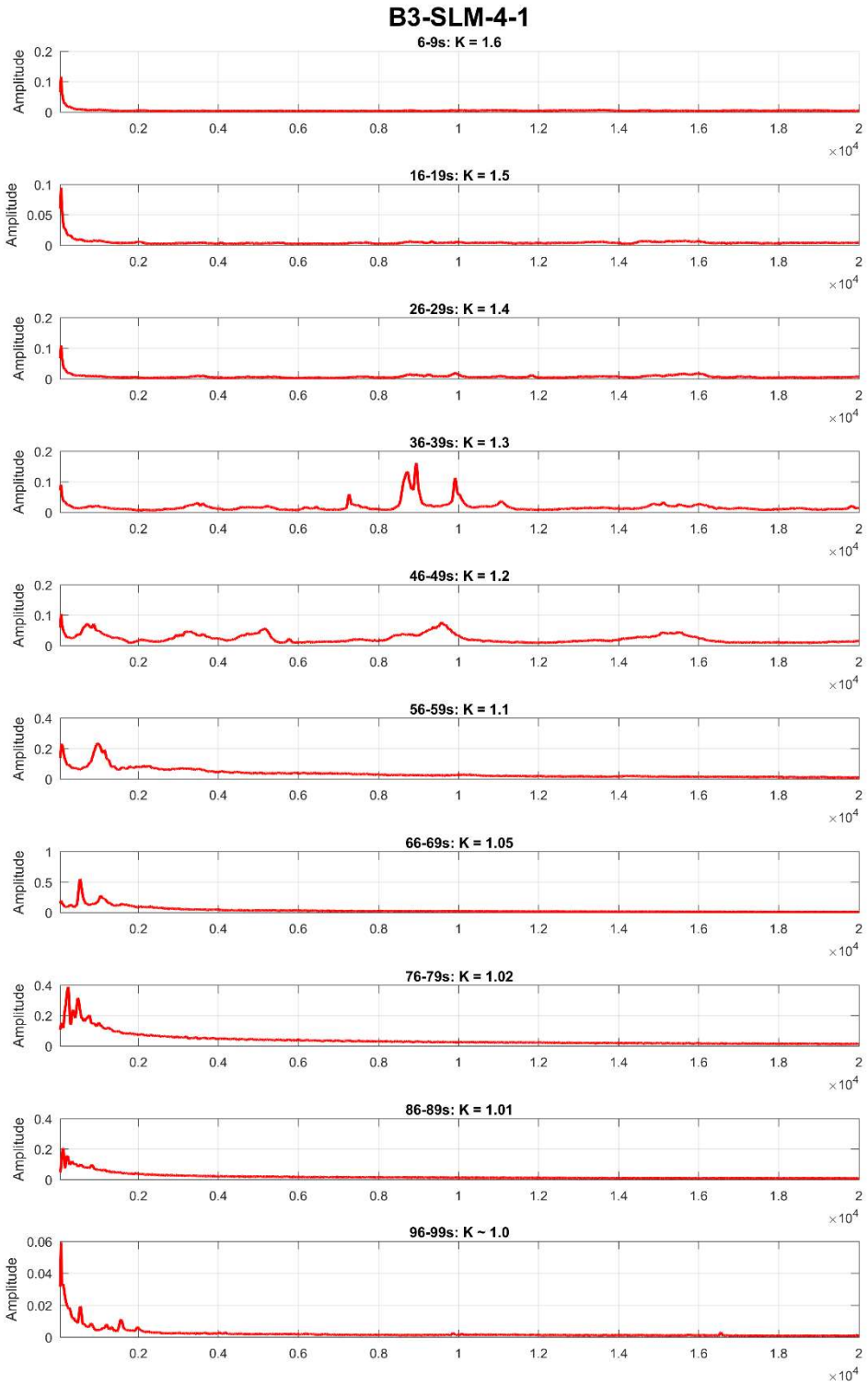
B3-SLM-4-1
6-9s: K = 1.6
16-19s: K = 1.5
26-29s: K = 1.4
36-39s: K = 1.3
46-49s: K = 1.2
56-59s: K = 1.1
66-69s: K = 1.05
76-79s: K = 1.02
86-89s: K = 1.01
96-99s: K ~ 1.0
Amplitude
×10^4

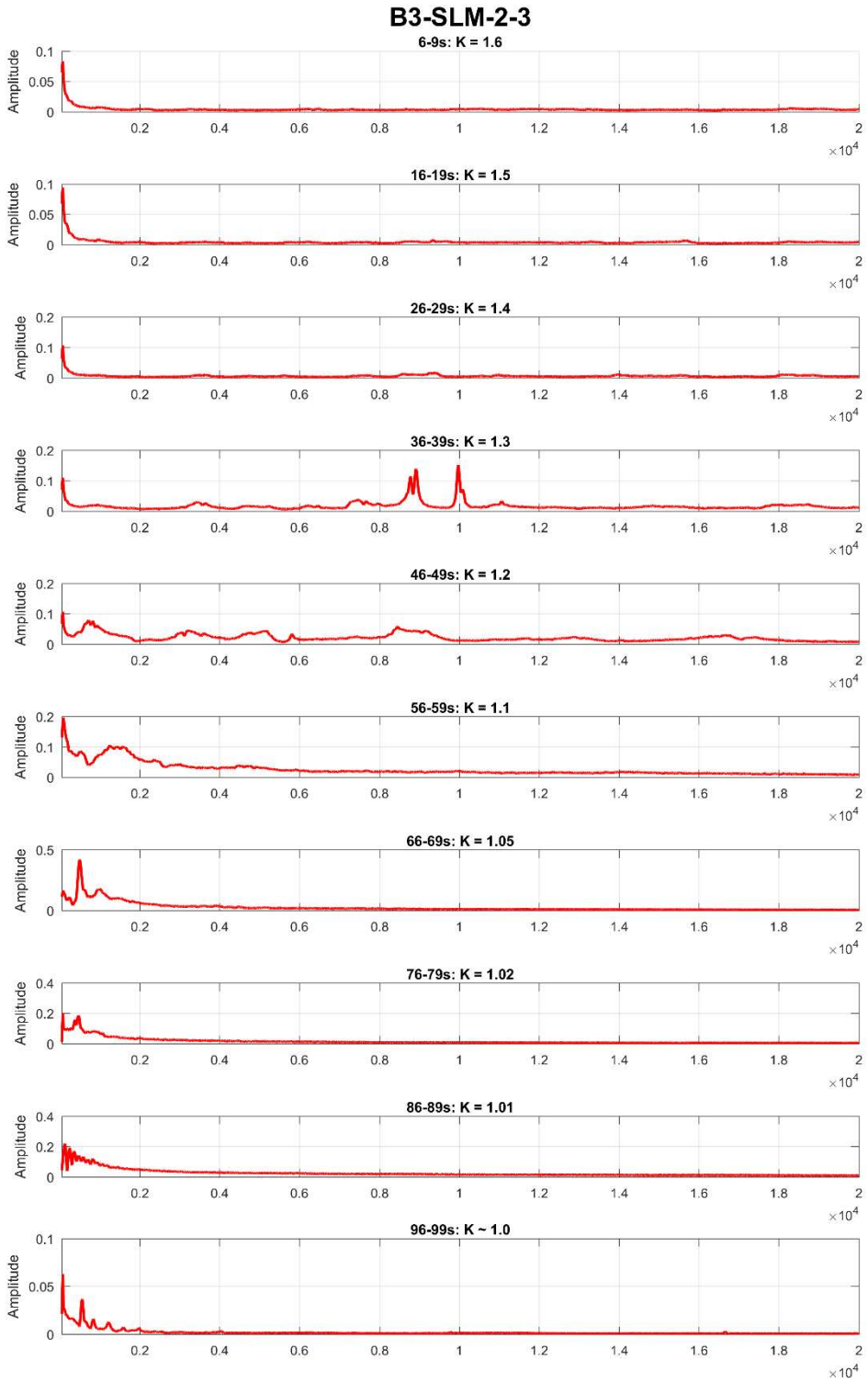
B3-SLM-2-3
6-9s: K = 1.6
16-19s: K = 1.5
26-29s: K = 1.4
36-39s: K = 1.3
46-49s: K = 1.2
56-59s: K = 1.1
66-69s: K = 1.05
76-79s: K = 1.02
86-89s: K = 1.01
96-99s: K ~ 1.0
Amplitude
×10^4

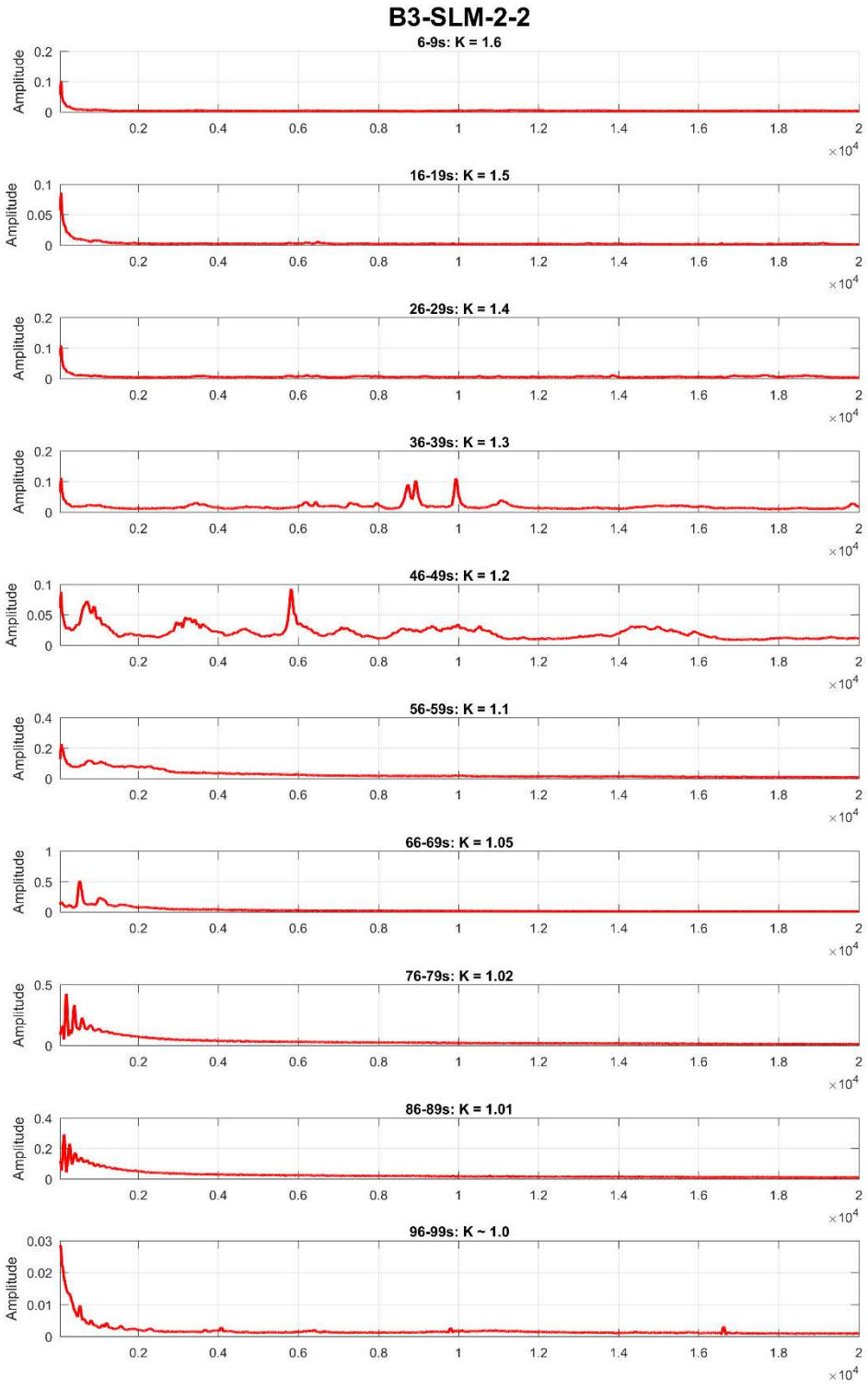
B3-SLM-2-2
6-9s: K = 1.6
16-19s: K = 1.5
26-29s: K = 1.4
36-39s: K = 1.3
46-49s: K = 1.2
56-59s: K = 1.1
66-69s: K = 1.05
76-79s: K = 1.02
86-89s: K = 1.01
96-99s: K ~ 1.0
Amplitude
×10^4

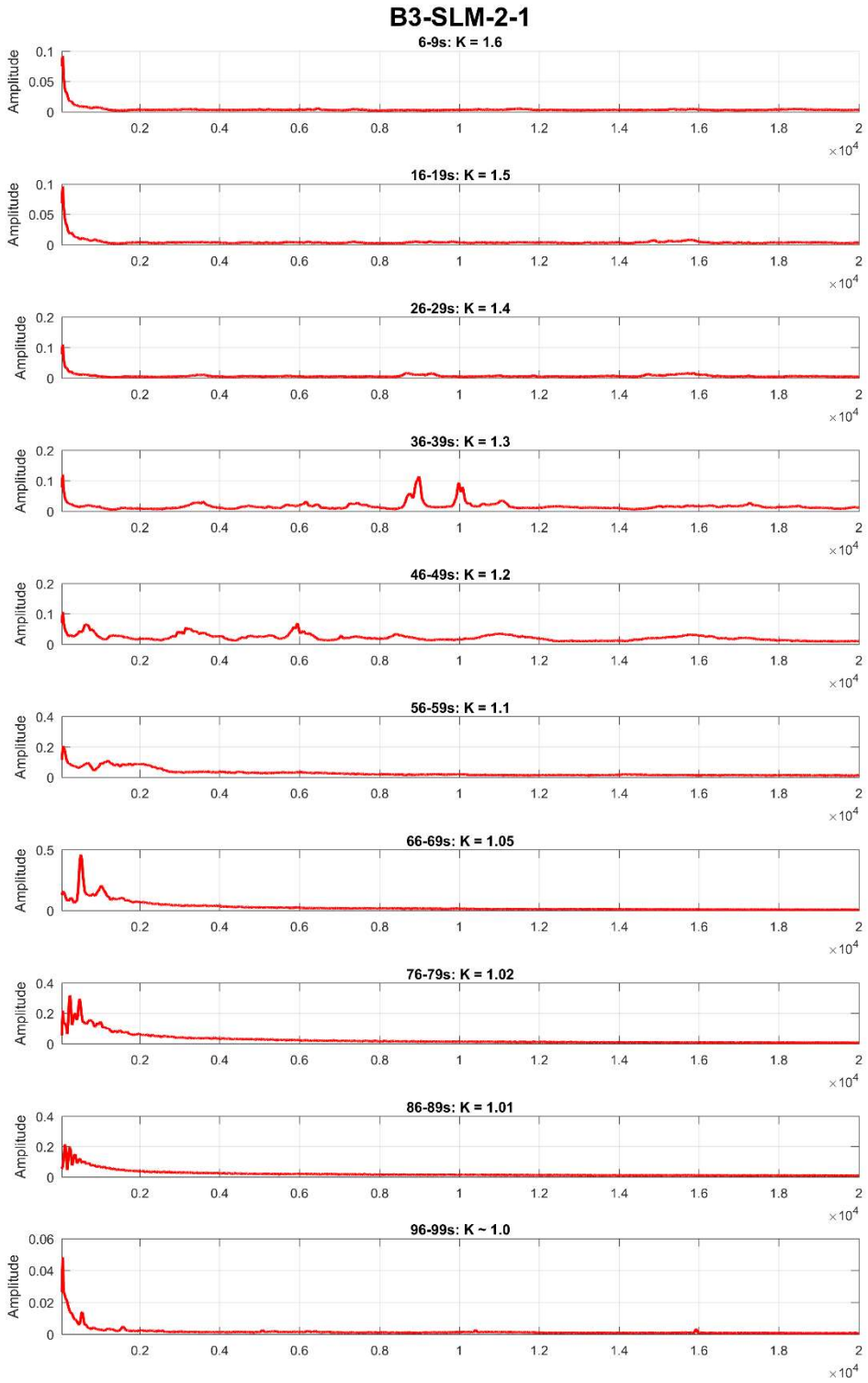
B3-SLM-2-1
6-9s: K = 1.6
16-19s: K = 1.5
26-29s: K = 1.4
36-39s: K = 1.3
46-49s: K = 1.2
56-59s: K = 1.1
66-69s: K = 1.05
76-79s: K = 1.02
86-89s: K = 1.01
96-99s: K ~ 1.0
Amplitude
×10^4

## Appendix G: Block 5 High Frequency Charts

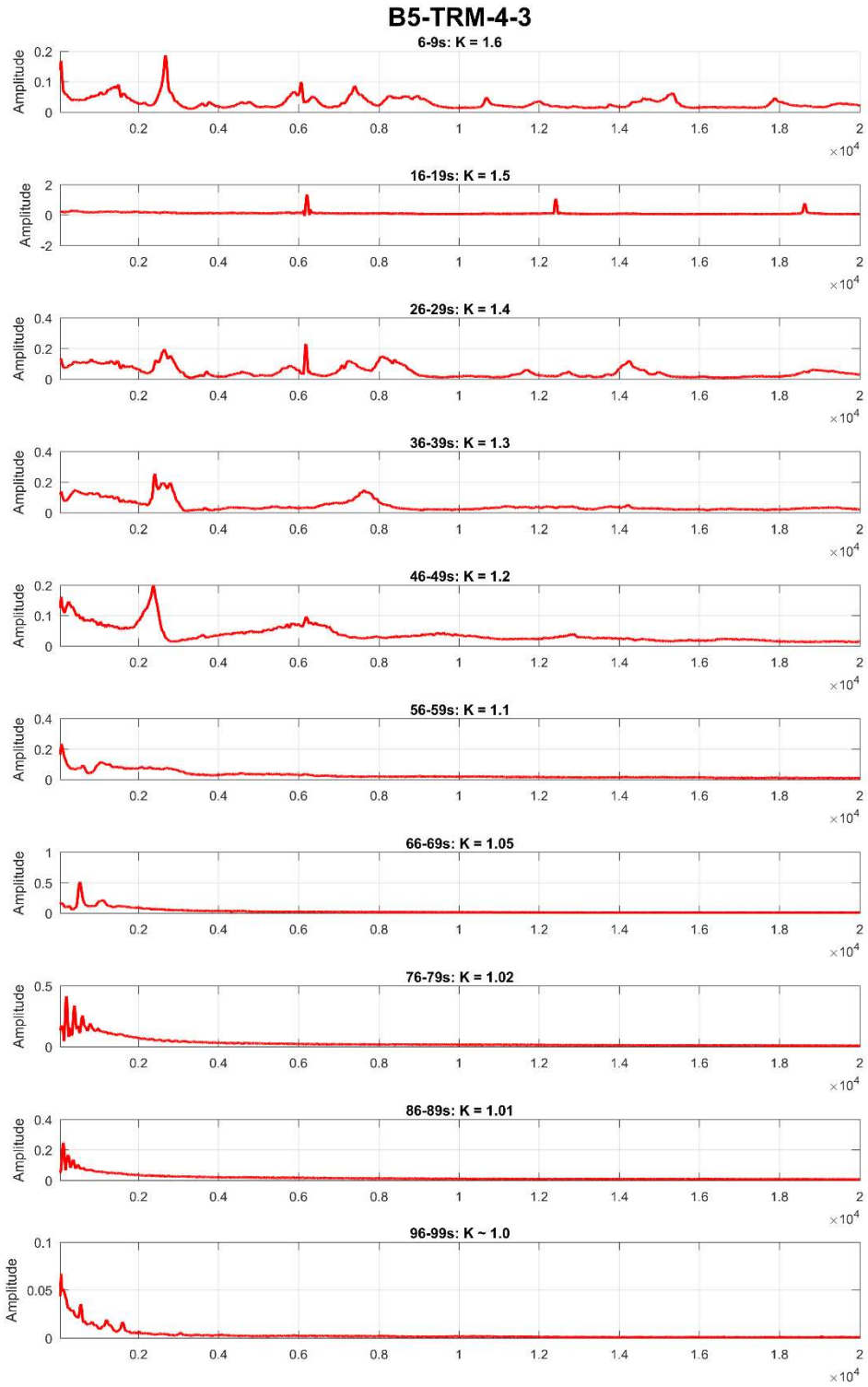
B5-TRM-4-3
6-9s: K = 1.6
16-19s: K = 1.5
26-29s: K = 1.4
36-39s: K = 1.3
46-49s: K = 1.2
56-59s: K = 1.1
66-69s: K = 1.05
76-79s: K = 1.02
86-89s: K = 1.01
96-99s: K ~ 1.0
Amplitude
×10^4

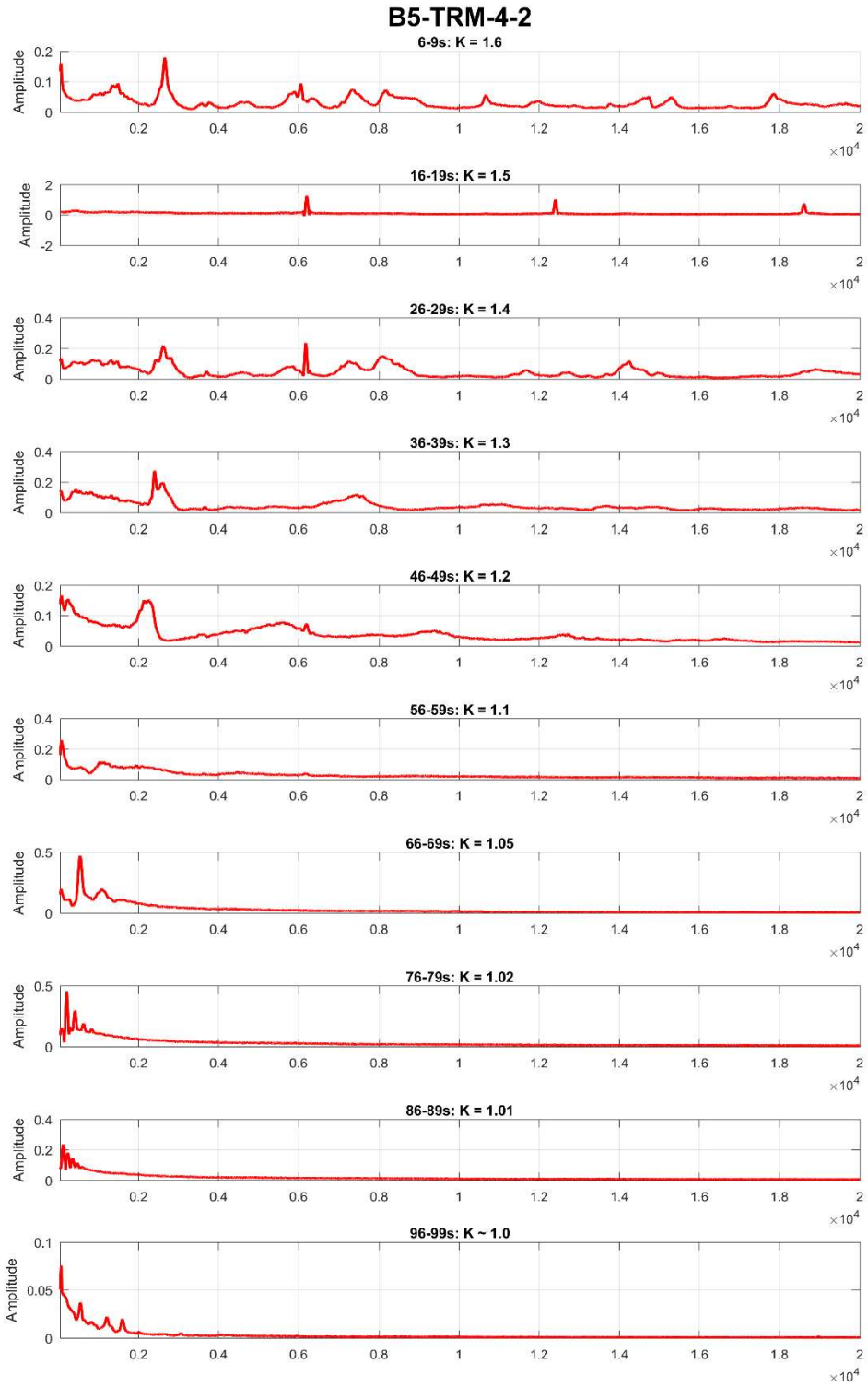
B5-TRM-4-2
6-9s: K = 1.6
16-19s: K = 1.5
26-29s: K = 1.4
36-39s: K = 1.3
46-49s: K = 1.2
56-59s: K = 1.1
66-69s: K = 1.05
76-79s: K = 1.02
86-89s: K = 1.01
96-99s: K ~ 1.0
Amplitude
×10^4

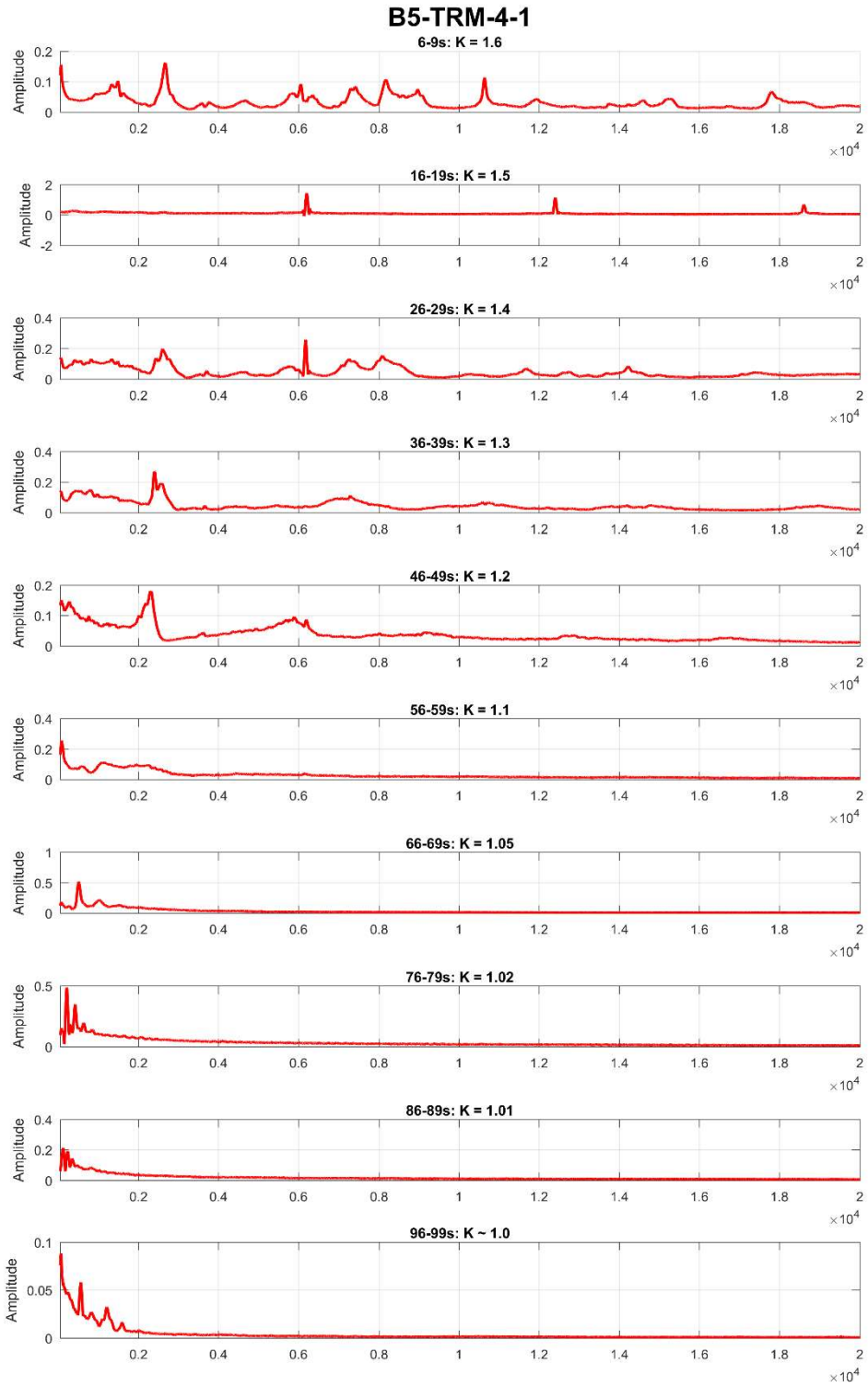
B5-TRM-4-1
6-9s: K = 1.6
16-19s: K = 1.5
26-29s: K = 1.4
36-39s: K = 1.3
46-49s: K = 1.2
56-59s: K = 1.1
66-69s: K = 1.05
76-79s: K = 1.02
86-89s: K = 1.01
96-99s: K ~ 1.0
Amplitude
×10^4

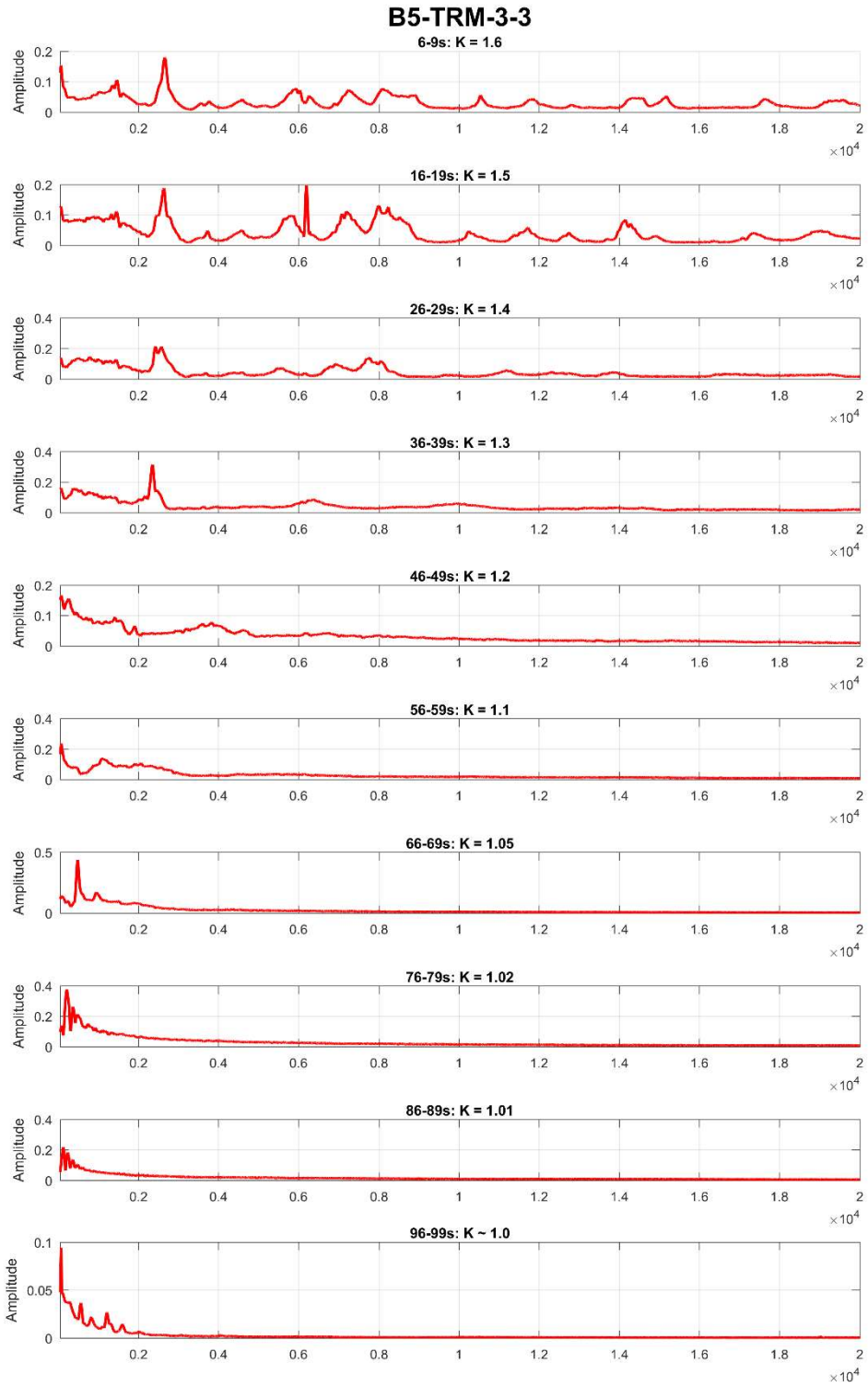
B5-TRM-3-3
6-9s: K = 1.6
16-19s: K = 1.5
26-29s: K = 1.4
36-39s: K = 1.3
46-49s: K = 1.2
56-59s: K = 1.1
66-69s: K = 1.05
76-79s: K = 1.02
86-89s: K = 1.01
96-99s: K ~ 1.0
Amplitude
×10^4

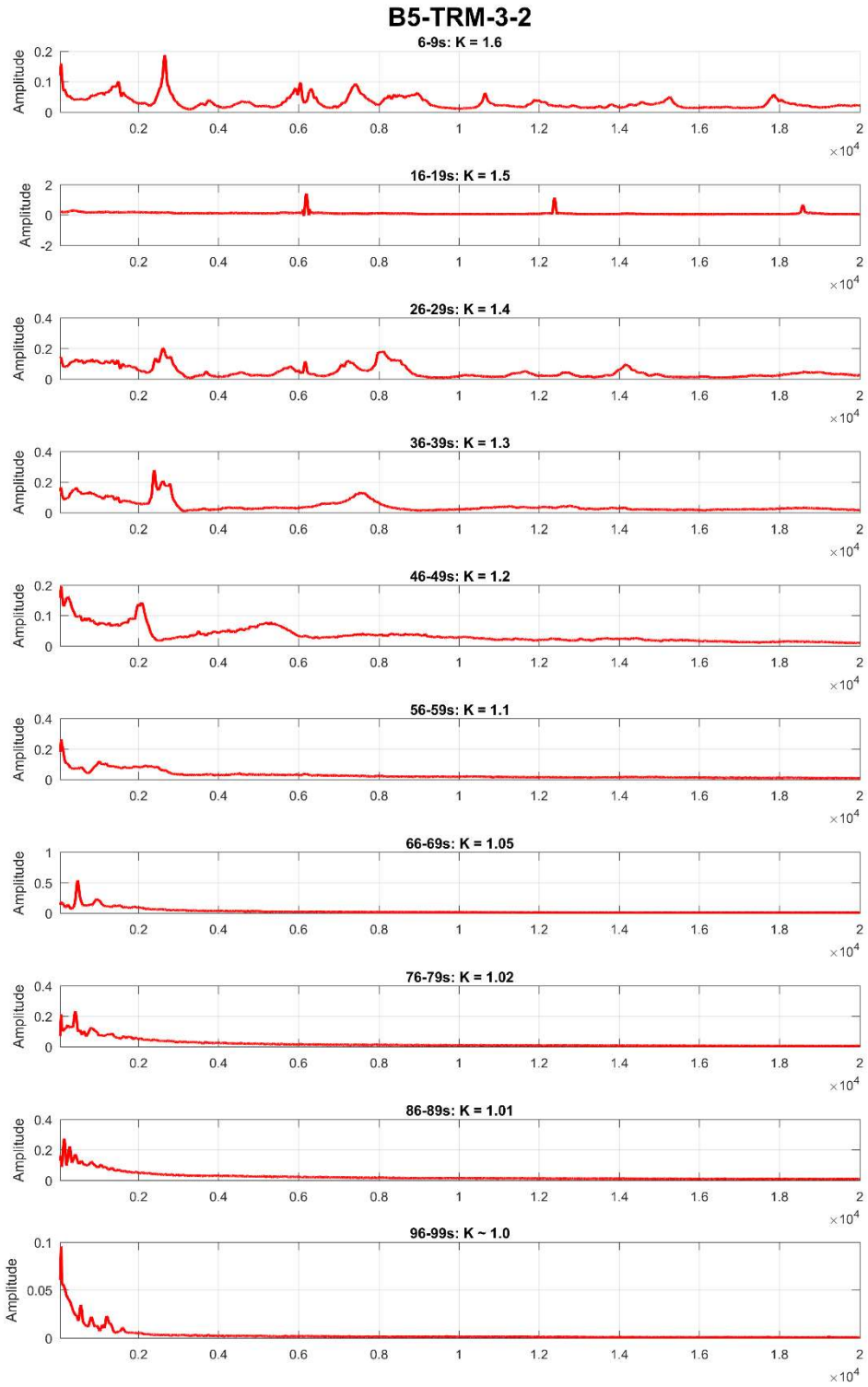
B5-TRM-3-2
6-9s: K = 1.6
16-19s: K = 1.5
26-29s: K = 1.4
36-39s: K = 1.3
46-49s: K = 1.2
56-59s: K = 1.1
66-69s: K = 1.05
76-79s: K = 1.02
86-89s: K = 1.01
96-99s: K ~ 1.0
Amplitude
×10^4

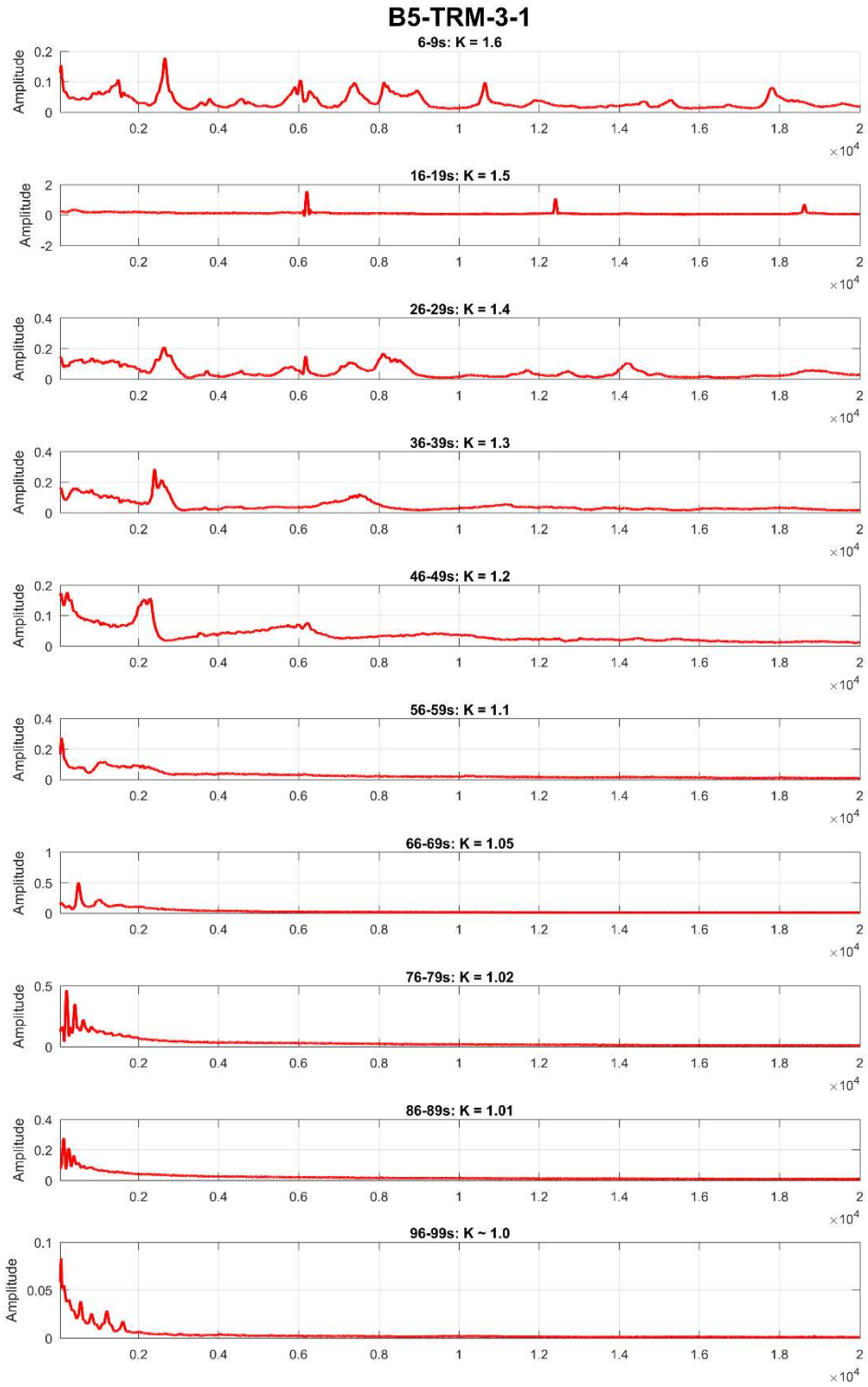
B5-TRM-3-1
6-9s: K = 1.6
16-19s: K = 1.5
26-29s: K = 1.4
36-39s: K = 1.3
46-49s: K = 1.2
56-59s: K = 1.1
66-69s: K = 1.05
76-79s: K = 1.02
86-89s: K = 1.01
96-99s: K ~ 1.0
Amplitude
×10^4

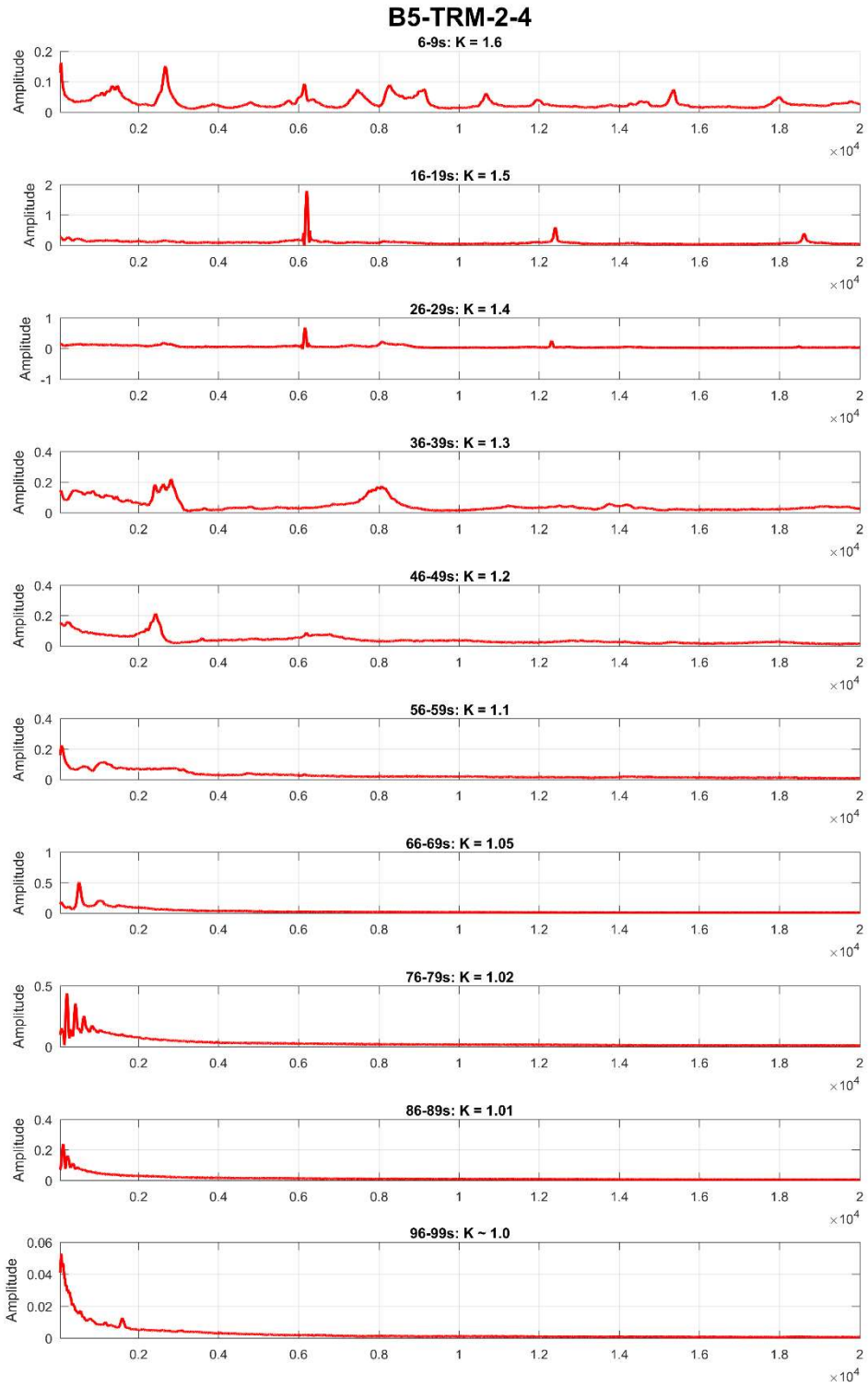
B5-TRM-2-4
6-9s: K = 1.6
16-19s: K = 1.5
26-29s: K = 1.4
36-39s: K = 1.3
46-49s: K = 1.2
56-59s: K = 1.1
66-69s: K = 1.05
76-79s: K = 1.02
86-89s: K = 1.01
96-99s: K ~ 1.0
Amplitude
×10^4

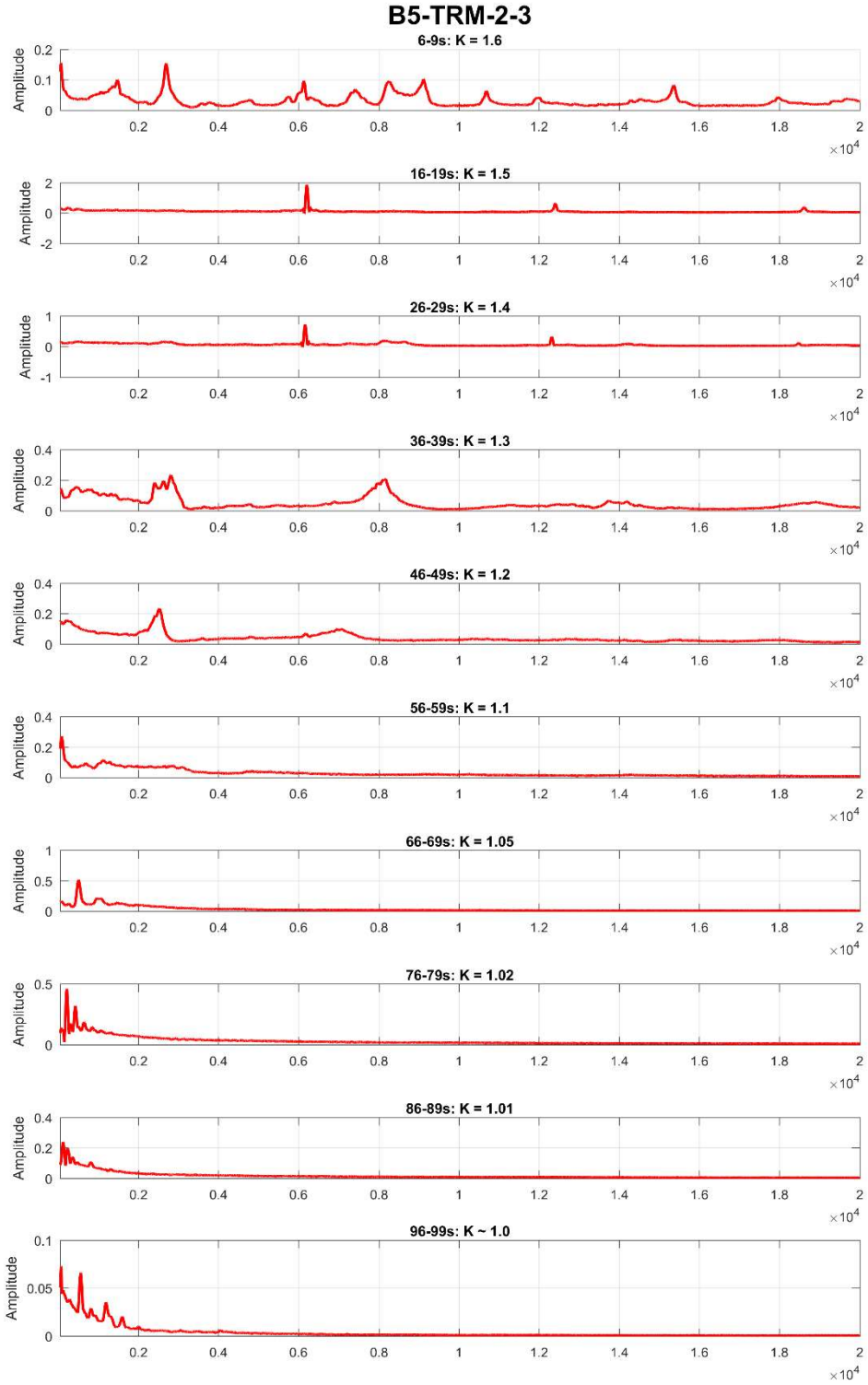
B5-TRM-2-3
6-9s: K = 1.6
16-19s: K = 1.5
26-29s: K = 1.4
36-39s: K = 1.3
46-49s: K = 1.2
56-59s: K = 1.1
66-69s: K = 1.05
76-79s: K = 1.02
86-89s: K = 1.01
96-99s: K ~ 1.0
Amplitude
×10^4

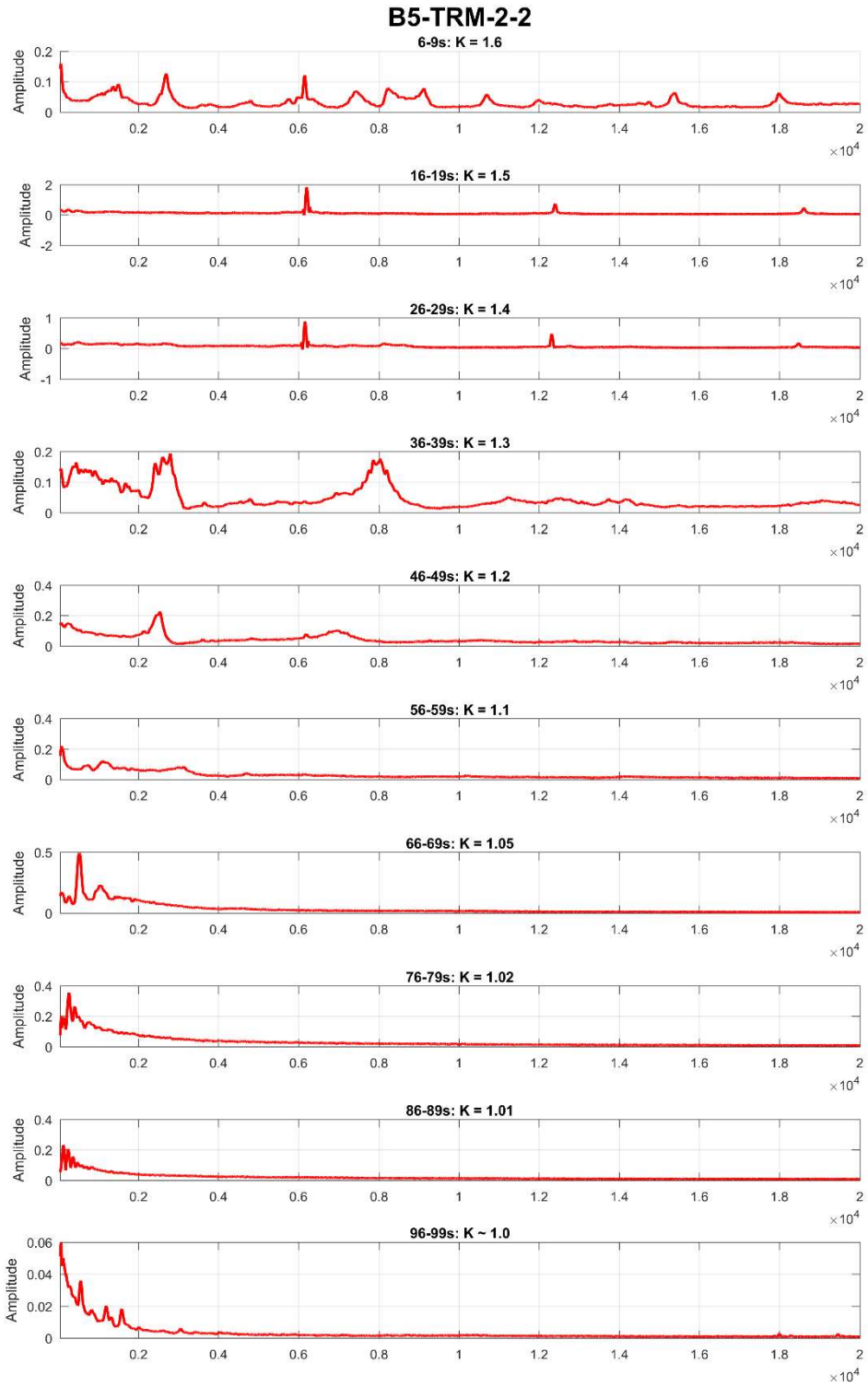
B5-TRM-2-2
6-9s: K = 1.6
16-19s: K = 1.5
26-29s: K = 1.4
36-39s: K = 1.3
46-49s: K = 1.2
56-59s: K = 1.1
66-69s: K = 1.05
76-79s: K = 1.02
86-89s: K = 1.01
96-99s: K ~ 1.0
Amplitude
×10^4

# Appendix H: Cavitation Test Setup Plumbing & Instrumentation Diagram

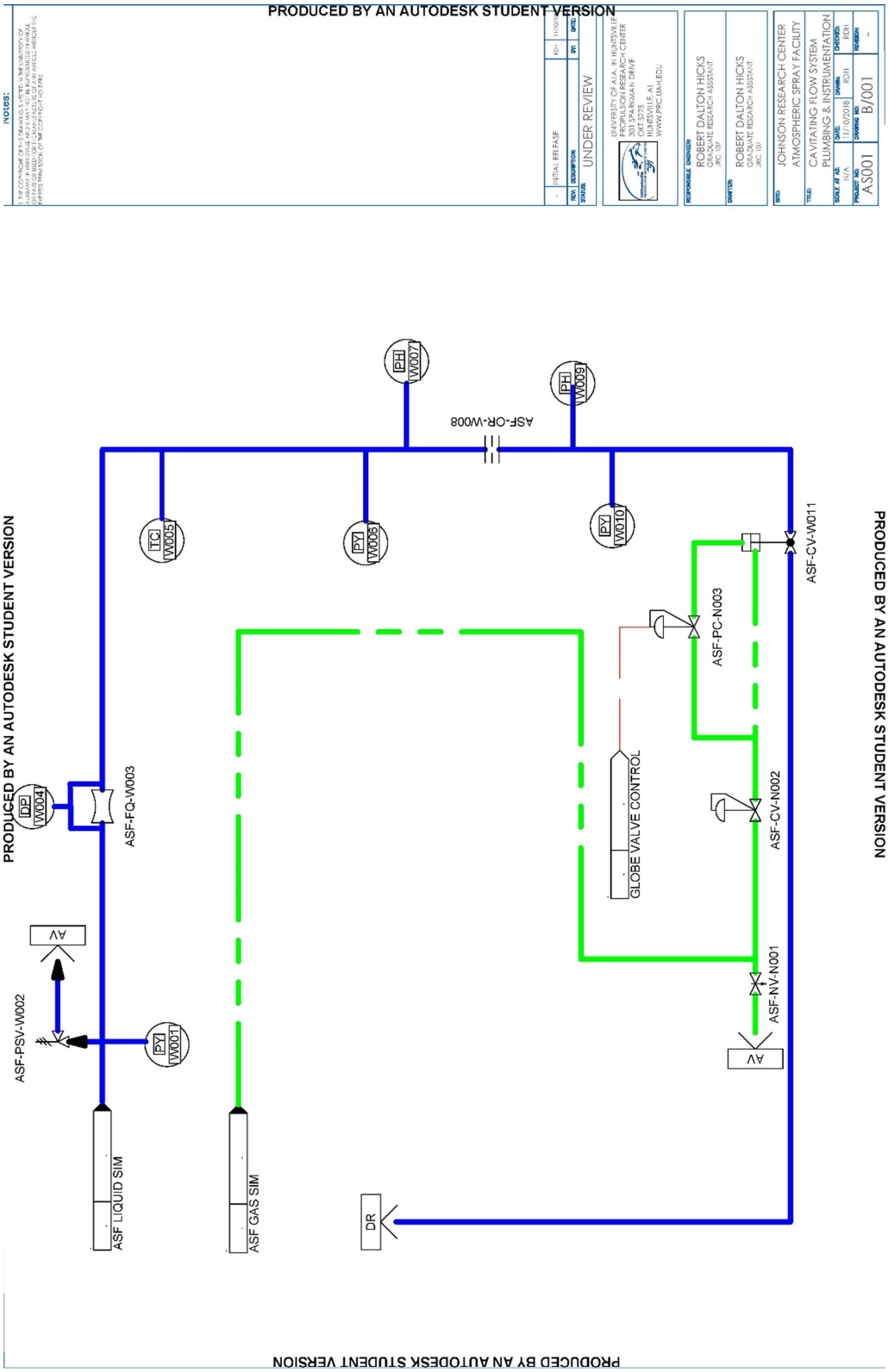

## Appendix I: Uncertainty Analysis of $C_c$

First step was to separate the $C_c$ equation into multiple functional parts

$$C_c = \left(\frac{C_E}{A_{geo}}\right)\sqrt{\frac{DP_{meter}}{P_1 - P_v}}$$

With functional parts described by separate functions

$$X_1 = P_1 - P_v$$

$$X_2 = \sqrt{X_1}$$

$$X_4 = \sqrt{DP_{meter}}$$

$$X_3 = \frac{X_4}{X_2}$$

$$X_5 = \frac{C_E}{A_{geo}}$$

$$X_6 = X_5 * X_3$$

$$A_{geo} = \frac{\pi}{4}D^2$$

These were then used to determine the uncertainty of each functional part using uncertainty propagation methods.

$$\delta X_1 = \sqrt{{\delta P_1}^2 + {\delta P_v}^2}$$

$$\delta X_2 = \frac{1}{2}\frac{\delta X_1}{|X_1|}|X_2|$$

$$\delta X_4 = \frac{1}{2}\frac{\delta DP_{meter}}{|DP_{meter}|}|X_4|$$

$$\delta X_3 = |X_3|\sqrt{\left(\frac{\delta X_4}{X_4}\right)^2 + \left(\frac{\delta X_2}{X_2}\right)^2}$$

$$\delta X_5 = |X_5|\sqrt{\left(\frac{\delta C_E}{C_E}\right)^2 + \left(\frac{\delta A_{geo}}{A_{geo}}\right)^2}$$

$$\delta X_6 = |X_6|\sqrt{\left(\frac{\delta X_5}{X_5}\right)^2 + \left(\frac{\delta X_3}{X_3}\right)^2}$$

$$\delta A_{geo} = \frac{\pi}{2} * \delta D * D$$

With the values of the constituent variable uncertainties as:

$$\delta D = 0.0005\ in$$

$$\delta C_E = 9.216E - 08\ m^2$$

$$\delta P_1 = \sigma_{P_1}$$

$$\delta P_v = \sigma_{P_v}$$

$$\delta DP_{meter} = \sigma_{DP_{meter}}$$

This is then used to find the total uncertainty of the test average $C_c$. After the total uncertainty of the test is determined the largest uncertainty value is used for each configuration as the standard deviation of the mean $C_c$. This is then used to find the 95% confidence limits of the mean using:

$$U_{mean,95\%\ conf} = \frac{t}{\sqrt{N}} * \delta X_{6,max}$$

Where *t* is the 2-tail t-test parameter for N-1 degrees of freedom. The confidence limits of the mean are therefore:

$$C_{c,mean,configuratin} \pm U_{mean,95\%\ conf}$$

Uncertainty when determining the sharp-edge equivalent value for $C_c$ is found as follows. First is to define the relation as follows.

$$C_{C,\frac{r}{d}=0} = \left[\left(\frac{1}{C_{C,\frac{r}{d}}}\right)^2 + 11.4\left(\frac{r}{d}\right)\right]^{-\frac{1}{2}}$$

Functional parts can then be described by separate functions as such,

$$X_7 = \frac{1}{C_{C,\frac{r}{d}}}$$

$$X_8 = (X_7)^2$$

$$X_9 = 11.4\left(\frac{r}{d}\right)$$

$$X_{10} = X_8 + X_9$$

$$X_{11} = (X_{10})^{-\frac{1}{2}}$$

The uncertainty propagation for each function can then be computed as such,

$$\delta X_7 = \frac{\delta C_{C,\frac{r}{d}}}{\left|C_{C,\frac{r}{d}}\right|}|X_7|$$

$$\delta X_8 = 2\frac{\delta X_7}{|X_7|}|X_8|$$

$$\delta X_9 = |11.4| * \left|\frac{r}{d}\right| * \sqrt{\left(\frac{\delta r}{r}\right)^2 + \left(\frac{\delta d}{d}\right)^2}$$

$$\delta X_{10} = \sqrt{(\delta X_8)^2 + (\delta X_9)^2}$$

$$\delta X_{11} = \left|-\frac{1}{2}\right|\frac{\delta X_{10}}{|X_{10}|}|X_{11}|$$

With the following definitions for the variable uncertainties,

$$\delta C_{C,\frac{r}{d}} = \delta X_6$$

$$\delta r = \sigma_r$$

$$\delta d = \sigma_d$$

The uncertainty for the sharp-edge equivalent value for $C_c$ can be determined. After the total uncertainty of the of the sharp-edge equivalent value of $C_c$ for each test is determined the largest uncertainty value for each configuration is used as the standard deviation of the mean sharp-edge equivalent $C_c$ for that configuration. This is then used to find the 95% confidence limits of the mean using:

$$U_{mean,95\%\,co} = \frac{t}{\sqrt{N}} * \delta X_{11,max}$$

Where *t* is the 2-tail t-test parameter for N-1 degrees of freedom. The confidence limits of the mean are therefore:

$$C_{c,\frac{r}{d}=0,mean,configuration} \pm U_{mean,95\%\,conf}$$

## Appendix J: Method and Data from Roughness Measurements

In order to measure the roughness of the parts, 6 parts were cut in half using various processes. One of these halves was then sent to the Center for Applied Optics Profilometry Lab where they performed nine tests per part as per the diagram in Figure 53. The “Left”, “Middle”, and “Right” areas are separated by 15° of angular distance and each line represents one evaluation length of 12.5-13mm.

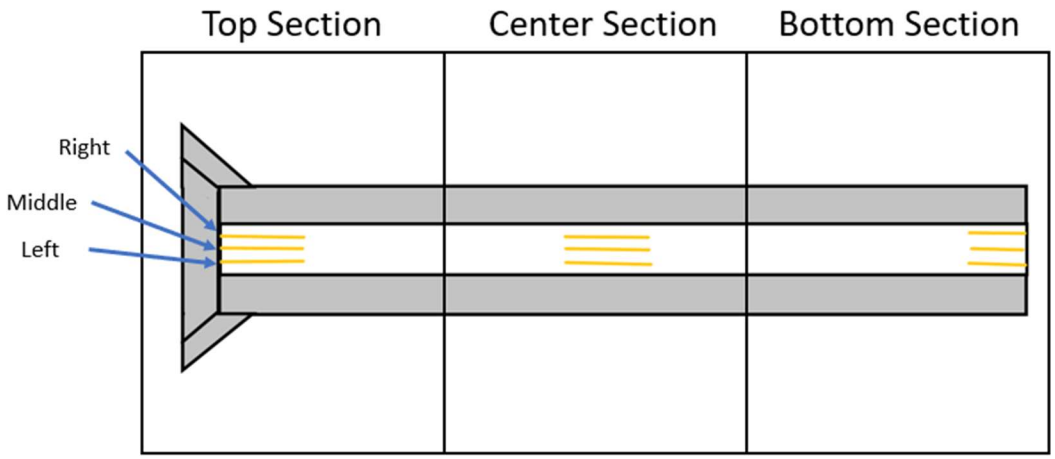


**Figure 53: Roughness Testing Locations**

A photo of the setup is shown in Figure 54 showing the orientation of the parts and the profilometer. After each evaluation length the variables are calculated. These are recorded in the tables in this appendix. With nine tests per part the roughness variations over the angular displacement and length of the part can be averaged out.

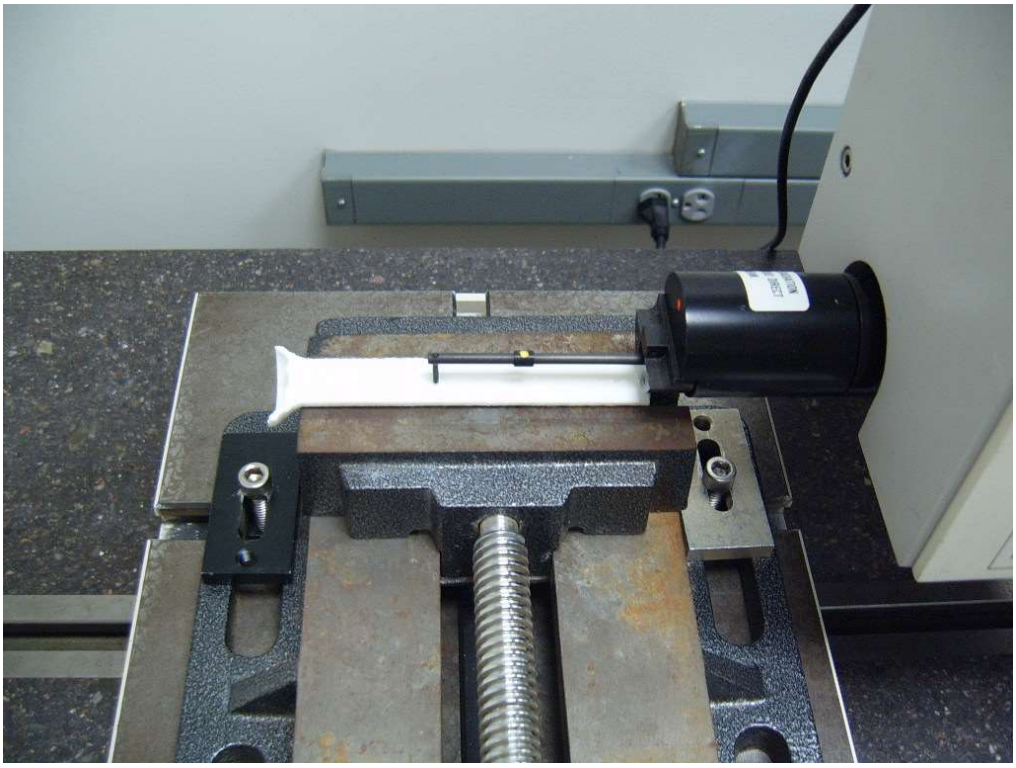

**Figure 54: Testing Setup**

**Table 12: Roughness Data – 100 µm FDM #4**

| 100 µm FDM #4 | | | | | | | | | |
|---|---|---|---|---|---|---|---|---|---|
| | LB | LC | LT | MB | MC | MT | RB | RC | RT |
| Ra [µm] | 12.485 | 13.934 | 18.93 | 13.507 | 13.19 | 14.173 | 13.673 | 12.748 | 15.756 |
| Rq [µm] | 15.89 | 17.49 | 24.872 | 17.626 | 16.557 | 17.587 | 16.821 | 15.824 | 20.236 |
| Rsk [µm] | -0.6 | -0.5 | 0.4 | -0.7 | -0.3 | 0.2 | 0 | 0.1 | -0.4 |
| Rku [µm] | 3.7 | 3.7 | 3.5 | 4.6 | 3.1 | 2.8 | 2.6 | 2.7 | 3.6 |
| Delq [°] | 30.06 | 30.09 | 27.08 | 30.29 | 30.35 | 30.83 | 29.71 | 28.9 | 31.62 |
| Lamq [µm] | 172.536 | 189.628 | 305.692 | 189.629 | 177.679 | 185.116 | 185.21 | 180.102 | 206.521 |
| S [µm] | 98.666 | 105.561 | 115.737 | 100.321 | 101.343 | 103.097 | 111.537 | 102.095 | 109.558 |
| Sm [µm] | 143.504 | 168.879 | 254.91 | 165.95 | 165.642 | 173.915 | 176.16 | 169.633 | 172.236 |
| R3z [µm] | 56.748 | 55.19 | 65.849 | 59.143 | 57.612 | 62.956 | 57.996 | 56.407 | 69.036 |
| R3y [µm] | 79.815 | 66.744 | 106.272 | 77.511 | 68.156 | 72.803 | 73.046 | 71.98 | 78.433 |
| Rp [µm] | 38.1 | 48.465 | 69.348 | 49.646 | 42.83 | 53.894 | 43.008 | 38.977 | 45.415 |
| Rv [µm] | 56.727 | 73.042 | 66.11 | 78.796 | 54.075 | 44.775 | 46.273 | 45.749 | 78.705 |
| Rt [µm] | 94.827 | 121.507 | 135.458 | 128.443 | 96.905 | 98.669 | 89.281 | 84.726 | 124.119 |
| Rtm [µm] | 79.819 | 89.068 | 95.803 | 86.053 | 80.39 | 83.895 | 75.16 | 74.67 | 91.743 |
| Rpm [µm] | 30.954 | 35.614 | 46.981 | 35.437 | 35.771 | 43.039 | 35.777 | 35.388 | 38.875 |
| Ry [µm] | 89.793 | 109.451 | 135.458 | 110.098 | 96.905 | 95.95 | 89.002 | 84.726 | 120.059 |
| Rt1 [µm] | 80.803 | 66.431 | 135.458 | 66.018 | 96.905 | 84.37 | 52.291 | 84.726 | 101.625 |
| Rt2 [µm] | 82.631 | 96.338 | 125.826 | 61.344 | 84.893 | 95.95 | 89.002 | 68.782 | 75.677 |
| Rt3 [µm] | 88.227 | 109.451 | 83.989 | 107.72 | 72.842 | 81.834 | 71.717 | 77.096 | 83.499 |
| Rt4 [µm] | 89.793 | 87.09 | 75.021 | 85.086 | 65.646 | 74.271 | 81.52 | 67.667 | 77.853 |
| Rt5 [µm] | 57.64 | 86.032 | 58.72 | 110.098 | 81.665 | 83.051 | 81.27 | 75.08 | 120.059 |

**Table 13: 200 µm FDM #3**

| 200 µm FDM #3 | | | | | | | | | |
|---|---|---|---|---|---|---|---|---|---|
| | LB | LC | LT | MB | MC | MT | RB | RC | RT |
| Ra [µm] | 19.846 | 17.763 | 17.031 | 17.135 | 16.681 | 23.575 | 19.349 | 22 | 18.592 |
| Rq [µm] | 25.855 | 21.73 | 21.376 | 20.734 | 20.456 | 30.486 | 24.933 | 28.56 | 23.588 |
| Rsk [µm] | -0.9 | -0.2 | -0.4 | -0.2 | -0.3 | 0.3 | -0.9 | -0.6 | -0.2 |
| Rku [µm] | 4.9 | 2.5 | 3.1 | 2.4 | 2.6 | 3.9 | 4.3 | 3.6 | 3.2 |
| Delq [°] | 32.99 | 33.28 | 32.13 | 32.32 | 32.97 | 32.42 | 32.97 | 31.87 | 30.75 |
| Lamq [µm] | 250.25 | 208.043 | 213.883 | 205.946 | 198.125 | 301.629 | 241.478 | 288.585 | 249.105 |
| S [µm] | 186.915 | 190.1 | 182.606 | 196.03 | 196.335 | 175.218 | 184.54 | 184.789 | 171.11 |
| Sm [µm] | 232.136 | 224.222 | 221.648 | 228.797 | 210.048 | 362.346 | 221.147 | 257.121 | 246.635 |
| R3z [µm] | 81.443 | 76.497 | 72.969 | 68.96 | 68.655 | 94.95 | 81.346 | 84.97 | 75.656 |
| R3y [µm] | 122.648 | 84.29 | 84.797 | 77.794 | 73.46 | 120.671 | 134.567 | 132.236 | 80.571 |
| Rp [µm] | 57.779 | 53.53 | 51.598 | 45.465 | 56.662 | 113.014 | 67.405 | 72.052 | 58.482 |
| Rv [µm] | 115.112 | 63.568 | 84.691 | 52.006 | 53.21 | 86.69 | 103.143 | 91.827 | 87.523 |
| Rt [µm] | 172.891 | 117.098 | 136.289 | 97.47 | 109.872 | 199.704 | 170.548 | 163.879 | 146.005 |
| Rtm [µm] | 99.043 | 94.202 | 97.48 | 79.799 | 92.949 | 148.101 | 103.374 | 131.378 | 114.735 |
| Rpm [µm] | 38.914 | 42.636 | 41.676 | 34.038 | 42.114 | 80.086 | 45.605 | 52.876 | 47.754 |
| Ry [µm] | 149.411 | 107.594 | 123.686 | 97.47 | 107.201 | 197.549 | 150.84 | 163.879 | 137.253 |
| Rt1 [µm] | 81.785 | 89.389 | 84.509 | 80.589 | 85.328 | 91 | 83.765 | 154.113 | 137.253 |
| Rt2 [µm] | 91.615 | 82.086 | 87.08 | 76.05 | 91.619 | 197.549 | 150.84 | 163.879 | 103.621 |
| Rt3 [µm] | 100.797 | 84.556 | 93.093 | 97.47 | 91.605 | 142.112 | 89.341 | 102.798 | 100.229 |
| Rt4 [µm] | 149.411 | 107.594 | 99.03 | 74.017 | 88.99 | 151.191 | 114.063 | 124.735 | 121.515 |
| Rt5 [µm] | 71.608 | 107.387 | 123.686 | 70.872 | 107.201 | 158.653 | 78.86 | 111.362 | 111.055 |

**Table 14: 300 µm FDM #1**

| 300 µm FDM #1 | | | | | | | | | |
|---|---|---|---|---|---|---|---|---|---|
| | LB | LC | LT | MB | MC | MT | RB | RC | RT |
| Ra [µm] | 39.738 | 19.018 | 26.484 | 24.559 | 25.659 | 24.927 | 25.3 | 30.324 | 25.652 |
| Rq [µm] | 57.256 | 23.781 | 31.704 | 29.231 | 30.799 | 30.206 | 30.634 | 36.806 | 30.958 |
| Rsk [µm] | 1.5 | -0.1 | -0.5 | -0.4 | -0.4 | -0.3 | -0.3 | -0.5 | -0.4 |
| Rku [µm] | 8.2 | 3 | 2.6 | 2.3 | 2.3 | 2.3 | 2.5 | 2.8 | 2.3 |
| Delq [°] | 36.57 | 22.19 | 34.2 | 32.68 | 34.89 | 33.98 | 33.49 | 34.59 | 34.25 |
| Lamq [µm] | 484.87 | 366.364 | 293.128 | 286.286 | 277.497 | 281.59 | 290.96 | 335.373 | 285.732 |
| S [µm] | 298.856 | 292.25 | 288.307 | 278.692 | 299.49 | 292.437 | 285.438 | 292.272 | 291.47 |
| Sm [µm] | 395.557 | 410.177 | 305.213 | 322.072 | 314.137 | 315.235 | 333.011 | 330.896 | 320.596 |
| R3z [µm] | 121.313 | 64.226 | 92.4 | 93.35 | 102.666 | 104.097 | 95.935 | 107.804 | 99.601 |
| R3y [µm] | 199.316 | 95.755 | 103.424 | 105.88 | 104.137 | 116.307 | 99.136 | 116.89 | 109.859 |
| Rp [µm] | 296.026 | 63.184 | 56.754 | 55.609 | 58.971 | 58.581 | 72.872 | 75.755 | 53.17 |
| Rv [µm] | 156.083 | 81.497 | 106.327 | 77.421 | 81.527 | 78.611 | 88.86 | 125.33 | 81.604 |
| Rt [µm] | 452.109 | 144.681 | 163.081 | 133.029 | 140.497 | 137.192 | 161.732 | 201.085 | 134.774 |
| Rtm [µm] | 209.65 | 98.256 | 135.737 | 116.034 | 122.996 | 122.139 | 128.231 | 159.969 | 128.926 |
| Rpm [µm] | 101.441 | 45.056 | 49.659 | 48.063 | 51.288 | 51.286 | 55.74 | 64.951 | 50.484 |
| Ry [µm] | 452.109 | 144.681 | 156.109 | 121.022 | 140.497 | 127.945 | 161.732 | 197.083 | 132.316 |
| Rt1 [µm] | 164.509 | 87.474 | 107.406 | 118.549 | 122.4 | 124.947 | 102.509 | 163.192 | 132.316 |
| Rt2 [µm] | 175.877 | 144.681 | 153.822 | 113.685 | 116.051 | 110.986 | 116.566 | 197.083 | 127.853 |
| Rt3 [µm] | 452.109 | 87.983 | 124.344 | 121.022 | 115.261 | 127.489 | 119.562 | 137.317 | 129.615 |
| Rt4 [µm] | 132.546 | 70.69 | 137.005 | 113.607 | 140.497 | 119.328 | 140.785 | 167.967 | 122.534 |
| Rt5 [µm] | 123.21 | 100.45 | 156.109 | 113.31 | 120.768 | 127.945 | 161.732 | 134.287 | 132.311 |

**Table 15: SLM #1**

| SLM #1 | | | | | | | | | |
|---|---|---|---|---|---|---|---|---|---|
| | LB | LC | LT | MB | MC | MT | RB | RC | RT |
| Ra [µm] | 6.58 | 5.443 | 5.337 | 7.088 | 4.969 | 5.229 | 8.455 | 5.14 | 5.393 |
| Rq [µm] | 8.835 | 7.045 | 6.827 | 9.476 | 6.466 | 7.096 | 11.048 | 7.185 | 7.259 |
| Rsk [µm] | 1.1 | 0.8 | 0.8 | 1.1 | 1 | 1.2 | 1.1 | 1.7 | 1.3 |
| Rku [µm] | 5.1 | 3.7 | 4 | 4.5 | 4.8 | 5.1 | 3.9 | 8 | 5.3 |
| Delq [°] | 15.82 | 14.48 | 15.9 | 18.58 | 14.16 | 15.71 | 19.75 | 15.08 | 17.17 |
| Lamq [µm] | 195.955 | 171.464 | 150.6 | 177.098 | 161.054 | 158.545 | 193.302 | 167.592 | 147.583 |
| S [µm] | 101.794 | 101.906 | 93.039 | 105.797 | 96.251 | 99.328 | 105.077 | 97.27 | 90.84 |
| Sm [µm] | 241.511 | 208.215 | 191.465 | 207.294 | 236.721 | 254.036 | 260.057 | 209.178 | 205.462 |
| R3z [µm] | 31.542 | 24.809 | 25.874 | 34.221 | 24.082 | 28.354 | 40.397 | 28.3 | 30.018 |
| R3y [µm] | 37.342 | 28.647 | 29.098 | 41.056 | 28.68 | 30.002 | 50.48 | 36.821 | 39.674 |
| Rp [µm] | 35.359 | 24.216 | 27.401 | 36.045 | 32.764 | 31.379 | 37.949 | 40.96 | 33.32 |
| Rv [µm] | 24.564 | 15.563 | 17.955 | 22.939 | 13.788 | 20.19 | 20.206 | 15.192 | 15.597 |
| Rt [µm] | 59.923 | 39.779 | 45.356 | 58.984 | 46.552 | 51.569 | 58.155 | 56.152 | 48.917 |
| Rtm [µm] | 47.597 | 35.641 | 37.362 | 50.333 | 37.026 | 39.426 | 50.362 | 40.427 | 38.53 |
| Rpm [µm] | 31.022 | 22.254 | 24.344 | 33.014 | 24.948 | 26.735 | 31.845 | 27.578 | 25.325 |
| Ry [µm] | 59.024 | 38.345 | 41.128 | 54.084 | 43.433 | 45.396 | 56.977 | 56.152 | 48.917 |
| Rt1 [µm] | 51.694 | 38.345 | 38.588 | 50.541 | 41.752 | 45.396 | 56.977 | 37.761 | 36.219 |
| Rt2 [µm] | 42.786 | 35.528 | 41.128 | 46.597 | 39.285 | 30.554 | 42.733 | 29.137 | 36.769 |
| Rt3 [µm] | 48.243 | 33.97 | 37.649 | 51.084 | 43.433 | 41.447 | 55.117 | 56.152 | 37.64 |
| Rt4 [µm] | 59.024 | 38.146 | 36.092 | 49.357 | 33.587 | 40.245 | 40.455 | 45.72 | 48.917 |
| Rt5 [µm] | 36.237 | 32.218 | 33.353 | 54.084 | 27.072 | 39.487 | 56.528 | 33.365 | 33.104 |

**Table 16: Subtractive #1**

| Subtractively Manufactured #1 | | | | | | | | | |
|---|---|---|---|---|---|---|---|---|---|
| | LB | LC | LT | MB | MC | MT | RB | RC | RT |
| Ra [µm] | 0.382 | 0.113 | 0.483 | 0.393 | 0.123 | 0.562 | 0.369 | 0.122 | 0.8 |
| Rq [µm] | 0.478 | 0.145 | 0.606 | 0.5 | 0.164 | 0.67 | 0.47 | 0.162 | 1.016 |
| Rsk [µm] | 0.2 | -0.3 | -0.5 | 0.3 | 0.7 | -0.3 | -0.3 | 0.5 | -1.1 |
| Rku [µm] | 3.1 | 6.8 | 2.7 | 3.1 | 5.2 | 2.2 | 3.8 | 5.1 | 5.5 |
| Delq [°] | 0.38 | 0.28 | 0.27 | 0.3 | 0.25 | 0.3 | 0.38 | 0.23 | 0.54 |
| Lamq [µm] | 456.758 | 184.632 | 806.066 | 593.253 | 234.915 | 794.59 | 444.32 | 253.265 | 681.301 |
| S [µm] | 70.426 | 58.941 | 82.57 | 59.427 | 54.79 | 94.888 | 66.302 | 56.198 | 174.137 |
| Sm [µm] | 527.821 | 257.31 | 1.157 | 583.055 | 231.297 | 1.331 | 690.236 | 373.647 | 1.485 |
| R3z [µm] | 1.445 | 0.491 | 1.702 | 1.266 | 0.602 | 1.932 | 1.187 | 0.656 | 1.943 |
| R3y [µm] | 2.329 | 0.619 | 2.201 | 1.761 | 0.796 | 2.329 | 2.25 | 0.947 | 2.653 |
| Rp [µm] | 1.477 | 0.438 | 1.24 | 1.475 | 0.693 | 1.186 | 1.229 | 0.638 | 2.29 |
| Rv [µm] | 1.2 | 1.18 | 1.496 | 1.104 | 0.682 | 1.922 | 1.996 | 0.594 | 4.781 |
| Rt [µm] | 2.677 | 1.618 | 2.737 | 2.578 | 1.375 | 3.108 | 3.225 | 1.232 | 7.072 |
| Rtm [µm] | 1.682 | 0.81 | 1.909 | 1.429 | 0.778 | 2.422 | 1.647 | 0.678 | 3.171 |
| Rpm [µm] | 0.877 | 0.289 | 0.868 | 0.699 | 0.339 | 0.99 | 0.696 | 0.293 | 1.524 |
| Ry [µm] | 2.677 | 1.451 | 2.44 | 1.932 | 1.004 | 2.529 | 3.225 | 1.031 | 7.072 |
| Rt1 [µm] | 1.314 | 0.731 | 2.409 | 1.24 | 1.004 | 2.354 | 1.423 | 1.031 | 7.072 |
| Rt2 [µm] | 1.208 | 1.451 | 1.37 | 1.144 | 0.643 | 2.199 | 0.7 | 0.502 | 2.284 |
| Rt3 [µm] | 1.782 | 0.721 | 2.44 | 1.447 | 0.543 | 2.506 | 1.509 | 0.338 | 2.437 |
| Rt4 [µm] | 2.677 | 0.485 | 1.781 | 1.381 | 0.931 | 2.529 | 3.225 | 0.633 | 1.895 |
| Rt5 [µm] | 1.428 | 0.663 | 1.544 | 1.932 | 0.771 | 2.523 | 1.376 | 0.887 | 2.165 |

**Table 17: Subtractive #2**

| Subtractively Manufactured #2 | | | | | | | | | |
|---|---|---|---|---|---|---|---|---|---|
| | LB | LC | LT | MB | MC | MT | RB | RC | RT |
| Ra [µm] | 0.216 | 0.228 | 0.583 | 0.205 | 0.157 | 0.209 | 0.223 | 0.127 | 0.408 |
| Rq [µm] | 0.346 | 0.285 | 1.018 | 0.284 | 0.206 | 0.258 | 0.29 | 0.166 | 0.663 |
| Rsk [µm] | -1.3 | -0.2 | -3.1 | -0.2 | 0.1 | -0.6 | 0 | 0.3 | -2.8 |
| Rku [µm] | 12.8 | 2.6 | 12.5 | 6.1 | 3.6 | 3.2 | 4.3 | 3.4 | 11.3 |
| Delq [°] | 0.63 | 0.32 | 0.39 | 0.55 | 0.29 | 0.4 | 0.5 | 0.28 | 0.52 |
| Lamq [µm] | 196.297 | 321.143 | 947.681 | 187.417 | 255.181 | 231.641 | 207.914 | 214.62 | 455.163 |
| S [µm] | 60.938 | 54.521 | 89.635 | 58.236 | 51.876 | 57.004 | 52.536 | 48.038 | 72.809 |
| Sm [µm] | 213.253 | 288.855 | 740.209 | 239.929 | 232.591 | 288.223 | 242.577 | 190.758 | 629.016 |
| R3z [µm] | 1.199 | 0.74 | 1.245 | 0.884 | 0.711 | 0.795 | 0.819 | 0.525 | 1.305 |
| R3y [µm] | 2.302 | 0.896 | 3.237 | 1.363 | 0.884 | 0.988 | 1.228 | 0.828 | 2.993 |
| Rp [µm] | 1.739 | 0.606 | 0.812 | 0.984 | 0.596 | 0.565 | 1.006 | 0.505 | 0.758 |
| Rv [µm] | 2.285 | 0.795 | 5.308 | 1.748 | 0.695 | 1.024 | 1.399 | 0.564 | 3.284 |
| Rt [µm] | 4.024 | 1.401 | 6.12 | 2.732 | 1.291 | 1.588 | 2.405 | 1.068 | 4.042 |
| Rtm [µm] | 1.817 | 0.974 | 2.129 | 1.22 | 0.873 | 1.075 | 1.247 | 0.725 | 2.072 |
| Rpm [µm] | 0.722 | 0.422 | 0.627 | 0.501 | 0.42 | 0.402 | 0.589 | 0.306 | 0.561 |
| Ry [µm] | 4.024 | 1.401 | 5.546 | 2.185 | 1.078 | 1.33 | 1.774 | 0.926 | 3.49 |
| Rt1 [µm] | 1.092 | 0.828 | 5.546 | 1.353 | 0.739 | 1.33 | 1.099 | 0.535 | 3.49 |
| Rt2 [µm] | 1.418 | 0.951 | 0.792 | 0.804 | 0.537 | 0.882 | 0.973 | 0.918 | 1.024 |
| Rt3 [µm] | 4.024 | 0.74 | 1.822 | 0.986 | 0.974 | 1.002 | 1.13 | 0.926 | 1.789 |
| Rt4 [µm] | 0.832 | 1.401 | 1.386 | 0.771 | 1.078 | 0.909 | 1.26 | 0.616 | 2.962 |
| Rt5 [µm] | 1.716 | 0.948 | 1.101 | 2.185 | 1.04 | 1.252 | 1.774 | 0.628 | 1.097 |

# Appendix K: Experiment Procedure

UAH Propulsion Research Center

EXPERIMENTAL PROCEDURE FOR:

***Axisymmetric Cavitation Testing***

Revision: A

Test Location: JRC Atmospheric Spray Facility

Test Date: _____

Test Time Start: _____ Finish: _____

Notes: _____

_____

**This Procedure Contains the Following Hazards**

| | |
|---|---|
| | Radioisotopes or X-Rays |
| | Carcinogenic/mutagenic/teratogenic chemicals |
| X | Pressurized Gases |
| | Propellants/Combustion |
| X | High Electrical Voltage and/or Current |

| | |
|---|---|
| | Lasers |
| | Microbial and viral agents |
| | Recombinant DNA/RNA molecules |
| | Animal Subjects |

**R Dalton Hicks:** _____ **Date:** _____

**Author**

## SECTION I. TEST PROCEDURES

### PRETEST FACILITY PREPARATION

- 1 If not already performed, perform PRC-SOP-JRC-032-A2
- 2 Ensure all personnel are wearing personal protective equipment (PPE).
- 3 Turn 3-way Gas Sim diverter valve to Pressurize.
- 4 Open Gas Sim Fire Valve.
- 5 Set Gas Sim Regulator to Full open.
- 6 Set Control Valve Regulator to 65 psig.

### EXPERIMENT PROCEDURE

- 7 Open LabView.
- 8 Run: _____.vi
- 9 Verify nominal pressure readings of zero
- 10 Verify nominal thermocouple readings
- 11 Verify/Install Test Article for Next Test
- 12 Log in Test Matrix
- 13 Choose Filename for Test and log in Test Matrix
- 14 Enable Datalogging
- 15 Verify Backpressure Valve is open
- 16 Open Liquid Sim Fire
- 17 Click “Start Routine”
- 18 Once Routine is complete Shut off Liquid Sim Fire
- 19 Disable Logging
- 20 Switch Pressure/Vent to Vent
- 21 Start Tank Fill Procedure
- 22 During Tank Fill Replace Test Article with next Article
- 23 Repeat Steps 12-22 until Testing has completed for the day

## FACILITY SHUTDOWN PREPARATION

- 24 Back out Control Valve Regulator
- 25 Close Gas Sim Fire
- 26 Vent Gas Sim Line
- 27 Back Out Gas Sim Regulator
- 28 Continue with the rest of the steps in PRC-SOP-JRC-032-A2

## Appendix L: SLM Printing Parameters

Material: Monel K500

Powder Size: -45/+15, Average of 31.8 μm

Power: 180W

Scan Speed: 600 mm/sec

Hatch Spacing: 0.105 mm

Layer thickness: 0.03 mm

Pattern: 3 mm island pattern, with islands offset 1 mm in the x and y directions every layer

# References


[1] B. Ebrahimi *et al.*, "Characterization of high-pressure cavitating flow through a thick orifice plate in a pipe of constant cross section," *Int. J. Therm. Sci.*, vol. 114, pp. 229–240, Apr. 2017.

[2] O. Reynolds, "The Causes of the Racing of the Engines of Screw Steamers Investigated Theoretically and by Experiment.," *Trans Inst Nav. Arch*, vol. 14, pp. 56–67, 1873.

[3] F. Echouchene, H. Belmabrouk, L. Le Penven, and M. Buffat, "Numerical simulation of wall roughness effects in cavitating flow," *Int. J. Heat Fluid Flow*, vol. 32, no. 5, pp. 1068–1075, Oct. 2011.

[4] C. E. Brennen, *Cavitation and Bubble Dynamics*. Cambridge: Cambridge University Press, 2013.

[5] K. Peng, S. Tian, G. Li, and H. Alehossein, "Mapping cavitation impact field in a submerged cavitating jet," *Wear*, vol. 396–397, pp. 22–33, Feb. 2018.

[6] J. M. Desantes, R. Payri, F. J. Salvador, and J. Gimeno, "Measurements of Spray Momentum for the Study of Cavitation in Diesel Injection Nozzles," presented at the SAE 2003 World Congress & Exhibition, 2003.

[7] M. S. Plesset, "Tensile Strength of Liquids," California Institute of Technology, Pasadena, California, Contract Report 85–47, Apr. 1969.

[8] W. H. Nurick, "Orifice Cavitation and its Effect on Spray Mixing," *J. Fluids Eng.*, vol. 98, no. 4, pp. 681–687, 1976.

[9] *NIST Thermophysical Properties of Fluid Systems*. National Institute of Standards and Technology, 2018.

[10] R. Knapp, "Recent Investigations of the Mechanics of Cavitation and Cavitation Damage," *Trans. ASME*, vol. 77, pp. 1045–1054, 1955.

[11] F. G. Hammitt, "Damage to Solids Caused by Cavitation," *Philos. Trans. R. Soc. Math. Phys. Eng. Sci.*, vol. 260, no. 1110, pp. 245–255, Jul. 1966.

[12] D. R. Stinebring, R. E. A. Arndt, and J. W. Holl, "Scaling of Cavitation Damage," *J. Hydronautics*, vol. 11, no. 3, pp. 67–73, Jul. 1977.

[13] N. K. Bourne and J. E. Field, "A High-Speed Photographic Study of Cavitation Damage," *J. Appl. Phys.*, vol. 78, no. 7, pp. 4423–4427, Oct. 1995.

[14] A. Thiruvengadam, "A Comparative Evaluation of Cavitation Damage Test Devices," Office of Naval Research, Department of the Navy, Cameron Station, Alexandria, Virginia, Technical Report 233–2, Dec. 1963.

[15] D. R. Stinebring, J. W. Holl, and R. E. A. Arndt, "Two Aspects of Cavitation Damage in the Incubation Zone: Scaling by Energy Considerations and Leading Edge Damage," *J. Fluids Eng.*, vol. 102, no. 4, p. 481, 1980.

[16] D. P. Schmidt and M. L. Corradini, "Analytical Prediction of the Exit Flow of Cavitating Orifices," *At. Sprays*, vol. 7, no. 6, pp. 603–616, 1997.

[17] G. Bayada, S. Martin, and C. Vázquez, "An Average Flow Model of the Reynolds Roughness Including a Mass-Flow Preserving Cavitation Model," *J. Tribol.*, vol. 127, no. 4, p. 793, 2005.

[18] S. Pope, *Turbulent Flows*. Cambridge University Press, 2017.

[19] B. Stutz, "Influence of Roughness on the Two-Phase Flow Structure of Sheet Cavitation," *J. Fluids Eng.*, vol. 125, no. 4, p. 652, 2003.

[20] M. Hitt, D. Lineberry, V. Ahuja, and R. Frederick, “Experimental Investigation of Cavitation Induced Feedline Instability from an Orifice,” in *48th AIAA/ASME/SAE/ASEE Joint Propulsion Conference & Exhibit*, Atlanta, Georgia, 2012.
[21] P. Moussou, Ph. Testud, Y. Aurégan, and A. Hirschberg, “An Acoustic Criterion for the Whistling of Orifices in Pipes,” in *Volume 4: Fluid-Structure Interaction*, San Antonio, Texas, USA, 2007, pp. 345–353.
[22] P. Testud, A. Hirschberg, P. Moussou, and Y. Aurégan, “Cavitating Orifice: Flow Regime Transitions and Low Frequency Sound Production,” in *Volume 4: Fluid Structure Interaction*, Denver, Colorado, USA, 2005, vol. 4, pp. 437–445.
[23] A. Jocksch and C. P. Gravett, “Effect of the Vortex Whistle on the Discharge Coefficient of Orifices,” *AIAA J.*, vol. 42, no. 5, pp. 1048–1050, May 2004.
[24] M. K. Roul and S. K. Dash, “Single-Phase and Two-Phase Flow Through Thin and Thick Orifices in Horizontal Pipes,” *J. Fluids Eng.*, vol. 134, no. 9, p. 091301, 2012.
[25] P. Testud, Y. Aurégan, P. Moussou, and A. Hirschberg, “The whistling potentiality of an orifice in a confined flow using an energetic criterion,” *J. Sound Vib.*, vol. 325, no. 4–5, pp. 769–780, Sep. 2009.
[26] R. C. Chanaud, “Experiments Concerning the Vortex Whistle,” *J. Acounstical Soc. Am.*, vol. 35, no. 7, pp. 953–960, 1963.
[27] K. Sato and Y. Saito, “Unstable Cavitation Behabvior in a Circular-Cylindrical Orifice Flow,” *JSME Int. J. Ser. B Fluids Therm. Eng.*, vol. 45, no. 3, pp. 638–645, 2002.
[28] W. E. Howland and J. D. Richetta, “Derivation of Coefficients of Orifices,” *J. Frankl. Inst.*, vol. 223, no. 1, pp. 83–94, Jan. 1937.
[29] J. Cui, H. Lai, K. Feng, and Y. Ma, “Quantitative analysis of the minor deviations in nozzle internal geometry effect on the cavitating flow,” *Exp. Therm. Fluid Sci.*, vol. 94, pp. 89–98, Jun. 2018.
[30] D. P. Schmidt, C. J. Rutland, and M. L. Corradini, “A Numerical Study of Cavitating Flow Through Various Nozzle Shapes,” presented at the International Spring Fuels & Lubricants Meeting & Exposition, 1997.
[31] T. Wohlers and T. Gornet, “History of Additive Manufacturing,” p. 38, 2016.
[32] D.-K. Ahn, S.-M. Kwon, and S.-H. Lee, “Expression for Surface Roughness Distribution of FDM Processed Parts,” in *2008 International Conference on Smart Manufacturing Application*, Goyang-si, South Korea, 2008, pp. 490–493.
[33] G. Strano, L. Hao, R. M. Everson, and K. E. Evans, “Surface roughness analysis, modelling and prediction in selective laser melting,” *J. Mater. Process. Technol.*, vol. 213, no. 4, pp. 589–597, Apr. 2013.
[34] J. Kacmarcik, D. Spahic, K. Varda, E. Porca, and N. Zaimovic-Uzunovic, “An investigation of geometrical accuracy of desktop 3D printers using CMM,” *IOP Conf. Ser. Mater. Sci. Eng.*, vol. 393, p. 012085, Aug. 2018.
[35] J. Hanssen, “Fortus 900mc Accuracy Study.” Stratasys, 2013.
[36] *MATLAB Release 2017a*. Natick, Massachusetts: The MathWorks, Inc., 2017.
[37] F. White, *Fluid Mechanics*, 4th ed. New York, NY: McGraw-Hill, 1998.